Dissertation

submitted to the
Combined Faculties for the Natural Sciences and for Mathematics
of the Ruperto-Carola University of Heidelberg, Germany
for the degree of
Doctor of Natural Sciences

Put forward by
Christoph Alexander Brand
born in Karlsruhe
Oral examination: 03.02.2016

Forces and Flow of Contractile Networks

Referees: Prof. Dr. Ulrich Schwarz
Prof. Dr. Heinz Horner

Forces and Flow of Contractile Networks

Biological cells use contractile networks of cross-linked semiflexible biopolymers, the so-called actin cytoskeleton, to control their shapes and to probe the mechanical properties of their environment. These processes are essential for cell survival and function. In this thesis we present a general framework to model two-dimensional contractile networks embedded in either two- or three-dimensional space. A surface representation with triangles and edges allows us to explicitly address the heterogeneity of biopolymer networks. In adherent cells, thick polymer bundles called stress fibers strongly influence cellular mechanics. We establish methods to assess their contribution to traction force generation, intracellular force balance, and intracellular flow from experimental data. Further, we develop a theory for the excitable nature of the cell cortex, which is a thin polymer layer lining the inner side of the cell membrane, and show how it is related to global cell shape changes.

Kräfte und Fluss von kontraktilen Netzwerken

Biologische Zellen benutzen kontraktile Netzwerke von miteinander verknüpften, semiflexiblen Biopolymeren, um ihre Form zu steuern und die mechanischen Eigenschaften ihrer Umgebung zu erkunden. Diese Prozesse sind entscheidend für das Überleben und die Funktionsfähigkeit der Zellen. Die vorliegende Arbeit zeigt einen allgemeinen Rahmen auf, um zweidimensionale kontraktile Netzwerke zu modellieren, die in den zwei- oder dreidimensionalen Raum eingebettet sind. Eine Beschreibung von Oberflächen mit Dreiecken und Kanten ermöglicht es uns, explizit auf die Heterogenität von Biopolymernetzwerken einzugehen. In adhärierenden Zellen beeinflussen dicke Polymerbündel, die Stressfasern genannt werden, die Zellmechanik. Wir führen Methoden ein, um deren Einfluss auf die Erzeugung von Traktionskräften, das intrazelluläre Kräftegleichgewicht und den intrazellulären Fluss auf der Grundlage experimenteller Daten festzustellen. Darüber hinaus entwickeln wir eine Theorie für die Anregbarkeit des Zellkortexes, einer dünnen Polymerschicht auf der Innenseite der Zellmembran, und zeigen wie diese mit globalen Veränderungen der Zellform zusammenhängt.

Contents

List of Collaboration Partners

Studies of cellular mechanics benefit from a close collaboration between theory and experiment. For this reason we worked together with experimental groups in all of the projects presented in this thesis. Here we explicitly list which partners have contributed to which projects.

Chapter	Experiments	Collaboration partners
3	Ablation of stress fibers at the cell periphery	Elena Kassianidou and Sanjay Kumar, Kumar Laboratory, University of California, Berkeley
3	Cell shapes in three-dimensional scaffolds	Benjamin Richter, Mona Jaggy, and Martin Bastmeyer, Bastmeyer group, Karlsruher Institut für Technologie, Karlsruhe
4	U2OS-cells on soft elastic substrates	Jonathan Stricker, Patrick Oakes, and Margaret Gardel, Gardel Laboratory, University of Chicago, Chicago
5	Spatially controlled force generation in 3T3 fibroblasts	Patrick Oakes and Margaret Gardel, Gardel Laboratory, University of Chicago, Chicago, and Elizabeth Wagner and Michael Glotzer, Glotzer Laboratory, University of Chicago, Chicago
6	Surface contraction waves in starfish oocytes	Johanna Bischof and Peter Lénárt, Lénárt Laboratory, European Molecular Biology Laboratory, Heidelberg

Table 1: List of collaboration partners

1 Introduction

1.1 Fundamentals of Cellular Mechanics

Cellular forces are essential for our lives. We need them to open our eyes in the morning when we wake up, to stand up, and to eat breakfast. They are necessary to gather food, to breath and to pump blood through our vessels. Many of the 10^{13} cells in our body have to work together in order to accomplish these tasks that require forces in the range of $1 - 10^3 N$ and act on the length scale of meters. Forces are also very important on the scale of single cells though, which is on the order of $30\mu m$. For instance, when a suspended cell first makes contact with a surface, it needs forces in order to adhere to it and spread. Moreover, cells actively probe the mechanical properties of their surrounding and adapt to what they sense. If mesenchymal stem cells are seeded on substrates of the stiffness of brain, they differentiate into brain cells. However, if the same cells adhere to stiffer bone-like substrates, they become bone cells [1]. Conversely, if cells cannot exert forces to their environment over longer times, they die [2]. During cell division forces are necessary to pull the chromosomes apart from each other, and for the mechanical division process itself. Forces generated by single cells are in the range of μN.

Not only do cells actively generate forces, but they are also subject to mechanical stresses exerted from the extracellular environment. It is important for them to withstand these forces in order to maintain the integrity of intracellular organelles like the nucleus to guarantee their functionality. Thus they have developed networks of polymeric filaments that provide them with rigidity, which are summarized as the cytoskeleton (CSK). With the help of the CSK, the cell defines a reference shape in a fluid environment and resists stretch and shear; the cell behaves like an elastic solid. However, being purely elastic would hinder the cell in vital processes. Often cells need to adapt their shape, for example when they grow, divide or migrate. To allow for rapid reorganization, the CSK undergoes continuous turn-over, which means that it permanently dis- and reassembles. Thus the reference shape changes with time; the cell behaves like a viscoelastic-plastic fluid.

Cells naturally live in a three-dimensional environment. Some are suspended without external connections, like for example eggs or red blood cells (RBCs). Others sense

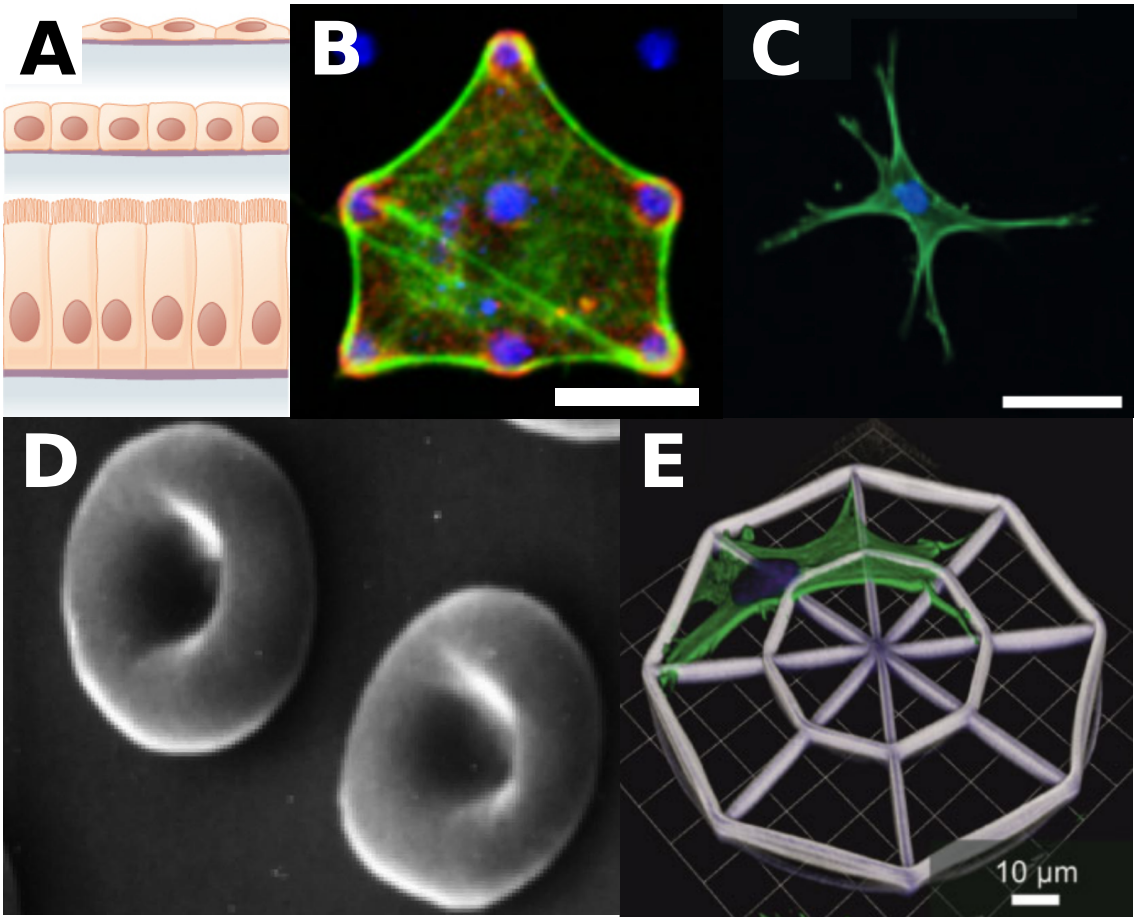

Figure 1.1: Cellular shapes. (A) Epithelial cells show typically squamous (top), cuboidal (middle), or columnar (bottom) shapes. Taken from [3]. (B) Fibroblast on two-dimensional micropatterned substrate with circular invaginations at the periphery. Functionalized substrate regions the cell can adhere to are colored blue. Scale bar: $10\mu m$. Taken from [4]. (C) Human Mesenchymal Stem Cell in engineered three-dimensional matrix. Scale bar: $50\mu m$. Taken from [5]. (D) Biconcave red blood cells. Taken from [6] (E) Cell in three-dimensional scaffold. Taken from [7].

and interact with surrounding cells in all spatial directions and form tight tissues. Dependent on their environment and function, cells assume characteristic shapes. In animal tissue, epithelial cells that line inner and outer surfaces in the body are usually cuboidal, columnar, or squamous (thin and flat), Fig. 1.1 A. Each of these configurations allows for dense packing and therefore a protective effect. Fibroblasts, which are cells that form connective tissue, exhibit circular invaginations in their contour when they are cultured on patterned substrates where they can only adhere to functionalized parts of the flat surface (Fig. 1.1 B). In fact, circular arcs also occurs for many other cell types and even on the scale of tissues [8]. Some cells form long extensions to connect to each other (Fig. 1.1 C). Egg cells are typically spherical, while RBCs maintain a characteristic biconcave discocyte shape under

physiological conditions (Fig. 1.1 D). In all cases, cell shape is an expression of intra- and intercellular mechanics. Observing the shape can therefore help to deduce the cell's state and is sometimes used to diagnose diseases. For instance, RBCs lose their discocyte shape when they get infected with malaria parasites or if their CSK is altered, e. g. by hereditary diseases like sickle cell anemia [6, 9].

Cell shapes can also be used to infer mechanical forces. This approach was recently taken for fibroblasts that were cultured on flat substrates with specific regions the cells could adhere to [4]. The use of flat substrates is traditionally very common in cell culture and facilitates imaging. It breaks the symmetry of space though and constricts adhesion to the ventral surface of the cell (the surface in contact with the substrate). In the aforementioned work, the fibroblasts show circular invaginations in their contour (Fig. 1.1 B), which represent a force balance between a line tension along the contour and a surface tension acting in the normal direction. By theoretical modeling, one can estimate the forces that lead to these shapes [4, 10]. Recently it has become possible to build three-dimensional scaffolds that allow to observe cells in a controlled geometry in three dimensions (Fig. 1.1 E).

Cells exhibit active, elastic, and viscous properties that determine their shape and functions. They control their mechanics mainly via the CSK, which is a dynamic viscoelastic network with embedded active molecular motors. As the interactions between the different components are very complex, theoretical modeling is needed to carve out the relevant factors and quantify experimental results. In order to understand the details of cellular forces, some knowledge about the molecular structure of the CSK is required, which we review in the following section. We then summarize previous theoretical approaches and outline how this work helps to understand CSK mechanics.

1.2 The Cytoskeleton

The CSK consists of three parts, namely microtubules, intermediate filaments, and the actin-CSK. In the case of microtubules, the protein tubulin polymerizes into polar protofilaments that in turn form polar hollow cylindrical structures. These structures have a persistence length of several millimeters [12], which means that they are very hard to bend; in fact, if microtubules were an homogeneous and isotropic elastic material, the corresponding Young's modulus would be about the same as Plexiglas [13]. Microtubules are important for cell division, as they form the spindle apparatus which segregates the chromosomes. They also provide cargo routes on which specialized motor proteins can walk for directed intracellular transport [14]. Tubulin is present in all animal cells [12].

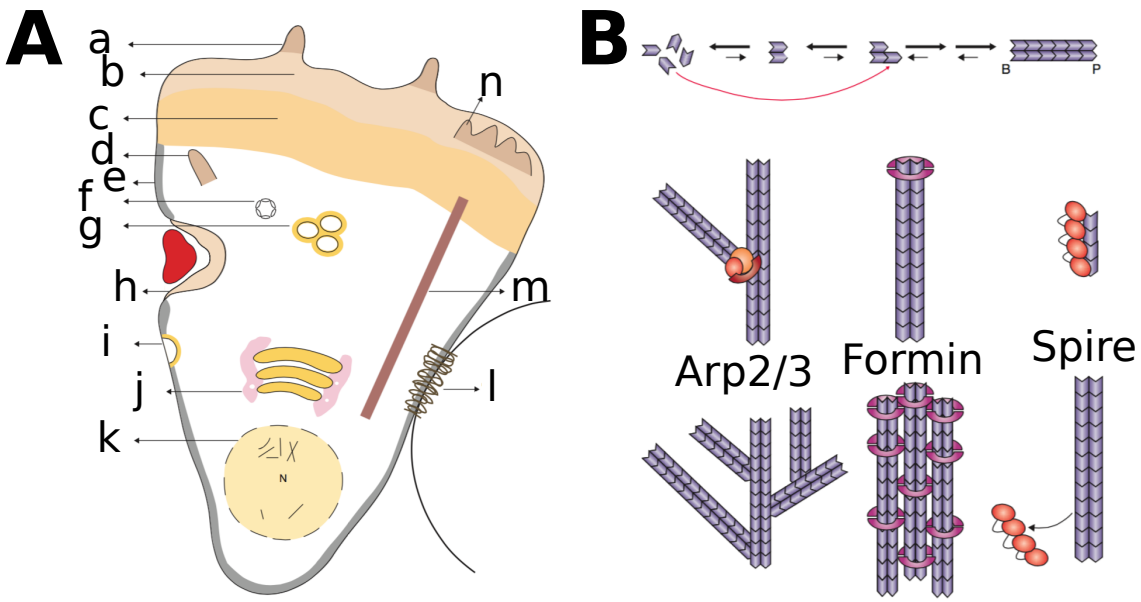

Figure 1.2: Actin cytoskeleton. (A) Actin-based structures include *a.* filopodium, *b.* lamellopodium, *c.* lamellum, *d.* microvilus, *e.* cortical actin, *f.* podosome, *g.* endosome, *h.* phagocytic cup, *i.* endocytic pit, *j.* Golgi-associated actin, *k.* nuclear actin, *l.* cadherin-based adherens juctions, *m.* stress fibers, *n.* ruffles. (B) *Top*: a nucleation factor is needed for initial assembly of F-actin (steps along the red arrow). *Middle*: Different assembly factors lead to different characteristics of single filaments or bundles and networks (*bottom*). Images adapted from [11].

Intermediate filaments (IFs) are fibrous biopolymers that form bundles and networks that provide the cell with mechanical rigidity [15]. IFs have obtained their name from the fact that their cross-section diameter of $10nm$ is smaller than the one of microtubules, which is about $20nm$, but thicker than that of actin filaments ($8nm$) [12]. Different than the other two main CSK constituents, IFs do not occur in all animal cells and the monomeric constituents vary. Malfunctions are known to lead to, for example, skin diseases [16].

As the name suggests, the actin-CSK is mainly built from the protein actin. It plays an important role in many processes in the cell (Fig. 1.2 A). In its monomeric form, actin is a globular protein of $4nm$ in diameter and is referred to as G-actin. In its center, actin provides a binding site fore adenosine triphosphate (ATP), which serves as an energy source in cells, or its inactive form adenosine diphosphate (ADP). In the actin monomers the ATP-bound state dominates, since usually there is more ATP than ADP in the cytoplasm [12]. The molecular structure is asymmetric: the direction into which the cleft towards the ATP/ADP binding site points is referred to as the *plus* or *barbed* end, while the opposite direction is called the *minus* or *pointed* end.

Actin monomers can assemble into double-helical filaments called F-actin (Fig. 1.2

B, top). In F-actin, all monomers are aligned such that all plus and minus ends point in the same direction, respectively. We denote the on and off rates at the plus end as k_{on}^{+}, k_{off}^{+}, and as k_{on}^{-}, k_{off}^{-} at the minus end. As the binding interface and therefore the free energy associated with binding is the same on both sides, the ratio of on and off rates has to be equal if ADP/ATP hydrolysis is not considered [17],

$$\frac{k_{on}^{+}}{k_{off}^{+}} = \frac{k_{on}^{-}}{k_{off}^{-}} \ . \tag{1.1}$$

However, the monomers have to undergo a conformational change when they bind to the filament which leads to a higher k_{on} at the plus end than at the minus end [12]. If the concentration of G-actin is high, both ends grow.

While ATP is very stable in G-actin, its probability to be hydrolyzed to ADP increases in the filamentous form. Thus it is possible for a certain range of G-actin concentration that the typical time between two monomer bindings at the plus end t_+ is larger than the mean ATP hydrolysis time t_H, $t_+ > t_H$, while the binding time at the minus end t_- is smaller than t_H, $t_- < t_H$. Thus it is more likely to find ADP-bound actin at the minus end of the filament than at the plus end. Further, the ADP-bound actin monomers are more likely to leave the filament, which implies that the off rate is higher at the minus end and Eq. 1.1 does not hold any more. It follows that the critical free monomer concentration for the plus end to grow is now lower than the critical concentration at the minus end. If the actual G-actin concentration lies between the two, the filament grows at the plus end and shrinks at the minus end at the same time. This effect is called treadmilling [18].

In the next structural step, F-actin can form various types of networks and bundles, which are present at different locations within the cell (Fig. 1.2 B, middle and bottom). The actin cortex, for instance, lies directly underneath the plasma membrane and forms a dense but thin network that provides the cell hull with in-plane elasticity. Another example are actin stress fibers (SFs), which are tight, highly cross-linked actin bundles. There are many more forms of actin structures in animal cells, including filopodia, lamellopodia, lamella, dorsal ruffles, microvilli, podosomes, endosomes, phagocytic cups, endocytic pits, Gogli-associated actin, nuclear actin, and adherens junctions (Fig. 1.2 A). We refer the interested reader to [11] to learn more about these structures and their assembly mechanisms. Briefly, the assembly of F-actin into the different structures is guided by so-called assembly factors. The first to be found was the protein complex Arp2/3, which serves as a nucleation point for new actin filament assembly on the side of an existing one with a branching angle of 70° (Fig. 1.2 B)[11]. Thus Arp2/3 leads to a dendritic structure as in the case of the lamellopodium, for example. Other actin nucleators are proteins of the formin and spire class. While the former enhance straight filament assembly, the latter can cross-link multiple actin filaments [11]. Cross-linking is very important for both

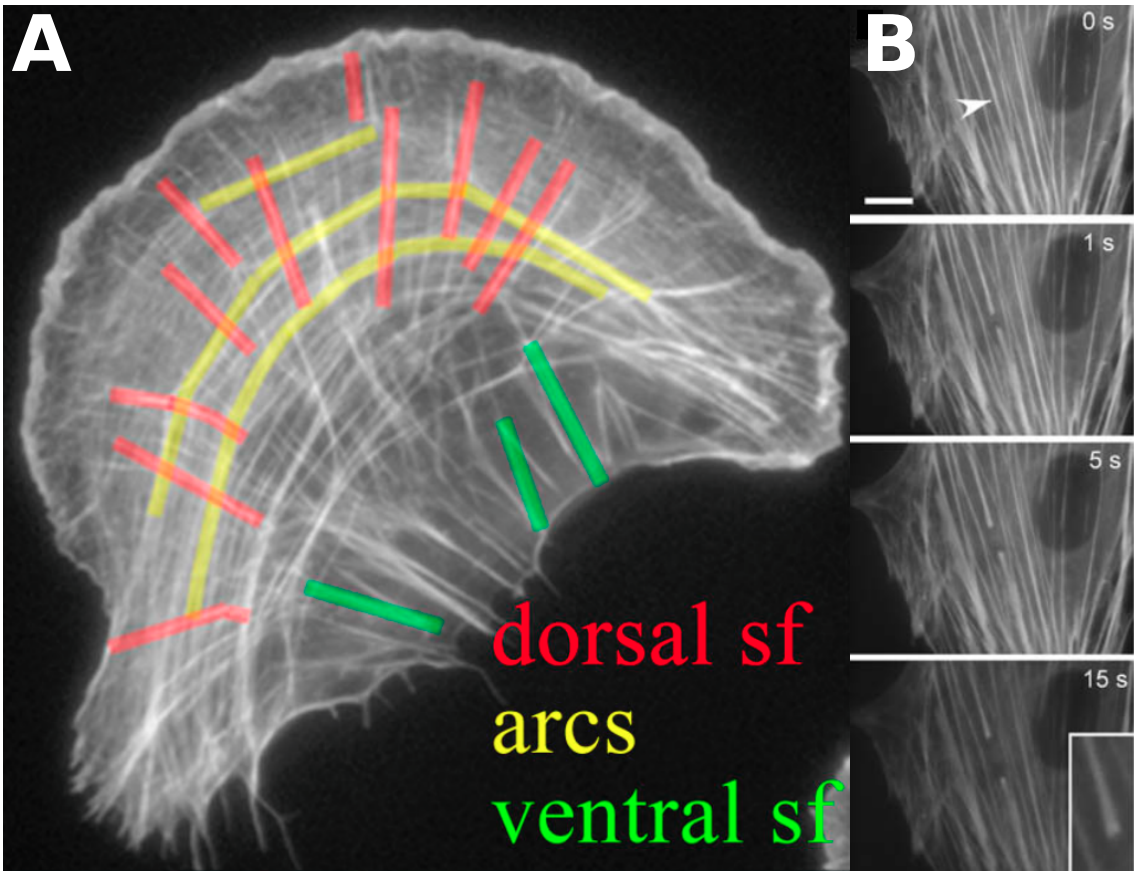

Figure 1.3: Actin stress fibers. (A) Classification following Hotulainen et al. from whom the image is taken [19]. (B) SF severing. The ablation point is marked by a white arrow. Scale bar: $2\mu m$.

network and bundle structures and is also accomplished by other protein such as α-actinin or aggregates of myosin motor proteins, the myosin bipolar filaments (cf. Fig. 1.4 A).

The aforementioned SFs are one of the most prominent actin structures in cells adhering to flat surfaces. Cellular adhesions are mediated by micrometer-sized hierarchic protein assemblies called focal adhesions (FAs) [12]. FAs connect the actin CSK to the extracellular environment and are important for the mechanical sensing of the cell [20]. SFs consist of 10 - 30 F-actin filaments that are cross-linked into bundles [21]. They can be further classified into different categories by their connectivity to FAs [19]. Dorsal SFs (DSFs) emanate from a FA at the cell's periphery and grow radially into the center along the dorsal membrane (Fig. 1.3 A, red). At their free ends, they are typically connected to transverse arcs (TAs), which run parallel to the cell edge and are only indirectly connected to FAs via DSFs (Fig. 1.3 A, yellow). Ventral SFs (VSFs) are close to the ventral surface of the cell and terminate in FAs at both ends (Fig. 1.3 A, green). The assembly mechanisms of different fiber types are not yet completely understood, but there is indication for

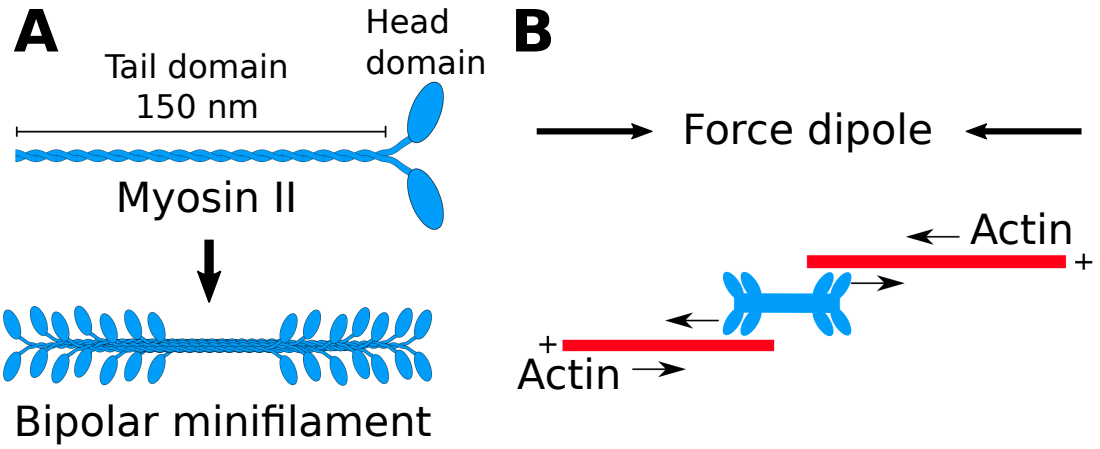

Figure 1.4: Non-muscle myosin II molecular motors. (A) 14 - 20 single myosin motor proteins assemble to bipolar minifilaments by binding with their tail domains. (B) Bipolar filaments move towards the plus end of F-actin. They thereby exert relative forces and act as force dipoles. Images adapted from [25].

the following processes [19]: DSFs grow from focal adhesions supported by formin assembly factors and α-actinin cross-linking. These fibers are mechanically passive, as they do not contain motor proteins [22]. The emergence of TAs follows a very different scheme. When the dendritic lamellopodium polymerizes against the plasma membrane, the counter forces push the whole network towards the interior of the cell, generating the so-called retrograde flow. Some microns away from the membrane, the flow is hindered by FAs, and the dendritic network breaks. Myosin motor proteins attach to the ends of the pieces and connect several filaments to a new structure that develops into a TA. VSFs seem to form by fusion of two DSFs and one TA. If a VSF is ablated by a femtosecond laser pulse, the two severed ends spontaneously retract (Fig. 1.3 B, [23]). The initial retraction speed is very high in the cellular context at about $1\mu m/s$ and decays exponentially. The whole recoil process lasts about $15s$ and completes a distance of $2 - 5nm$. The kinetics can be fitted well with a Kelvin-Voigt viscoelastic model. In this material model a viscous dashpot element and a Hookean spring are connected in parallel. Thus the dashpot damps the motion induced by the spring. In the context of SFs this means that VSFs are typically under appreciable mechanical load, which can be described as an elastic prestress, i. e. the rest length of the SF is smaller than its actual length in the cell. Note the difference towards active motor forces; if the SF only featured a constant force dipole (cf. Fig. 1.4), one would expect constant retraction speeds through the viscous environment of the cell. The kinetics could be also explained by an active force that decreases over time or a constant active force working against increasing mechanical resistance [24].

Myosin motors have been mentioned before in this introduction. They convert

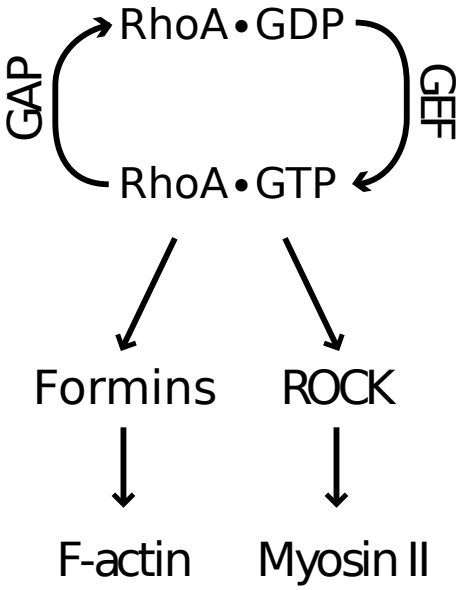

Figure 1.5: Simplified RhoA pathway. RhoA can be switched between its inactive GDP-bound state and the active GTP-bound state. In the latter, it activates both actin polymerization and myosin through formin proteins (actin) and the rho-associated protein kinase (ROCK, myosin). Adapted from a draft by Patrick Oakes.

chemical energy into motion. In contact with actin filaments, they move towards the plus end of the filament (with the exception of myosin VI, which moves in the inverse direction) [12]. Myosin proteins consist of a head and a tail domain (Fig. 1.4 A). The former contains the actual molecular motor, and the latter offers the opportunity for many proteins to stick their tails together and form a bipolar filament that has head groups on both sides. Bipolar filaments can cross-link and contract actin networks, as they can attach to two filaments at the same time and exert relative forces that lead to F-actin sliding (Fig. 1.4 B). Myosin activity always introduces a contractile effect in actin networks and fibers. Many different forms of myosin exist [12], but we restrict ourselves here to non-muscle myosin II, which is the type that causes contractility in tissue cells.

Interestingly, both actin polymerization and myosin activity are controlled, among other factors, by the protein RhoA (Fig. 1.5). Similar to actin and myosin, RhoA carries a source of energy. Here, the nucleoside that binds either two or three phosphate groups is called guanosine, and the high and low energy forms are abbreviated GTP and GDP, respectively. In its active GTP-bound state, RhoA activates both formins that enhance actin polymerization as discussed above and myosin II. The conversion of the GTP-bound to the GDP-bound state is regulated by so-called RhoGAP, and the reverse by RhoGEF proteins (Fig. 1.5). Activation of RhoA takes place close to the plasma membrane, however the GEFs diffuse through the whole cell. Recently, a new experimental technique was developed by Elizabeth Wagner and Michael Glotzer from the University of Chicago where the GEFs can be bound to the membrane via a photo-activatable binding site. In this way one can exert spatial control over RhoA and thus actomyosin activity. We will use this technique in chapter 5 to clarify the relative contributions of active, elastic and viscous components in the CSK.

1.3 Modeling Shape and Mechanics of Cells

Many approaches have been taken in the last decade to model the CSK on different length scales in order to explain the underlying mechanisms and understand the system quantitatively. Here we constrict ourselves to models for the whole cell for the sake of brevity. For a more detailed and comprehensive discussion, we refer the interested reader to a recent review of Schwarz and Safran [26]. In the case of a cell adhering to a flat surface, an obvious approach is to describe it by its two-dimensional projection, as those cells typically spread out widely and their height is small compared to their lateral dimensions. The simplest setting is assumed by contour models, which disregard the internal structure of the cell and only consider the force balance along the rim of the cell. This approach is justified if the cell's interior is sufficiently homogeneous and has been proven useful to explain invaginations between sites of adhesion. As these inwards curved arcs that are reinforced by SFs are often circular, they were seen as the expression of a lower-dimensional analog to the Laplace law for a spherical soap bubble, $R = 2\sigma/\Delta p$, where R is the radius of curvature (equivalent to the radius of the sphere), σ the surface tension and Δp the pressure difference between inside and outside of the bubble. Here σ contracts the surface against the pressure that conserves volume. In the case of contractile cells on substrates, the relation is slightly different, as the shape has to be balanced by adhesive connections of the cell to the surrounding space. The radius of the invagination is then determined by the local force balance between a line tension λ along the contour and the surface tension, $\lambda\, d\vec{t}(s)/ds = \sigma\vec{n}(s)$, where s is the arc length coordinate, $\vec{t}$ the tangential vector, and $\vec{n}$ the normal vector. Exploiting the definition of the radius of curvature, this amounts to $\sigma = \lambda/R$ or $R = \lambda/\sigma$. However, this relation cannot account for the experimentally observed dependence of the arc radius on the spanning distance between neighboring adhesion sites. The problem can be solved by assuming that the line tension is of an elastic origin, $\lambda = EA(L - L_0)/L_0$, where EA is the one-dimensional Young's modulus of the arc SF, and L, L_0 its current and resting length, respectively (Fig. 1.6 A) [4].

Cellular Potts Models (CPMs, Fig. 1.6 B) are closely related to contour models. CPMs discretize space to a lattice of spins like in an Ising model, and represent space occupied by the cell by spin up and extracellular space by spin down. Though they thereby technically include a description of the interior of the cell, spin flips are usually assumed to only happen at the interface between the two regions to avoid holes in the cell. In this way, they can also be regarded as contour models. The propagation of the contour is achieved by Metropolis dynamics in a quasi-static manner. CPMs have been used among other applications to describe cell sorting in tissues [27] and the shape of single cells [28]. Recently, a single cell CPM was extended to include cell spreading, division, cell-cell interaction and migration to

predict the shape of multiple cells on large patterned substrates [29, 30].

If the interior of the cell plays an important mechanical role (e. g. bulk elasticity), contour models are not sufficient. Recently, Oakes et al. combined the idea of an actively contracting elastic interior of the cell with a line tension along the contour to appreciate the difference in convex and concave regions of the contour [31]. Another reason for modeling the cell's interior is if chemical and mechanical properties of the bulk are of interest. In this spirit, Deshpande et al. introduced a continuum elastic model to explain the spatial organization of the CSK in adherent cells [32]. Here, the idea is to assume a homogeneous passive elastic material and superpose a spatially and directionally inhomogeneous active stress associated with stress fibers. For this purpose, angular space $[0, 2\pi]$ is discretized at each point in space, and the angle is referred to as Φ. In each Φ direction and at each point in space, they define a SF activity level $0 \leq \eta \leq 1$, which is governed by the first order kinetics

$$\dot{\eta}(\Phi) = \alpha \left(1 - \eta(\Phi)\right) e^{-t/\tau} - \beta \left(1 - \frac{\sigma(\Phi)}{\sigma_0}\right) \eta(\Phi) \ , \tag{1.2}$$

which is supposed to follow an initial signal that decays exponentially with time constant τ. The system can only assume a steady state if the local stress $\sigma(\Phi)$ reaches the isometric stress σ_0. This condition is in their work related to the strain rate $\dot{\epsilon}$ along the SF axis. If $\dot{\epsilon}$ is positive in the course of the decaying activation signal and reaches the steady state $\dot{\epsilon} = 0$ from above, the SF activation level is conserved. Where this is true depends primarily on the boundary conditions. On a square cell with four supports at the corners, they retrieve high SF activation near the free edges and in the direction towards the center. However, the cell shape does not exhibit the characteristic circular arcs expected in these situations (Fig. 1.6 C).

In three spatial dimensions, shapes of suspended cells and vesicles are predominantly discussed along the lines of the pioneering work of Helfrich in the literature [33]. He reasoned that the bending energy of the membrane provides the dominant energy contribution. The so-called Hamiltonian reads

$$H_{\text{Helfrich}} = \int \ dA \ \left(\frac{\kappa_b}{2} \left(\frac{1}{R_1} + \frac{1}{R_2} - c_0 \right)^2 + \kappa_g \frac{1}{R_1 R_2} \right), \tag{1.3}$$

where R_1, R_2 denote the principal radii of curvature and κ_b, κ_g the bending moduli associated with the mean and Gaussian curvature, respectively. The integral over a closed surface over the second term in Eq. 1.3 is a topological invariant due to the Gauss-Bonnet theorem and is therefore often not considered. Fig. 1.6 D shows the discocyte, which is a minimal energy shape of Eq. 1.3 for $c_0 = 0$ at fixed volume and surface area. An excellent review of the history of different models and studies based on this Hamiltonian is given in [34]. The development of this model culminates in the theoretical calculations of the shapes of the red blood cells, which we review

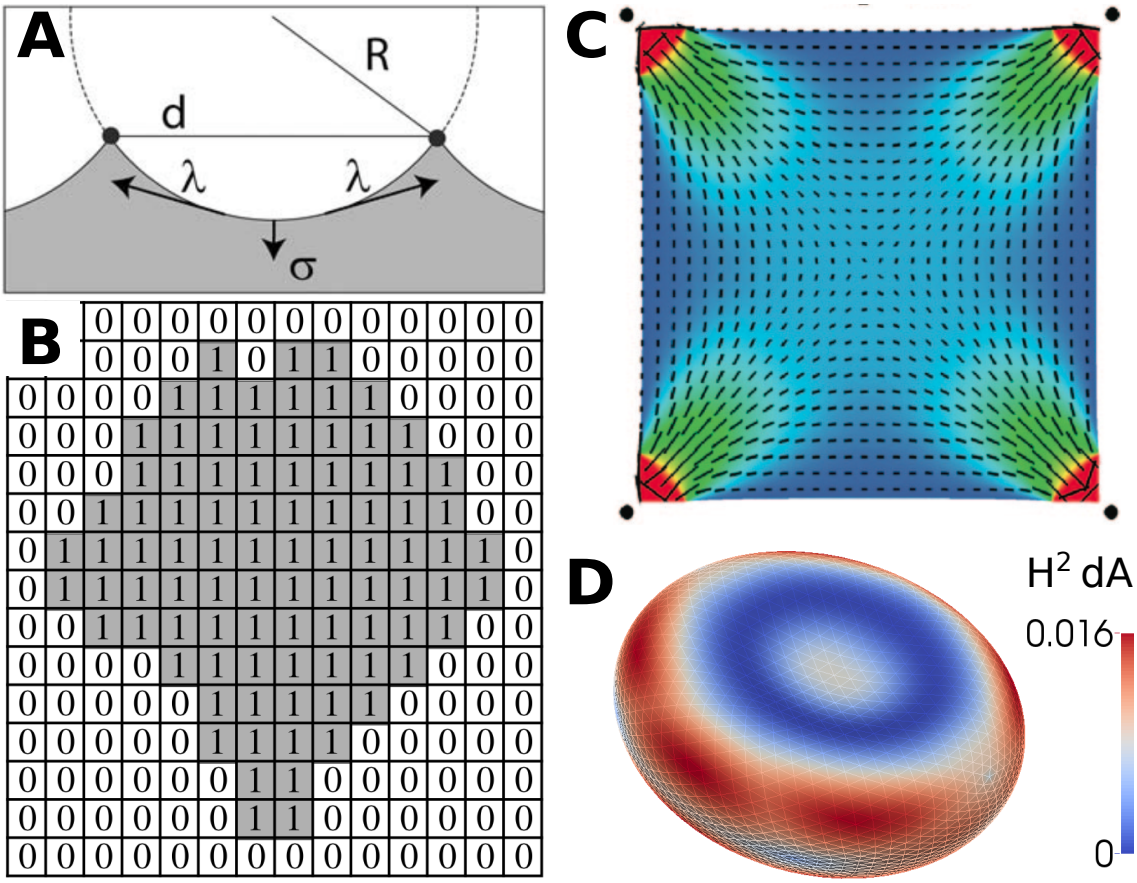

Figure 1.6: Whole cell models. (A) The tension-elasticity model predicts the dependence of the arc radius R from the spanning distance d. Taken from [4]. (B) Lattice-based cellular Potts model. Taken from [29]. (C) Continuum mechanical model that predicts the orientation of the cytoskeleton. Taken from [32]. (D) The discocyte shape as the minimal energy shape for the Helfrich-Hamiltonian with $c_0 = 0$ at fixed volume and surface area, cf. main text.

and reproduce in the next chapter in order to demonstrate the capabilities of our software.

1.4 Outline and Main Results

The theoretical work we present in this thesis was inspired by the versatile effects of contractile actomyosin networks that control force generation in cells and thereby their shape. We aim at providing a common framework to investigate contractile networks in both two and three spatial dimensions. We specifically consider the heterogeneity of the networks introduced by SFs and show that SFs strongly impact force generation and distribution. We here outline the content of the separate chapters and summarize the main results.

In chapter 2 we describe the software we use throughout this work. We use triangulation methods to represent surface models that can be embedded either in a two- or three-dimensional space. In this way we can model cells that adhere to flat substrates or three-dimensional scaffolds, and also suspended cells in the same framework. Further, triangulated surfaces provide a natural way to embed one-dimensional structures such as SFs on the edges of the triangles. We describe how different energy contributions can be defined on triangulated surfaces and reproduce different shapes from the shape spectrum of red blood cells.

In chapter 3 we investigate the forces and shapes of cells on patterned environments in two and three dimensions. We pay special attention to inner SFs that connect to invaginated arcs between two adhesive regions. We discuss the special importance of the orientation of the inner SFs as well as the location of the connection point along the peripheral arc. We then turn towards three-dimensional representations of the cell and discuss the effect of enclosed volume and radii of curvatures in different intersection planes on three-dimensional cell shapes.

In chapter 4 we develop a novel technique to reconstruct heterogeneous cellular tensions. We discuss that previous methods suffer from the fact that the inverse problem of elasticity theory is ill-posed and how regularization schemes are introduced to stabilize the solution in the presence of noise. However, regularization also biases the final result. We use a whole cell model with embedded SFs similar as in chapter 3 in an approach we call model-based traction force microscopy and find that SFs are the main source of contractility in the cell type of interest. Further, we show that the force of SFs depend on the fiber type in a statistically significant way.

In chapter 5 we introduce viscosity and dynamics to triangulated surfaces to model an experimental system, where we can control the spatial distribution of RhoA and therefore actomyosin contractility. We establish new methods to dynamically alter the triangulation in order to preserve mesh integrity in the presence of sources and sinks of material. In this way, we can investigate the behavior of discrete one-dimensional SFs in the viscous flow of the surrounding medium. In agreement with the results from chapter 4, we find that if SFs exist, their contraction is the main source of flow within the cell, and that they further provide the main part of cellular elasticity.

In chapter 6 we investigate the dynamics of a contraction wave that runs across the surface of a suspended cell. We propose simple relations for an activator inhibitor system encouraged by observations discussed in the literature. We derive the phase plane diagram for the system and find that this system gives rise to excitable behavior and allows pulses of high myosin concentrations to travel at constant speed.

Further, we investigate the mechanical impact of the contractile ring that propagates over the surface of the cell from one pole to the other and find that the contraction from the myosin activity working against a passive elastic material can account for the flattened shapes observed in the experiments.

2 Numerical Methods

2.1 Introduction

The description of surfaces in three-dimensional space has fascinated physicists and mathematicians ever since Euklid summarized the axioms of geometry around the year 300 BC and surely even before. The reason is that the configuration of the surface is linked to its properties and functions. In architecture and construction, stability, weight and material usage are primary concerns in building for example roofs, bridges, and dams [35, 36]. From ancient up to medieval times, soldiers had to find a balance between coverage, stability, and weight of their shields. Mathematicians have investigated the area of surfaces in three-dimensional space. The most famous example is probably Gauss, who invented modern geodesy in order to survey his home region around Braunschweig geologically. They are also interested in minimal surfaces, where the mean curvature vanishes at every point of the surface. Minimal surfaces can be infinitely extended or confined by a closed boundary that might be rigid (Plateau's problem, see [37]) or elastic [38]. In physics, two-dimensional surfaces in three-dimensional space are of interest in many research areas, e. g. interfaces between different fluids [39], configurations of foams [40], and wetting [41, 42].

In biophysics, the description of membranes that consist of lipid bilayers has a long tradition. Biomembranes are essentially two-dimensional, since their lateral extension of some μm is much larger than their thickness of $4nm$. The simplest model system is the one of vesicles [34, 43], whose shapes can be well described with the Canham-Helfrich Hamiltonian [33, 44]. Famous is also the shape spectrum of red blood cells (RBCs), which ranges from the cup-shaped stomatocyte over the physiologically most relevant biconcave discocyte up to the echinocyte, which resembles a sphere with spikes [45, 46]. Here it is not sufficient to only describe the mechanics of the lipid bilayer, but one also needs to take a network of biopolymers that lies underneath the membrane into consideration. This network is about $50nm$ thick, which is considerably more than the membrane thickness. Nevertheless, both layers together are still very thin compared to the diameter of the cell, which is approximately $8\mu m$, such that it is still justified to describe the composite with a

surface model. The network consists of spectrin proteins that respond non-linearly elastic to stretch and shear, which stabilizes the spiculated shapes of RBCs.

Several methods have been developed to describe surfaces in order to investigate their properties and find their equilibrium shapes. Equilibrium here defines an optimal configuration with respect to some energy functional that depends on the shape of the surface and additional constraints. Such energies can relate to, for example, stretch, bending rigidity, and tension, while constraints include among others area and volume conservation, and adherence to some defined points or surfaces in space. Simulations typically start from a reference surface and iteratively alter their description until it arrives at a stationary result.

For some energy functionals and well parameterizable surfaces it is possible to derive shape equations in an Euler-Lagrange formalism. This has been exploited before in various publications [43, 47–51]. The description of the surface then completely depends on a set of initial conditions, which are integrated to assess the energy associated with the surface. Often constraints are formulated in terms of requirements for the endpoint of integration. Shooting methods can be applied to seek solutions for an individual parameter set, and parameters have to be varied to find possible shapes and associated energies.

An interesting method was recently introduced by Khairy et al. which uses an expansion of the surface in spherical harmonic functions $Y_{L,K}(\theta, \Phi)$,

$$x(\theta, \Phi) = \sum_{L=0}^{L_{\max}} \sum_{K=-L}^{L} C^x_{L,K} Y_{L,K}(\theta, \Phi) \ ,$$

and similar for y and z [52]. The optimization then consists of finding the set of coefficients $C^i_{L,K}$, $i \in \{x, y, z\}$, that lead to minimal energy. The method has been demonstrated in the context of RBC shape and can be used to both fit experimental data and calculate theoretical shapes depending on the optimization measure applied. The method is capable of reproducing surfaces that do not form a star-shaped domain. This means that there is no need for a center that directly "sees" all points of the surface, as it would be the case for the classical spherical harmonics parameterization, where the radius R replaces the components x, y, and z. It is computationally efficient if spherical harmonics provide a sufficient description already for low L as in the case of RBC shapes [52].

Another approach of simulating surfaces are level set methods. Here one describes the surface with the help of an implicit representation by an isocontour of a function $\Phi(\vec{x})$ [53]. Usually $\Phi = 0$ is used and Φ is defined such that the gradient does not vanish at the zero isocontour. This allows to differentiate between the inside and the outside of a closed surface just by evaluation of the sign. Level set methods come at the cost that one needs to discretize a domain of the whole embedding

space, in contrast to surface tracking methods that only discretize the surface itself. Conversely, it avoids the issue of mesh homogeneity, which becomes problematic with surface tracking methods for large deformations or if surfaces merge or divide.

Triangulated surfaces constitute a surface description which is widely used in image processing [54], computer-aided design [55], and the calculation of surface shapes and dynamics [45, 46, 56]. The surface is described by a set of vertices, which are interconnected by a set of edges. The connection is such that all faces defined by minimal closed edge loops are triangles. When simulating membranes, one has to differentiate between fluid and polymerized membranes. In fluid membranes like the lipid bilayer in vesicles, the connectivity of neighbors is not fixed. Vertices need to be allowed to change connections to other vertices and can thus move across the surface. Thus a fluid membrane cannot withstand shear stresses and elastic energy contributions are limited to stretch and bending. In a polymerized membrane like in RBC, where the lipid bilayer is connected to a stable elastic spectrin network, the coordination is fixed and it thus resists shear stresses. An open source software focused on tension problems that incorporates a wide set of features for the optimization of triangulated surfaces and meshing is the *SurfaceEvolver* [56]. Here the user specifies the geometry of the reference surface and the energies of interest in an input file and can then interactively minimize the surface. In this way it is possible to utilize optimization steps of different solvers, change the mesh size, or apply noise to the vertices while the resulting surface is displayed. One can also solve more difficult partial differential equations like reaction diffusion systems on the surface with the help of finite element surface methods [39].

2.2 The Software SurfaceMaster

In this thesis we present an approach using triangulated surfaces for most numerical tasks. The range of applications includes cell shapes on patterns in two and three dimensions (chapter 3), traction force reconstruction (chapter 4), viscous flow (chapter 5) and three-dimensional shapes of spheroids with contractile elements (chapter 6). We choose this method out of the ones explained above since it is equally appropriate to consider shapes and forces in two and three dimensions and as it defines a natural way of embedding one-dimensional heterogeneities into the structures by setting special properties on a sequence of edges in the mesh. The latter part enables us to consider especially strong bundled structures in the cell's cytoskeleton which we will need in the chapters 3, 4, and 5. We need to apply several energy and force dependent solvers, including deterministic energy minimizers and a dynamical model. Since we need a great flexibility in controlling the reference surface, appropriate energies, their minimization, and data output, we decided to develop a new

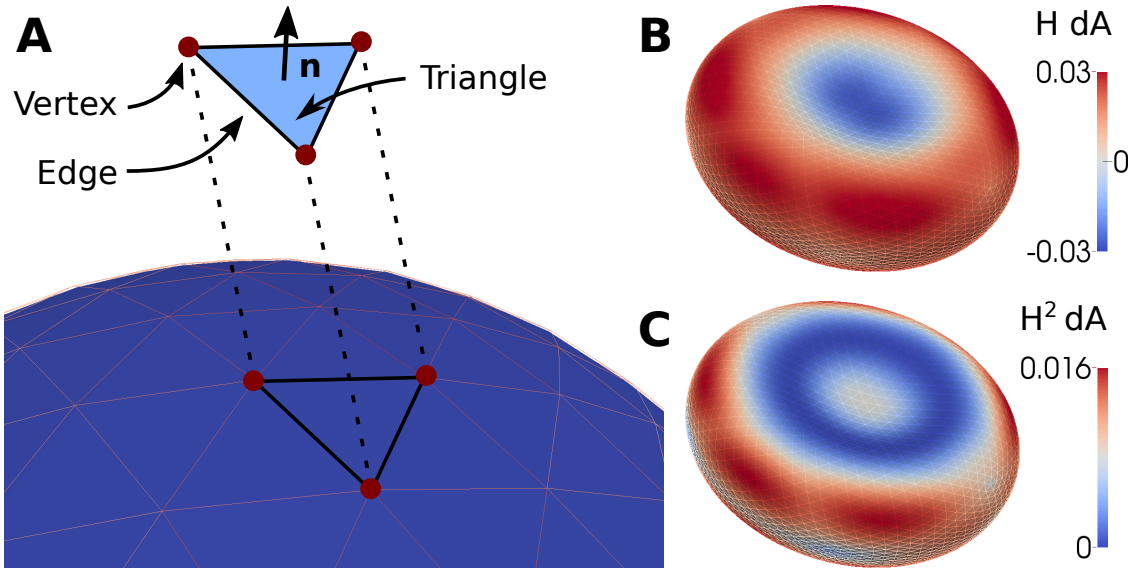

Figure 2.1: Triangulated surfaces with the software *SurfaceMaster*. (A) Piece of a spherical triangulated surface. The surfaces is represented by a set of vertices that are interconnected by edges to form triangles. (B), (C) *SurfaceMaster* can output VTK files ([57], cf. main text) with associated data for vertices, edges, and triangles. Here the same discocyte is shown with the local mean curvature (B) and the local squared mean curvature (C) in color coding.

software, though many of the features are also implemented in the *SurfaceEvolver* mentioned above. In analogy to this software, we will call our own software *SurfaceMaster*. In the following, we will introduce its design principles and its internal organization.

2.2.1 Overview

The purpose of *SurfaceMaster* is to deform and evolve triangular meshes with respect to specified energies and forces. The code is written in the programming language C++. In order to provide the greatest flexibility possible, the software is organized in a modular way and offers the user to pick the parts of interest. It is also possible to extend the software in a straight forward way. The core components of the software are:

1. The GeomObject, which stores all geometrical information about all vertices, edges, and triangles of the mesh as well as their connectivity.
2. Energies, which store information about the current energy configuration and its gradients.
3. Constraints under which the energies are to be minimized.

4. The Minimizer, which implements an optimization scheme to change the configuration of the GeomObject according to the defined energies.

It is then the user's task to write a controller class that defines the work flow. This includes initializing the individual components and connecting instances of the GeomObject, Energy, Constraint, and Minimizer classes. Then the controller can define the iteration of the chosen optimization scheme and organize data output.

2.2.2 The GeomObject

The GeomObject contains all information about the current geometry of the surface. For this purpose it holds a list of objects of each of the three basic entities it consists of, namely vertex, edge, and triangle. Vertex objects store their three-dimensional locations and define basic functions, e. g. scalar and vector product, and the norm. They also store information about their connection to edges and triangles. Edges store their two end points as vertex objects, and keep a list of the triangles in which the are contained. They also offer some geometrical functions like intersection checking and can store additional information, like for example a rest length which is necessary to determine elastic energies. Triangles know about vertices and edges they contain and methods to calculate their normal, area, and volume contribution as is explained e. g. in [46, 56, 58]. Note that the information about the connection between vertices, edges, and triangles is stored redundantly, which one need to take special care of if the mesh is to be changed. However, this redundancy yields large performance benefits.

The GeomObject class itself adds some more features that relate to the sum of its parts. It offers methods to calculate area and volume, and adds input and output features. GeomObjects can be assembled automatically from VTK files [57], or constructed manually. The output is in the VTK format as well. Here the mesh can be annotated with data readouts through subclasses of a template class, which defines methods that collect data associated with points or triangles. Instances of these classes can be stacked according to the decorator pattern to allow for multiple data output (cf. e. g. [59]). We recommend the free software ParaViewer to view input and output meshes in the VTK format [60].

2.2.3 Energies

Energies that control the evolution of the surface are defined as subclasses of the superclass *Energy*. The subclasses are basically prescribed to implement methods to calculate the energy of the whole surface and its gradient on single vertices. A

generic numerical gradient determination is implemented already in the superclass but may be overridden by subclass methods. For performance reasons, energies contain two Boolean fields that indicate if a new calculation of energies and gradients is necessary. They are supposed to be set to true by the optimizer in the beginning of an iteration. This allows the energy classes to perform an efficient calculation of energy and all gradients in one step, save the results, and answer with subsets of the saved data to calls for gradients of single vertices. It also allows to calculate gradients that are used in several energies only once per iteration.

Here we give a summary of all energy formulations implemented in *SurfaceMaster*:

- Surface tension energy $E_\sigma = \sigma A$: The energy is proportional to the area A of the surface, and the coefficient is called the surface tension σ. A guide how to determine surface gradients can be found in [46, 56, 58].

- Adaptive surface tension energy: In addition to the background surface tension σ, one can store individual surface tensions for each triangle i. The energy is then computed as $E = \sum_i (\sigma + \sigma_i) A_i$, where A_i is the area of triangle i.

- Quadratic area difference energy $E_A = c_A/2 \cdot (A - A_0)^2$: This energy can be used to enforce area conservation. A and A_0 are the current area and a reference area of the surface, and c_A the proportionality coefficient.

- Quadratic volume difference energy $E_V = c_V/2 \cdot (V - V_0)^2$: This works analogously to the quadratic area difference energy. An introduction to volume and volume gradient calculations for triangulated surfaces is given in [46, 56, 58].

- Different implementations of bending energies are provided that calculate $E = \alpha \int H^2 \; dA + \beta \int H \; dA + \gamma (\int H \; dA)^2$, where $H = (\kappa_1 + \kappa_2)/2$ is the mean curvature of the surface and κ_1, κ_2 are the principal curvatures. The parameters α, β, and γ allow to control the bending stiffness, spontaneous curvature and area-difference elasticity [34]. The last is related to a difference of the resting area in the two sheets of a lipid bilayer and is often considered for biological membranes. Gaussian curvature bending was not implemented, since its integral over a closed surface is a topological invariant, and we are not interested in changes of the topology here [37]. The methods we implemented are the one described by Jülicher [61] and Wintz [58]. While the first is easier to calculate and computationally more efficient, the idea of Wintz provides the correct scaling of the energy for sharp edges.

- Hookean spring and active cable energies: These energies are defined on the edges alone. A passive cable is defined as a spring in the extension regime $l > l_0$, where l, l_0 are the length and rest length of the cable. In contrast, it does not resist compression, so the force is zero for $l \leq l_0$. An active cable is a

passive cable which features an additional constant force dipole that actively contracts the cable.

- Nonlinear two-dimensional elasticity is described by

$$E = \int dA_0 \left[K_\alpha/2 \cdot (\alpha^2 + a_3\alpha^3 + a_4\alpha^4) + \mu(\beta + b_1\alpha\beta + b_2\beta^2) \right] . \qquad (2.1)$$

We refer to the book chapter of Lim, Wortis, and Mukhopadhyay in [46] for a derivation and an explanation of its numerical discretization for triangulated surfaces.

2.2.4 Constraints

Constraints can be treated in different ways. Vertices contain a special flag which can be set if they are supposed to keep their spatial position. Other constraints can be treated as quadratic potentials, which are simply stated as energy classes explained above. It is however also possible to specify hard constraints. The constraint classes calculate the deviation from the given value, e. g. the difference between current volume and target volume, and a gradient. The optimizer must then include a method to project forces onto all constraints and perform an compensation for any deviation between current and target value. The method implemented in the deterministic minimizers is taken from the *SurfaceEvolver* and can be looked up in its documentation [56].

2.2.5 Optimization

Optimal configurations can be found by minimizing the energy, which can be done in multiple ways. A very robust and fast method is deterministic minimization using gradients. We implement a steepest decent algorithm which always follows the direction down the local energy gradient. As this method is inefficient for tight valleys in the energy landscape, we also implement the conjugated gradient method as described in the book *Numerical Recipes in C++* [62]. Here, a history vector is created and updated over all iterations in order to find directions together with the local energy gradient that are more efficient to find the optimum. The algorithm is constructed such that it can find the minimum of any N-dimensional quadratic function in N iterations.

If energy barriers need to be crossed and local minima occur in the energy landscape, deterministic optimization methods do not automatically converge to the minimal energy. For this reason, we also implement a Monte Carlo solver with the Metropolis algorithm [46, 63]. The idea is that vertices are subjected to trial moves that cause

a small difference in energy ΔE. If $\Delta E < 0$, the trial move is accepted. However, even if $\Delta E > 0$ we accept it with a probability of $\exp(-\Delta E/(k_B T))$, where k_B is the Boltzmann constant and T is called *computational temperature*. This procedure is linked to statistical mechanics as it reproduces the thermal ensemble of shapes at the computational temperature.

We also include a possibility of simulating dynamics in a noiseless overdamped way. This means that the velocity of vertex i, $\vec{v}_i$, is proportional to the force it experiences, $\vec{F}_i$, which leads to $\vec{F}_i = \eta \vec{v}_i$. Here, η is the effective viscosity of the medium. This method will be explained in more detail in chapter 5, where we consider flow in filamentous networks.

2.3 Example: Red Blood Cell Shapes

Red blood cells (RBCs) show a variety of shapes under different conditions that are used to identify certain diseases. As early as in 1675, the dutch microscopist Antonie van Leeuwenhoek observed that RBCs are soft and can deform from their round resting shape into ovals and back [6]. Some 340 years later, we know that RBCs show a rich spectrum of shapes at different conditions and that the shapes are determined mainly by the membrane and the underlying network of spectrin polymers [46, 64].

During growth and maturation in the bone marrow, RBCs first expel their nucleus and then sequentially degrade other organelles [64]. The remainder consists mainly of hemoglobin, electrolytes and water enclosed in a hull of membrane and membrane associated cytoskeleton (see e. g. [44]). It is therefore an ideal model system for physicists, since the cell has lost most of its biological activity. The mature RBC exhibit a physiological volume of about $V = 100\mu m^2$ and a surface area of approximately $140\mu m^2$, which means that it has an excess area of ca. 35% compared to a sphere with the same volume [46]. Without external forces it relaxes to a resting shape of the biconcave discocyte, which is about $8\mu m$ in diameter and $1.7\mu m$ thick (Fig. 2.3 C).

2.3.1 Theoretical Background

The shape spectrum of RBCs is very rich and requires many of the energy terms implemented in *SurfaceMaster*. We will therefore demonstrate the computing capability of the software by calculating theoretical RBC shapes. Before we do so, we briefly review how the Hamiltonian describing RBC shapes was found and the

effects of its single parts on the shape spectrum. The biconcave resting shape was first explained by Canham, Deuling and Helfrich, who proposed that it was determined by the minimal energy state of the membrane with respect to bending [44, 65]. The bending energy is given by

$$H_{\text{bend}} = \frac{\kappa_b}{2} \int (2H - C_0)^2 \, dA = \frac{\kappa_b}{2} \int \left(\frac{1}{R_1} + \frac{1}{R_2} - C_0 \right)^2 dA \, , \tag{2.2}$$

where κ_b is the bending rigidity, H the mean curvature of the surface, C_0 the spontaneous curvature, and R_1, R_2 the principal curvatures. This Hamiltonian can be derived either from the elastic description of a thin plate [66, 67] or with an expansion in curvature [33, 34] : As the energy cannot depend on the choice of the coordinate system, it has to consist of a combination of the two invariants of the curvature tensor, namely the the mean curvature H and the Gaussian curvature $K = 1/(R_1 R_2)$. If one requires that the energy should not depend on whether the surface is bent inwards or outwards, terms linear in H drop out and we arrive at

$$H_{\text{bend}} = \alpha \int H^2 \, dA + \beta \int K \, dA \, . \tag{2.3}$$

Here we expanded to lowest order and ignored a constant term that would correspond to a surface tension. The second integral is a topological invariant though, which is stated by the Gauss-Bonnet theorem [37]. As RBCs do not change their topology, we arrive at Eq. 2.2 as the relevant part of the expansion. There, the spontaneous curvature accounts for an asymmetry in the membrane, which reintroduces a term linear in H.

Minimizing Eq. 2.2 at constant volume and area indeed reproduces the resting biconcave shape of RBCs and can also account for cup-shaped stomatocytes (Fig. 2.3 B). However, especially the spikes in the shapes of echinocytes and spiculed shapes (Fig. 2.3 D, E) show that minimization of the squared mean curvature is not enough to explain the full spectrum of RBC shapes. There needs to be a mechanism which drives the system towards a locally more curved state, and an explanation for this is found in the area-difference elasticity (ADE) model.

An excellent review of its history and different variations is found in [34]. The main idea is that the membrane does not consist of a single layer, for which Eq. 2.2 was appropriate, but of a bilayer. As the lipids can hardly be exchanged between the two layers, they may possess different resting areas and consequently a resting area difference ΔA_0. Now consider two patches of membranes of equal area, one in each layer. When the membrane is bend and the layers are assumed to remain parallel surfaces, the local difference in area between the patches is to first order proportional to $D \cdot H$, where D is the distance between the two layers and H the local mean curvature. We can now write down a quadratic potential which accounts

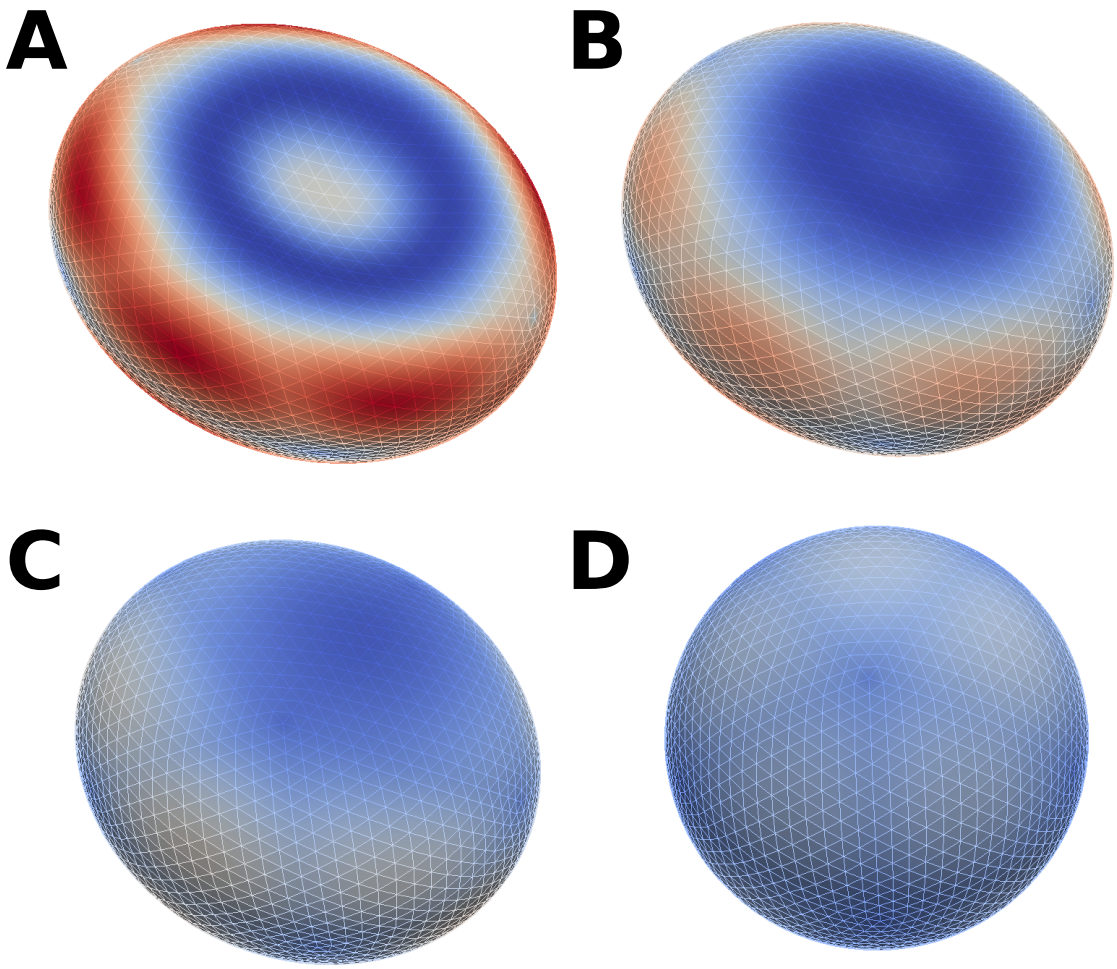

Figure 2.2: Initial shapes for RBC shape determination at different volumes. The initial volume defines the resting state of the membrane skeleton. The final RBC shapes all exhibit the same physiological volume of $100\mu m^3$. Surface area $A = 140\mu m^2$ is held constant for all initial and final RBC shapes. (A) $V = 100\mu m^3$ (B) $V = 130\mu m^3$ (C) $V = 148\mu m^3$ (D) $V = V_{\text{sphere}}(A = 140\mu m^2) = 155.8\mu m^3$

for the trend of the two monolayers to assume the preferred state in area difference,

$$H_{ADE} = \alpha \left(\Delta A - \Delta A_0\right)^2 = \alpha \left(D \cdot \int H \; dA - \Delta A_0\right)^2 , \tag{2.4}$$

where α can be calculated from the elastic response to stretching membrane patches.

Combining Eqs. 2.2 and 2.4 yields the complete Hamiltonian for a lipid bilayer that includes its bending elasticity and the area difference between the two layers. Both the spontaneous curvature and the ADE model introduce a term linear in $\int H \; dA$ that can be combined and written in terms of an effective spontaneous curvature. Controlling this quantity can drive budding in vesicles [34], which is also interesting in the context of RBCs. In the simplest case, a spherical extension appears on a

spherical vesicle, and the two domains are connected by a narrow neck region (see e. g. [47]). In terms of Eq. 2.2 at $C_0 = 0$, the neck does not cost energy since the two principal curvatures are equal in their absolute value but of different signs. Further, in this equation the energy for a sphere is independent of its radius, as $\int H^2 \, dA = 4\pi/3$.

With RBCs we do not observe budding but the formation of spikes or spicules. From the bending energy alone, one would expect buds instead of spicules [68]. Iglic and others proposed that the elasticity of the membrane associated cytoskeleton could stabilize the spicules [68, 69]. One can account for this by considering the non-linear elastic Hamiltonian

$$H_{\text{elastic}} = \frac{K_\alpha}{2} \int dA_0 \left(\alpha^2 + a_3\alpha^3 + a_4\alpha^4\right) + \mu \int dA_0 \left(\beta + b_1\alpha\beta + b_2\beta^2\right) \ . \qquad (2.5)$$

Here, K_α and μ are the modules for stretch and shear, α and β are the area and shear strain invariants, and a_i, b_i are the coefficients that define the nonlinear behavior. A detailed derivation of these terms as well as a discretization approach for triangulated surfaces can be found in [46].

2.3.2 Numerical Determination of RBC Shapes

For a demonstration of the software *SurfaceMaster*, we follow the study conducted by Lim, Wortis, and Mukhopadhyay [45, 46], where all parameters can be found. As explained above, all necessary energies are implemented in *SurfaceMaster*. The procedure is as follows. First, the initial shapes for the algorithm are determined by specifying the resting state volume V_{ms} for the membrane skeleton and calculating the according shape on the discocyte sphere transition sequence, where the surface area is always fixed at $A = 140\mu m^2$. The calculations start at spherical shapes that are constructed from icosahedrons and refined subsequently. Deviating from the work of Lim et. al. [45, 46], we here employ a deterministic energy minimization scheme with conjugated gradients instead of a Monte Carlo simulation. This is sufficient after a small initial symmetry break as no local minima arise. As the software allows to switch the optimization method, it is easy to set up and we can therefore exploit the benefit of shorter computation times for deterministic minimization. Exemplary resting shapes for different V_{ms} are depicted in Fig. 2.2.

In the second step, an appropriate initial shape and the effective spontaneous curvature are chosen as parameters. A Monte Carlo simulation is performed, where the number of sweeps is sufficiently high to arrive at the shape class of interest. Instead of gradually decreasing the simulation temperature as done by Lim and coworkers, we again use a deterministic energy minimization to calculate the $T = 0$ shapes.

The results agree with those presented in [46] and are shown in Fig. 2.3. We reproduced shapes for non-axisymmetric and axisymmetric stomatocytes, discocytes, echinocytes, and spiculated shapes from the parameter space investigated in the work by Lim and coworkers. We conclude that *SurfaceMaster* is a suitable tool to compute even highly nontrivial shapes such as the ones shown here for RBCs.

2.4 Discussion & Outlook

In this chapter we introduced the software *SurfaceMaster*, which we use for most numerical tasks presented in this thesis. We chose the representation of surfaces by triangulation, as this is especially well suited to model shapes in both two and three spatial dimensions. Furthermore, this kind of discretization provides a natural way to include one-dimensional fiber-like structures into a two-dimensional surface embedded in either two or three spatial dimensions. Such structures will be important for the investigation of cellular force generation, cellular elasticity and three-dimensional shape problems in the subsequent chapters.

The internal structure of *SurfaceMaster* is modular, which allows it to be easily extended in terms of additional definitions of energies, constraints, and optimization schemes. We refrain from providing a general input file structure as offered by e. g. the *SurfaceEvolver*, and encourage the user to write their own controllers together with the source code of *SurfaceMaster* directly in the programming language C++. In this way one can combine all features of interest while retaining the flexibility which is needed for most numerical studies. The implemented energies and optimization schemes allow to set up a project quickly and to concentrate on the biophysical aspects instead of programming.

One of the convenient features of the software is that it uses standard VTK files for input and output meshes. By sticking to this standard, *SurfaceMaster* can be used together with other software without the need for converters. Input files can be constructed and results viewed with 3rd party programs. We recommend the software *gmsh* [70] for generating initial meshes, since it offers advanced meshing features and is easy to use. For two-dimensional image segmentation combined with mesh generation, we also provide an extension for the image processing software ImageJ [71], which will be discussed in chapter 4. In order to view the output files, we used the software *ParaView* throughout this work.

For demonstration purposes, we calculated representative shapes of RBCs. We briefly reviewed the parts of the Hamiltonian. The area-difference elasticity term can drive the system to different shapes, where the spiculated echinocytes are stabilized by the nonlinear elasticity of the membrane cytoskeleton. In this study we

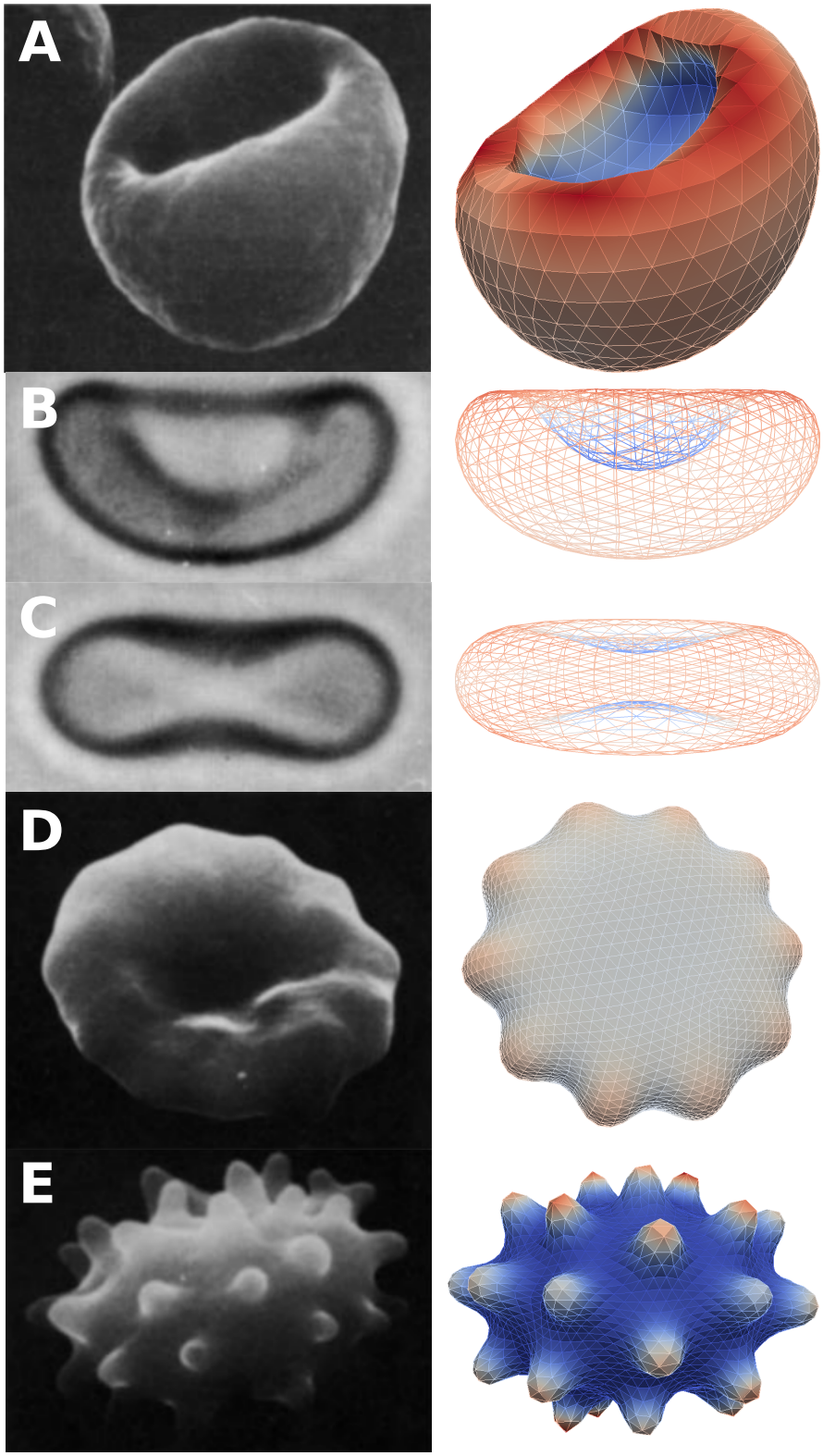

Figure 2.3: Experimental and calculated shapes for RBCs. $V = 100\mu m^3$ and $A = 140\mu m^2$ for all calculated shapes. Initial shape volume $V_m s$ and ADE parameter $\bar{m}_0$ (cf. [46]) vary. (A) Non-axisymmetric stomatocyte, $V_{ms} = 130\mu m^3$, $\bar{m}_0 = -45$ (B) Axisymmetric stomatocyte, $V_{ms} = 148\mu m^3$, $\bar{m}_0 = -10$ (C) Axisymmetric discocyte $V_{ms} = 100\mu m^3$, $\bar{m}_0 = 15$ (D) Echinocyte, $V_{ms} = 100\mu m^3$, $\bar{m}_0 = 100$, (E) Spiculated shape, $V_{ms} = 148\mu m^3$, $\bar{m}_0 = 120$

showed how different energy definitions and optimization schemes implemented in *SurfaceMaster* can be utilized to calculate highly nontrivial cell shapes.

3 Force and Shape of Geometrically Constrained Cells

3.1 Introduction

In the past 20 years, micro-patterned substrates have become an important tool in cell culture (cf. Fig. 3.1). If cells are cultured in homogeneous environments, they develop a rich variety of shapes, sizes, and internal organizations. Often this biological variability impedes the reproducibility of experiments and hinders the acquisition of statistically significant data. By their ability to regulate and normalize cell geometry, patterns have helped to unravel details of important biological processes such as migration [Refs from Philipp] or proliferation [72–74]. Further, patterns have shed light on the direct influence of geometry on cellular function. Chen and coworkers discovered that cells die if they do not find enough space to adhere to [2]. Cell geometry was also found to regulate the organization of the cytoskeleton (CSK) [75, 76] and to influence traction stresses [29–31]. A recent study even inverts the problem and predicts the optimal shape of pattern networks that allow cells to divide and migrate on them with the help of a cellular Potts model and a genetic algorithm [30].

A recurring feature of cells cultured on structured substrates in two dimensions are circular invaginations which form between adhesive islands (Fig. 3.1). Interestingly, such arcs also form on the larger scale of a tissue [4]. In cells, these arcs are often reinforced by actin filament bundles, so called stress fibers (SF) [77]. The circular shape of the invaginations expresses the equilibrium between two local forces, namely a line tension λ and a surface tension σ (Fig. 3.1 D). The line tension acts in the direction of the arc tangent $\vec{t}$, while the surface tension pulls perpendicular to this direction. In two dimensions, this direction is uniquely defined by the normal of the arc contour, $\kappa\vec{n} = d\vec{t}(s)/ds$. κ denotes the curvature of the line and s is the arc length coordinate which means that $|\vec{x}\prime(s)| = \sqrt{x\prime(s)^2 + y\prime(s)^2} = 1$. Together with the tensions, we can now formulate the simple tension model by assuming force

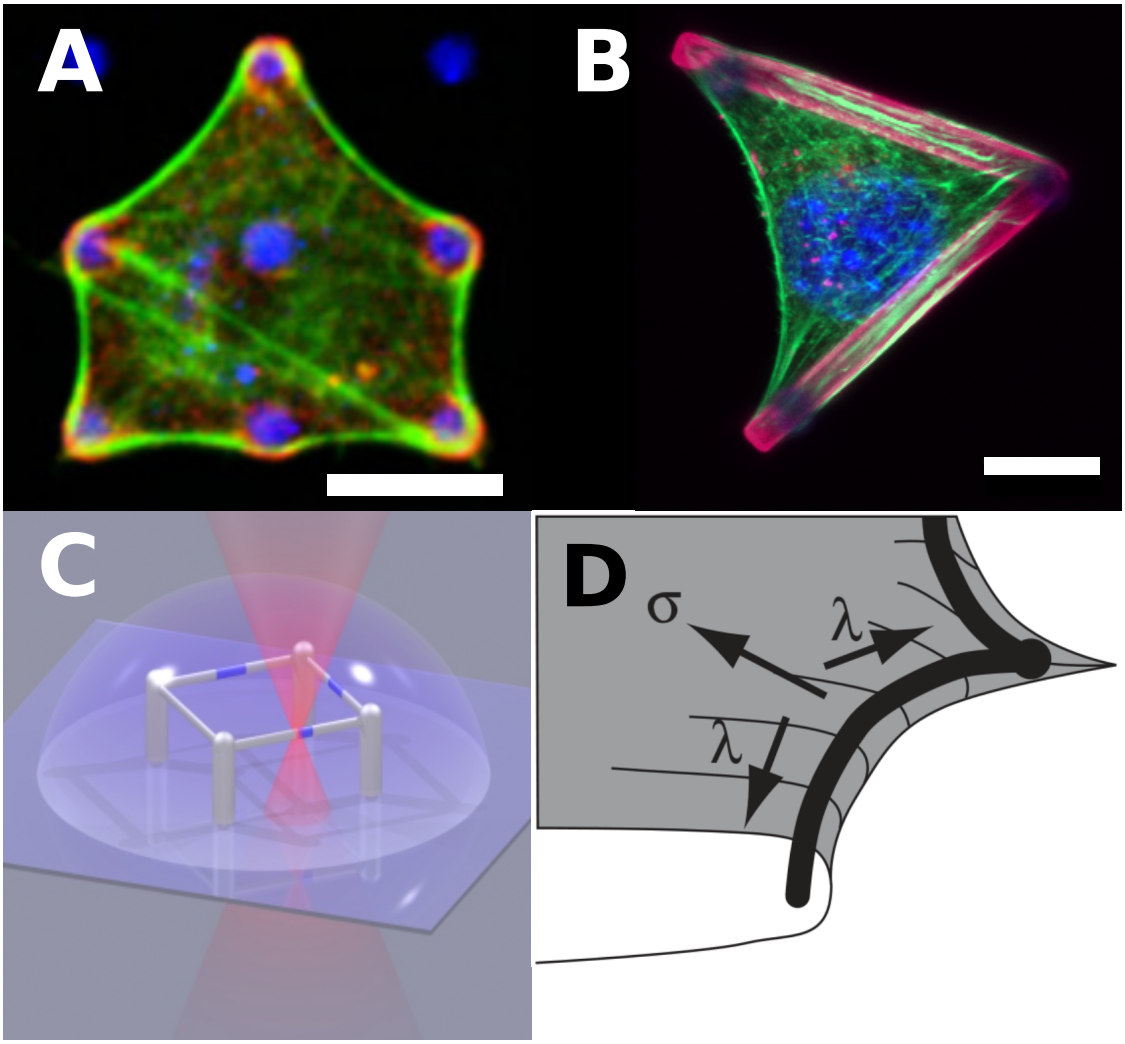

Figure 3.1: Cells on patterned substrates. (A) Cell adhering to microdots on a flat substrate (taken from [4]). Scale bar: $10\mu m$. (B) Cell in a V-shaped pattern that is lifted from the ground by microposts. Scale bar: $10\mu m$. (C) Three-dimensional scaffold with the geometry of a box ring for normalizing three-dimensional cell shape. (D) Line tension λ and surface tension σ determine arc shape in the tension elasticity model (taken from [10]). (B), (C): Courtesy of the group of Martin Bastmeyer, Karlsruhe Institute of Technology.

balance in the normal direction,

$$\begin{aligned} \lambda \frac{d\vec{t}}{ds} &= \lambda \kappa \vec{n} = \sigma \vec{n} \\ \frac{1}{\kappa} &= R = \frac{\lambda}{\sigma} \ . \end{aligned} \tag{3.1}$$

In the second equation we introduced the radius of curvature, $R = 1/\kappa$, which is constant as long as σ and λ are. Thus circular arcs form. However, this concept cannot explain the observation that the arc radius depends on the spanning distance d [4]. The dependence on an reference length suggests an elastic effect. This is

incorporated by the tension-elasticity model (TEM) proposed by Bischofs *et al.* in [4]. The line tension is assumed to be of elastic origin, $\lambda = EA(L - L_0)/L_0$, for which case one can derive a self-consistent equation for the radius R,

$$R = l_f \left(\frac{2R}{\alpha d} \arcsin\left(\frac{d}{2R} \right) - 1 \right) . \tag{3.2}$$

In the equations above, E denotes the Young's modulus and A is the cross section of the arc, L and L_0 its length and rest length. The rest length parameter $\alpha = L_0/d$ defines the prestrain for a straight connection between the anchoring points. Together with the length scale $l_f = EA/\sigma$, it completely describes the two dimensional system.

In this chapter we will extend the TEM in two different ways in order to learn more about the internal force distribution in the CSK. We will first give up the idea of a homogeneous surface tension as the driving force for the invaginations. This is meaningful if the CSK condenses to fiber structures also in the interior of the cell, and if these fibers connect to the peripheral one. We predict the force distribution for such cases and verify our results by a comparison to the distance the fiber retracts when severed with a laser nanoscissor [23], which is done by Elena Kassiandiou in the group of Sanjay Kumar at the University of California, Berkeley. Further, we will extend the TEM to three dimensions and investigate the effects of volume constraints and curvature. The latter part is inspired by experiments performed in the group of Martin Bastmeyer at the Karlsruhe Institute of Technology, to which we will compare our findings. For both extensions we use the fact that TEM shapes can be simulated with cable networks under isometric tension [4, 78, 79]. Here we will alter either the isometric towards a directed tension in the first part, while in the latter we will consider non-planar networks with finite enclosed volume.

3.2 Force Distribution on the Cell Contour

Stress fibers (SF) are thick tightly bundled and cross-linked structures build mainly of actin filaments. They have attracted high attention over the past decade regarding their formation, molecular composition, and mechanical properties [19, 21, 22, 24, 32, 76, 77, 80–87]. Though stress fibers were associated with forces already in the 1980s [81], it is a difficult task to measure the internal stress. Precise methods could only be used in the last decade. After laser ablation of SFs, one can measure the either retraction velocity or retraction length to infer forces [23, 24, 83, 88]. Laser ablation is also used to measure tension in the cell cortex [8, 89]. Atomic force microscopy was used to indent SFs and retrieve forces [90]. In a recent study, we presented an approach how one can measure SF tensions in a whole cell in a non-

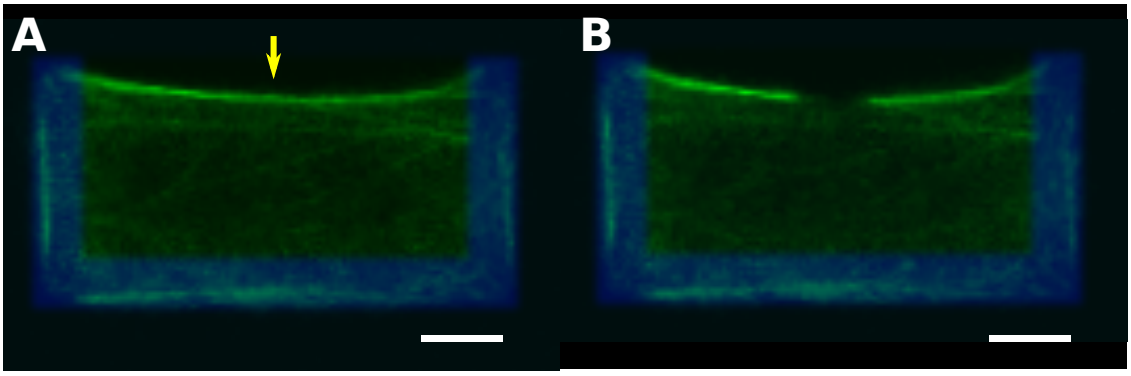

Figure 3.2: Ablation of peripheral stress fibers. (A) Actin CSK (green) of a U2OS cell on a flat, U-shaped pattern (blue) with one free spanning arc. The yellow arrow indicates the location where the fiber is severed. (B) Steady state after fiber retraction. Scale bar: $10\mu m$. Courtesy of Elena Kassianidou.

intrusive way [91]. The latter approach will be discussed in detail in chapter 4 of this thesis.

Recent experiments by Kassianidou and Kumar (unpublished) have raised the question how the force load of a peripheral SF depends on the connectivity to other internal SFs. U2OS-cells were seeded on U-shaped pattern, on which they assume rectangular shapes with one freely spanned arc. This invagination is reinforced by a peripheral SF, to which other internal SFs can attach (cf. Fig. 3.5 A, B). Connection angles were recorded in the experiment, before the peripheral SF was severed (Fig. 3.2). The retraction dynamics were fitted to a Kelvin-Voigt model [CIT], where a viscous and an elastic element are connected in parallel. The model predicts an exponential law for the retraction length, $l(t) = l_0 \cdot (1 - \exp(-t/\tau)) + D_a$, where l_0 is the asymptotic retraction length, D_a the length of the SF destroyed by the laser, and $\tau = \eta/E$ a the decay time scale which is usually on the order of some seconds [23]. The latter is determined by the ratio of the viscosity η and the Young's modulus E of the viscous and elastic element, respectively.

3.2.1 Symmetrical Stress Fiber Configuration

In order to understand the effect of internal SFs pulling a peripheral SFs inwards, we develop a simple mechanical model of connected cables subjected to external force (Fig. 3.3 A). The internal SFs are modeled by an active force F_0 that encloses an angle α with the horizontal axis. The peripheral SF is modeled by an active cable, that is dissected by the connection points of the internal SF. Both parts feature a constant force dipole of the same tension F_0 and can be under elastic stress. The elastic stress builds up because they are located at the periphery and are therefore

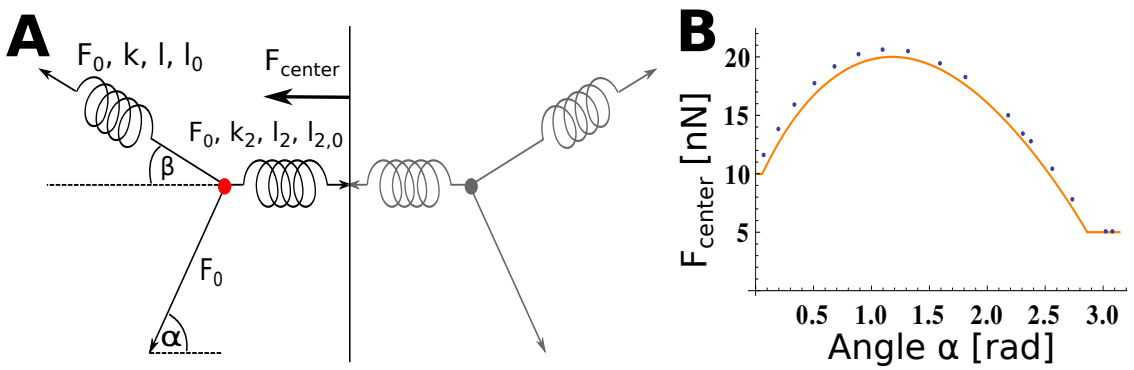

Figure 3.3: Theoretical model for a symmetric configuration of connected stress fibers. (A) One half of the peripheral stress fiber is modeled by two cables with different elastic properties. The connecting fiber from the interior is purely active, since it is in the compression regime. (B) Solution of the implicit equations (orange line) and network calculations (blue dots) show excellent agreement. The slight force overestimation in the network model is due to a small active tension on each network link, which is added in order to regularize triangle shapes. The parameters used were $F_0 = 5nN$, $k = EA/l_0$, $k_2 = EA/l_{2,0}$, $EA = 500nN$, $l_0 = 26\mu m$, $l_{2,0} = 4\mu m$.

stretched when the contour is pulled inwards. We are interested now in the force F_{central} in the central part, as this would determine retraction after the peripheral SF is severed along the symmetry line. Note that the configuration resembles a common situation observed in experiments, see Fig. 3.5 A.

It is sufficient to evaluate the left side of the picture shown in Fig. 3.3 A, since we focus on a symmetrical situation for simplicity. Without elastic elements, force balance in x and y direction immediately leads to $\alpha = \beta$, $F_{\text{central}} = 2F_0 \cos(\alpha)$. In this simple picture one might naively assume, one would expect that retraction is strongest for small α. However, experiments indicate that this is not the case.

With the full model including the elastic elements, the force balance and geometrical conditions read

$$\begin{aligned} F_0 \cdot \sin(\alpha) - ((F_0 + k(l - l_0)) \cdot \sin(\beta) &= 0 \\ F_0 \cdot \cos(\alpha) + (F_0 + k(l - l_0)) \cdot \cos(\beta) &= F_0 + k_2(l_2 - l_{2,0}) \\ \cos(\beta) &= \frac{l_0 + l_{2,0} - l_2}{l} \\ 0 \leq \beta \leq \frac{\pi}{2} \, . & \end{aligned} \tag{3.3}$$

Note that the elastic parts are only evaluated if $l - l_0 > 0$, which represents the cable asymmetry between stretch and compression. We numerically solved this system of equations with the software *Mathematica*. For the parameters we chose $F_0 = 5nN$, $k = EA/l_0$, $k_2 = EA/l_{2,0}$, $EA = 500nN$, $l_0 = 26\mu m$, $l_{2,0} = 4\mu m$, which are typical values for U2OS-cells [91]. The result is shown in Fig. 3.3 B (orange line). Different

from the naively expected simple force decay with increasing α, the force distribution shows a peak at $\alpha \approx 70°$, and the maximal force is considerably higher than the active forces involved. The force the decreases for higher α until it reaches the active force level close to $\alpha = 180°$. The plateaus on the left and right end of the curve are the regimes where either the outer (left) or central (right) cable is in the compression regime. This result is confirmed by network simulations with active cables for the same parameters (Fig. 3.3 B, blue dots). The slight overestimation of force is due to a small active tension in the background network which was put for numerical reasons.

In terms of the experiment, this simple model gives the remarkable hint, that the exact magnitude of active forces might not be the only determinant for the retraction length. As the internal SFs pull the contour inwards, an elastic stress occurs in the peripheral SF that might be higher than the active force of the internal SF. This elastic stress is released when the fiber is severed. Experiments confirm that the contour not only retracts along itself after ablation but also moves inwards in this process. This indicates that there is indeed a stress caused by inwards pulling internal SFs. This stress is primarily determined by the connection location of internal and peripheral SF, and by the connection angle.

We investigated the impact of the different parameters further by changing the connection point along the peripheral SF determined by l_0, the active force F_0 and the fiber stiffness EA respectively (Fig. 3.4). If the connection angle α is either close to zero or π, the rest length of the fiber does not matter as no elastic contributions occur. At intermediate connection angles the effect becomes stronger when the connection points are closer to the center (large l_0, Fig. 3.4 left). In contrast, the variation of the active forces changes the base force level and affects also the extreme ends of the range of α (Fig. 3.4 middle). As expected, SF stiffness induces only an elastic effect, which leaves the force levels unchanged for large and small α. We conclude that configurations with either only small or only large α are well suited to figure out the scale of active forces in experiments.

3.2.2 Asymmetric Stress Fiber Configurations

The symmetric model provided insight in the important characteristics of force distribution with active and elastic elements. We now want to evaluate whether this describes the situation found in laser ablation experiments. However, cells on micropatterns hardly show purely symmetric situations. It is therefore difficult to gather enough data to support or reject the symmetric model. We pursued a different approach using simulations with active cable networks (ACN). Fig. 3.3 B shows the agreement between solving the system of equations 3.3 and ACN simulations.

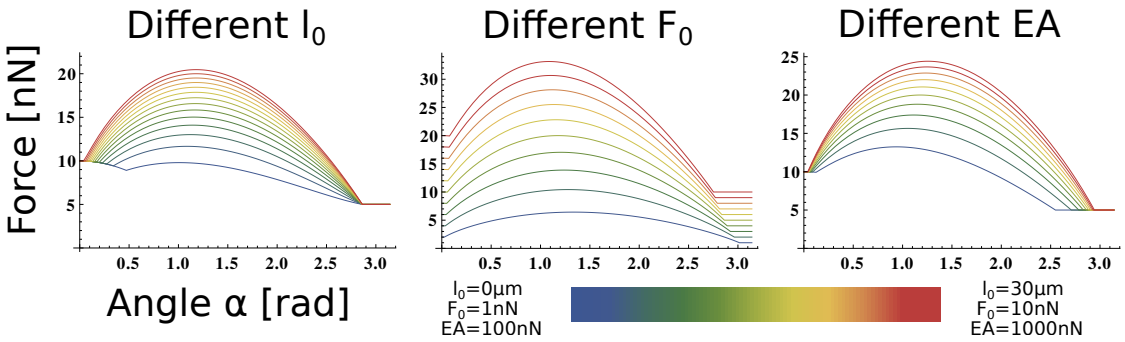

Figure 3.4: Parameter variation in the symmetric model with respect to the choice in Fig. 3.3 B. All plots show the total force in the inner cable, cf. Fig. 3.3 A. When the rest length l_0 of the outer cable is altered, the rest length of the inner cable changes to $l_{2,0} = l_{tot} - l_0 = 30\mu m - l_0$. The effect of inner SFs is strongest when they connect close to the center (left). As expected, stronger active forces lead to higher total force levels in the central part (middle). Most elastic stress is generated when the fiber is stiffest (right).

The advantages of ACN simulations are that they are very flexible regarding the geometry of the fiber distribution and that they allow us to introduce a background network tension.

The workflow is illustrated in Fig. 3.5 and is as follows. We take the actin fluorescence image and enhance the contrast in ImageJ [71] such that the fibers are clearly visible (Fig. 3.5 A). We then use our plugin for the **S**egmentation **o**f **F**ocal **A**dhesions and **ST**ress fibers (SoFAST), which we discuss in detail in chapter 4. Briefly, the user can manually segment SFs by marking them with segmented lines, Fig. 3.5 B. The plugin also allows to segment cell area from the actin image. It then generates a triangular network that covers the whole cell area and embeds the stress fibers as marked edges.

It is however difficult to segment the cell in such a way that a curved SF lies exactly at the cell rim. For this reason, we implemented a mesh alteration routine in *SurfaceMaster* which removes the network part on the outside of the peripheral SF. We then perform an optimization with respect to the ACN energy. Here we chose the same active force and one-dimensional Young's modulus as for the symmetric model, $F_0 = 5nN$ and $EA = 500nN$ for all SFs. As we segment already the invaginated contour of the cell, we set the rest length of the peripheral SF to 98% of its segmented length. The background network was chosen to be softer by an order of magnitude and with a very small active component, which was added for numerical reasons. An example of a network after energy optimization with the software *SurfaceMaster* is shown in Fig. 3.5 C, where the force magnitude is shown in color code.

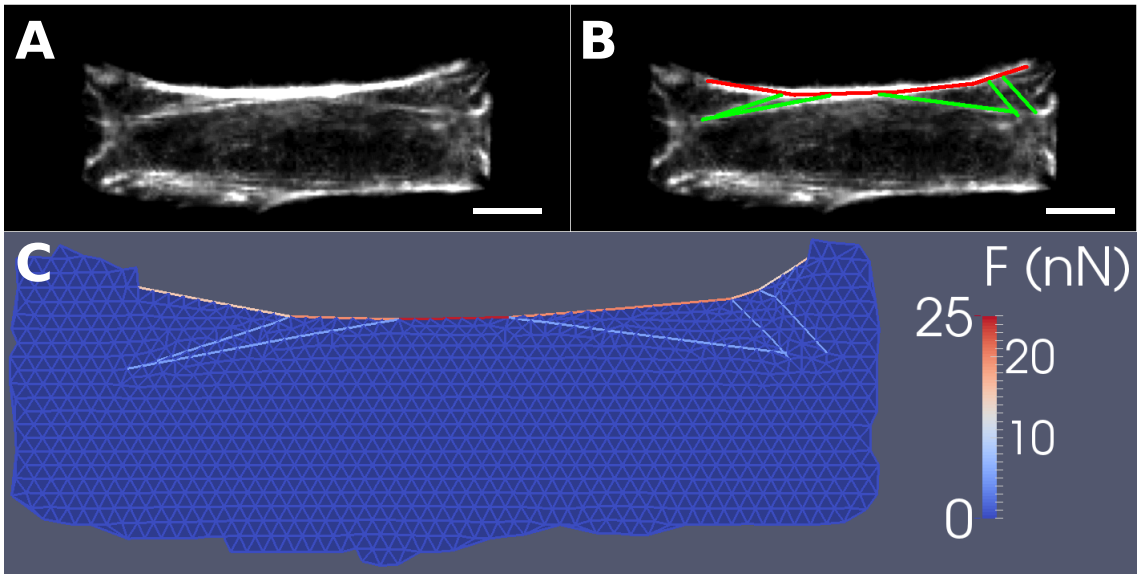

Figure 3.5: Segmentation and predicted force distribution. (A) Actin fluorescence image of an U2OS-cell on an U-shaped pattern with dimensions of $60\mu m$ by $20\mu m$. The thick actin bundles are clearly visible. (B) Segmentation of the stress fibers with the ImageJ plugin SoFAST discussed in chapter 4. (C) Predicted force distribution in the cytoskeleton. (A) and (B): Scale bar: $10\mu m$, courtesy of Elena Kassianidou.

Fig. 3.5 C shows that the qualitative behavior found for the symmetric model also transfers to the ACN simulation. Although the individual SFs add only $5nN$ of active force, the total force in the fiber is as high as $25nN$ at the center. The other segments show lower forces depending on the connectivity of the internal SFs. We can now use these force predictions to compare the model to experiments. We investigate two data sets, where either $n = 8$ or $n = 5$ cells where cultured on U-shaped patterns with dimensions of $25\mu m$ by $48\mu m$ and $20\mu m$ by $60\mu m$, respectively. We used the same parameters that were noted in the last paragraph for all simulations, so the difference between simulations is reduced to the different segmentations. We then recorded the predicted force at the location of ablation in the corresponding experiment. We converted these forces to lengths l_F for comparison with the retraction length l_0 using a simple spring model, $F_{\text{sim}} = k \cdot l_F + F_{\text{res}}$. We chose $k = 3nN/\mu m$, $F_{\text{res}} = 9nN$ for the first data set, and $k = 1.5nN/\mu m$, $F_{\text{res}} = 4.8nN$ for the second one. An intuitive interpretation of the meaning of these parameters is difficult. First, it is clear that there needs to be a spring constant which describes the effective stiffness of the surrounding CSK close to the cut, which eventually balances the retracting forces. The residual force is then the effective active force in this part of the cell. However, it is not obvious why these parameters should vary between the different patterns. It seems more reasonable that in the $20\mu m$ by $60\mu m$ pattern, the peripheral SF experiences more load and is therefore reinforced more strongly, leading to other elastic and active force parameters. In the future, one

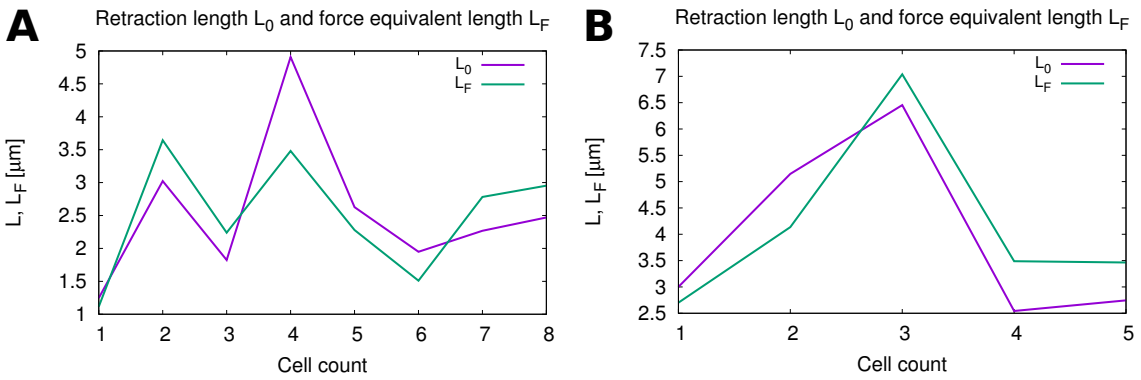

Figure 3.6: Comparison of model predictions L_F and experimentally measured retraction lengths L_0. As the model only predicts forces in the cytoskeleton prior to ablation, the forces are converted to retraction length by a simple Hookean spring model, $F = kL_F + F_{\text{center}}$ (cf. main text). The model parameters were always as follows: $F_{active} = 5nN$, $\alpha = 0.98$, $EA_{fiber} = 500nN$. (A) Result for $n = 8$ cells on a pattern of $25x48\mu m$ dimensions for $k = 3nN/\mu m$ and $F_{\text{res}} = 9nN$. (B) Result for $n = 5$ cells on a pattern of $20x60\mu m$ for $k = 1.5nN/\mu m$ and $F_{\text{res}} = 4.8nN$.

should therefore invert the force reconstruction by postulating that k, F_{res} be the same on all geometries and optimize for the best parameter choice. It is remarkable though that we obtain the same qualitative result with the same choice of parameters, which implies that their absolute values do not change the qualitative aspects of the result.

The results are shown in Fig. 3.6. The retraction lengths and the force lengths l_0 and l_F match surprisingly well. Apart from one cell in each data set, the difference $\Delta l = |l_0 - l_F|$ is below $1\mu m$. Cells that show large retraction lengths show high forces at the point of ablation in the simulations, and, conversely, SFs with low retraction lengths are predicted to be under low force. We emphasize that information about the experimental retraction length did not enter the force prediction process, and that the parameter settings were the same for all simulations. This means that the active force was assumed to be the same for all SFs within all cells in both data sets. This is obviously a very strong assumption and underlines the claim from the symmetric model that the connectivity determines peripheral SF forces more than force magnitudes. We conclude that ACN simulations are a fast and reliable way of estimating the force distribution along the contour.

3.3 Cellular Tension and Elasticity in Three Dimensions

Inside organisms, cells naturally live in three dimensions. However, some cells only feel a two-dimensional space around them. For example, epithelial cells that line inner and outer surfaces in the body are only attached to them on one side of the cell. The same is true for endothelial cells that line inner organs and blood vessels. For theses cells, culture on flat surfaces provides a natural environment. Other cells like fibroblasts that form connective tissue live in a three-dimensional matrix. For them, flat substrates are an artificial surrounding. The lower dimensionality breaks the symmetry in the vertical direction of space and forces the cells to rearrange internal organelles such as the nucleus. It is therefore unclear if the behavior of such cells on flat substrates is comparable to *in vivo* situations. At the same time, the task to observe and analyze cells in three-dimensional contexts is a challenge to imaging, segmentation, and modeling. The group of Martin Bastmeyer at the Karlsruhe Institute of Technology uses the method of direct laser writing to produce full three-dimensional scaffolds, into which cells can spread and attach only to some functionalized adhesive regions [CIT]. This three-dimensional equivalent of flat patterned substrates again allows to normalize the variability between different cells. To gather quantitative information is still problematic though, especially since conventional optical microscopes only allow for a resolution up to $800nm$ in the z direction.

In the following we will look at two different situations. First we will look at a quasi two-dimensional V-shaped pattern, which is lifted from the grounds *via* microposts. As it is embedded in 3D space but still directs the cell towards a flat shape, we will refer to this situation as 2.5-dimensional. We then turn towards a full three-dimensional scaffold with the shape of a pyramid with a pentagon base.

3.3.1 Tension-Elasticity Model in Three Dimensions

Regarding TEM, the situation is now different from the previous section. Stress fibers do not occur as frequently in three-dimensional situations, and are often limited to arc structures at the periphery. We will therefore return to the view of a homogeneous surface tension σ instead of discrete elements contributing the main part of the inward forces. However, in three spatial dimensions the cell cannot be modeled by its two-dimensional projection as we have previously done for cells on flat substrates.

The three-dimensional analogue to the TEM in two dimensions is shown in Fig. 3.7.

The cell model resides in a 2.5-dimensional pattern which fixes cell shapes along two lines in the shape of the letter V. The model includes elastic responses only at the free edge that would complete the V to a triangle, where one can observe actin bundles in the experiments which were conducted by Mona Jaggy in her master thesis (unpublished) [92]. Apart from the elasticity and the fixed outer geometry, the shape is completely determined by a surface tension and a non-vanishing enclosed volume. The latter causes the upper and lower membrane connecting to the peripheral SF to enclose an effective opening angle $\phi > 0$. If the enclosed volume tends towards zero, $V \to 0$, ϕ becomes very small as well. Thus this limit corresponds to the two-dimensional TEM with $\sigma_{2D} = 2\sigma_{3D}$. Note, however, that the bending rigidity of the membrane prohibits sharp edges on microscopic length scales. Thus ϕ has to be defined at the intersection of two straight lines that are embedded in the membrane a bit away from the arc where the influence of bending is small compared to that of the surface tension. In the triangulated surface representation, ϕ can be defined as the angle of two triangles that are adjacent to an edge of the peripheral arc. As the situation is symmetric in the z direction, we can calculate the local force balance condition similar to the two-dimensional TEM,

$$\begin{aligned} \lambda \frac{d\vec{t}}{ds} &= \lambda \kappa \vec{n} = 2\sigma \cos(\phi/2)\vec{n} \\ \Rightarrow R &= \frac{\lambda}{2\cos(\phi/2)\sigma} \ . \end{aligned} \tag{3.4}$$

Note though that the effective opening angle ϕ does not need to be constant, which leads to non-circular arcs.

3.3.2 V-Shaped Patterns

One factor that might affect the opening angle ϕ in the three-dimensional extension of the TEM, Eq. 3.4, is a finite enclosed volume condition. The V-shaped 2.5-dimensional pattern is ideal to investigate this effect, since it defines a single, usually well developed arc, whose curvature we can quantitatively explore in the model. In experiments, these arcs often appear to be flattened at the central region, cf. Fig. 3.1 B. As a model system, we rebuild the pattern from the experiment in a surface mesh. The opening angle of the V shape is 60°, such that both the lateral sides of the pattern and the spanning distance of the free arc share the same length, in this case $30\mu m$. As the reference volume we chose the volume of a pyramid with height $h = 6\mu m$, $V_0 = 780\mu m^3$, which is also shown in Fig. 3.7.

Numerically, the optimization of an isometric tension on triangles is challenging, since it is a purely local energy. This means that the triangles away from the free arc are not affected when the arc invaginates from its straight starting position.

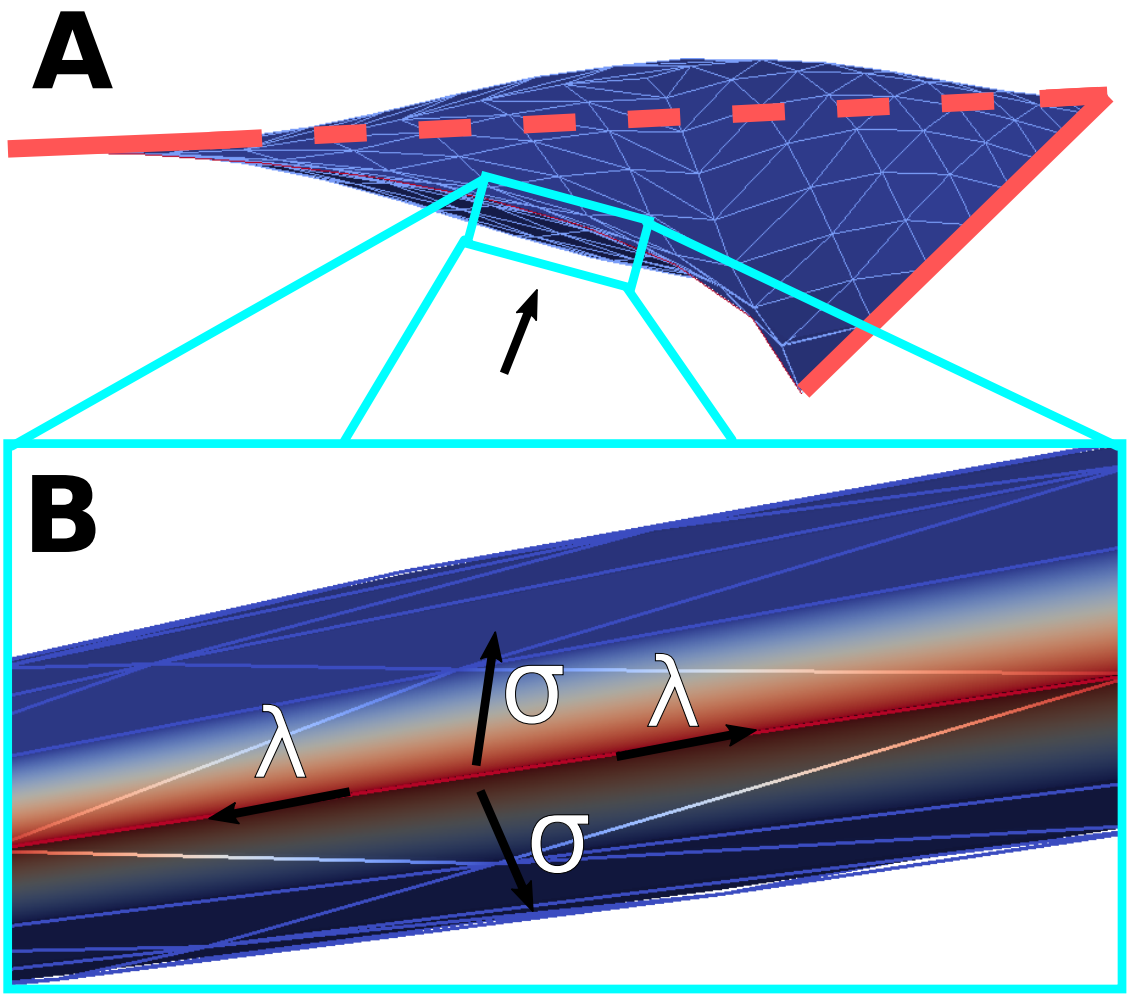

Figure 3.7: Tension-elasticity model in three dimensions. (A) TEM model for a cell on a V-shaped pattern lifted away from the ground. The turquoise box marks the region magnified in part (B), and the arrow indicates the view direction. The red lines indicate where vertex locations are fixed in the model due to the geometry of the pattern. (B) In three dimensions the surface tensions σ of the two membrane patches connected to the stress fiber (red line) add vectorially.

As a consequence, triangles at the border become very thin and impede numerical optimization. We circumvent this problem by splitting the optimization into two runs. During the first we add a small linear elastic shear and compression energy on the triangles as presented in the numerical methods chapter, and find the optimal configuration for the combined energy assay. As the prefactor of the elastic energy is small, the optimal shape is already close to the one for the system without elastic energy. The triangle coverage of the surface remains much more homogeneous though. In a second optimization run, we then minimize the surface energy without the elastic contribution to the triangles. As the deformations are now small, triangle sizes are not hindering the numerical procedure. Elastic regularization of triangulations are also used with other surface functionals that do not specify a reference

shape for each triangle, for example in the case of bending energies [46, 93, 94].

Apart from the volume, we retain both control parameters of the two-dimensional TEM, namely the rest length parameter $\alpha = l_0/d$, where l_0 is the rest length of the elastic component and d the spanning distance, and the length scale $l_f = 2EA/\sigma$. The factor of two comes from the consideration, that l_f should converge to the definition of the two-dimensional TEM for $\phi \to 0$. We now want to qualitatively evaluate the effect of finite enclosed volume. As the numerical procedure has to be adjusted in terms of the elastic prefactor for each l_f, and different values of l_f lead to the same overall qualitative behavior in control samples, we confine the systematic variation to the volume fraction V/V_0 and the rest length parameter α and fix $l_f = 250\mu m$, which is a typical value for the two-dimensional TEM.

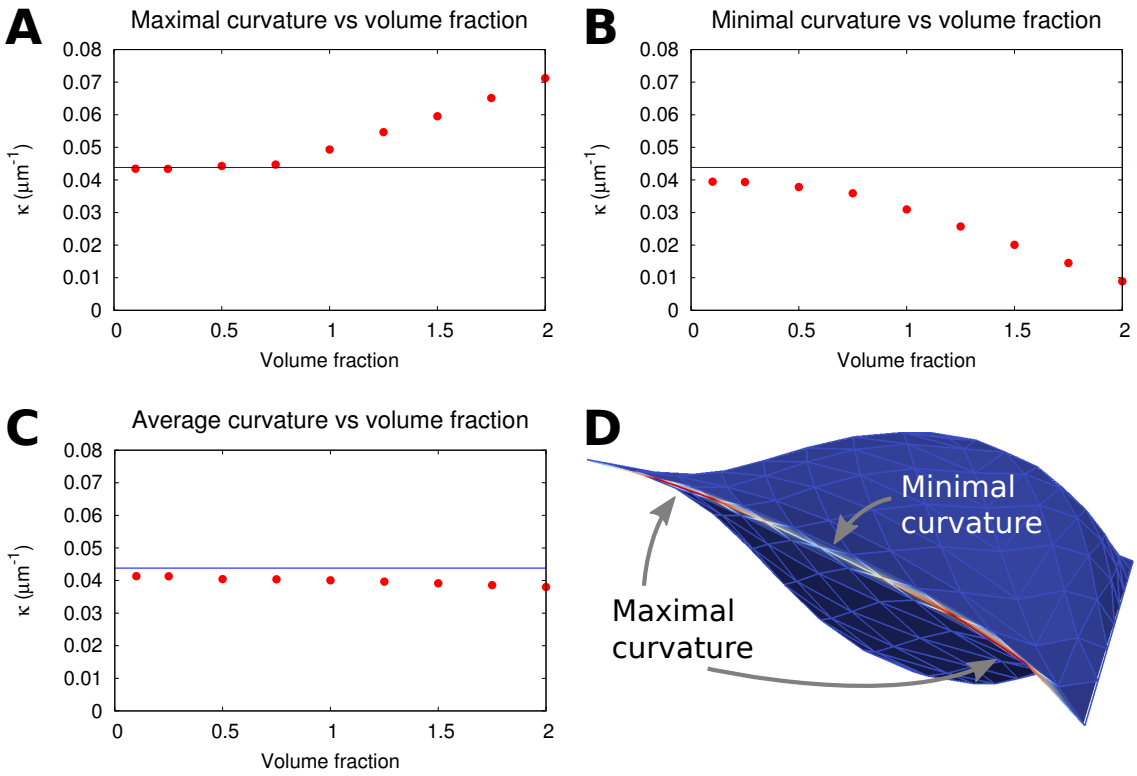

Figure 3.8: Non-circular arcs as a result of the fixed volume condition at $\alpha = 1$. The volume is measured relative to the reference volume shown in Fig. 3.7. The blue lines indicate the analytic predictions by the two-dimensional tension-elasticity model. Red circles mark simulation results at finite volume in a triangular network (see main text). (A) Maximal curvature increases for higher enclosed volumes, while the minimal curvature decreases (B), which leads to flattened arcs. (C) The mean curvature along the arc is only slightly decreased. (D) Example of a cell with volume fraction $V/V_0 = 2$, where regions of minimal and maximal curvature are indicated by arrows.

The results are shown in Fig. 3.8. For small volume fractions, the maximal line

curvature along the peripheral converges towards the two-dimensional prediction, while the minimal and average line curvature fall slightly lower. When the volume fraction is increased, the maximal curvature increases (Fig. 3.8 A), while the minimal curvature drops (Fig. 3.8 B). The reason is that the enclosed volume forces a large opening angle ϕ in the central region of the peripheral SF, which is illustrated for the highest volume fraction of $V/V_0 = 2$ in Fig. 3.8 D. Consequently, the arc is not pulled inwards there, and the curvature is reduced. Further, it reduces the overall elastic tension in the peripheral SF (not shown), which leads to higher maximal curvatures at locations with smaller ϕ. The effect is more pronounced for large α (not shown). This is expected, because large α allow the arc to be pulled further inwards, and therefore interfere more strongly with the volume condition. Surprisingly, the mean curvature along the arc is only marginally affected. This implies that fitting circular arcs to experimental data in the three-dimensional environment is still meaningful, even if the arcs are flattened.

We also investigated the effect of the bending stiffness of the membrane. In experimental units, the stiffness constant takes a value of $\kappa_b = 0.0002nN \cdot \mu m$, which leads to small bending energy contribution compared to the ones associated with a surface tension of $\sigma \approx 1nN/\mu m$ and the elastic response of the peripheral SF at $l_f = 250$. Further, around the peripheral SF, the local surface shape is already close to optimal with respect to bending energy, since the two principal curvatures are of different sign. Qualitatively, the curvature perpendicular to the fiber direction also seems to be higher in regions of high SF line curvature and the other way round. This means that the local structure around the SF resembles the neck configuration, where the two principal curvatures are equal but of different signs. Thus, the mean curvature vanishes and its square of the mean curvature is assumes its minimal value zero, $H^2 = 0$. In this context it is not surprising that including bending energy terms at the experimentally relevant stiffness or even an order of magnitude higher does not influence the line curvature of the peripheral SF in this configuration.

3.3.3 Pyramid Scaffolds

We now take another step and arrive at full three-dimensional scaffolds. An exemplary scaffold is shown in Fig. 3.1 C, that shows the geometry of a box ring. Here we now turn towards cells in the geometry of an upside down pyramid, Fig. 3.9. The experiments are performed by Benjamin Richter in the Bastmeyer lab. Interestingly, there are still arc-like structures that reinforce invaginations. In terms of the TEM, difference to the 2.5-dimensional case is that the outer geometry now offers anchoring points for the contractile cell to assume a fully three-dimensional structure without a fixed volume condition. We now generalize the TEM in such a

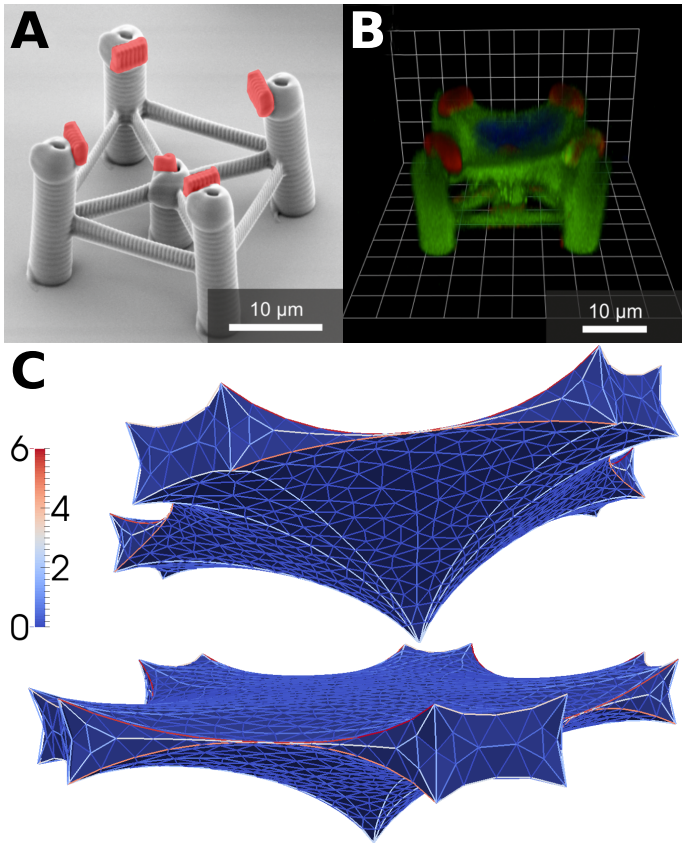

Figure 3.9: Cells cultured in a three-dimensional scaffold with the geometry of an upside down pyramid. (A) Scanning electron microscope image of a pyramid structure with square base. (B) Three-dimensional image of a 3T3 cell adhering to the structure shown in (A) constructed from confocal microcope image stacks. (A), (B) Courtesy of Benjamin Richter from the Bastmeyer group, Karlsruhe. (C) Three-dimensional TEM model for a cell in a pyramid structure with pentagon base (cf. main text).

way, that we assume that all links in the network model are elastic and obey the same cable law.

Fig. 3.1 B shows a 3D view on both the model and the segmented arcs from the experiment in the same outer geometry. The arcs resemble contracting elastic stripes to which multiple radii can be assigned depending on which plane it is projected to. Here two planes were chosen for segmentation:

1. The xy plane in the standard coordinate system parallel to the ground and pentagon base at the height of maximal intensity over the whole arc.

2. A plane spanned by the two upper anchoring points of the stripe and the point of highest intensity at its center. We will refer to this as the *tilted plane*.

For the model calculations, we used $l_f = 50\mu m$ and $\alpha = 1$. Note that the latter means that the equilibrium shape of the model cell is assumed if the corners of the outer geometry are connected by straight edges only. In the experiment, we could determine the radii of the arc spanned between neighboring posts of the pentagon to be $R_{\text{tilted,exp}} = 5.6 \pm 0.7\mu m$ and $R_{\text{xy,exp}} = 6.8 \pm 1.4\mu m$ with a custom software written by Marco Linke from the Schwarz group. For our simulation parameters, we achieve excellent agreement with simulated arc radii of $R_{\text{tilted,sim}} = 5.9\mu m$ and $R_{\text{xy,sim}} = 7.7\mu m$.

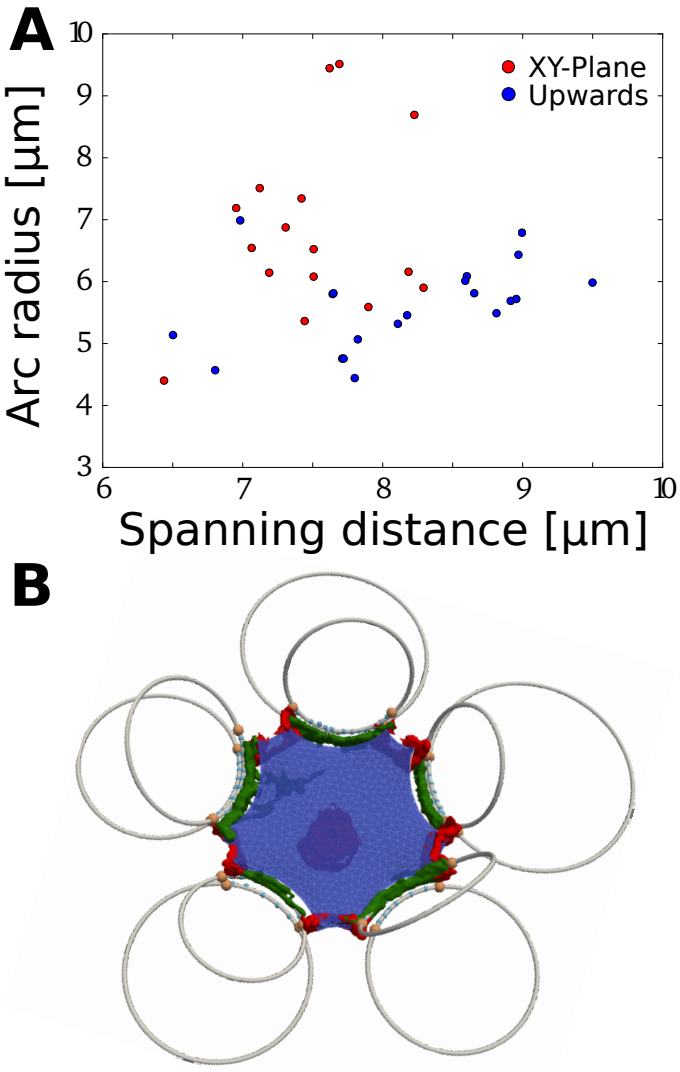

Figure 3.10: TEM in three dimensions. (A) Measured arc radius vs. spanning distance in the plane of the pentagon (red) and in an upwards tilted direction (blue, cf. main text). The circle fitting to experimental data was done by Marco Linke. (B) The triangulated surface fits nicely to the arcs segmented from experiments (green) for $\alpha = 1$, $l_f = 50\mu m$. The parts of the scaffold functionalized for adhesion are shown in red. The circles correspond to the arc radii plotted for all cells in (A). The segmentation of arcs and structure was done by Marco Linke with the image processing software Imaris.

Interestingly, SFs occuring in experiments co-localize with regions where stress condenses to single links in the model, emphasizing that these structures are needed to provide the cell with rigidity. This means that with the simple model assumptions that all links obey the same relation, we can also predict where actin bundles form in a three-dimensional structure. Interestingly, the cellular cortex is under much lower stress between the connection points of the adhesive regions at the top of the posts and at the central one at the bottom. Accordingly, we could only observe a single arc in this direction in $n = 4$ representative cells, whereas we observed $n = 15$ arcs between connected adhesive regions at the top of the posts.

3.4 Discussion & Outlook

In this chapter we discussed several extensions to the tension-elasticity model to address cells with prominent internal SFs in patterned environments and cells in three-dimensional scaffolds. First, we presented an approach to investigate the ten-

sion in different segments of a peripheral SF that is pulled inwards by discrete inner SFs rather than by a homogeneous surface tension. The investigated cells were cultured on flat substrates, and develop thick actin bundles mostly in one plane. For these reasons, it is adequate to model the mechanics only in a two-dimensional projection of the cell. With the help of a simple semi-analytical model, we could demonstrate that apart from force magnitudes, especially the connection location and angle are important to predict the force along the contour. We then turned to a typical experimental situation, where the symmetry assumptions of the simple model do not hold. We used an active cable network with embedded fiber structures to predict the force distributions. We chose the simplest assumptions possible, i. e. the same active and elastic properties for all SFs in all cells of two data sets. Further, these properties were set solely from approximate values reported for similar situations, but do not rely on measurements in this setting. Surprisingly though, we could accurately predict the retraction length up to two constants we needed to convert forces to lengths. These constants had to be chosen differently for the different pattern aspect ratios of the two data set. This highlights that the variability in active tension among the SFs of the same cell type is only of secondary importance for the retraction of peripheral SFs. It is rather the connectivity with inner SFs that plays a fundamental role for force distribution and retraction.

Further experiments are necessary to shed more light onto peripheral SF retraction. One interesting option is to sever an contour arc at two different locations subsequently in the same cell. Together with the model, this provides an estimate of the relation between forces at two different points in the same cell, which would help to better understand the meaning of the force to length conversion constants. We also aim at performing model-based traction force microscopy on some cells on the patterned substrates. This technique is the topic of the next chapter and provides insight into the absolute force scale, specifically for the active forces along inner SFs. Once these are known, it will also be possible to assess the elastic properties of the peripheral SF in more detail.

In the second part of the chapter we addressed an assay where cells where cultured in three-dimensional environments. First, we looked at an essentially flat structure that was lifted away from the surface. Without a finite enclosed volume, cells in such structures which exhibit a surface tension should also be flat and do not differ from cells on two-dimensional patterns, which is why we refer to those structures as 2.5-dimensional. However, the basic principle of the cell's membrane is to partition space and separate its interior from the outside space. Thus it is not surprising that the cells are not flat in experiments. At the same time, they often show arc-like structures at free edges, which are however often not circular. We extended the TEM to contain a fixed volume and used triangulated closed surfaces pinned to the

geometry of a V-shaped pattern to simulate 3D cell shape. In this way we could show that the flattening of peripheral arc can be caused by the enclosed volume. We explained this effect with the change in the opening angle ϕ that the two membrane patches enclose at the peripheral arc. This angle changes along the contour, reaching a maximum at the center of the arc. Consequently, here the line curvature along the arc is lowest by the local TEM force balance. The interaction of enclosed volume and arc shape becomes stronger if the enclosed volume is higher or the elastic force along the arc is reduced. Apart from the flattened region, arcs affected by the volume condition also exhibit stronger curved regions in these patterns. This is due to the fact that the elastic force on the arc is reduced while the surface tension is not, and the effective opening angle is still small close to the adhesive areas at the end of the arcs. Surprisingly, the mean curvature along the arc is only very slightly decreased, meaning that circle fits are still a valid tool to assess tension and elasticity in this situation. This statement is not general though and has to be validated for each structure of interest.

Finally we have adapted the TEM for full cable networks with homogeneous properties to investigate cells in pyramid structures. We have found that $\alpha = 1$, $l_f = 50\mu m$ reproduce arc radii of the experiments, which are also typical for two-dimensional TEM fits. The condition $\alpha = 1$ means that the reference shape for the elastic energy is assumed by connecting adhesion points by straight lines. The length scale $l_f = EA/\sigma$ denotes the relative impact of active force and passive elasticity. Different from the 2D situation, we defined to planes for each arc and measured the radius in the projection to each of it. Interestingly, both radii could be reliably predicted with the same parameter set which is typical also for the two-dimensional TEM [4]. We have also observed that the elastic stress in the model condenses at the locations where cells in the patterns develop actin bundles, though the network links all obey the same relation. We also saw that another possible location for actin arcs between the adhesive areas at the base of the pyramid and the top bear considerably less stress in the model of this geometry. This is in agreement with the fact that we could only observe a single SF in this direction compared to $n = 15$ arcs between neighboring adhesive regions at the base. In the future, one could change the geometry of the pyramid to see also arcs at different locations and different spanning distances. Further, it would be interesting to alter the stiffness of the scaffold, as cells sense and respond to the stiffness of their surrounding. The three-dimensional TEM could help to understand and quantify changes in cell elasticity in these settings.

4 Model-based Traction Force Microscopy

4.1 Introduction

This chapter contains joint work obtained with Jérôme Soiné and was published in [91].

Adherent cells continuously exert forces to their extracellular environment in order to adapt and respond to its mechanical properties. This process is vital, as cells make fate decisions like proliferation, differentiation or even cell death dependent on their mechanical surroundings [1, 2, 95, 96]. It enables them to sense the stiffness of the surrounding matrix, which is important for cell spreading and even capacitates them to migrate along stiffness gradients [97]. Contractile forces are mainly generated in the system of actin filaments and myosin II motor proteins and are mediated to the extracellular space by large protein assemblies called focal adhesions (FAs, cf. chapter 1). FAs exhibit over 150 different proteins constituents and are important for mechanotransduction [20, 98].

The actin cytoskeleton (CSK) plays a central role in cellular force generation. Actin can generate forces that push the cell edge outwards by polymerizing against the plasma membrane during spreading or migration [99]. Molecular myosin motors generate forces that actively contract filamentous actin networks. Especially distinct structures visible under normal fluorescence microscopes are stress fibers (SFs), which are highly cross-linked actin bundles. They occur in different locations within the cell and exhibit different molecular compositions, and are therefore classified into different subtypes [19, 77] (cf. Fig. 4.1 A and also chapter 1). Dorsal stress fibers (DSFs) are typically anchored at an FA at the cell's leading edge and grow radially towards the center along the dorsal membrane. Transverse arcs (TA) connect to the free ends of the DSFs and run parallel to the cell edge. They are not directly linked to FAs. Conversely, ventral stress fibers (VSF) are anchored at FAs at both ends and run along the ventral side of the cell. SFs are believed to play a key role in cellular mechanics for both stability and force generation [21, 77, 84].

As cell-generated forces are fundamental for their integrity and function, it is essential to develop tools and methods to measure them. One well known technique is traction force microscopy, where forces at the cell-substrate interface are inferred from elastic deformations of the substrate material [100]. In this chapter, we present a new way to combine traction force microscopy with biophysical modeling in order to increase resolution and assess the internal force distribution within the CSK, which specifically includes the estimation of SF contractility. We give a new perspective on regularization and investigate the effects of different regularization schemes.

4.2 Traction Force Microscopy

As force is an invisible physical quantity, it is necessary to quantify its impact on its surrounding in order to make measurements. For example, one could observe the acceleration of a freely falling ball to measure the earth's gravitational force, or the velocity of a sphere being dragged through a fluid with Stokes friction. The classical case is of course the measurement of a Hookean spring's extension.

Many established methods to measure cell-generated forces from utilize elastic deformations. The most direct way is the use of fluorescent force sensors, where an elastic linker polymer connects two fluorophores that interact via fluorescence resonance energy transfer (FRET). As the FRET signal depends with the sixth power on the distance of the fluorophores, it constitutes a very sensitive signal for the stretch in the linker polymer, and thereby force [101, 102]. These molecular force sensors can be integrated in proteins, e. g. the FA constituent Vinculin [101], or functionalized to bind to transmembrane and the extracellular environment [102–104].

Traction force microscopy (TFM) measures forces at the cell-substate interface via the deformation of an elastic material the cell adheres to. In pillar assays, the cell sits on top of a grid of elastic rods. In the limit of small bending, the force extension curve is linear and the stiffness can easily be controlled by the geometry of the posts [105, 106]:

$$\frac{F}{x} \propto \frac{r^4}{L^3} \tag{4.1}$$

Here, F, x, r, and L denote force, deflection, pillar radius, and pillar length, respectively. However, one disadvantage of this method is that cells seem to sense the non-homogeneous underground [100, 107]. They form FAs that enclose the tips of the posts, indicating that they deviate from their normal size and shape [108]. Further, the global distribution of FAs is limited to positions and sizes of the rods

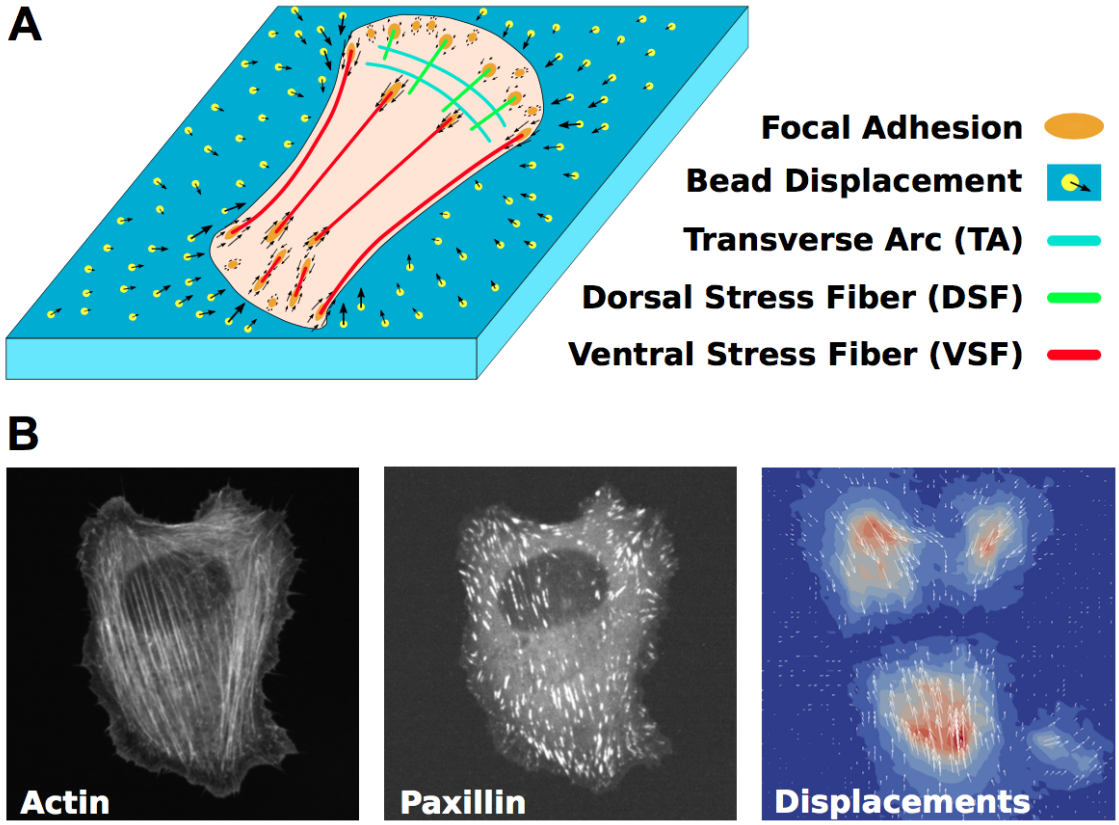

Figure 4.1: Traction force microscopy on soft elastic substrates. (A) The cell adheres to a planar substrate. The deformation field caused by cellular traction forces can be tracked *via* marker beads embedded in the substrate. (B) Typical data set for MBTFM. In addition to the bead displacement field, we acquire fluorescence images of the actin CSK and the focal adhesion protein paxillin.

that are covered by the cell.

Here we focus on TFM on flat elastic substrates. A typical experimental setup is illustrated in Fig. 4.1 A. Fluorescent marker beads are embedded in a soft thick elastic polymer film. When the cell adheres to the substrate and contracts, one can record the material displacement field by tracking bead movements (Fig. 4.1 B). The main advantages compared to elastic posts are that cells can be presented to a smoothly functionalized surface, and that they can be cultured only with minimal deviations from standard cell culture protocols. This however comes at the cost that stress and strain at different positions in the material are now coupled, which renders it more difficult to determine them.

In the framework of continuum elasticity theory we are interested in displacements $\vec{u}$, and the tensor quantities strain and stress, which we will denote by ϵ and σ. From the absolute material movements, the displacements, we can define the symmetric strain tensor

$$\epsilon_{ik} = \frac{1}{2}\left(\partial_k u_i + \partial_i u_k + \partial_i u_l \partial_k u_l\right) \approx \frac{1}{2}\left(\partial_k u_i + \partial_i u_k\right) \ , \tag{4.2}$$

which contains information about local changes in the displacement field in all directions. Note that only these changes in the displacement field lead to elastic forces or stress, as a constant displacement field corresponds to a non-deformational rigid body motion. In the following we will always assume that all $\partial_k u_i \ll 1$, so the third term in Eq. 4.2 is small to second order and the approximation holds true. If for any k, i, $\partial_k u_i \simeq 1$ holds, one speaks of geometric nonlinearities. In linear elasticity theory, we also assume that the material stress tensor σ depends linearly on the strain tensor ϵ. Then, in an isotropic material, the dependency is characterized by two material constants, namely the Young's modulus E and the Poisson ratio ν:

$$\sigma_{ik} = \frac{E}{1+\nu}\left(\epsilon_{ik} + \frac{\nu}{1-2\nu}\epsilon_{ll}\delta_{ik}\right) \tag{4.3}$$

In TFM, one can directly calculate the local stress tensor from local strain in the framework of linear elasticity theory [109]. However, this approach needs very well resolved bead positions, as not only displacements but also strains, i. e. derivatives of displacements, have to be calculated from the image data. For more information about the different kinds of TFM, their best-suited applications and a collection of useful software, we refer the reader to a recent review by Schwarz and Soiné [100]. Here we focus on the standard approach, which is to invert and solve the force balance equation of linear elasticity theory, $\nabla\sigma = \vec{f}$, where $\vec{f}$ denotes the body forces. This is called the inverse problem of elasticity theory.

In order to understand the scope and the ideas of model-based traction force microscopy (MBTFM), the method we introduce in this chapter, one has to know about two different approaches to solve the inverse problem. First, we will explain Fourier Transform Traction Cytometry (FTTC), which will serve as a reference technique [110–112]. Then we describe how to state the inverse problem as a boundary value problem and solve it with the help of finite element methods (FEM), since MBTFM includes the method of FEM-TFM.

The theoretical basis of FTTC is that there exists a Green's function G for the effect of a point force on the boundary of an infinite linearly elastic half space, which is called the Boussinesq solution [66]:

$$G(\vec{x}) = \frac{1+\nu}{\pi E r^3}\begin{pmatrix} (1-\nu)r^2 + \nu x^2 & \nu xy \\ \nu xy & (1-\nu)r^2 + \nu y^2 \end{pmatrix} \ . \tag{4.4}$$

Here we confined ourselves to the solution along the boundary surface of the elastic

half space and used the two spatial coordinates x and y, and the two-dimensional distance $r = \sqrt{x^2 + y^2}$. We note for completeness, that a solution is also known for an elastic film of finite thickness [113]. With a known Green's function, one can use the superposition principle to calculate the resulting displacement $\vec{u}$ for any traction distribution:

$$\vec{u}(\vec{x}) = \int_S G(\vec{x} - \vec{x}')\vec{t}(\vec{x}')d^2x' \tag{4.5}$$

The inversion is done easiest in Fourier space, since Eq. 4.5 is a convolution integral. Hence we can exploit the convolution theorem that tells us that a convolution in real space decomposes into a simple product in Fourier space. This allows to compute a numerical solution efficiently [110].

We now describe how to reconstruct tensions with FEM in the context of a boundary value problem (BVP). A more complete text on the method and the particular implementation used in MBTFM can be found in [114]. The substrate is modeled as a linear elastic cuboid Ω that is discretized. With a given cellular traction distribution $\vec{t}$, the force balance equation $\nabla\sigma = 0$ is solved for the following boundary conditions:

$$\begin{aligned} \sigma \cdot \vec{n} &= \vec{t} \quad \text{for } \partial\Omega_{\text{top}} \\ \sigma \cdot \vec{n} &= 0 \quad \text{for } \partial\Omega_{\text{sides}} \\ \vec{u} &= 0 \quad \text{for } \partial\Omega_{\text{bottom}} \end{aligned} \tag{4.6}$$

This means that the traction boundary on the top surface is given by the forces the cell exerts on the substrate, while the sides are assumed stress-free. The bottom is fixed to a glass substrate, hence a no-slip boundary is assumed. The problem is now well-posed, and one can calculate the displacement field, especially at the top surface of the material for comparison with experimental data, which we call u_{sim} here.

Now we have solved the forward problem of calculating displacements for a given traction field. The purpose of TFM is, however, to infer tractions from displacements, which is known as the inverse problem. To achieve this, the forward method is complemented with an optimization scheme as follows. By the discretization of the cuboid, also the cell traction boundary condition is discretized and can be represented by N individual tractions $\vec{t}_i$, $i \in \{1...N\}$. Now the displacement solution $\vec{u}_{\text{sim}}$ is completely determined by the finitely many $\{\vec{t}_i\}$, which we will refer to as the degrees of freedom (DoF) of the optimization. By comparing $\vec{u}_{\text{sim}}$ to the displacements measured in the experiment, $\vec{u}_{\text{exp}}$, one can define a least squares estimator L_2 by

$$L_2 = \sum_k \left(\vec{u}_{\mathrm{sim},k} - \vec{u}_{\mathrm{exp},k}\right)^2 \ , \tag{4.7}$$

which measures the deviation of the two displacement field. Consequently, a perfect reconstruction yields $L_2 \to 0$. One now implements a standard minimization scheme such as the conjugated gradient method [62] to vary the DoFs and minimize the L_2 value. The final set of $\vec{t}_i$'s, which yield the minimal L_2, is the solution to the inverse problem of elasticity theory. However, the inverse problem is ill-posed and requires additional stabilization techniques to gain unique approximate results, which we discuss below.

4.3 Inverse Ill-posed Problems and Regularization

The methods for traction reconstruction seem fine at first glance, however there is a fundamental issue. Since the elastic interaction is long-ranged, the inverse problem is ill-posed. We will now explain what this means, how the two methods explained above deal with the issue by regularization, and which possible problems might arise from that. This part is fundamental to understand one of the main goals of MBTFM, which is to rebase regularization on biophysical arguments. The following is mainly based on the books of Kabanikhin [115], Engl and coworkers [116], and Ababarnel and coworkers [117].

4.3.1 Inverse Ill-posed Problems

A problem in mathematical physics is called a *direct problem*, if the governing equation and its domain, initial conditions and boundary conditions are known and the problem is well-posed in the sense of Hadamard. This means that a solution function exists, which is unique and varies smoothly with both boundary and initial conditions [115]. The last part means, that the operator A mapping all known functions and quantities to the solution, is continuous. In the *inverse problem*, the solution function is given but parts of the governing equation, the domain, the initial or the boundary conditions are unknown. Such inverse problems are often ill-posed, which means not well-posed. The problem in data evaluation is usually not the existence of a solution, but difficulties typically arise from uniqueness or the stability of the unknown functions against small perturbations in the data. These two issues might both cause problems in the inverse problem of elasticity theory and shall be addressed in this introduction.

We introduced Eq. 4.5 as the governing equation for FTTC. It is a Fretholm integral equation of the first kind, whose general form is

$$\int_a^b K(x,s)q(s)ds = f(x) \ . \tag{4.8}$$

In the context of TFM, the solution function $f(x)$ (the data) and the integration kernel $K(x,s)$ (the Green's function) are known and $q(s)$ (the traction) is to be inferred. This kind of equation can be either well-posed or ill-posed, depending on the form of K, and especially the interaction range. This can be easily seen from the two extreme cases of interaction ranges, if we assume that both q and f are smooth functions that are defined for all real numbers. If K is the delta function (infinitely short interaction), $K(x,s) = \delta(x,s)$, then by definition:

$$\int_a^b K(x,s)q(s)ds = \int_a^b \delta(x,s)q(s)ds = q(x) = f(x) \quad \text{for } a \leq x \leq b \tag{4.9}$$

If the integration boundaries are extended to $\pm\infty$ we can uniquely infer $q(x) \equiv f(x)$. On the other hand, if K and f are constants (infinitely long interaction), Eq. 4.8 transforms into determining the area below a curve, or more precisely: determining the curve that encloses area f, which is obviously not unique and therefore ill-posed.

Like all integral equations, Eq. 4.8 represents a smoothing operation in the sense that high-frequency oszillations are suppressed [116]. This can be made plausible by considering the integrand $g(x) = n\sin(nx/\delta)$, where $n \gg \delta$. Integrating yields $G(x) = f_0 - \delta\cos(nx/\delta)$, i. e. the amplitude of high frequency modes has dropped significantly. In the inverse problem to such equations, one can consequently expect small errors with high frequencies to have large effects.

4.3.2 Tikhonov Regularization

We take a step back and introduce Tikhonov regularization along the lines of the book of Engl [116]. Since the operator theoretical foundation is substantial, we will dispense with showing proofs and rather concentrate on presenting a clear picture of the general line of thoughts that leads to a regularization approach for both FEM-TFM and FTTC. All proofs can be found in [116] and references therein.

We begin with formally writing the inverse problem as

$$Tx = y \ , \tag{4.10}$$

where T is a bounded linear operator that maps $x \in X$ to $y \in Y$, X, Y are Hilbert spaces, and we search for a solution for x. In our problem, clearly x represents

cellular traction and y the displacement field, and the elastic half space convolution integral the operator T:

$$Tx = T\left[\vec{t}(\vec{x})\right] = \int_S G(\vec{x}-\vec{x}')\vec{t}(\vec{x}')d^2x' = \vec{u}(\vec{x}) = y \ , \tag{4.11}$$

where G is the Green's function from Eq. 4.4. Note that since G is only weakly singular [111], the operator T is compact [116]. One can now define what we seek for.

Definitions [116]
$x \in X$ is called *least-squares solution* of $Tx = y$ if

$$\|Tx - y\| = \inf\{\|Tz - y\| \mid z \in X\} \tag{4.12}$$

$x \in X$ is called *best-approximate solution* of $Tx = y$ if x is least-squares solution and

$$\|x\| = \inf\{\|z\| \mid z \text{ is least-squares solution of } Tz = y\} \tag{4.13}$$

We note that if T^{-1} exists and is bounded, i. e. the problem is well-posed, it is trivial to find the unique least-squares and best-approximate solution as $x = T^{-1}y$. However, existence may fail due to $y \notin \mathrm{im}(T)$ or $\ker(T) \neq \{0\}$. For this reason, one constructs the well-defined *Moore-Penrose generalized inverse* $T^\dagger$ of T as the unique linear extension to $\tilde{T}^{-1}$ by

$$\begin{aligned} \tilde{T} &:= T|_{\ker(T)^\perp} \ : \ \ker(T)^\perp \to \mathrm{im}(T) \\ \mathrm{D}(T^\dagger) &:= \mathrm{im}(T) \dotplus \mathrm{im}(T)^\perp \\ \ker(T^\dagger) &= \mathrm{im}(T)^\perp \end{aligned} \tag{4.14}$$

Here $D(\cdot)$ denotes the domain of an operator. If $y \in D(T^\dagger)$, then the following two statements hold:

$$\begin{aligned} x^\dagger := T^\dagger y \text{ is a unique best-approximate solution to } Tx = y \\ T^*Tx = T^*y \Leftrightarrow \text{ x is a least-squares solution to } Tx = y \end{aligned} \tag{4.15}$$

Being well-defined, $T^\dagger$ might still be unbounded (not continuous). In fact, for any compact T with $\dim(\mathrm{im}(T)) = \infty$, the Moore-Penrose inverse is a densely defined unbounded operator, just as in the Boussinesq case. The effects become best visible, if we use the fact that for any compact linear operator T there exists a singular system $(\sigma_n; v_n, u_n)$ that allows us to write

$$Tx = \sum_{n=1}^{\infty} \sigma_n \langle x, v_n \rangle u_n \tag{4.16}$$

$$T^*y = \sum_{n=1}^{\infty} \sigma_n \langle y, u_n \rangle v_n \tag{4.17}$$

$$T^*Tx = \sum_{n=1}^{\infty} \sigma_n^2 \langle x, v_n \rangle v_n \ , \tag{4.18}$$

the latter meaning that (σ_n^2, v_n) is an eigensystem for the self-adjoined operator T^*T. This also motivates the definition of a function of T^*T, which reads

$$f(T^*T) = \sum_{n=1}^{\infty} f(\sigma_n^2) \langle \cdot, v_n \rangle v_n \ . \tag{4.19}$$

If T^*T is continuously invertible, we can write down its inversion of explicitly via the eigensystem diagonalization,

$$(T^*T)^{-1}x = \sum_{n=1}^{\infty} \frac{1}{\sigma_n^2} \langle x, v_n \rangle v_n \ , \tag{4.20}$$

and characterize the best-approximate solution with the second part of 4.15 and Eq. 4.20 by

$$\begin{aligned} x^\dagger &= (T^*T)^{-1}T^*y \\ &= \sum_{n=1}^{\infty} \frac{1}{\sigma_n} \langle y, u_n \rangle v_n. \end{aligned} \tag{4.21}$$

If, however, the problem is ill-posed, $0 \in \{\sigma_n\}$ holds and the sum does not converge. Even if $\sigma_n \neq 0 \ \forall n$, some eigenvalues of T^*T might still be very small, such that a small error in $\langle y, u_n \rangle$ is amplified by an unacceptably large factor.

Now the problem has become visible: If we have a small error in the data $\|y - y^\delta\| < \delta$, where we call δ the *noise level*, then $\|T^\dagger y^\delta - T^\dagger y\|$ can still be very large. In other words: $x^\delta = (T^*T)^{-1}T^*y^\delta$ is not a good estimate for x^δ.

The idea is to replace $(T^*T)^{-1}$ by some function $g_\lambda(T^*T)$ other than $g_0(T^*T) = 1/(T^*T) = (T^*T)^{-1}$, such that the error between

$$x_\lambda = g_\lambda(T^*T)T^*y \tag{4.22}$$

and

$$x_\lambda^\delta = g_\lambda(T^*T)T^*y^\delta \tag{4.23}$$

is bounded.

In classical Tikhonov regularization theory, we choose

$$g_\lambda(\alpha) = \frac{1}{\alpha + \lambda} \ , \tag{4.24}$$

which leads to

$$g_\lambda(T^*T) = \sum_{n=1}^{\infty} \frac{1}{\sigma_n^2 + \lambda} \langle \cdot, v_n \rangle v_n = (T^*T + \lambda I)^{-1} \ . \tag{4.25}$$

The latter part can be easily seen by using Eq. 4.19:

$$T^*T + \lambda I = \sum_n \sigma_n^2 \langle \cdot, v_n \rangle v_n + \lambda \sum_m \langle \cdot, v_n \rangle v_n = \sum_n (\sigma_n^2 + \lambda) \langle \cdot, v_n \rangle v_n \tag{4.26}$$

We can directly see in comparison with Eq. 4.21 that errors are no longer amplified unboundedly,

$$x_\lambda^\delta = \sum_{n=1}^{\infty} \frac{\sigma_n}{\sigma_n^2 + \lambda} \langle y, u_n \rangle \, . \tag{4.27}$$

Indeed, this choice for g_λ yields a clear relation between Eqs. 4.22 and 4.23, as the following theorem states [116].

Theorem. Let $y \in \mathrm{im}(T)$ and $\|y - y^\delta\| < \delta$. If $\lambda = \lambda(\delta)$ fulfills

$$\lim_{\delta \to 0} \lambda(\delta) = 0 \tag{4.28}$$

$$\lim_{\delta \to 0} \frac{\delta^2}{\lambda(\delta)} = 0 \ , \tag{4.29}$$

then

$$\lim_{\delta \to 0} x_{\lambda(\delta)}^\delta = T^\dagger y \ . \tag{4.30}$$

One can also show, that x_λ^δ for this choice of g_λ is the unique minimizer of the Tikhonov functional [116]

$$x \mapsto \|Tx - y^\delta\|^2 + \lambda \|x\|^2 \ . \tag{4.31}$$

4.3.3 Effect of the Regularization Parameter

In the context of TFM we seek a solution for the traction field $\vec{t}$, which we therefore identify with the solution x of the last section. An interpretation of the practical effect of this regularization can be gained from the variational characterization of the Tikhonov functional, Eq. 4.31. Here we see that the regularization is achieved by setting a side constraint: The residual norm $\|Tx - y^\delta\|^2$ is minimized, as expected, but under the condition that the norm of the solution $\|x\|^2$ be small. In other words, the presented Tikhonov regularization achieves stability by postulating that the overall traction magnitude of the force field be low. The regularization parameter λ controls how strongly this side constraint is weighted.

This postulate makes sense also from a heuristic point of view. We already discussed that instability in the integral equation emerges from high frequency modes that are damped in the forward problem but are consequently amplified during reconstruction. The regularization now filters high noise amplitudes that increase the overall traction but do not decrease the residual norm by the necessary amount. Here the regularization parameter λ defines what *necessary* means.

Typical traction reconstructions derived with FTTC for different regularization parameters are shown in Fig. 4.2. The underlying displacement field was already shown in Fig. 4.1 B. It is obvious that the traction field is noise dominated for $\lambda = 0$ and

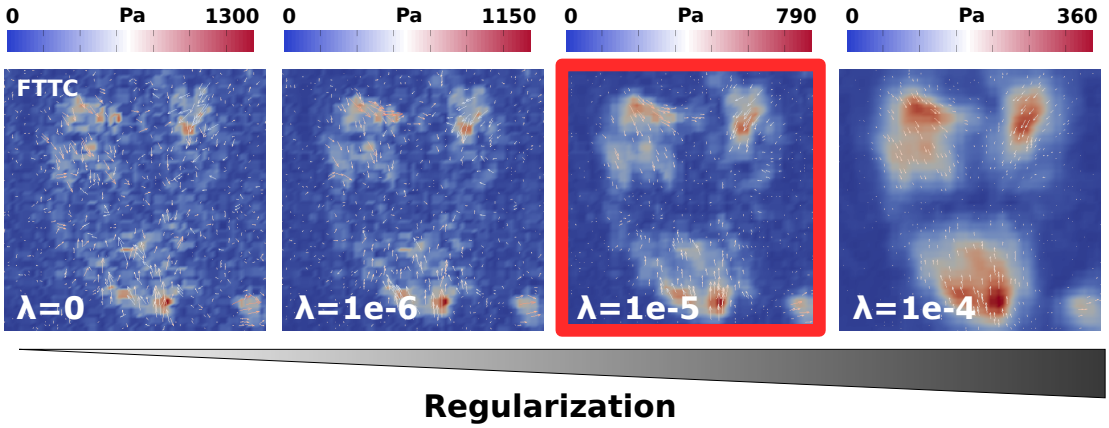

Figure 4.2: Effect of the regularization parameter on traction reconstruction. Higher values for λ lead to smoother traction fields with lower traction magnitudes. The Bayesian estimate choice is marked by a red frame.

becomes gradually smoother as the regularization parameter is increased until it is finally much less detailed as one would expect for a biological cell on an unstructured flat substrate at $\lambda = 10^{-4}$. Here, the disadvantage of regularization becomes visible: as we increase the regularization parameter, the reconstructed solution veers away from the data. The details of the traction field vanish and the overall force magnitude decreases as the regularization parameter increases.

The question is now, how an optimal intermediate value for the regularization parameter can be found, which efficiently suppresses noise, but does not smooth the traction field too heavily. A heuristic argument can be found by the L-curve criterion [118, 119]. The norm of the regularized solution is plotted against the residual norm $\|Tx - y^\delta\|^2$ for different λ, and the resulting curve has the shape of the letter L. The optimal regularization parameter is then found at the corner of the L. From there, further increasing λ leads almost only to a larger deviation from the data (larger residual norm) without improving the regularization condition, while decreasing λ from there does increase $\|x\|^2$, i. e. the noise contribution, without decreasing the residual norm. Another way of estimating the regularization parameter is *via* Bayesian theory [112, 119].

4.4 Method

4.4.1 General Idea

With model-based traction force microscopy, our aim is to overcome the need for regularization and to increase the resolution in observing biological structures of

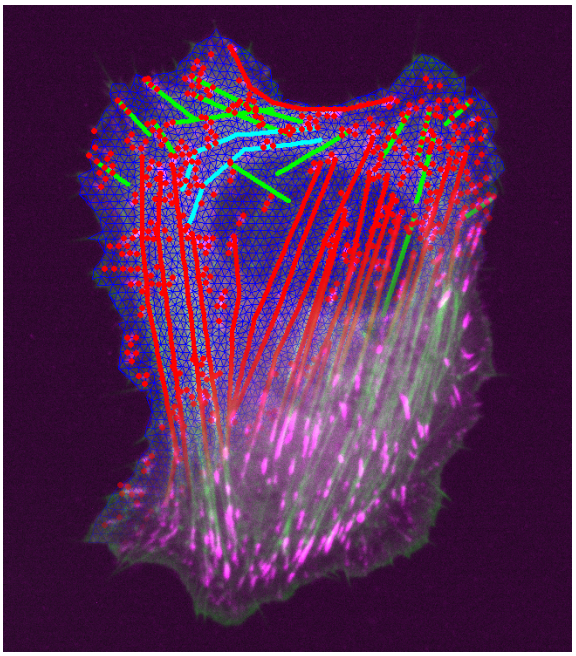

Figure 4.3: Model-based traction force microscopy utilizes additional data to regularize traction reconstruction geometrically. FA locations (purple) are used to select fixed points in the mesh (red dots), and actin SFs (green bundles in the experimental part) are segmented and classified into DSFs (green lines), TAs (light blue lines), and VSFs (red lines).

interest. The idea originates from recalling how Tikhonov regularization effects the reconstruction. The decision between different possible traction solutions is systematically biased towards the one with the least norm, which suppresses local noise contributions. Traction noise is characterized by not contributing enough to decrease the residual norm. Typical for such noise contributions is that they are not systematically oriented and that their magnitude shows high spatial variations. Traction reconstruction can also be regularized by prescribing the local traction field directions as well as their spatial distribution and homogeneity. This process can be regarded as a geometrical regularization. Noise is filtered as its contributions are just not contained in the solution space. In this way, geometrical optimization works fundamentally different than Tikhonov regularization, as they address two different properties of Hadamard's definition of well-posed problems. Tikhonov regularization reestablishes the continuity of the solution from the boundary and initial condition in an ill-posed problem. In contrast, geometric regularization restricts the solution space in a way that the problem is well-posed from the beginning. The number of degrees of freedom is reduced from typically 10^5 in FEM-TFM to about 10^2 model parameters.

The geometric rules that govern traction field organization need to be provided by a biophysical model, which is why the method is called *model-based*. The model has to contain additional information about the system of interest. In our study, the investigated cells show pronounced SFs and FAs, that together provide a structural picture of the cells force generating and transmitting machinery. Fig. 4.3 illustrates how this information can be turned into a model *via* image processing. Stress fibers are segmented, classified, and embedded into a network that also contains information about FA locations.

The introduction of a biophysical model to the reconstruction has another advantage, as it can be interrogated for biophysical questions. In this work we investigate the forces at FAs and in SFs. Without MBTFM, one had to apply the model after regularized traction reconstruction where the regularization parameter is a potentially critical degree of freedom. In our method, we directly project the data on the biophysical questions during reconstruction.

4.4.2 Model Choice

In our study we correlate cellular forces with SFs and FAs. For this purpose we need to utilize a mechanical model for the entire cell that allows us to describe its force generating and transmitting behavior. Several models describing forces of adherent cells have been developed over the past decade. Contour models have been shown to give reasonable estimates for cell forces and shapes if there are no prominent internal structures [4, 29]. Continuum mechanics models focus on the elastic properties of the bulk cell material [32, 120, 121]. In a recent study, these approaches have been combined in a continuum mechanics model with line tension similar as in the tension-elasticity model (TEM) [31]. In contrast to the TEM, here the tension runs along outwards curved regions of the cell leading to an inwards directed force. All of these models have a continuum character and none of them can easily implement differential tensions in discrete stress fibers. For pillar assays, truss models have been used to estimate tension in internal stress fibers from post displacements [122, 123], but these models did not consider the effect of the cell body and work only for a small number of adhesion sites.

For our model choice, we were guided by the following four principles:

1. The considered cell type is characterized by prominent stress fibers that have to be modeled as discrete elements.

2. Stress fibers are under tension and the tension may vary between individual SFs.

3. There is a homogeneous contractile tension in the cell resulting from various distributed actomyosin networks not visible with a standard optical microscope.

4. Forces are transmitted to the extracellular space mainly via focal adhesions.

A suitable framework to implement these assumptions is a network of active cables [78]. A cable responds like a Hookean spring to extension while it does not resist compression, and an active cable additionally features a constant contractile tension (see also Fig. 4.4). Each link of the network is therefore associated with the energy

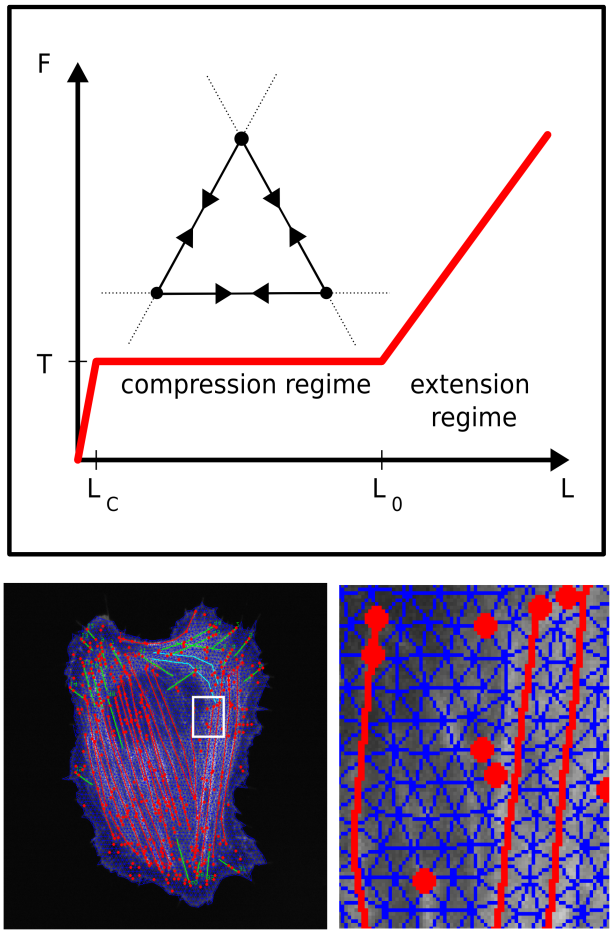

Figure 4.4: Network optimization. Each link in the network follows the depicted force extension curve of an active cable. The active tension T may vary between different stress fibers and the background network. Stress fibers are smoothly integrated into the surrounding network. Vertices near focal adhesions are fixed (red dots).

$E_i = L_i T_i + k(L_i - L_{i,0})^2/2$ for $L_i > L_{i,0}$ and $E_i = L_i T_i$ for $L_i \leq L_{i,0}$, where L_i, $L_{i,0}$ represent the actual and the rest length of link i, respectively, T_i is its active tension, and k is the spring constant for the elastic regime. We also introduce a cutoff length $L_{i,c} \ll L_{i,0}$, where we interpolate a continuous transition $T_i \to 0$ for $L_i \to 0$. This model represents several typical mechanical properties of the actin CSK. If under compressive load, filaments can slide telescopically along each other, or depolymerize or buckle, while they respond elastically to stretch [124]. Cell area is not conserved because the model only considers the two-dimensional projection onto the substrate, thus cellular material can be exchanged with the third dimension. The constant contractile tension arises from myosin II motors that work in the stall regime. Active cable models have been shown to correctly predict shapes of adherent cells on micro-patterned substrates and yield force distributions that are robust with respect to local changes in network geometry or topography [4, 78, 79]. Note that this differs remarkably from networks of Hookean springs. Springs in particular propagate compressive force modes over long distances, which do not appear in cables by definition. In order to achieve a close relation to experiments, the model is built directly from image data.

Regarding the model's parameters, we allow for individual tension values for each

SF and one more for the background network. So the number of parameters is $P = n + 1$, where n is the number of segmented stress fibers. The one-dimensional Young's modulus for all links is chosen to be $EA = 50nN$, which can be justified for SFs and looser cytoskeletal actin structures [79]. Note that this stiffness is only of minor importance, since most of the links are in the $L_i < L_{i,0}$ regime where their force is determined by the active tension alone. Only at the border links are typically elongated to balance forces directed to the interior.

4.4.3 Image Processing

The data we use to construct the active cable model has to be extracted from fluorescence images. For quicker image processing, we wrote a extension for the software ImageJ [71] which we call plugin for the **S**egmentation **o**f **F**ocal **A**dhesions and **ST**ress Fibers (SoFAST plugin). With this software, one can use ImageJ's powerful tools specifically composed for the segmentation of the CSK. We show three sample segmentations in Fig. 4.5.

The workflow begins by loading the actin fluorescence image and starting the software. Stress fibers can be identified and manually segmented as piecewise straight lines. The user can then classify a segmented fiber into one of the three different types, namely dorsal SF (DSF), ventral SF (VSF), and transverse arcs (TA). For classification one can also switch back and forth to a fluorescence image of the FA distribution. In our study, we followed the characterization of the fibers according to [19]. SFs emanating from a FA at the outer rim that grow radially towards the center are classified as DSFs, SFs that lie parallel to the cell edge and do not connect to FAs are TAs. VSFs are typically straight and connected to FAs at both ends.

Focal adhesions are segmented in the second step. Here we apply several steps of ImageJ's outlier finding algorithm and remove everything but the outliers from the image. Afterwards we apply the despeckling algorithm to remove very small outliers and we apply a global threshold to remove outliers in the background noise. After that, another application of despeckling completes the segmentation. We now additionally fit ellipses to all FAs and record the center coordinates, the lengths of the major and minor axis, their orientation, and the distance to cell edge.

The third step concerns cell area segmentation. We use different global thresholding techniques already implemented for ImageJ and tools directly from the palette of the software.

In the last step we generate the network model from the segmented data. We first introduce vertices and links along stress fibers, before the whole cell area is covered with a homogeneous density of vertices. From these vertices we construct a Delauney

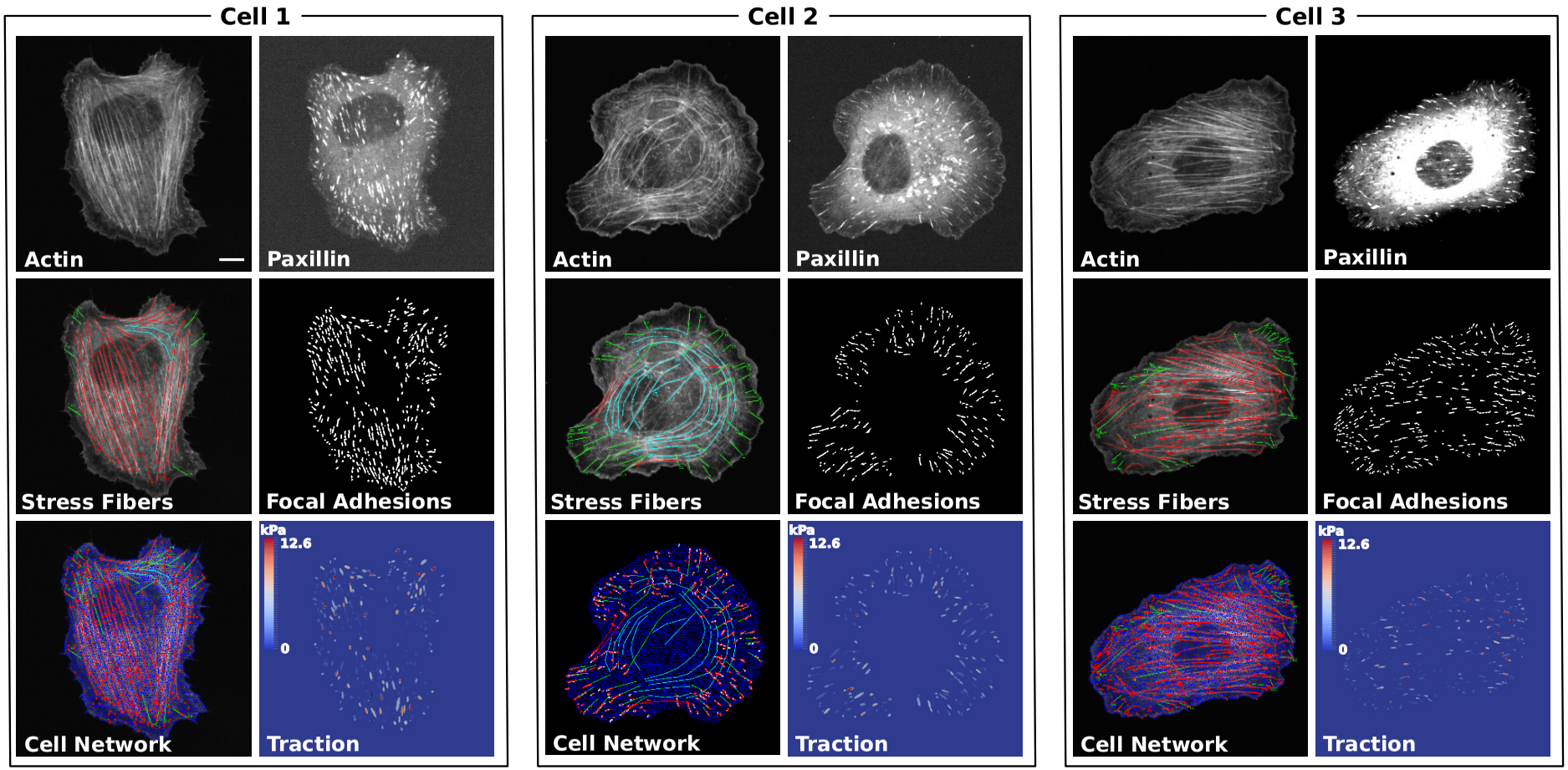

Figure 4.5: Sample segmentation of three representative U2OS cells. The first row shows the raw experimental data of the actin CSK and the focal adhesion protein paxillin. The segmentation of stress fibers and focal adhesions is depicted in the second row. In the third row, the full network model for each cell and the acquired traction map are shown.

triangulation with the help of the open source software Java Delauney Triangulation [125]. The stress fiber links are kept in the network. We then perform a modified version of the distmesh algorithm [126] to achieve a homogeneous triangulation. In the last step, links are considered as compressed springs that introduce a linear force distance relation for neighboring vertices. The vertices and links that belong to SFs are not moved. Finally, all vertices that lie in the neighborhood of segmented FAs are fixed.

4.4.4 Optimization

In the following we describe how we determine a complete set of tension values for our model from an experimental displacement field with the help of a cell-specific active cable network model. There are three different optimization schemes involved:

1. Network energy equilibration
2. Displacement calculation in the finite element substrate model
3. Combined optimization of the forward problem to solve the inverse problem

Network optimization

The minimal energy configuration of the active cable network is determined with the software *SurfaceMaster* as discussed in chapter 2. After equilibration, the only force bearing vertices are the ones that were fixed in the neighborhood of FAs during image processing (Fig. 4.4, red dots). These forces are mapped to the FA ellipse fit that is closest to the vertex position. All forces mapped to the same FA are added vectorially and converted into tractions by division through the ellipse's area. In summary, the network model for n SFs maps a set of $n+1$ tensions to a set of N elliptic traction patches, where N is the number of segmented FAs.

Substrate model displacements

For obtaining the substrate's displacement field in response to the traction patches, we use finite element methods as explained for the forward problem in FEM-TFM. The Young's modulus for the substrate is on the order of several kPa in this study. The optimization scheme mentioned above is used to iteratively solve the system of linear equations associated with the finite element method. We use the open source library deal.II [127] for FEM calculations. As we want to resolve the shape of individual FAs, the mesh size for the FEM needs to be two orders of magnitude smaller

than usual in TFM. To achieve this, we iteratively refine the three-dimensional mesh around FA locations at the top surface until the desired resolution is achieved. In order to ensure that the lateral sides of the mesh are stress free, we extend the visible image area of typically $100 \times 100\mu m^2$ for the mesh by $30\mu m$ in each lateral direction. We hereby defined a method to map elliptic traction patches to a three dimensional traction field in the substrate model. We finally restrict this result to the two-dimensional projection of the top surface boundary displacements in order to compare them to experimental data.

Joint optimization

With subsequent calculations of the cell and substrate models we can solve the forward or direct problem of mapping SF and background tensions to simulated substrate displacements at the cell's top surface. The direct problem is summarized in Fig. 4.6 A and schematically shown in the middle column of Fig. 4.6 B. Here it is also shown that the substrate displacements are the available experimental data. By comparing the two displacement fields, we obtain an error estimate for the deviation between experimental and simulated displacement fields. In practice, we use a least squares estimator defined by $L2 = \sum_i (\vec{x}_{s,i} - \vec{x}_{e_i})$. The sum runs over all locations where displacement information is available from the experiment, $\vec{x}_{e_i}$ denotes the experimental displacements at these locations, and $\vec{x}_{s,i}$ is the projected interpolated displacement at the top surface of the FEM mesh. In the following we describe how we can solve the inverse problem of calculating the tensions from the experimental data.

The whole process is depicted in Fig. 4.6 B, where the first two columns summarize the usage of experimental data and the calculation of the direct problem. The inverse problem is solved by minimizing the error estimate with respect to the tension parameters of the active cable model. We start by setting all tensions to zero and implement a conjugated gradient scheme for optimizing the tensions from this initial value configuration. Here we treat the degree of freedom of the background tension differently, as we optimize it separately after each ten steps of SF tension optimization. This procedure is necessary to achieve quick convergence (cf. chapter 4.5).

4.5 Method Validation

In order to test our method we simulate an experimental displacement field which can be reconstructed afterwards. The benefit of this procedure is that the expected

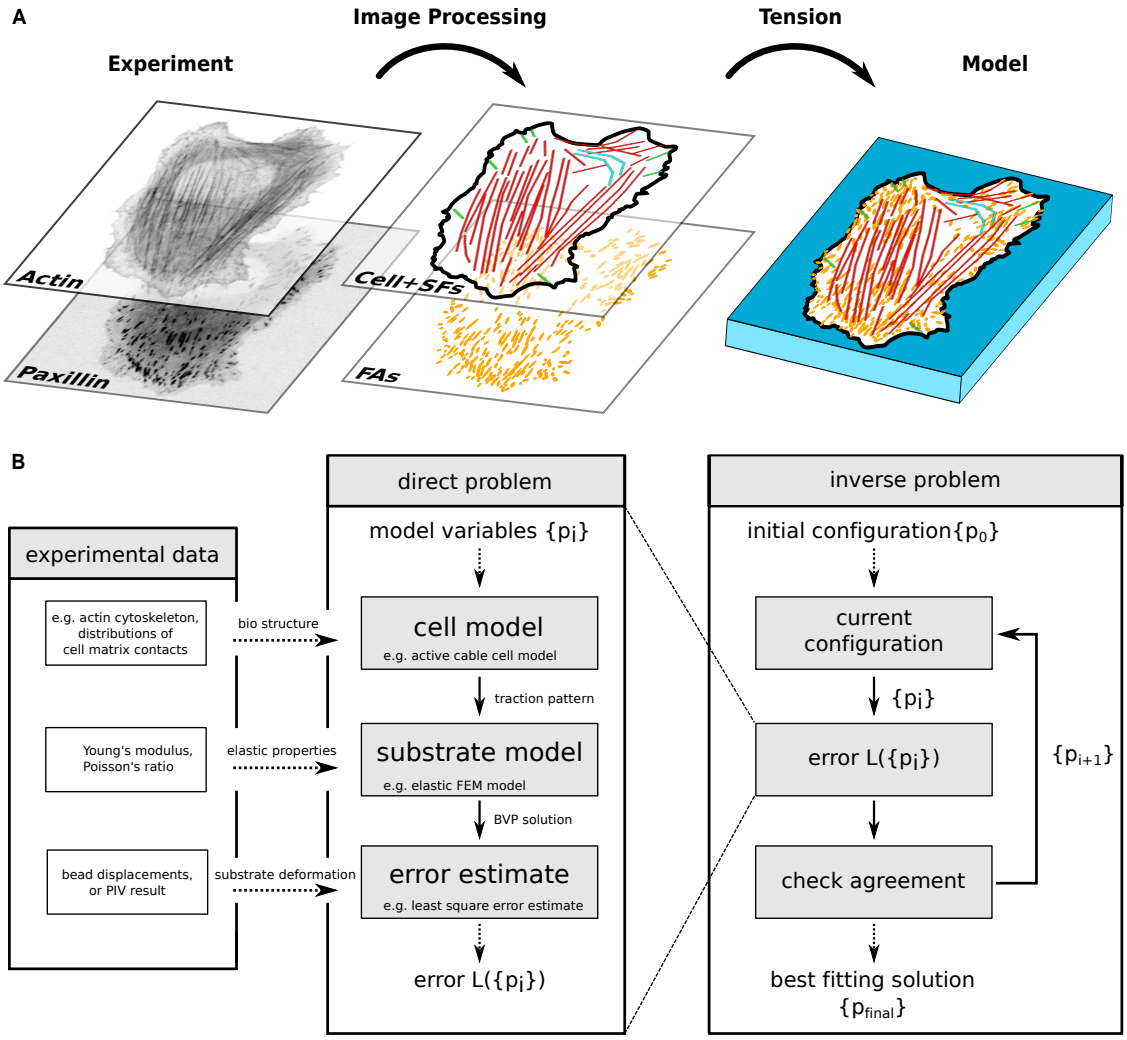

Figure 4.6: Computational workflow of MBTFM. (A) Structural information about the cell's force generating and transmitting machinery is converted into a cell-specific descriptive model. (B) In the direct problem, one can calculate displacement fields from tension parameters, which leads to an error estimate in comparison with experimental data. Repeatedly solving the inverse problem allows to optimize the tension parameter set for the cell.

result is known and that one can systematically investigate the performance of the method. We take the test segmentation shown in Fig. 4.7 A and sample SF tensions from a homogeneous probability distribution on the interval $[0, 10]nN$. As the network tension is expected to be smaller than typical SF tensions, we assign a value of $t_{\text{network}} = 0.06nN$. We then perform the direct problem to convert the full set of tension parameters into a simulated displacement field. We sample $N = 10000$ displacements at random positions of the displacement field which yields the simulated data.

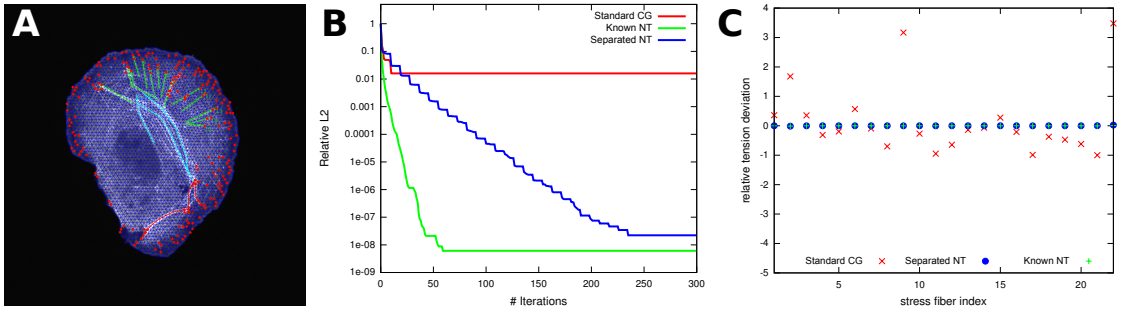

Figure 4.7: Reconstruction of simulated data. (A) Test segmentation. (B) Reconstruction of the same noiseless data set. Separation of the network tension degree of freedom is necessary to achieve satisfactory results. (C) Deviation of the reconstructed tension from the simulation values.

4.5.1 Reconstruction of Simulated Data

Fig. 4.7 shows the relative $L2$ value during the iterative reconstruction, and the number of iterations is counted for the joint optimization. An unchanged conjugated gradient method stalls early and does not show the desired convergence (red line). The problem is associated with the network tension. If this parameter is known from the beginning, optimization is only limited by numerical accuracy. This degree of freedom differs from the stress fiber tensions in two ways. First, its numerical value is lower than typical SF values. This issue could be fixed by rescaling the quantity in the conjugated gradient algorithm. However, secondly, its nature is more global compared to other degrees of freedom. While the tensions of SFs are typically only transmitted to FAs at their ends or kinks, the network tension alters the traction at all FAs at the periphery. For this reason, we decided to optimize the network tension parameter seperately after each ten steps of SF tension optimization. The result of this procedure is shown by the blue curve in Fig. 4.7 B.

Fig. 4.7 C confirms that the results for the convergence of the $L2$ value can be transferred to the reconstruction of tension parameters. While for the standard conjugated gradient approach the reconstructed tensions differ widely from their original value (red), reconstruction is nearly perfect if the network tension is known (green). Separating the network degree of freedom allows to reliably reconstruct the network tension as well (blue).

4.5.2 Influence of Noise

The effect of noise in the data is of primary concern in the context of regularization. In order to test the performance of our method, we added Gaussian noise of different

strengths to the simulated data. We define the noise level by the ratio of the standard deviation of the noise and the maximal displacement in the data set. Experimental noise levels can be determined from image regions without cells and range between 5% and 10% in our study. For the validation of this method, we covered a larger range and produced $n = 10$ different noisy displacement fields at each of the noise levels 3%, 5%, 7%, 10%, 15%, 20%, and 25%.

Fig. 4.8 exemplary shows the traction reconstruction with noisy data for 25% noise level. The traction stress field calculated with the network model is mapped to a noise-free displacement field (direct problem), to which Gaussian noise is added. The noisy displacement field is then reconstructed using MBTFM. Note that 25% is a very high noise level, since the noise level is defined relative to the maximal displacement. Average displacements are well smaller, so the noise plays a dominant role at this level. FTTC cannot recover the original stress field in these situations. With MBTFM we can recover the main features of data, though with slight deviations.

We systematically show the influence of noise in Fig. 4.9, where the experimentally relevant range is marked by the light grey boxes. The relative $L2$ error estimate is very low for noiseless data (cf. Fig. 4.7). As expected, it gradually increases with increasing noise since the displacement noise cannot be reconstructed by the model. The $L2$ value saturates for noise levels of about 25% and larger, since the noise then dominates the displacement field (Fig. 4.9 A).

We are now interested in how the noise influences the reconstruction result rather than the residual norm. We therefore define the total force of the cell as $F_{\text{tot}} = \int_A |\vec{T}(\vec{x})| dA = \sum_i |\vec{T}_i| \cdot A_i$, where $\vec{T}(\vec{x})$ is the traction on the substrate, $\vec{T}_i$ is the traction of traction patch i in the network model, A_i its area, and the sum runs over all traction patches. We also define the network force by the total force when the SF tensions are all set to zero in the model, which means that it is determined by the background tension alone.

Fig. 4.9 B shows the dependence of both total and network force on the noise level. As expected, the congruence between data (black lines) and reconstruction (blue / green dots) is very good for small noise levels. However, even for very large noise values, both whole cell force quantities differ only very slightly from the correct value, and variances remain small. In summary, total force and network force are very robust against noise. The latter also means that the reconstruction of the background tension is very robust.

This picture changes a bit when we investigate the influence of noise on the reconstruction of single stress fiber tensions. To quantify the effect, we introduce the mean relative deformation $MRD = 1/n \sum_{i=1}^{n} \left(1/N_{SF} \sum_{j=1}^{N_{SF}} |t_{i,j} - t_j^0|/t_j^0 \right)$. Here $n = 10$ is the number of reconstructions with different noisy displacement fields, N_{SF} the

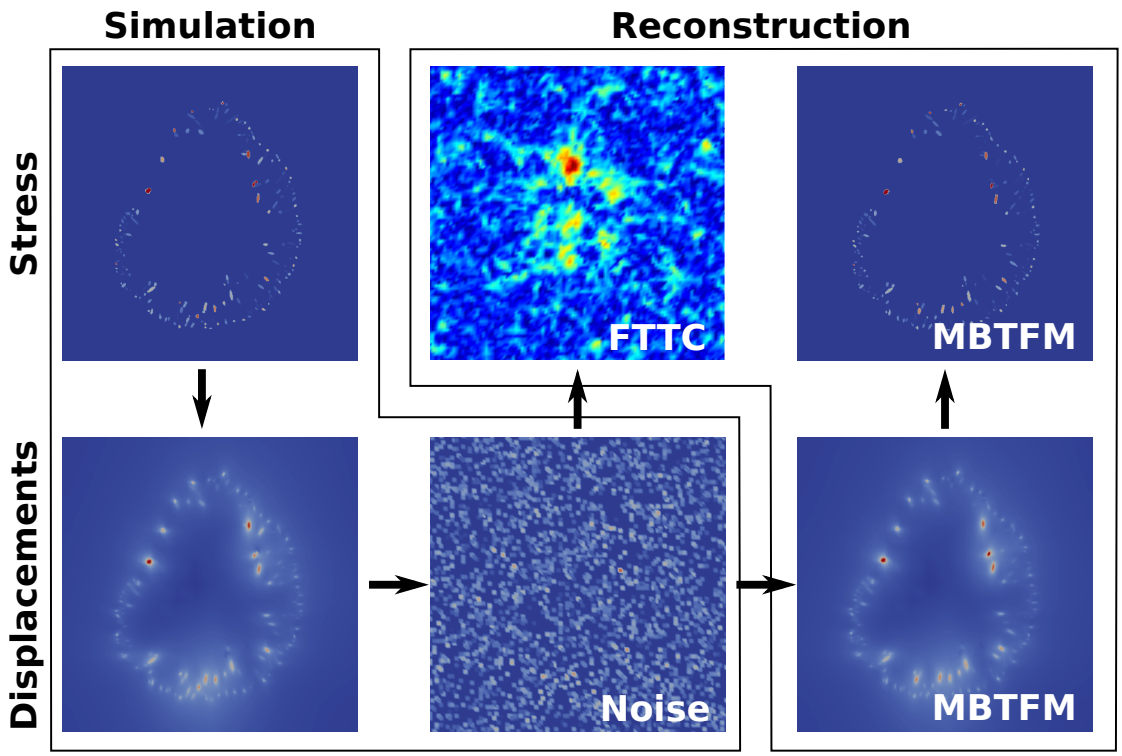

Figure 4.8: Influence of high noise levels in simulated data (25% noise level is shown). Standard regularization techniques in FTTC fail to recover the details of the displacement field. Structural information enables MBTFM to still determine a good approximate solution.

number of segmented stress fibers in the model, $t_{i,j}$ the reconstructed tension of SF j with displacement field i, and t_j^0 the correct value for the tension of SF j. The quantity averages the relative deviations of SF tensions after reconstruction from their correct value over all SFs in the segmentation and all reconstructions with different noise and thereby provides an estimate of the fiber tension reconstruction quality.

Fig. 4.9 C shows that average deviations reach over 50% for high noise levels. This dependence, in contrast to the stable reconstruction of the background tension, is caused by the more localized nature of SF tractions. SFs transmit their forces to the substrate mainly at FAs in the neighborhood of their ends. Reversely, displacement noise at the end of stress fibers induces errors in tension reconstruction more rapidly than for the background tension. To alter the latter, all FAs at the periphery had to show consistent displacement noise, which is very unlikely. From this perspective, it is surprising that the total force that includes the effect of SF tensions is that robust even for high noise. However, the MRD value drops approximately quadratically with decreasing noise level. In the experimentally relevant range, typical reconstruction deviations are of the order of 10%. This value is acceptable and well below

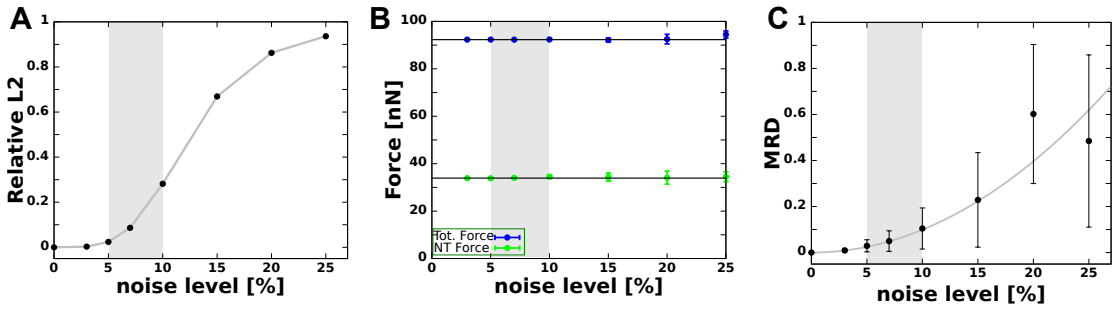

Figure 4.9: Reconstruction in the presence of noise. Typical experimental noise levels are highlighted by grey boxes. (A) The relative $L2$ estimate increases with the noise level as the segmented structure cannot reproduce the noisy displacement field. (B) Even at high noise levels, overall network forces and stress fiber forces are estimated well. (C) Tensions of individual stress fibers are well estimated if the noise level is below 10%. (B), (C) We used $n = 10$ different noisy displacement fields.

typical biological variability.

4.5.3 Segmentation Uncertainties

Segmentation of SFs is a manual process and as such prone to errors. In this section we investigate how either segmenting too many or too few stress fibers influences the result, which we call oversegmentation and undersegmentation, respectively. In the case of oversegmentation, we artificially embed more stress fibers into the reconstruction model than we had in the model that the data was produced with. Fig. 4.10 A shows the segmentation where three VSF have been added in an otherwise SF-free area. The additional fibers have been marked with yellow triangles.

The effect of oversegmentation can already be seen by looking at the development of the relative $L2$ estimate during optimization (Fig. 4.10 D). Only small numerical inaccuracies separate the oversegmented model from the correct segmentation. Also the relative SF tension deviations (Fig. 4.10 E) and the total and network force estimates (Fig. 4.10 F) are very close to the reconstruction with the correct segmentation. The reason for this is that if there are no displacements that can be associated to the effect of the tension of the additional SFs, they are optimized to bear zero tension. In this way they do not influence the surrounding network.

Undersegmentation is more problematic. Since degrees of freedom are missing to describe the data sufficiently, the system is forced into a new configuration. We investigated this scenario by removing two DSFs (Fig. 4.10 B) or one VSF (Fig. 4.10 C). Each removed fiber is marked with a yellow triangle. In the first case the tension is mainly redistributed to neighboring parallel bundles (red triangles).

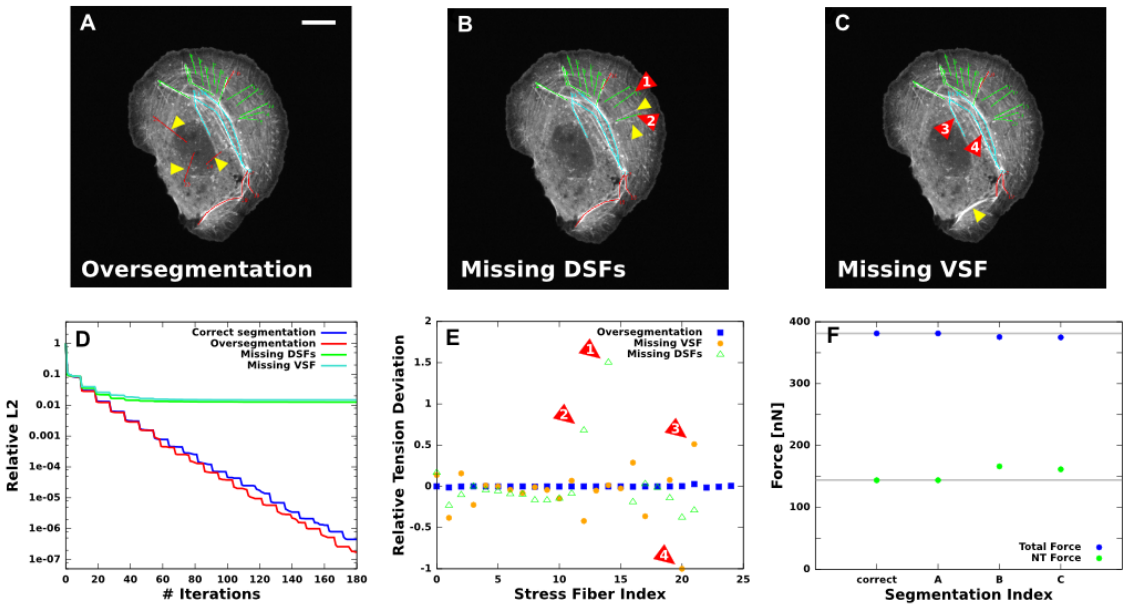

Figure 4.10: Influence of oversegmentation and undersegmentation of stress fibers. (A) - (C) Indication of additionally segmented and missing stress fibers, respectively. (D) Optimization results for different segmentations. (E) Relative tension deviations for individual stress fibers. (F) Network and total force for different segmentations.

Their reconstructed tensions are considerably increased compared to the original value (Fig. 4.10 E). The effect is local in the sense that other SFs are not disturbed as much. However, some compensate the higher tension in their surrounding by exerting less tension than in the original forward problem. As expected, the total force is slightly decreased in this case, while we can see a small increase in the network force (Fig. 4.10 F). This means that the contribution of the SFs to the total force is decreased as expected.

Removing the VSF shows more long-ranged effects. Since its traction was partly balanced by another VSF, there appears to be a different stress configuration in the center of the cell. Here, the TAs marked by the red triangles redistribute their tension. Still most other SFs are agnostic of the change and do not show an altered tension. Again, the SF contribution to the total force is decreased. In terms of the relative $L2$ estimate, undersegmentation prohibits the very good convergence of the oversegmented and correct model in the noiseless state. We conclude that in the segmentation process it is important to segment rather too many SFs than too few.

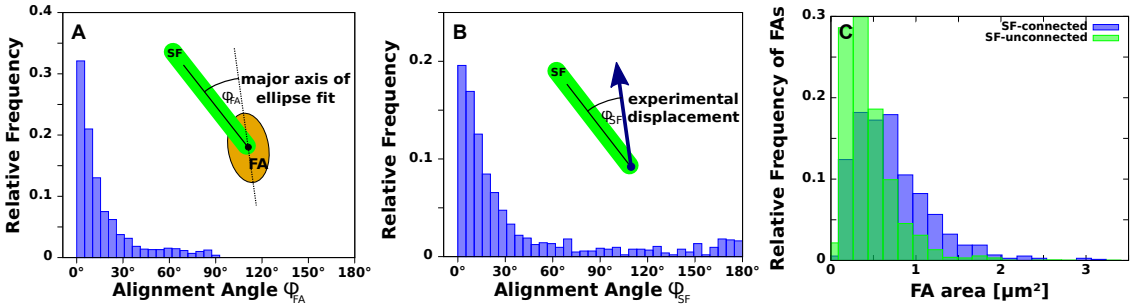

Figure 4.11: Orientation of SFs, FAs, and local displacements. (A) Alignment of the long axis of the ellipse fit to the FA with the connected SF ($n = 1305$). (B) Alignment of SF directions with local substrate deformations ($n = 1297$). (C) Area distribution of mature FAs that are connected (blue) or not connected (green) to a SF ($n = 3612$). The underlying data set encompasses 19 U2OS cells.

4.6 Force Distribution in the Cytoskeleton of U2OS Cells

In this section we present a MBTFM study with U2OS-cells that adhere to polyacrylamid substrates with a Young's modulus of $E = 8.4kPa$. The experiments where performed by Jonathan Stricker and Patrick Oakes from the lab of Margaret Gardel at the University of Chicago, USA. Our focus will be on the force distribution among different parts of the CSK.

4.6.1 Alignment of Stress Fibers and Focal Adhesion with Local Displacements

Before we begin reconstructing tensions with MBTFM, we perform a correlation analysis to check if our model assumptions were meaningful. Fig. 4.11 A shows that the orientations of FAs are correlated with the directions of SF that are attached to them. This already hints at forces in the stress fibers that act as growth templates for FAs, for which forces are important for maturation and growth [128–130]. The assumption that SFs carry force is also justified by the fact that local substrate displacements are aligned with the SF orientation where they are attached to FAs (Fig. 4.11 B). This means that FA orientation is aligned with the direction of local substrate displacements in the presence of SFs (data not shown). Another hint for force-dependent FA growth is given by Fig. 4.11 C, which shows that the probability for a FA to grow larger than $1\mu m^2$ is considerably higher for FAs attached to a SF than compared to unattached FAs.

4.6.2 Comparison to FTTC

A side by side comparison of the two TFM methods MBTFM and FTTC is illustrated in Fig. 4.12. FTTC only uses information about the elastic properties of the substrate and the experimentally measured displacement field to reconstruct tension (Fig. 4.12 B, first row). As discussed before, it is necessary to apply regularization techniques to receive an unique approximate solution. At the same time, the regularization scheme biases the reconstructed solution in the sense that stronger regularization (higher λ) leads to smoother traction fields with increasing feature size and to a decrease in the overall traction magnitude. In this picture, it becomes increasingly difficult to associate forces with cellular structures, such as SFs or FAs.

In contrast, MBTFM uses more information as it takes the cytoskeletal structure of the individual cell into account and only allows for solutions which are compatible with the applied model. In this way the method can dispense with Tikhonov regularization, as the inverse problem gets well-posed by restriction of the solution space to its biophysically relevant subspace. By the choice of our model, we can naturally correlate tractions with FAs, as they are the only force transmitting structures and thereby forces are uniquely associated with FAs. Even simpler, tensions in SFs are the direct result of our reconstruction and can be analyzed directly.

We will exploit these features of MBTFM in the following sections but first ensure that the force scale is consistent with MBTFM. For this purpose, we performed TFM with both MBTFM and FTTC for the cells in our data set and plotted the results in terms of total force against each other (Fig. 4.12 A). With a prescribed regularization parameter in FTTC of $\lambda = 10^{-4}$, we observe a linear correlation with the results of MBTFM, though the absolute values are slightly lower (red dots). The linear relation between both methods in terms of total forces is preserved when we change the regularization parameter, but the slope of fitted line changes. The last part was to be expected, since the choice of λ directly influences the total force of the reconstruction, as high total forces are penalized in the regularization term (cf. Eq. 4.31). We can now estimate FTTC's regularization parameter by fitting the linear relation of total forces to a line of slope one. In this way, we get $\lambda = 10^{-5}$. Note that this is approximately the same value as one would pick from a Bayesian estimate for this data (see Fig. 4.2).

4.6.3 Forces on Focal Adhesions

FAs play an important role in mechanosensing [20, 131], i. e. they help to translate mechanical cues to biochemical signals within the cell. Consequently, forces on FAs and their effect on FA maturation and growth and their correlation to cell properties

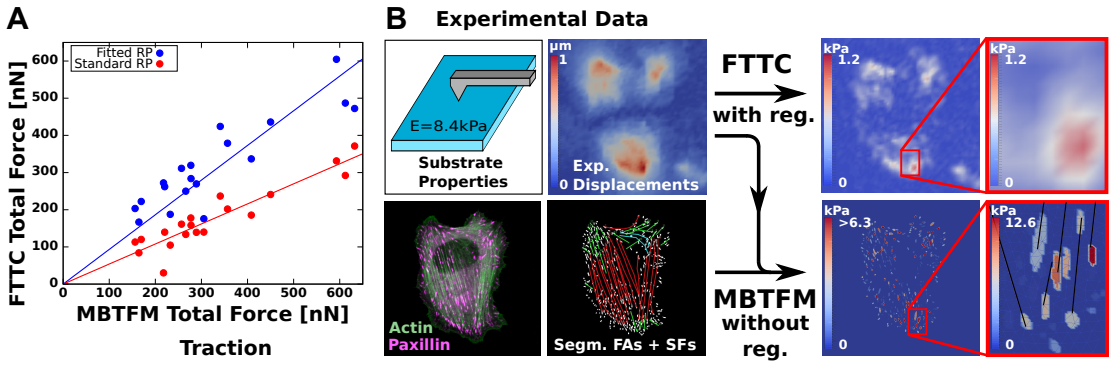

Figure 4.12: Comparison of MBTFM and FTTC. (A) There is a linear correlation for total forces determined with both methods for $n = 19$ cells (red). The slope is determined by the regularization parameter in FTTC, which can be chosen to yield a one-to-one correspondence (blue). (B) The MBTFM method uses additional data to avoid standard regularization techniques.

like cell area, number of FAs, and total FA area have been thoroughly investigated [128, 129, 132, 133]. Despite this fact, the results do not show a consistent picture. Both FA area and number have been shown to correlate positively with traction forces [129, 133], but also cell area and geometry [31, 134–137]. The reasons for sometimes even contradicting results are twofold. First, very different cell times have been investigated, ranging from epethelial cells [134] over airway muscle cells [138] and tendon fibroblasts [137] up to multipotent stem cells [133]. They are exposed to different forces at their typical location in the body and fulfill different functions. It is therefore expected that they also follow different strategies and control mechanisms for force generation and transmission. The second reason is that the methods to achieve these results were very different. Apart from homogeneous soft elastic substrates [134], also patterned substrates [139] and pillar assays [133, 136] were used. Pillar assays and also patterned substrates influence the distribution and shape of focal adhesions. On flat elastic substrates, one still faces the challenge of mapping smoothed traction fields to single FAs. This can be done manually by drawing ellipses around FAs and integrating the traction in this area [132].

With MBTFM, all tractions are uniquely associated with individual FAs directly after reconstruction. We contribute to the versatile picture of FA forces with an evaluation of our data set of human osteosarcoma U2OS-cells where we use MBTFM. In order to check if the results are really determined by force, we also introduce two variations to the wild type (WT) U2OS-cells. If we apply Y-27632, we inhibit the rho-associated kinase (ROCK) signaling pathway and thereby reduce the activity of molecular myosin II motors. The other alteration we perform is a knockdown (KD) of α-actinin 1, which is a cross-linker for actin and important for the bundling of actin filaments into SFs.

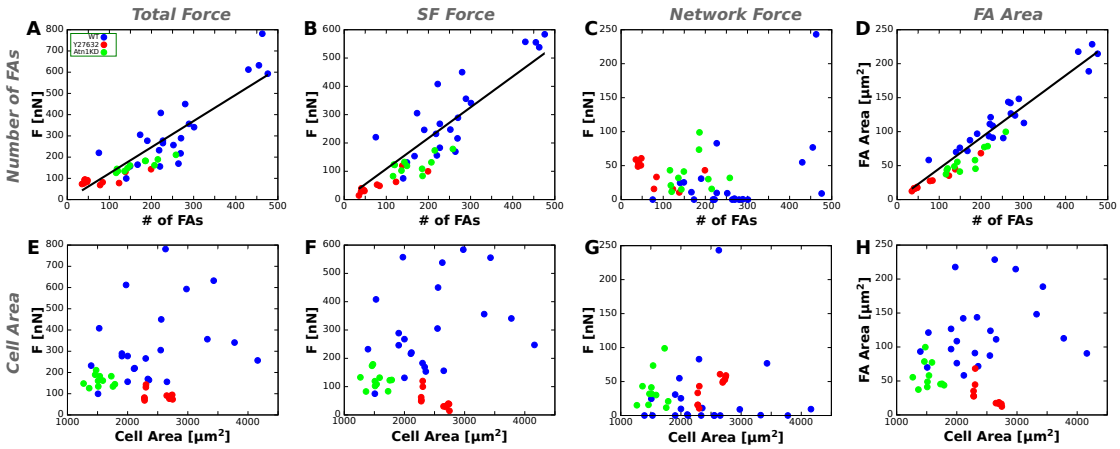

Figure 4.13: Correlation of force, focal adhesion area, and cell area for $n = 40$ cells, which are either wild type (blue dots), Y-27632 inhibited (red dots), or with α-actinin knockdown (green dots). (A) - (D) The total force exerted by stress fibers correlates linearly with the number of FAs and total FA area. (E) - (F) We cannot find a clear scaling of traction forces with cell area.

Our findings are depicted in Fig. 4.13. We find a clear linear dependence of the total force with the number of FAs (Fig. 4.13 A). Interestingly this is true for wild type cells (blue dots) as well as for the less contractile and less cross-linked variations (red and green dots). As expected, those cells show weaker forces than WT cells. At the same time, they develop fewer FAs, such that the force per FA is conserved. We calculate the average force per FA to be $1.9 \pm 0.05nN$. Note that our result is consistent with an analysis with FTTC, since total forces are estimated to the same value in both methods if the regularization parameter is chosen accordingly. Even if it is not, the linear correlation is conserved and so is the result for the correlation of force and FA number.

With MBTFM, we find that this scaling is due to force generation in SFs, as the isotropic network force shows no clear scaling with the number of FAs (Fig. 4.13 C). The relation is thus due to anisotropic stress fiber forces (Fig. 4.13 B), which also contribute approximately six times as much to the total force compared to the background tension. An exception is constituted by the cells from the KD and inhibition experiments. For cells treated with Y-27632 the network force is even larger than the SF contribution.

We can also assess the relation between the number of FAs and their total area directly from our segmentation. Interestingly, for WT and non-WT cells alike, there is a strong linear correlation which allows us to determine an average size per FA of $0.46 \pm 0.1\mu m^2$, though individual FAs very widely in their size. We can now also retrieve the average traction per FA to be $4.13 \pm 0.1N/\mu m^2$, which is in the same range as it was previously found for cardiac myocytes ($5.5 \pm 2nN/\mu m^2$, [129]),

human mesenchymal stem cells ($1.98 \pm 0.28 - 3.66 \pm 0.46 nN/\mu m^2$, depending on pillar stiffness [133]), and human umbilical vein endothelial cells ($2.25 \pm 0.42 - 4.14 \pm 0.50 nN/\mu m^2$, depending on pillar stiffness [133]).

However, different from the results shown in [133], we cannot find a clear scaling between FA area and cell size (Fig. 4.13 H). The same is true for total force, stress fiber force, and network force (Fig. 4.13 E-G). We therefore conclude that in U2OS-cells, force is associated with total FA size and number, and not with cell area.

4.6.4 Force Distribution Among Different Stress Fiber Types

SF tensions are directly available as the reconstruction result in MBTFM. It is therefore easy to evaluate the tension distribution in different SF types. As explained before, we classified SF during segmentation in three categories, namely DSFs, VSFs and TAs. We emphasize that the reconstruction algorithm in MBTFM is absolutely agnostic of this classification and that it was used only after the tension reconstruction was completed.

The different SF types vary in their location within the cell as well as their molecular composition. DSFs are anchored in a FA typically at the leading edge of the cell and grow towards the center in the retrograde flow. They are bundled and cross-linked, but do not contain myosin II [22]. TAs are typically connected to DSFs at their free end and run parallel to the cell edge, and they contract actively [19]. VSFs are attached to FAs at both ends and are close to the ventral surface of the cell. It is typical for VSF to show myosin II striation patterns [19, 77].

Sorted by the different types, we find the tension distributions shown in Fig. 4.14 A. While the occurrence of SFs bearing higher tensions decreases for all types, SFs bearing tensions of $5nN$ and more are most often VSFs. They are also the strongest SF type on average. DSFs are the weakest type, reflecting the absence of active force generation of myosin. Still there are DSFs which bear considerable tension, which seems to be a contradiction if the fiber is indeed passive. Here we refer to the limits of our model that allows for contraction as the only force generating process. It is however possible, that the measured forces arise through a different mechanism that does not require myosin inside the bundle, e. g. frictional forces of the surrounding retrograde flow or pull exerted through the DSF by an TA. TAs adopt an intermediate state between VSFs and DSFs. As they are not directly connected to FAs, the determination of their tensions is the most indirect one. It is though expected that TAs should be stronger than DSFs as they contain myosin II, but should be weaker than VSFs since they cannot transmit their force directly to the cell's outside.

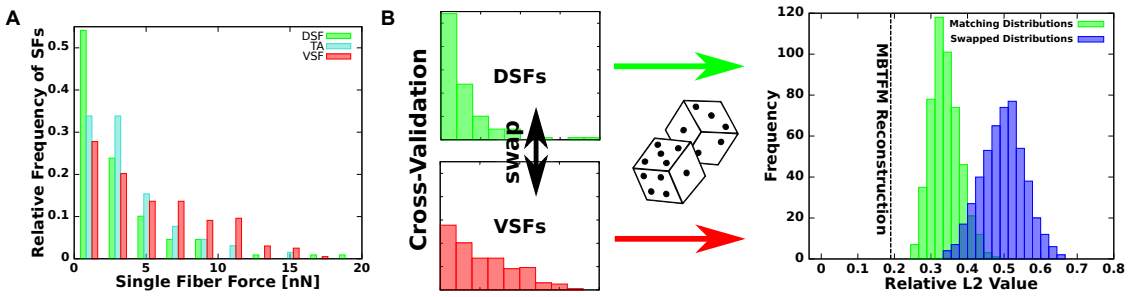

Figure 4.14: Distribution of tension among different stress fiber types. (A) Histogram of single stress fiber tensions sorted by fiber type (16 U2OS-cells, $N = 369$ SFs). Ventral SFs (red) show the highest tension on average. (B) Cross-Validation of the statistical significance. When we sample SF tensions from the distributions shown in (A), we get a Gaussian distribution of $L2$ values for one cell (green). If the distributions for ventral SF and dorsal SF are switched, the estimates become significantly worse (blue).

In order to check the statistical relevance of the SF tension distributions, we performed a cross-check of the result in the following way (Fig. 4.14 B). We took an arbitrary cell from the data set and sampled tensions for the individual stress fibers from the distributions shown in Fig. 4.14 A. We then calculated the direct problem (middle column in Fig. 4.6 B) to achieve an $L2$ error estimate in combination with the cells displacement field recorded in the experiment. When we repeat this process for many times, we get a Gaussian distributions of $L2$ values (Fig. 4.14 B, green distribution). When we exchange the distributions for VSFs and DSFs, which differ the most, we get a similar but broader Gaussian distribution, and at a significantly higher mean $L2$ value (Fig. 4.14 B, blue distribution). We conclude that albeit the distributions for the different SF types are not clearly separated, their detailed structure is important and of statistical significance.

4.7 Discussion & Outlook

With MBTFM we have introduced a novel technique to reconstruct cellular traction fields from displacement data of soft elastic planar substrates. The key idea is to use additional image data and biophysical modeling to dispense with Tikhonov regularization. MBTFM can directly relate model properties to experimental data without any influence of a regularization parameter.

We coined the term *geometrical regularization* in analogy to Tikhonov regularization as both methods yield a stable way to reconstruct cellular traction fields in the presence of noise. We have shown that geometric regularization is very robust to

noise in terms of total force estimates and that even single SF tensions can be reliably reconstructed at noise conditions typical for experiments. Still geometric regularization pursues a very different approach than Tikhonov regularization, as it does not continuously bias different almost identical solutions to a single one based on *a priory* assumptions, but restricts the solution space of the inverse problem to a biophysically relevant subspace. In this way we do not need to estimate any regularization parameter.

A further advantage of MBTFM is that it relates model parameters directly to experimental data. We have explained that other techniques bias FA size and distributions, or need to quantify traction forces exerted by single FAs by specifying elliptic areas around FAs, where traction is integrated. MBTFM directly projects the data on the model parameters, which in our case means that they are related to SF and background tensions, and with that, to FA tractions.

The projection of data to model parameters also means that one has to be very careful about choosing an appropriate model for MBTFM. In this study, we thoroughly checked the model assumptions with a correlation analysis based on the segmented images alone, without using any results of the reconstruction. The result ensured us that it is justified to model the SFs as stress generating structures. One also needs to know the descriptive limits of the model, since it is important not to interpret results as biological facts which are in reality due to the details of the model definition. Again, we stress that the results we acquired for FAs could be obtained with FTTC in a similar manner, but they are more conveniently assessed from the segmentation for the MBTFM model. For the SF type tension distribution analysis, the MBTFM algorithm is unaware of any SF classification. Therefore we regard both results not to be influenced by the description of the model. We are further encouraged by the fact that FTTC and MBTFM reconstruct the same total forces if the regularization parameter is set in the vicinity of the Bayesian estimate.

In terms of biological results, we have attained two very important findings. Firstly, FAs in U2OS-cells bear a sharply defined average force and traction, and the cell scales their number and total area with the total force the cell exerts. The average traction per FA of $4.1 \pm 0.1 nN/\mu m^2$ is in line with the values for other cell types found in the literature. Secondly, we have shown that different SF types show characteristic tension distributions, and that the difference in the distributions is of statistical significance. The latter result can only be obtained with MBTFM, since it is the only technique so far to our knowledge that allows to assess the tension of multiple SFs in a cell in a non-invasive manner.

MBTFM as presented here requires good-quality images of both the actin CSK and FA locations. This poses a challenge to experiments and limits its applicability in

knockdown and inhibition experiments. Here we found that segmentation becomes increasingly difficult and that no consistent picture for stress fiber tensions could be found in the case of ROCK inhibition or α-actinin knockdown. However, because total force measurements are very robust, we could still use this data for our FA force analysis.

In future assays MBTFM can be implemented with different models and different experimental settings. Though experimentally difficult, precise data for three-dimensional traction fields could yield deep insights in combination with three-dimensional whole cell modeling. It would also be interesting to combine MBTFM with laser cutting in order to assess the tension of the same SFs with two independent methods.

5 Viscous Flow in Cable Networks

5.1 Introduction

Viscous flow is omnipresent in cells. Starting at the cell's outer envelope, the plasma membrane is a two-dimensional fluid of lipids and membrane-associated proteins. Up to 70% of the cell's volume consist of water, which constitutes a viscous environment for many active flow processes [140]. The driving forces are usually provided by actin polymerization or molecular motors, though in a variety of different fashions. In some organisms like starfish or Xenopus, surface contraction waves occuring in oocytes prior to cytokinesis induce flow in the cytosol [141]. Active drag on organelles by myosin XI motors induces flow in plant cells that enhances and directs diffusion [142]. One of the most prominent examples is the retrograde actin flow in motile cells [143, 144]. At the leading edge of the cell actin monomers polymerize into filaments that push against the plasma membrane. The counter forces then drive the filaments backwards to the center of the cell, where they are eventually disassembled.

Despite the fact that many cellular components show properties of liquids, cells and their constituents can also exhibit the behavior of solids. The main difference of a solid and a fluid is that the solid has an internal memory of an original resting state, and that it exerts restoring forces when it is deformed. The physical theory to describe these forces and their effects is elasticity theory. Again, a prominent biological example is given by the actin cytoskeleton (CSK). Individual filaments can be cross-linked and bundled to form highly elastic structures, so called stress fibers (SFs) as explained in the introduction [19, 21]. But also less stable components show elastic behavior on short time scales.

The combination of viscous, elastic and active components is a challenge to theoretical modeling. The classical framework to describe materials that show both liquid and solid properties is viscoelasticity (see e. g. [145] for an introduction in the context of polymers and [146] for a discussion of growth models). Continuum models are useful whenever one can define an intermediate length scale that is larger than the microscopic elements and smaller than the system size. Tlili et al. describe a general modeling approach starting from a constitutive mechanical relation, that

can either show a viscous or an elastic behavior in the long time limit [147]. Active gel theory has been developed in the past decade with a strong focus on active components and long time properties of a fluid as reviewed in [148]. However, all of these continuum approaches struggle if the material of interest is not sufficiently homogeneous in its internal organization.

In this chapter, we present a new discrete modeling approach to viscous flows in the actin CSK with triangular networks of cables. Cable networks have been used previously as mechanical models for the whole cell, e. g. to predict cell shapes on micro-patterned substrates [4, 78], or to assess the internal distribution of tension within the CSK as described also in chapter 4 [91, 114]. A cable responds like a Hookean spring under tension, but does not resist compressive forces. These properties reflect the polymeric nature of the CSK. While stretched cross-linked filaments can bear forces in the range of a few nN, they buckle and eventually depolymerize under compressive loads. The discrete modeling enables us to investigate the different viscoelastic properties of distinct cytoskeletal structures, namely stress fibers and more distributed actin networks.

5.2 Modeling

Discrete viscoelastic models generally consist of two basic units, i. e. a viscous dashpot and an elastic spring. These two can be arranged in multiple different ways to form material models. The both simplest and most well known models are the Maxwell and the Kelvin-Voigt model (Fig 5.1). In the Maxwell case, spring and dashpot are connected in series. In a massless system, any external force applied will lead to an instant strain in the spring, which in turn transmits the force to the dashpot (Fig 5.1 A). The viscous unit then starts to flow, thereby altering the resting length of the component. It will only stop when no more force is transmitted by the spring. The behavior of the whole model is viscous in the long time limit. When the external force is released and the ends of the element are clamped, the spring force will still induce a flow in the dashpot, until the spring finally arrives in the unstrained state.

The behavior of the Kelvin-Voigt model is distinctly different (Fig 5.1 B). As spring and dashpot are arranged in parallel, the dashpot only delays the spring's strain buildup. Consequently, there exists a maximal strain at constant external force, which is set by the spring's stiffness and rest length alone. The element will further recover its original configuration eventually after the extension force is turned of. In summary, in the Kelvin-Voigt model the elastic properties determine the long time behavior of the system. For completeness, we note that there are many material

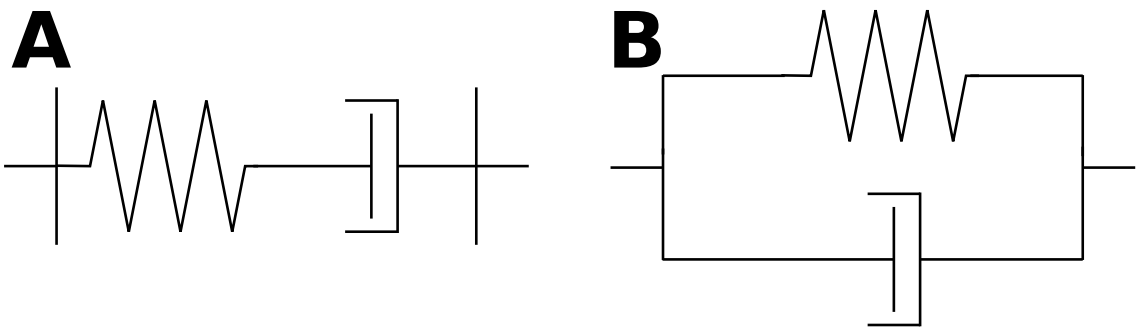

Figure 5.1: Discrete viscoelastic models. Under constant external force F, the Maxwell element (A) flows with constant velocity $v = F/\eta$ (viscous limit, dashpot viscosity η), while the Kelvin-Voigt element (B) balances the force and assumes a steady state with $v = 0$ (elastic limit).

models connecting more than just two units, e. g. the Zener, Lethersich, and Burgers models [149–151].

With our model we seek to describe the interplay between elastically and viscously dominated parts of the actin CSK on the intermediate time scale that the cell needs to rearrange its structure. We will focus on cells adhering to planar substrates, which induces rather flat cell shapes. This allows us to consider only the two-dimensional projection of the cell for our model. The various distributed actin networks are described by a triangular network as described in chapter 4. However, the mechanical model for the links between two vertices are chosen differently for this purpose.

The majority of actin filaments is organized in distributed networks that cannot be observed by standard resolution optical microscopy. As these networks are only weakly cross-linked and subject to high turnover rates, we assume that they obey a Maxwell type material model (Fig 5.2 A). However, for the polymeric nature of the CSK, we replace springs for cables and reference the corresponding element as *cable-Maxwell*. To account for the viscous environment of the cytoplasm, we additionally couple each vertex to the ground via a viscous Stokes drag element.

The situation is markedly different for actin stress fibers (SFs), which are clearly visible in standard fluorescence microscopy. Here, many actin filaments are tightly bundled and cross-linked, resulting in a much more stable structure on the time scale of a few minutes up to an hour. In the context of laser ablation, SF retraction dynamics have been successfully predicted with a Kelvin-Voigt type material [23]. However, here we are less interested in the short time dynamics of individual fibers, so we disregard the dashpot for simplicity and take cables alone (Fig 5.2 B).

The solution of the equations of motion for the network has been implemented in the

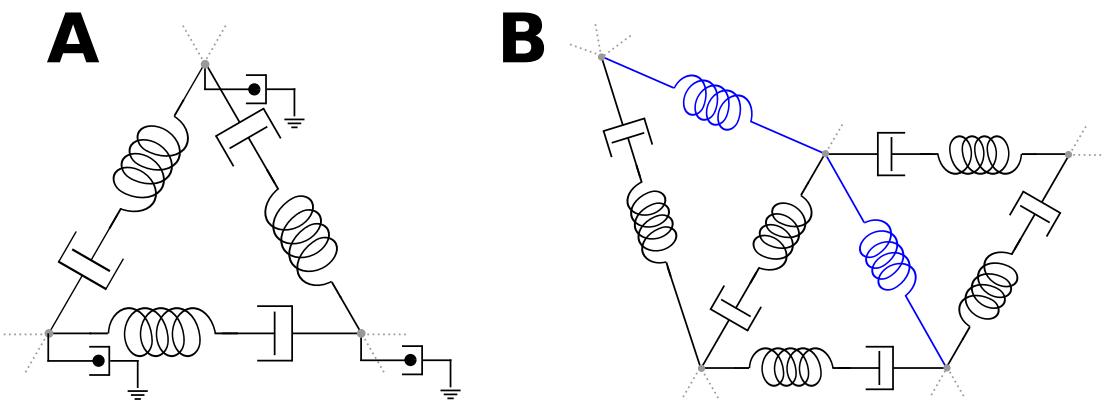

Figure 5.2: Viscoelastic network model. (A) Triangular network of cable-Maxwell elements, where springs of standard Maxwell elements are exchanged for cables. Vertices are coupled viscously to the environment by Stokes drag elements. (B) Modeled by cables alone, a stress fiber (blue) is embedded in the cable-Maxwell network. Viscous coupling to the environment is not shown for clarity.

software *SurfaceMaster*. Before we describe the details of the algorithm, we want to make some remarks on the definition of the dashpot model. From a single discrete viscous element, one might expect a constant velocity response to an external force, regardless of its length, like the velocity of a sphere being dragged through a viscous fluid in a tube at constant force against Stokes' friction does not depend on the tube's length. We will find a distinctly different behavior for the dashpot, however. Its constitutive relation is defined as

$$\sigma = \eta \cdot \dot{\epsilon} \tag{5.1}$$

with stress σ, dynamical viscosity η, and strain rate $\dot{\epsilon}$, which we substitute into the equation of motion,

$$\rho \frac{\partial^2 u}{\partial t^2} = \frac{\partial \sigma}{\partial x} \ , \tag{5.2}$$

where u is the displacement, ρ the mass density, and x the spacial coordinate, to get

$$\frac{\partial v}{\partial t} = \frac{\eta}{\rho} \frac{\partial^2 v}{\partial x^2} \ . \tag{5.3}$$

Here we substituted in the velocity $v = \partial u / \partial t$. This diffusion equation can now be solved for the boundary conditions $\sigma(a) = \sigma(b) = \eta\dot{\epsilon} = \eta \partial v / \partial x = f$ and $v\left((a+b)/2\right) = 0$, where a and b denote the borders of the dashpot and f is an external stress. The stationary solution found by setting $\partial v / \partial t = 0$, reads

$$v(x) = \frac{f}{\eta} \left(x - \frac{a+b}{2} \right) \tag{5.4}$$

Clearly, the velocity with which the endpoints move away from each other, $v_e = v(a) - v(b) = f/\eta \cdot (a-b)$, grows linear with the system's size. A constant force

velocity relation therefore only exists, if one artificially holds the system size constant. In contrast, if we identify the term $a - b$ as the system size l and v_e as its time derivative, we arrive at

$$\dot{l} = \frac{f}{\eta} \cdot l \ , \tag{5.5}$$

which obviously leads to an exponentially growing flow velocity of the dashpot model. Note that the last conclusion is only valid, if the steady state in the diffusion equation 5.3 is reached sufficiently fast. That holds true for high velocity diffusion constants $D_v = \eta/\rho$, which is especially valid in a massless system we investigate later. The result has been confirmed by finite element simulations of a Maxwell fluid by Dimitri Probst (personal communication).

This is consistent with the picture of a fixed line density λ of elements showing Stokes drag viscosity: The velocity of a single Stokes drag element is

$$v = \alpha \cdot F/\eta \ , \tag{5.6}$$

where α is a proportionality constant. Coupled in series, all elements contribute to the total velocity

$$\dot{l} = v_{tot} = n \cdot v = \lambda l \cdot \alpha \frac{F}{\eta} = \frac{F}{\tilde{\eta}} \cdot l \tag{5.7}$$

with effective viscosity $\tilde{\eta}$. Note that eqs. 5.5 and 5.7 are equivalent.

These findings match the expectations of a viscous polymeric system. If a piece of filamentous network of length l flows with velocity v in response to a force f, this is due to molecular processes like the unbinding and binding of crosslinker proteins, or polymerization. If the system size is doubled to $2 \cdot l$, the number of crosslinkers, binding sites, etc. is also twice as large, resulting in a flow velocity of $2 \cdot v$. In contrast, the viscous coupling of the vertices to the environment should not depend on any distance from an arbitrary initial position, but resemble the situation of Stokes' drag.

Though the viscous environment coupling does not depend on the initial position, it has to depend on the mesh size. We expect it to be the same regardless if an area A is triangulated with n or rather $2n$ vertices, for example. Further, the viscosity should remain constant over the whole triangulated region even if the vertex density is significantly higher in some regions as in others. We therefore set $\alpha = \alpha_i = \tilde{l}/A_i$ in Eq. 5.6, where $\tilde{l}$ is a characteristic length scale, and A_i the area associated with vertex i (one third of all triangles adjacent to the vertex).

In order to solve the equations of motion for the network, we employ an Euler algorithm that consists of repeating the following steps.

1. Determine the total contractile force F_ν on each link ν and its elastic part F_ν^e from the current cable configuration alone.

2. Determine the force $\vec{F}_i$ on each vertex i as $\sum_\nu F_\nu \cdot \vec{e}_\nu$, where the sum runs over all adjacent links and the $\vec{e}_\nu$ denote unit vectors along the links pointing away from v.

3. Move each vertex v by $\vec{s} = \left(\vec{F}_i \cdot \tilde{l} \cdot \Delta t\right) / (\eta^* \cdot A_i)$, where Δt is the chosen time step, η^* the viscosity of the surrounding medium, and $\tilde{l}$ is a characteristic friction length scale.

4. Account for the flow in the dashpot by adjusting the rest length $l_{0,\nu}$ of each cable in a cable-Maxwell element by

$$l_{0,\nu,\text{new}} = l_{0,\nu} + v \cdot \Delta t = l_{0,\nu} \cdot \left(1 + \frac{F^e_\nu}{\eta_\nu A_0} \cdot \Delta t\right) , \tag{5.8}$$

   where Δt is the same time step as above, A_0 is the cross section of the fiber and η_ν the viscosity of the cable-Maxwell element. Note that $l_{0,\nu}$ can never decrease in a cable-Maxwell model due to the absence of pushing forces. The rest lengths of pure cable links representing SFs are not adjusted.

5. Adjust the mesh to retain a good discretization.

5.3 Mesh Alterations

The description of a viscously flowing matter with a triangular mesh faces some challenges regarding mesh integrity. As discussed before, we expect sources and sinks of cytoskeletal material due to polymerization and depolymerization processes as well as compression and stretching. When we consider a source, we expect all vertices of the surrounding mesh to flow away from it. This results in increasingly large and pointed triangles in this area, until the material cannot be described with the desired resolution any more and discretization artifacts become visible in the simulations. The converse holds for sinks: as all vertices flow inwards, triangle sizes decrease until numerical difficulties arise. As a consequence we need to dynamically alter the mesh configuration by refining large triangles in source regions and removing small triangles at sinks. This necessarily comes at the cost that one destroys information contained in removed triangles, edges and vertices, or introduces artificial information for newly created mesh elements. Still one can retain most of the information of the original state, and we will show how to achieve this in the following sections.

To determine when mesh alterations are necessary, we define a characteristic link length $\bar{l}_0$ as the average of all resting lengths at the beginning of the simulation and a scale factor S. Then $\bar{l}_0 \cdot S$ constitutes an upper threshold for edge resting lengths, and $\bar{l}_0/S$ a lower threshold.

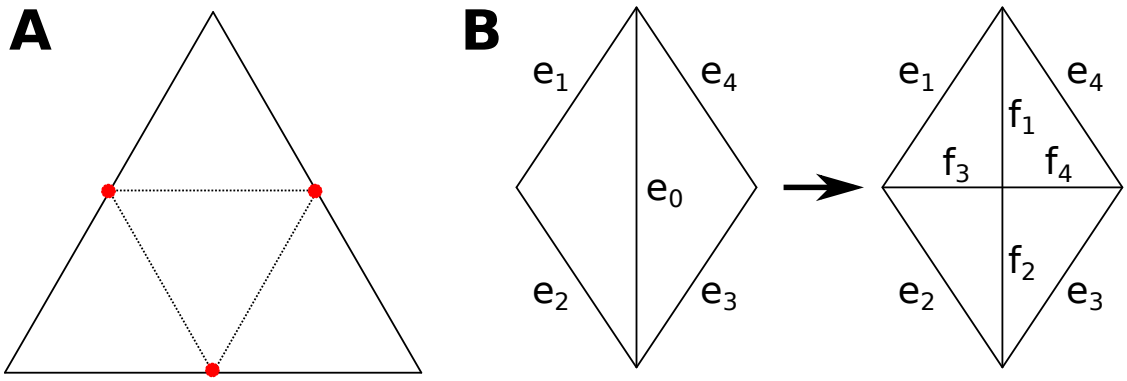

Figure 5.3: Triangle refinement. (A) Triangle refinement by splitting all edges yields three additional triangles but introduces hanging nodes (red). (B) Refining one long edge connecting two triangles. Only two additional triangles are created without hanging nodes. Edges are denoted by e_i prior to the refinement, and f_j afterwards.

5.3.1 Triangle Refinement

There are multiple ways to introduce new triangles into a triangular mesh. The first one that might come to one's mind is to replace one large triangle by four smaller ones of equal size (Fig 5.3 A). However, this introduces hanging nodes, if adjacent triangles are not refined as well. We therefore stick to an even simpler way to insert new triangles into the mesh, as shown in Fig 5.3 B. An edge connecting two triangles is split in half, if its length exceeds $\bar{l}_0 \cdot S$. The midpoint is connected to the two opposing tips of the triangles that shared the split edge. In this way, we introduce only two new triangles in one refinement step and preserve mesh integrity.

For triangle refinement it is also straightforward to define the viscous and elastic properties on the new edges. We are guided by the idea that we want to describe the same material with a different discretization, which in particular means that the forces on any vertex should not change and that the elastic properties of the links need to be adjusted. It is well known that two springs with spring constants k_0 in series behave like one spring with $k_1 = k_0/2$. So $k_{f_1} = k_{f_2} = 2k_{e_0}$ holds to describe the same material. In our simulations we will choose the spring constants for f_3, f_4 from a homogeneous background stiffness, which is set to represent the elasticity of the unstrained cytoskeleton. Regarding the viscous properties, $\eta(f_1) = \eta(f_2) = \eta(e_0)$ can be directly transferred from e_0 to f_1, f_2, since the viscosity is already defined per length. Similar to the spring constant, we choose the filament viscosity from a background viscosity for the newly created edges.

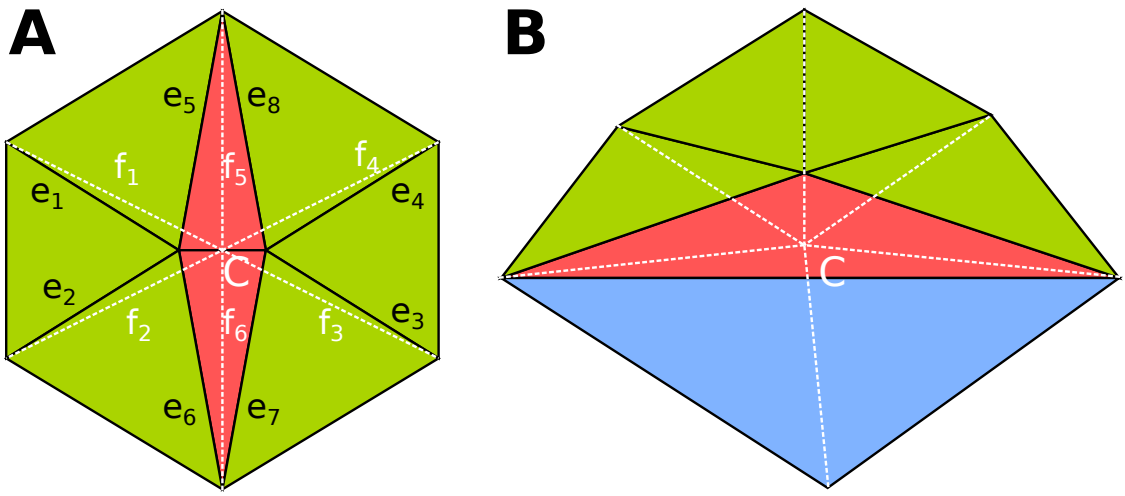

Figure 5.4: Triangle removal. (A) The short edge shared by the red triangles is collapsed, only the green triangles remain. (B) The height of the red triangle is small compared to its longest edge and is collapsed. At the same time, the blue triangle has to be split in half to avoid hanging nodes, so the overall number of triangles in the mesh is constant.

5.3.2 Triangle Removal

As for refinement, triangles can be removed from a mesh in many different ways. The minimal well known approach is the edge collapse algorithm, where an edge is replaced by a vertex, which is then connected to the surrounding vertices [152]. This technique is most appropriate if triangles contain one edge which is significantly shorter than the other two. In our simulations with flowing cable networks, we also observe another way of triangle shrinkage: one height of the triangle becomes small compared to the corresponding edge. These two cases are best treated with the two procedures described below (Fig 5.4).

Edge collapse

This is the standard case for triangle removal in our simulations, as it is the simplest way to reduce the overall number of triangles. The procedure is triggered if an edge becomes shorter than $\bar{l}_0/S$ and works as follows. First, the center of the short edge shared by the red triangles in Fig 5.4 A is obtained. Second, the red triangles are removed from the mesh. Third, the vertices where e_1, e_2 and e_3, e_4 meet are displaced to the center determined previously. In the last step, each of the two edges that a red triangle shared with green ones have to be merged.

Note that there are mesh configurations, in which the procedure as described above does not yield the desired results. We here list the three checks we perform before

the operation is executed. If any of the checks is positive, the operation is prohibited.

1. One of the dashed white lines may intersect with one of the outer edges of a green triangle. In this case, the application of the edge collapse algorithm would lead to a failure in the mesh (some area is covered by two triangles, while some other area is uncovered at the same time).
2. Either of the red triangles in Fig. 5.4 A may posses an internal structure of even smaller triangles. In this case, the algorithm would transform the sub-triangles into a straight line, which leads to undefined behavior.
3. One of the dashed white lines may become longer than a threshold for triangle refinement and thereby cause an infinite sequence of refinement and removal steps.

Height collapse

Edge collapse is not sufficient as the only way to remove triangles from the mesh. Each edge length might still be above a given threshold for a long and pointed triangle, but the triangle area can still tend towards zero. For this reason, we introduce another operation, which removes one triangle and splits another. Consequently, the overall number of triangles is conserved under this operation. However, it leads to more homogeneous distributions of triangle areas.

The procedure is triggered if the height of a triangle becomes smaller than $\bar{l}_0/(2S)$. As depicted in Fig 5.4 B, the central triangle (red) is removed, and the joint vertex of all green triangles is moved to the center of the red triangle. The blue triangle that shares the long edge of the red one is split in two in order to avoid hanging nodes. Note that the long edge is therefore split in two, and each of the parts is merged with one edge of the now neighboring green triangle.

Again, one has to check for several pitfalls that may occur for certain mesh configurations. If any of the following checks is positive, the operation is prohibited. The triangle colors now refer to the ones in Fig 5.4 B.

1. As for the edge collapse case, one of the dashed white lines may intersect with one of the outer edges of a green triangle. In this case, the application of the edge collapse algorithm would lead to a failure in the mesh (some area is covered by two triangles, while some other area is uncovered at the same time).
2. The four triangles that share an edge with the red triangle could match the height collapse criterion as well (the blue one counts as two once it is splitted).

If they do, this can lead to an infinite chain of refinements.

Conserving important structures during triangle removal

Note that we introduce one new vertex in each of the triangle removal operations. Its position is indicated in Fig. 5.4 by the point where the dotted white lines merge. However, this might not be appropriate if the operations are to be performed in the presence of fixed vertices, free boundaries, or stress fibers. These structures are to be preserved, as they are of special importance to some of the simulations. This means for fixed vertices to keep their position, and for edges at the boundary or edges of stress fibers to remain straight lines. If it is not possible to retain all structures unperturbed, we give highest priority to keeping the location of fixed vertices, followed by vertex locations at the boundary and within stress fibers in this order.

Cable properties during triangle removal

We are again guided by the idea to describe the same material, now with a coarser discretization. Forces on vertices and local elastic properties should not change. However, it is not possible to achieve this completely, since we are removing information from the mesh. In the edge collapse case, the orientation and therefore the force direction of edges e_1 - e_4 in Fig. 5.4 A changes only slightly, since the collapsed edge is short. However, force magnitudes may change significantly depending on the local spring constants. We therefore adjust the resting length for each of these edges such that $F(e_i) = F(f_i)$, where F denotes the edge force, while the spring constants are kept constant. As e_6, e_7 and e_5, e_8 are merged, their spring constants k are added to yield $k(f_5) = k(e_5) + k(e_8)$ and $k(f_6) = k(e_6) + k(e_7)$. In this sum we account only for edges that are in the extension limit, as cables cannot build up compression forces. Rest lengths l_0 are chosen such that force of the merged edge equals the sum of its two predecessors. If both preceding edges do not bear force, the rest length is ill-defined because of the flat force-extension curve for cables in the compression regime. In this case, we choose the new rest length such that the length difference Δl between current length l and rest lengthl_0, $\Delta l = l - l_0$, of the merged edge is the average of the two predecessors. If the preceding edges carry active forces, the new edge will carry the summed force.

In the height collapse case, we combine the algorithms for edge splitting and edge merging, that are adopted from the edge collapse and the triangle refinement operations. The edge shared by the red and the blue triangle is split as in the triangle insertion section, and each of the two parts is merged with the corresponding edge

Parameter	Symbol	Numerical value	Unit
Initial link length	$\bar{l}_0$	10	μm
Initial spring constant	k	$5\ /\ \bar{l}_0$	$nN/\mu m$
Effective filament viscosity	$\eta_{\text{fil}} = \eta_\nu \cdot A_0$	1000	$nN \cdot s$
Effective coupling viscosity	$\eta_c = \eta^*/\tilde{l}$	0.003	$nN \cdot s/\mu m^3$
Scale factor	S	2.3	
Central active tension	t	$0.3 \cdot \bar{l}_0$	nN

Table 5.1: Parameters used in the method validation section unless stated otherwise

share by the red and a green triangle.

Regarding the viscous properties, we note that splitting an edge does not change the filament viscosity as it is defined per length (cf. Modeling section). Merging however does increase the viscosity of the single dashpots to their sum in the joint element. So for merging, filament viscosities are treated just as it is explained above for the spring constants.

5.3.3 Edge Flipping

After some repetitions of triangle insertion and removal, some vertices show an increase in connectivity, i. e. in the number of edges connected to one vertex, which ultimately leads to numerical and algorithmic difficulties (e. g. the problems discussed in the triangle removal section). We introduce edge flipping in order to keep a homogeneous distribution of connectivity. If two triangles are connected by an edge e, and if the two triangle angles opposite to e are larger than a threshold angle $\alpha > \pi/2$, the edge is flipped and connects now the two vertices which where unconnected before. During this operation, we can conserve hardly any elastic properties of the material. We simply select the spring constant for the new edge from the background elasticity and apply zero strain. To keep these events rare, we use $\alpha = 110°$ in our simulations.

5.4 Method Validation

We now focus on how these mesh alterations change the simulations of a viscoelastic fiber network. We take a rectangle of $800\mu m$ by $300\mu m$ dimensions that is covered by a triangular network of active Maxwell cable elements. In the central region, the links feature a constant force dipole which actively contracts the network (Fig. 5.5 A). We impose no-displacement boundary conditions along the whole rim of the

rectangle. For the plots in this section, we use the parameters listed in Tab. 5.1 unless stated otherwise. Note the definitions for the effective filament viscosity η_{fil} for the dashpot in the cable-Maxwell elements and the effective coupling viscosity η_c for the Stokes drag elements determining the viscous coupling to the environment.

5.4.1 Effects of Different Mesh Alterations

First we investigate how the flow velocity profiles change with different stages of the mesh alteration algorithm: (a) without any alterations, (b) only with triangle splitting and edge flipping, (c) only with edge and height collapse, and (d) with the full alteration algorithm. For this purpose we average the flow velocities in x-direction in both space and time. The spatial averaging zones are illustrated in Fig. 5.5 B, and the temporal average is taken over $1s$.

Fig. 5.5 (C) - (H) show the resulting velocity courses at different mesh sizes and varying distance from the contractile zone. Qualitatively, the main features of the curves are similar for all algorithm variations. After an initial peak, where strain builds up in the cables, the velocities decrease until they assume a plateau which is determined by the dashpot viscosity η_{fil} and the coupling viscosity η_c. When the contraction is switched off at $t = 500s$, the flow immediately reverses its direction in box I and decays until the springs have reached their resting lengths. As box II is farther away from the contractile region, the response in both contraction and relaxation is slightly delayed and the magnitude of the flow velocities drops down. This is the expected behavior for the viscoelastic fluid, and we will show a comparison to finite element simulations of a corresponding continuum mechanics model later. The roughness of the red curve (no alterations) can be explained by the discrete number of vertices leaving the box to the interior at an velocity higher than the average and the vertices entering the box from the outwards facing direction with a velocity smaller than the average. For all other curves, discrete steps during mesh alterations cause additional roughness. This effect decreases for smaller mesh sizes, as discrete vertex displacements due to mesh alterations become very small.

In the details we expect to find some differences due to the different mesh alteration steps applied. Each additional alteration method leads to a slight increase in the creep velocities (plateau velocities). It is obvious that the collapse algorithm introduces periodic inclines to the flow field at $\bar{l}_0 = 10\mu m$ (Fig. 5.5 F). This is due to the highly homogeneous starting configuration of the mesh, which leads to the situation that many edges fall under the collapse threshold at the same time. The resulting finite displacement of vertices adds an effective force on short time scales. This effect is less pronounced at $\bar{l}_0 = 20\mu m$, where the mesh is distorted more rapidly and the effect vanishes in the general noise and at $\bar{l}_0 = 6\mu m$, where vertex displacements are

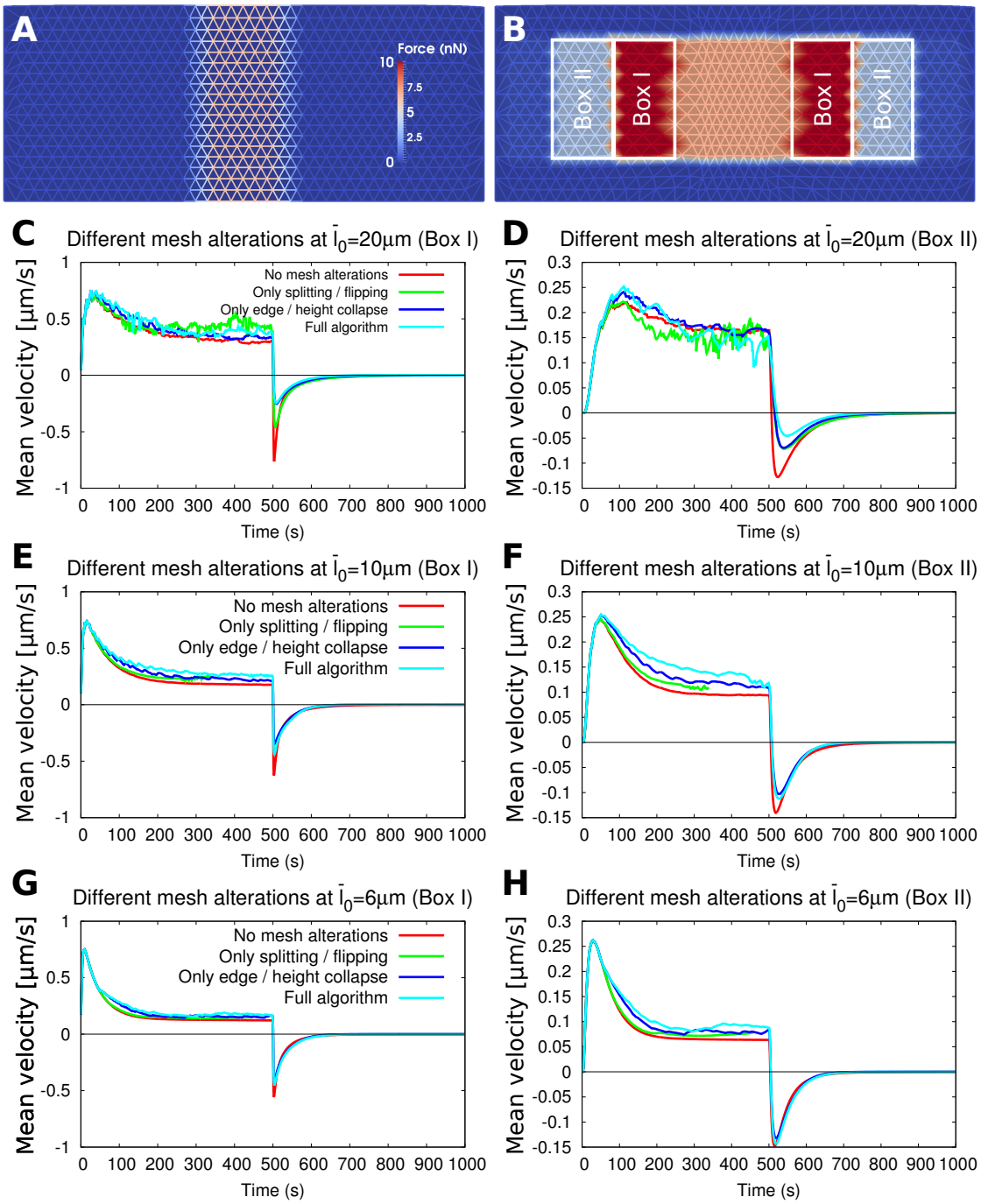

Figure 5.5: Average flow velocities towards the central contractile rectangle for different mesh sizes. The outer frame of the network is fixed. (A) The contraction zone is located in the central region. (B) Flow velocities are measured and averaged spacially within boxes I and II (horizontal velocity is shown in color code). Additional time averaging is applied within 1s. (C) - (D) Flow velocity profiles for $\bar{l}_0 = 20\mu m$ within each box over simulation time. At $t_0 = 500$, the contractility is switched off. (E) - (F) Flow velocity profiles for $\bar{l}_0 = 10\mu m$. (G) - (H) Flow velocity profiles for $\bar{l}_0 = 6\mu m$.

smaller due to the smaller mesh size.

A conserved feature between the different mesh sizes is the maximal peak velocity, which is mainly set by the contractile tension and the coupling viscosity to the environment. We conclude that the scaling for these quantities seem to yield the expected results, though we will investigate this further below. The decrease in the creep velocity for smaller $\bar{l}_0$ is mainly an effect of the different properties of dashpots added in the vertical or horizontal direction. If dashpots are added in the vertical direction, the effective viscosity of the network increases as there are more dashpots to be elongated at the same force. However, if more dashpots are added in the horizontal direction, we know that the viscosity has to remain unchanged. When the mesh size is altered, these two effects happen at the same time, and there is no simple relation to account for both.

This discussion about two-dimensional versus one-dimensional scaling of the filament viscosity in principle also applies to the cable stiffness k, though it is not as clearly visible from the velocity plots. The difference is that the one-dimensional scaling defined by $EA = k/\bar{l}_0$ is length dependent in that case, which at the same time accounts for the higher number of cables in the vertical direction if we decrease the mesh size in the rectangle.

In the expansion regime $t > 500s$, we find the expected results. The more mesh alterations are applied and the more elastic information is thereby destroyed, the lower are the expansion velocities in the outflow. The effect is less visible for smaller mesh sizes, since the mesh alterations induce only smaller vertex displacements, which leads to less loss of information. We conclude that with the full algorithm, we will underestimate the flow associated with relaxation in homogeneous meshes without stress fibers.

Fig. 5.6 reveals the necessity for mesh alterations. Without changing the mesh, it becomes obvious at $t = 500s$ that long and flat triangles lead to an unexpected stress in the y-direction which is a discretization artifact. At the same time, triangles densify at the rim of the contraction region close to the horizontal symmetry axis. For longer simulation times, this leads to numerical instabilities (not shown). This problem is even amplified when triangle refinement is allowed, since large triangles are split before reaching the contraction zone and therefore an even higher number of triangles arrives. This leads to stalling in the simulations (e. g. interrupted green curve in Fig. 5.5 F). Despite this fact, the flipping and splitting operations efficiently prevent the stress buildup in y-direction. Edge and height collapses on the other hand keep triangles at acceptable sizes close to the contraction zone, while triangles in the stream become more and more flattened. Only combined the algorithms retain a good discretization for the whole rectangle.

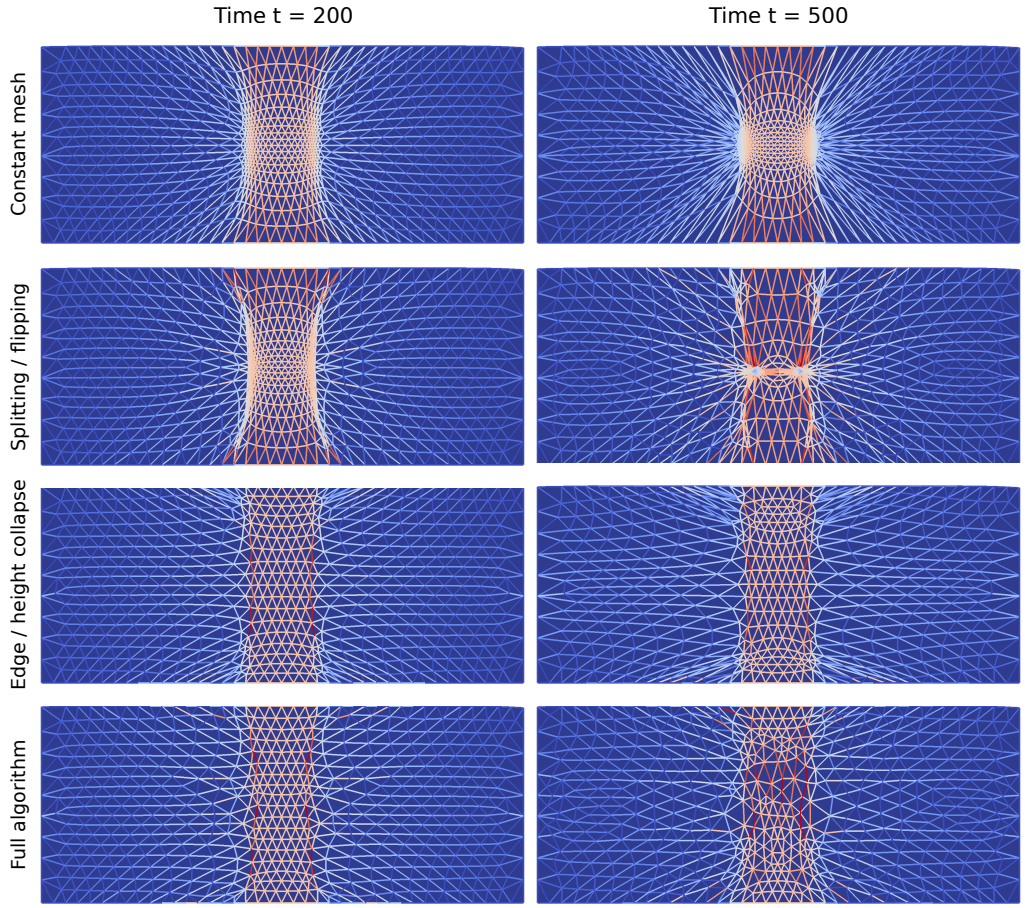

Figure 5.6: Representative mesh configurations $t = 200s$ and $t = 500s$ during contraction with different parts of the remeshing algorithm enabled. The starting position for $t = 0$ is the one shown in Fig. 5.5 (A). All simulations performed at $\bar{l}_0 = 20\mu m$.

5.4.2 Effects of Different Parameters of the Cable-Maxwell Elements

We now systematically vary four different parameters of the model, namely the scaling factor S, the contractile tension t (Fig. 5.7), the spring constant k, and the filament viscosity η_{fil} (Fig. 5.8). Note that the scaling factor sets the threshold for edge splitting and collapse by $l/\bar{l}_0 = S^{\pm 1}$. It is thereby also an important indicator for mesh homogeneity as it defines the maximal link length ratio within the mesh $l_{max}/l_{min} = S^2$. The choice of the scaling factor S does not influence the creep velocity (Fig. 5.7 A), though it determines when the first alterations occur and thereby when the curve forks away from the reference state without any mesh alterations (red line). Note that the seemingly periodical velocity inclines due to the collapse algorithm as discussed in the previous section (see e. g. $S = 2.3$, dark blue line) vanish for larger S (e. g. $S = 5$, black line). Again, this is due to smaller vertex

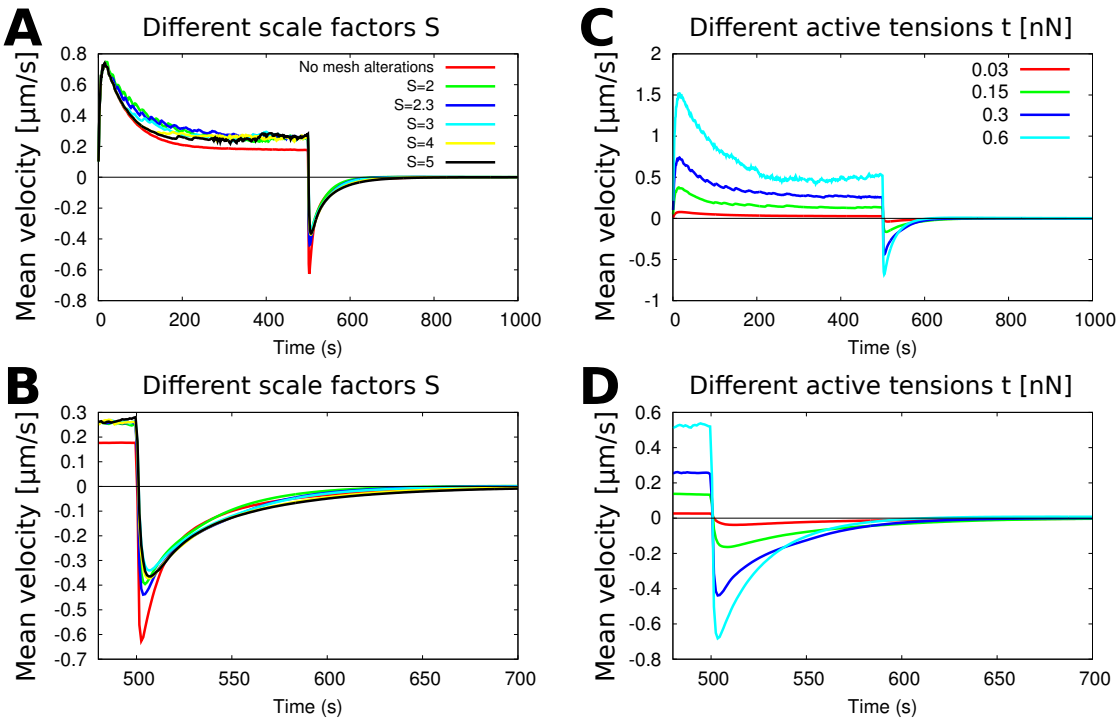

Figure 5.7: Effects of the scaling factor S and tension level t. (A) The scale factor controls the threshold for splitting and collapse relative to $\bar{l}_0$. (C) The tension is driving contraction and defines velocity magnitudes. (B), (D) Insets for (A),(C) for $480s \leq t \leq 700s$. All curves plotted for box I.

displacements during the collapse algorithm, as edges and heights to be collapse are already very small.

The tension t is the driving force of the flow. In all simulations of this section, we assume a homogeneous background tension, which is raised in the central region by a factor of 4. The transition between the high and the low tension zone is smoothly interpolated. Afterwards we subtract the background tension from all links, such that all links outside of the contractile zone and the transition region do not bear any tension. This is for the reason that any homogeneous line tension drives the system towards equilateral triangles, since an equilateral triangle has the minimal boundary length at fixed area. This however induces numerical artefacts in the relaxation process, since our starting configuration consists of almost equilateral triangles, i. e. the system appears to be elastic where it is actually viscous. Fig. 5.7 (C) and (D) show that the amount of elastic relaxation after the contraction is switched off directly depends on the creep velocity and with this, on tension. This is expected, since the stored elastic energy must be given by the ratio of two time scales: the one that determines strain buildup, i. e. the velocity, and the one governing strain dissipation, i. e. the filament viscosity.

The variation of the cable stiffness k illustrates that the initial peaks at the begin-

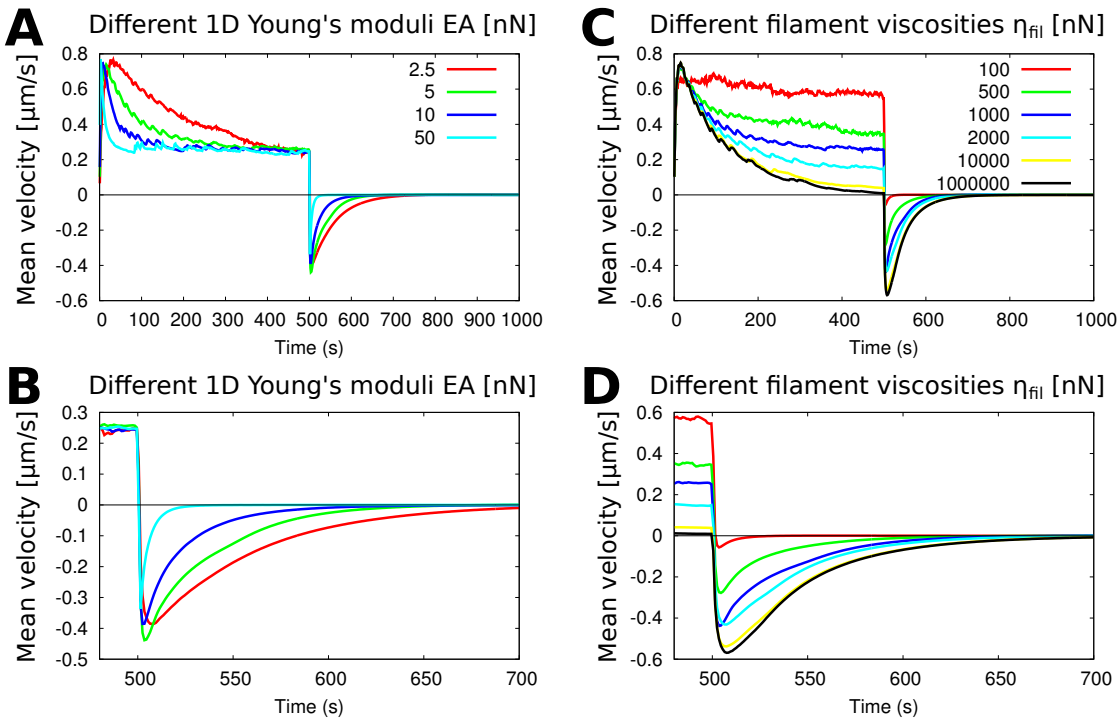

Figure 5.8: Effects of the spring constant k and filament viscosity η. (A), (B) The spring constant shapes the velocity peaks in the initial contraction and relaxation phases. (C), (D) Filament viscosities determine the creep velocity.

ning of both the contraction and relaxation phases are determined by the elastic properties of the mesh, though in different manners. At the beginning of contraction, all cable-Maxwell elements are in their resting state. Consequently, the forces from the contractile zone are only balanced by the viscous coupling to the environment, which results in rapid movement. As soon as the springs build up considerable stress, the forces that need to be balanced by the viscous environment drop until the velocity is determined by the dashpot part of the cable-Maxwell elements and the coupling viscosity. In a Maxwell fluid the decay is proportional to $\exp(E/\eta_{fil} \cdot t)$. It is clear that stiffer springs experience these stress levels earlier, since a lower amount of strain and therefore movement is necessary than for soft springs (cf. Fig. 5.8 A). Fig. 5.8 B shows the relaxation flow in more detail. In this regime, the springs are stressed from the beginning due to the previous contraction phase. Their internal stress is now the only force that drives the system. The decay of flow velocities is again determined by the spring constant k. The stiffer the cables are, the sharper is the initial peak. This is due to the fact that the same stress is stored at less strain for high k, which allows the system to relax quickly against the viscous environment. Conversely, low spring constants lead to a longer relaxation flow, since it takes longer until the larger movements caused by larger strains relax against the viscous coupling. This also means that more energy is dissipated through the dashpot elements during the relaxation flow for soft cables than for stiffer ones.

The filament viscosity parameter η_{fil} impacts the creep velocity as expected (Fig. 5.8 C). Low viscosities increase the fluidity of the system, which leads to larger dashpot movements in response to the same driving forces. In the relaxation regime, low filament viscosities lead to only weakly developed backwards flow (Fig. 5.8 D). The reason for this is twofold: First, the forces and therefore strains that can be maintained by the cable components are smaller if the dashpot yields more quickly. Consequently the elastic energy stored in the network is low, such that there is little potential for relaxation. Second, the dashpots still elongate the rest lengths of the cable-Maxwell elements during relaxation. This effect is also more pronounced if η_{fil} is low.

5.4.3 Comparison to Continuum Mechanics

An important issue to compare theory and experiment is to estimate model parameters which are valid for the experimental situation. The typical ways to retrieve parameters are either fitting of experimental data with the model of interest, or direct experimental measurements. For our model, we need to estimate

- line tension t,
- filament viscosity η_{fil},
- cable stiffness k,
- and coupling viscosity η_c.

The first three are one-dimensional properties of single links. However, quantities that describe active, elastic and viscous properties of the material gained from biological experiments are usually of higher spacial dimension, such as the surface tension σ, the bulk viscosity γ, and the Young's modulus E. As discussed before, it is not trivial to calculate the one-dimensional properties from the three-dimensional ones, since often the mesh size $\bar{l}_0$ is involved and conclusive theories about the scaling are often missing. We will therefore estimate the quantities from comparison to continuum theories, that can directly assess the experimentally obtainable values.

Edge tension versus surface tension

Edge tension is the easiest parameter to begin with, since the analogous quantity measured in experiments, the surface tension, can be simulated together with the flowing triangular mesh in the framework of our software. We begin with a short theoretical glimpse at the scaling between line tension t and surface tension σ. Let us assume that the triangles in the mesh are equilateral. In this case, the energy related

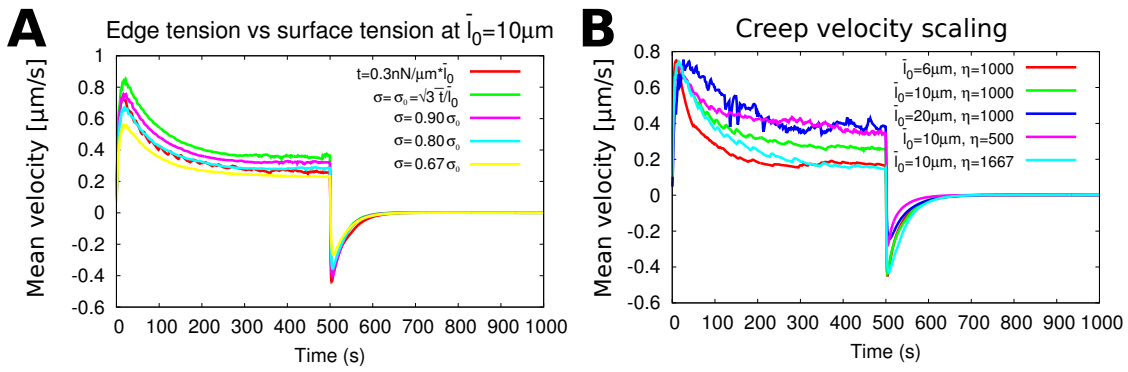

Figure 5.9: Homogeneous surface tension. (A) Edge tension versus surface tension at $\bar{l}_0 = 10\mu m$. Simulation with active tensions t defined on edges are equivalent to simulations with a surface tension $\sigma = 0.8\sqrt{3}t/l_0$ defined on the triangles, cf. main text. (B) Velocity curves at different mesh sizes and representative filament viscosities for a constant surface tension defined on the triangles. The creep velocities are equal (purple and dark blue line, red and light blue line) if filament viscosity and mesh size change by the same fraction from a reference state (green line).

with line tension is $E_t = 3/2 \cdot t \cdot l$, where l is the length of the edges. The factor $1/2$ comes from the fact that each edge is shared between two triangles. Similar, the surface tension energy can be expressed as $E_\sigma = \sigma A = \sqrt{3}/4 \cdot \sigma \cdot l^2$, where A is the area of the equilateral triangle. If we want both energies to yield the same driving forces for uniform shrinking or expansion, we need to set

$$F_t = \frac{\partial E_t}{\partial l} = \frac{\partial E_\sigma}{\partial l} = F_\sigma$$

$$\sigma = \sqrt{3}\frac{t}{\bar{l}} \ .$$

It is this $1/l$ scaling that motivates the definition of the tension in Tab. 5.1, which should lead to a constant surface tension. Fig. 5.9 A shows that this calculation overestimates the surface tension which is necessary to generate the same creep velocity. This can be explained by the fact that triangles become elongated in the transition zone between the zero and the high tension regime. Thus, t/l is actually smaller in this zone where the movement is generated. We determine the correction factor to be approximately 0.8 for all simulated mesh sizes.

In Fig. 5.9 B we plotted the velocity curves for the same surface tension at different mesh sizes and filament viscosities. Interestingly, if the filament viscosity is changed accordingly to the mesh size, the creep velocities remain constant. This is intuitively clear, as the number of dashpots per height unit is doubled when the mesh size is halved. If the viscosity is halved as well, the force-viscosity ratio stays constant. However, the exponential decay from the peak towards the creep region changes,

which is related to the fact that scaling for the viscosities should be different in the horizontal and vertical direction as discussed earlier.

Parameters controlling elasticity and viscosity

In order to validate the general behavior of the model and to assess the elastic and viscous properties that correspond to a continuum description, we fitted the model data with a one-dimensional Maxwell model that is viscously coupled to the ground (Fig. 5.10 A). All continuum simulations were done by Dimitri Probst. The one-dimensional continuum model is governed by the equation

$$\tau\gamma\frac{\partial^2 u_x}{\partial t^2} + \gamma\frac{\partial u_x}{\partial t} = (\lambda + 2\mu)\,\eta\frac{\partial^3 u_x}{\partial t \partial x^2}\,. \tag{5.9}$$

Here, γ is the friction coefficient equivalent to the coupling viscosity, η corresponds to η_{fil}, u_x is the displacement in the x-direction, λ and μ the elastic Lamé coefficients, and $\tau = E/\eta$ with the Young's modulus E. Fig. 5.10 B, C show that we could achieve a very good correspondence between the continuum model and the discrete algorithm. First, we set $\eta_{fil} = \infty$ to exclude the influence of the filament flow and used the parameters listed in Tab. 5.1 otherwise. In addition, we switched off the remeshing algorithm for better congruence between the models. We obtained the corresponding one-dimensional continuum parameters $E = 0.6kPa$, $\eta_c = 2.9 \cdot 10^6 kg/m^2$, and $\sigma_0 = 0.6kPa$, for which the models agree well (Fig. 5.10 B). Then, we also took η_{fil} from Tab. 5.1 in the discrete model. In the continuum model, we kept the parameters found before and only varied η. Optimal agreement between the two models was found for $\eta = 0.1MPa \cdot s$ (Fig. 5.10 C). We conclude that the velocity course of the two-dimensional discrete model matches an one-dimensional continuum description for an effective parameter set. The main limitation of the one-dimensional model is that it cannot account for the lateral no-displacement boundary conditions. They lead to a spatially varying flow in the two-dimensional model: at the boundary, the flow velocity has to be zero and then gradually increases towards a maximum in the center. In a Newtonian fluid, these considerations lead to the famous Hagen-Poiseuille law that states that the volume of fluid that can pass through a pipe at a constant pressure difference scales with R^4, where R is the radius of the pipe. To cover this effect, we aim at comparing the discrete model to a two-dimensional continuum model equivalent of Eq. 5.9, which is challenging because one has to account for the difference of cables in the discrete model and springs in the continuum theory. This is still work in progress and will be covered in the PhD thesis of Dimitri Probst.

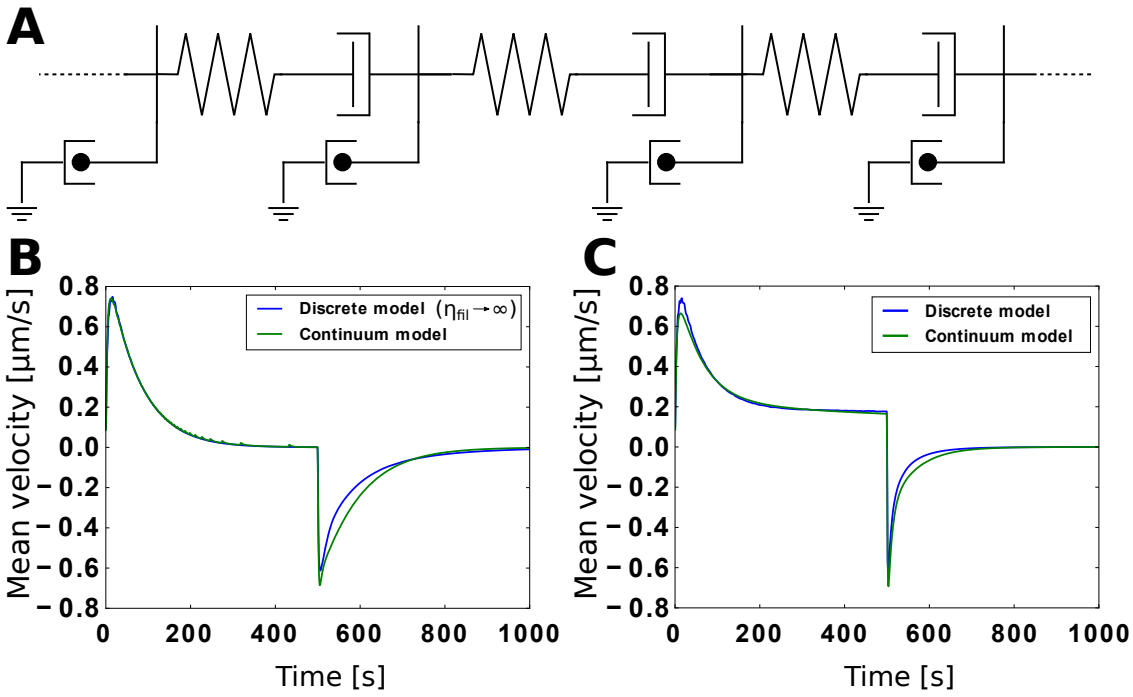

Figure 5.10: Comparison of a one-dimensional continuum mechanics model to the discrete model without remeshing. (A) Sketch of the continuum model. (B) Fit of the continuum model to the discrete model in the elastic limit. (C) Fit of the filament viscosity in the continuum model to the filament viscosity in the discrete model. All other parameters for the continuum model are taken from the fit in (B).

5.5 Application to Biological Data

We now apply our model to data obtained from experiments by our collaboration partners from the University of Chicago, Patrick Oakes, Elizabeth Wagner, Michael Glotzer, and Margaret Gardel. They use a novel experimental approach with tunable light-inducible dimerization tags (TULIPs) that was recently introduced in [153]. There, binding between a light-oxygen-voltage (LOV) domain that naturally occurs in oat plants and an engineered PDZ domain (ePDZ) can be controlled by laser light (Fig. 6.2 A). These groups can be used as tags on other proteins. In this study, the LOV group was attached to membrane-bound green fluorescence protein (GFP), and ePDZ via the fluorescent protein mCherry to a RhoGEF (Fig. 6.2 A). GEFs transfer the GDP-bound state of RhoA towards the GTP-bound state. Only in the latter state, RhoA induces actin polymerization and myosin activity (Fig. 6.2 B, also cf. chapter 1). Since RhoA is typically membrane-attached, this process predominantly occurs at the plasma membrane. When the binding between the tags of membrane-bound GFP and the GEF is activated, the GEF itself becomes membrane-bound and continuously activates RhoA in its proximity. Thus, by activating this binding via a laser, one can spatially and temporarily control the distribution of active

GTP-bound RhoA. The experiments are conducted in 3T3 fibroblast cells.

Fig. 6.2 C shows that actin and myosin activity is indeed increased in the regions that are photo-activated by laser light. The number of FAs and their distribution are not affected (Fig. 6.2 D). As expected from the higher myosin activity, traction stresses increase after activation. The increase happens at the boundary of the activated region only (Fig. 6.2 D), which underlines that the effect can be described by a surface tension. Only a gradient in tension leads to forces, which is in agreement with our model.

5.5.1 Stress Fibers Provide the Cell with Elasticity

So far we have investigated the system's behavior for homogeneous networks without any internal structure. However, the cells in our study exhibit many SF spanning the whole cell (compare Fig. 6.2 C), which renders them highly anisotropic. The strength of the approach we describe here is that it can account for distinct one-dimensional structures which are embedded in a two-dimensional viscoelastic material. For this reason, it is especially well suited to investigate the role of stress fibers in the mechanics of adherent cells. In the following, we systematically investigate the mechanical effects that one-dimensional structures of cable elements introduce to a cable-Maxwell network, i. e. the role of elastic SFs in a visco-elastic fluid environment.

As explained above, we introduce SFs as non-viscous cable-element line structures in the mesh of cable-Maxwell elements (cf. Fig. 5.2). A non-viscous cable element corresponds to a cable-Maxwell element for $\eta_{fil} = \eta_{SF} = \infty$. Further, here and below we decrease the filament viscosity of the viscous elements to $\eta_{fil} = 100nN \cdot s$ to emphasize the elastic effect of SFs on shorter time scales. All other parameters of Tab. 5.1 are kept unchanged for the background mesh. The active tension of SFs is chosen to be $t_{SF} = 5nN$, and we assume that the tension is by the factor of 4 higher in the activation region, like we assumed for the background mesh. The stiffness of the SFs is assumed to be $EA = 50nN$ like in chapter 4, where EA is the one-dimensional Young's modulus.

We now subsequently add SFs to the mesh. The first one is positioned in the vertically centered region of the simulation rectangle (Fig. 5.12 A, left). It spans the whole boxes I and II on both sides, and consequently also the activation region (cf. Fig. 5.5 B). Further SFs are added in parallel such that they are equally distributed among the vertical space between the topmost and the lowermost SF in the configuration with 9 SFs (Fig. 5.12 A, right).

Fig. 5.12 B shows that the addition of SFs gradually transforms the character of

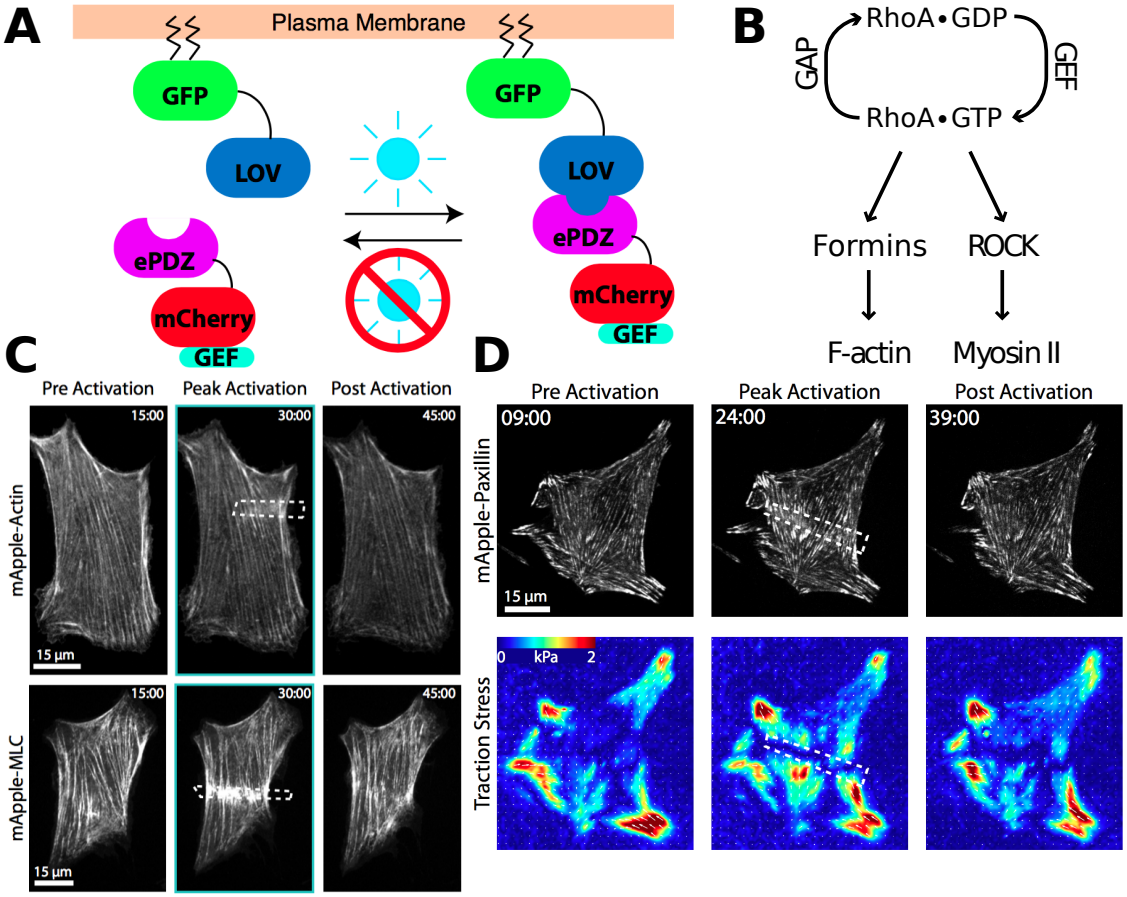

Figure 5.11: Optically controlling RhoA activity in 3T3 fibroblast cells. (A) Shining laser light on LOV domains attached to membrane-bound GFP activates the binding with engineered PDZ domains. As PDZ domains are attached to GEFs one can thereby locally bind GEFs to the membrane and control RhoA activity. (B) Simplified RhoA pathway. GEF proteins promote GDP-bound RhoA to active GTP-bound RhoA, which induces actin polymerization and myosin activity. (C) When the boxed regions are activated by laser light, actin and myosin activation increases locally. (D) The distribution of the FA protein paxillin is not affected by RhoA activation, but traction stresses increase at the boundary of the activated region. Courtesy of Gardel and Glotzer labs.

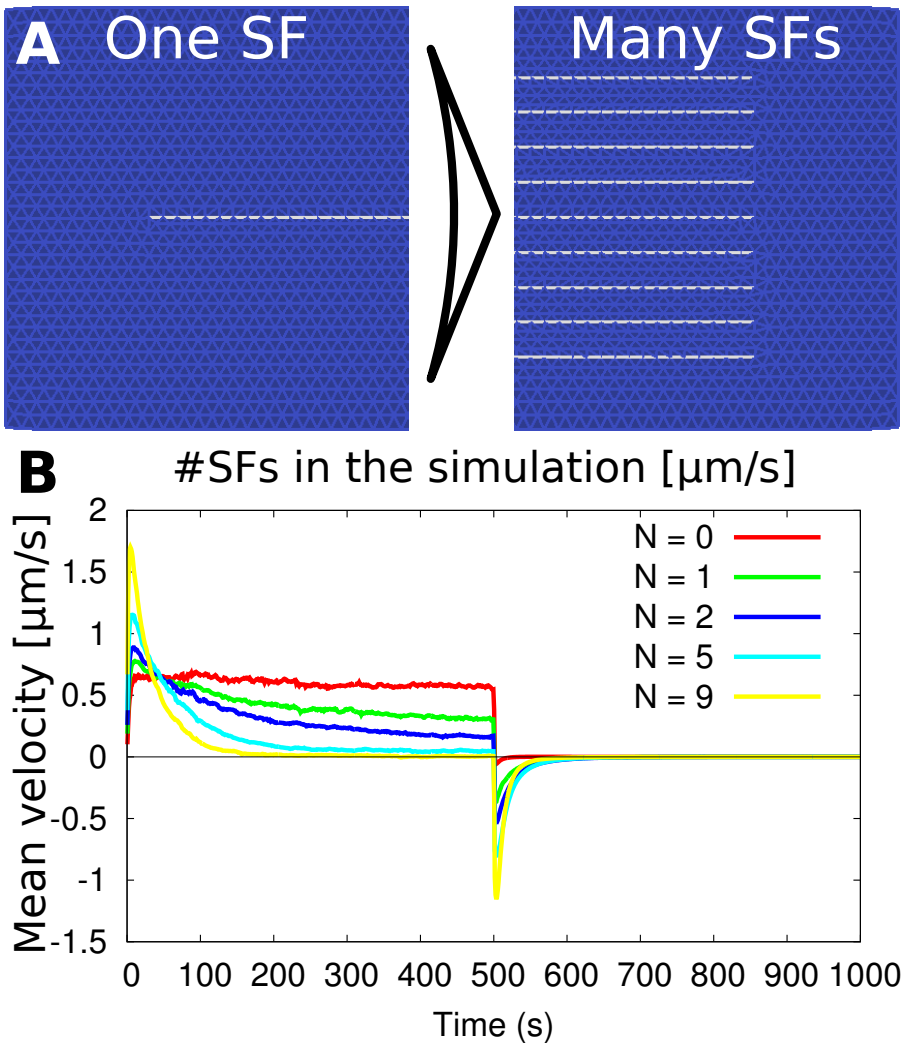

Figure 5.12: Stress fibers provide the cell with elasticity. (A) Computational setting. We subsequently add SFs (white lines) to the simulation box. *Left*: 1 SF. *Right*: 9 SFs. (B) The system gradually changes its behavior from viscous (red line, no SFs) to elastic (yellow line, 9 SFs).

the whole mesh from a Maxwell fluid (red line) towards a Kelvin-Voigt solid (yellow line). The creep velocity is decreased and is almost zero for $N = 5$ and $N = 9$ SFs. The reason is that during the flow, the SFs accumulate elastic energy. The elastic restoring forces eventually balance the active contractile forces and the SFs stall. In this situation, they act as additional no-displacement boundaries in the system. The remaining mesh can only move in the small channels between them. This situation is similar to the Hagen-Poiseuille law for a Newtonian fluid as discussed above. Likewise, the flow is greatly reduced for small channels in the cable-Maxwell case. In addition to the smaller creep flow, the backwards flow after the activation is switched off is also increased if more SFs are added, which also underlines the increasing elastic behavior.

5.5.2 Stress Fibers are the Main Contractile Elements

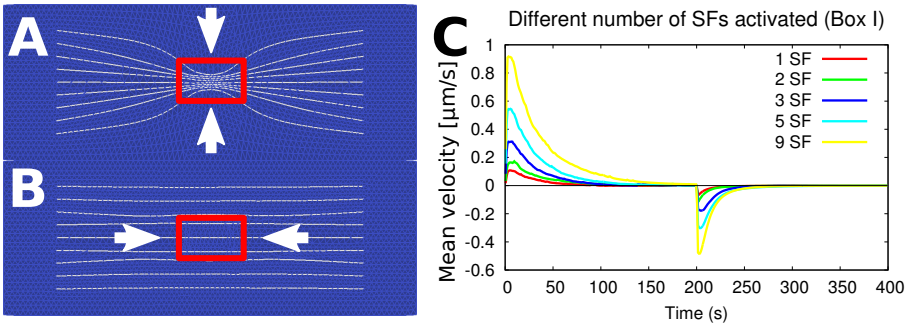

Figure 5.13: Stress fibers are the main source of contraction. The main flow directions in the steady state are marked with white arrows. (A) If isotropic contractility in the background network was significant, SFs should be dragged into the contractile zone (red box). (B) If only the SFs bear tension, flow is oriented parallel to the SFS. (C) If SFs are purely elastic and the main contractile elements, the flow stalls when the elastic forces balance the active forces.

In order to investigate the effect of active tension, we take the simulation box with $N = 9$ SFs from the previous section and restrict the activation zone in height, such that only $m = 1...9$ SFs run through the activation zone initially. The activation zone is always symmetrical to the central SF. Here, $m = 2$ means that the SFs adjacent to the central one are in the interpolation region between high and low tension. Remarkably, with the same parameters as before, SFs are pulled perpendicular to their orientation into the activation region (Fig. 5.13 A). This effect persists if SF tensions are increased, if SFs are assumed to have a larger spring constant, or if SFs are put under prestress. The inwards pull also occurs when the background tension is reduced by two orders of magnitude (Note that it was already assumed to be one order of magnitude smaller than the SF tension from the beginning).

In stark contrast, SFs remain completely straight in the experiments, even if only some of them run through the activation region. Thus the gradient in background tension has to be negligible compared to the forces in the SFs. As myosin is more active in the activation region, we conclude that it predominantly attaches to SFs and that it does not exert appreciable forces to distributed actin networks. This is in agreement with the results from chapter 4, where we also found that the total traction exerted by a cell is dominated by SF forces. In conclusion, the background network constitutes a mainly passive viscoelastic environment for active SF elements.

The observation that the background network has to be passive leads to another interesting consequence. If SFs are rather rigid objects on the scale of the extension they experience in the flow, they will eventually stall as discussed in the previous section. Due to the passiveness of the background, this implies that the overall flow

has to decay to zero (Fig. 5.13 C). Typical flow velocities in the experiments are on the order of $2nm/s$ and activation times on the order of 15 minutes. This means that the total extension is about $L = 2\mu m$, which compares to the total length of the SF of approximately $L_0 = 20\mu m$. Thus the strain is on the order of $\epsilon = L/L_0 = 0.1$, which at the assumed Young's modulus of $EA = 50nN$ amounts to a restoring force of $5nN$. This should lead to a significant reduction of the contraction speed towards the end of the activation period. However, this is not observed in the experiments (cf. Fig. 6.2 C, peak activation actin image). This means that either the active tensions are significantly larger than expected, or the SFs are significantly softer, or they are not purely elastic. The first possibility seems rather unlikely, since we have found in chapter 4 that $5nN$ is a very high tension for SFs in U2OS cells, which are known to exhibit very prominent SFs. It would be surprising if 3T3 cells built SFs with a significantly higher tension. At the same time, the analysis of SFs with the TEM in chapter 3 suggests that the Young's modulus is in the range of $50 - 500nN$. Thus $EA = 50nN$ assumed here is at the lower end of expected values. It is unlikely that SFs are considerably softer here. Consequently, the most likely explanation for the persistent flow is that SFs are also viscoelastic structures of the Maxwell type.

5.5.3 Stress Fibers are Viscoelastic Structures

Before we investigate the filament viscosity of SFs, we first refine our parameter choice. For this purpose, we observe that no initial peak is visible at the beginning of the activation period and that typical flow velocities are in the range of $2 - 5nm/s$ in the experiments. This indicates that the coupling viscosity η_c could be higher and the excess SF tension could be lower than we assumed so far. Fig. 5.14 A shows different choices for the coupling viscosity at an excess SF tension of $t_{SF} = 2nN$, which seems to be more appropriate than the $15nN$ assumed earlier. If η_c is increased, the initial peak becomes less pronounced as expected and is hardly recognizable at $\eta_c \geq 0.05nN \cdot s/\mu m^3$. There needs to exist a maximum though, since the velocity has to decrease eventually for purely elastic SFs.

Taking $t_{SF} = 2nN$ and $\eta_c = 0.05nN \cdot s/\mu m^3$, we now consider SFs as viscoelastic structures at finite viscosity η_{SF}. Fig. 5.14 B shows the velocity course for different SF viscosities. If η_{SF} is very high, an initial peak is visible since the creep velocity is limited by η_{SF}. If the SF viscosity is very low, however, the creep velocity is limited by the coupling viscosity instead. The velocity curves then asymptotically approach that limit for large times.

Note that the relaxation flow is reduced for small η_{SF}. This result is confirmed experimentally by inhibiting the protein zyxin, which is responsible for SF repair. Without zyxin the SF should become more fluid, which corresponds to lower η_{SF}. In

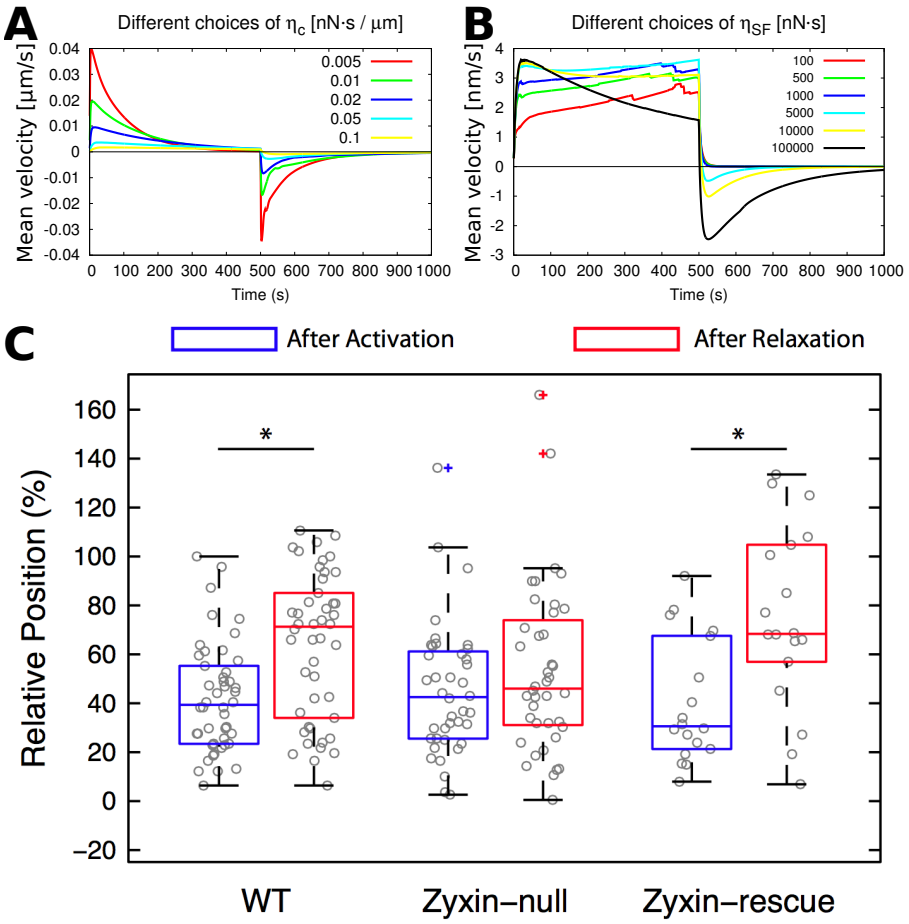

Figure 5.14: Parameter estimation for coupling viscosity, SF tension and SF filament viscosity. (A) For increasing coupling viscosities, the initial velocity peaks become less pronounced and overall movement is reduced. (B) Different choices for η_{SF} at $\eta_c = 0.05nN \cdot s/\mu m^3$ and excess tension $t_{SF} = 2nN$. (C) Zyxin-dependent relaxation flow. A relative position of 100% corresponds to a point $5\mu m$ away from the activation region. Measurements are performed in unperturbed wild type (WT) cells, cells where zyxin is inhibited (Zyxin-null) and rescued after inhibition (Zyxin-rescue; Zyxin-null + EGFP zyxin).

the experiments, zyxin null cells exhibit less relaxation, while rescuing zyxin restores the relaxation flow (Fig. 5.14 C).

5.6 Discussion & Outlook

In this chapter we have developed a novel approach to simulate viscous flow in cable networks. We explained the algorithm we implemented for overdamped dynamics to account for the dashpots in the cable-Maxwell model. The main challenge to such methods is preserving mesh integrity and homogeneity in the presence of sources

and sinks, and large mesh deformations. We have introduced one method to refine the mesh dynamically by replacing two triangles that share an edge by four new triangles. In this process, we need to introduce new information to the system to initialize the properties of the two new edges, which we choose from a homogeneous background stiffness and viscosity. We discussed how the viscous and elastic properties of the other edges have to be adjusted to describe the same material as before.

The second process necessary to preserve a good discretization is to remove small triangles from the mesh. We have introduced two methods to accomplish this by collapsing either a short edge or a short height of a triangle. The former reduces the total number of triangles in the mesh by two. However, in the latter we need to subsequently split an adjacent triangle, such that the overall number of triangles is constant under this operation, but triangle sizes are distributed more homogeneously after its application. We discussed how the viscous and elastic properties of the edges that remain in the mesh have to be altered by merging and splitting springs and dashpots.

We thoroughly investigated the impact on single parameters and mesh size on the velocity curves for the homogeneous model and found that they match with the expectations. For this purpose we used a rectangular box of 800 by $300\mu m$ and applied an active tension to the links in a horizontally central region across the whole height of the cell. The scaling of the active and elastic properties with mesh size was as expected. However, the scaling of the dashpot viscosity should be addressed in more detail in the future. This quantity is problematic, since it should be constant for refining dashpots connected in series but reduce by the factor of $1/n$ for n dashpots connected in parallel to yield the same effective viscosity. We also compared the model parameters with continuum descriptions. Here, a homogeneous surface tension instead of line tensions could be examined in the same framework of the triangulated mesh. We found that the simple assumption of a mesh with equilateral triangles gives a good approximation for the relation between surface tension and line tension. In order to compare the viscous and elastic properties of the discrete model to a continuum mechanics model, we fitted a one-dimensional Maxwell fluid with viscous coupling to the ground to the velocity curve of the discrete model and achieved very good agreement in the elastic limit as well as in the general setting. To associate model parameters with experimental accessible quantities we aim at comparing a two-dimensional continuum model to the discrete model in the future.

In order to investigate data from experiments with our model, we utilized its capability of introducing discrete one-dimensional structures on the edges of the triangles. In this way we can account for SFs that appear very prominently in the observed cells. We first assumed SFs to be purely elastic objects and found that subsequently

adding more SFs transforms the system from a fluid to a solid viscoelastic system. We conclude that SFs have to play an important role for the elastic properties of the cell, since they are mechanically more stable and bear higher tensions than distributed actin networks that are too small to be observed with standard light microscopy.

Next we constrained the activation region in height and found that initially straight SFs that run along outside of the activation region are pulled inwards by hypothetical forces in the background network. As this does not happen in experiments, we concluded that the background mesh is a passive viscoelastic medium for the stress fibers. This conclusion was only possible because we allowed for an active contribution of the background network from the start. In comparison in experiments that alter the mechanical integrity of the SFs, we observed that SFs are not purely elastic but also viscous on the time scale of our experiments. In agreement with the model, relaxation flows were found to be reduced for lower SF viscosities. In conclusion, the discrete modeling approach allowed us to establish SFs as the main active and elastic structures within the cell. With this knowledge, we can now better utilize traction force microscopy data to infer the absolute mean force change in SFs during activation, which would give a fixed value for one of the discrete model parameters. Regarding the viscosity, we need further experimental analysis that perturbs the properties of the viscous coupling towards the environment, or more fine-grained evaluation of the velocity curves at the beginning of the activation to dissect to which amounts the SF viscosity or the coupling and background network viscosity contribute to the creep velocity.

6 Cortical Network Dynamics and Shapes

6.1 Introduction

In the two preceding chapters we have addressed the active, elastic, and viscous properties of cells by modeling a two-dimensional projection of the cell. This is an approach that works well for cells adhering to flat substrates, since all important cellular components are mainly organized in a planar layer parallel to the substrate. However, such methods are not appropriate if non-planar cell shapes are to be considered. We have already discussed two such scenarios in chapter 2 (red blood cells, RBCs) and chapter 3 (three-dimensional scaffolds). In this chapter, we now turn towards cells with spherical resting shapes and focus on the shapes and dynamics induced by contractile activity in the cell cortex.

The cell cortex is a filamentous network that lies directly underneath the plasma membrane [154, 155]. Its thickness was measured for mitotic HeLa cells to be about $190nm$, and it is typically built of actin proteins, together with cross-linking and motor proteins [155]. The thickness is of special importance for the mechanics, since the bending energy of a thin sheet scales like $H_{\text{bend}} = E\, h^3$, where E is the Young's modulus. Due to the high cross-linking, these networks can provide the cell with structural rigidity that enables it to withstand external mechanical stresses. At the same time, the cortex is often highly dynamic, as its components undergo rapid turnover that can be further enhanced by molecular motors that are incorporated into the cortex and generate active tension [156].

An important aspect of the cortex is its mechanosensitivity [157], which denotes its capability of translating mechanical stimuli into biochemical signals. This enables the cell to not only react as a passive elastic medium to mechanical stresses, but to actively adapt and orchestrate cortical behavior. In some cases, cells even organize cortical contractility to contraction waves that run as ring-shaped contractile regions over the whole surface. This is important if cells become so large that diffusion is too slow to propagate signals efficiently. In contrast to diffusion, traveling waves in an excitable medium exhibit a constant wave speed and work equally well in small

and large cells. A typical example is constituted by the animal oocytes, that feature contraction wave during maturation. Starfish oocytes provide a good model system as these cells are very large with a diameter of $180\mu m$ and are transparent, which facilitates imaging [158].

In this chapter we will investigate contraction waves from two perspectives. First we investigate the dynamics of wave propagation with tools from the field of non-linear dynamics. We propose an excitable medium theory for the interplay of actin filaments and myosin II motors that features traveling pulses. We then look at how ring-shaped contractile regions influence cell shape and compare the results with measurements in starfish oocytes.

6.2 The Cellular Cortex as an Excitable Medium of Actin and Myosin

The cortex not only reacts passively but adapts actively to stimuli, which may be mechanical or chemical and originate from the outside or the cortex itself. Thus many possibilities for feedback systems arise, which are broadly discussed in the literature [159]. Sometimes a small perturbation is enough to drive the system out of equilibrium and cause a long trajectory in phase space before it returns to the same state as before. Such states are called *excitable*. Excitable media became famous in biophysics with the publication of Hodgkin and Huxley's model for the action potentials of neurons in 1952 (HH model) [160]. Some ten years later, FitzHugh generalized the equation of the van der Pol oscillator, $\ddot{u} + c(u^2 - 1)\dot{u} + u = 0$, to the system of equations [161]

$$\begin{aligned} \dot{u} &= c\,(v + u - u^3/3) \\ \dot{v} &= -(u - a + bv)/c\ . \end{aligned} \tag{6.1}$$

Here, a, b, and c are dimensionless parameters that determine the behavior of the system as we will see below. The equations include the van der Pol oscillator for the case $a = b = 0$, which can be verified applying Lienard's transformation, $v = \dot{u}/c + u^3/3 - u$, to the van der Pol equation [161]. The model provides a simplification of the complex HH model as it reduces the number of variables from four to two [161]. It was picked up and further analyzed by Nagumo and coworkers [162] and is therefore referred to as the FitzHugh-Nagumo model (FHN).

In the phase plane of the FHN model, the nullclines, where either of u, v is stationary, form a N-shaped curve and a straight line, respectively, that intersect in one, two, or three fixed points (FP; Fig. 6.1). The fixed points exhibit different stability properties, leading to three possible behaviors of the system. If the system only has

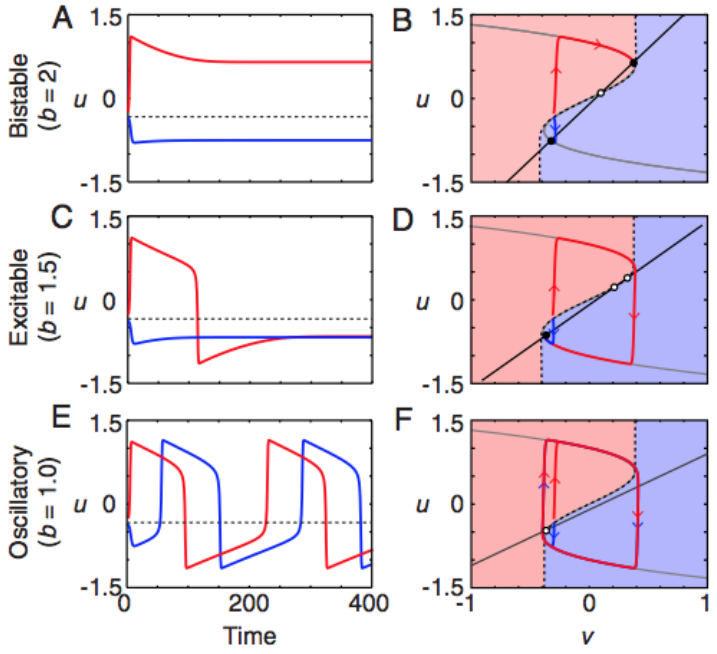

Figure 6.1: Bistable (A), (B), excitable (C), (D), and oscillatory (E), (F) behavior of the FHN model. Sample trajectories are displayed in red and blue for different starting positions. In the phase plane diagrams (B), (D), (E), black lines denote the nullclines, black dots stable and white dots unstable FPs. Taken from [163].

one unstable FP, oscillations arise around this point (Fig. 6.1 C). When the straight line is tilted by increasing the parameter b, two more FPs form, the first of which is always unstable. Depending on the stability of the second, the system is either excitable (FP unstable) or bistable (FP stable). In the bistable case (Fig. 6.1 A), the system relaxes into one of the stable states depending on its initial conditions. Only if a certain threshold is crossed, the system will assume the other stable state eventually. If the system is pushed away from the resting state in the excitable state and crosses the x nullcline, it first circles the unstable FP before it eventually relaxes to the stable FP (Fig. 6.1 B). In this way a small perturbation that is large enough to cross the threshold leads to a large loop in the phase space, which is the typical property of excitable media.

So far we have only investigated a system of two first-order ordinary differential equations of two time-dependent variables. However, cells utilize excitability mainly in order to transport information over large distances [163]. While diffusion processes are sufficient to synchronize the behavior of single cells on the length scale of $10\mu m$, time scales increase quadratically for longer distances d, $t = d^2/(2D)$ in one spatial dimension. $D \approx 250\mu m^2/s$ is a typical value for the diffusion constant in the cytoplasm [163]. This leads to diffusion times of circa 50 years on a meter scale. Even on the scale of a large cell like the starfish or Xenopus oocyte of $0.2 - 1mm$, diffusion takes tens of minutes to deliver signaling molecules. On the other hand, waves in excitable media offer length scale independent velocities. One example is constituted by action potentials in neurons that can travel through the body on the time scale of milliseconds. Others are calcium waves that occur on different occasions in animal cells, or waves of the protein kinase Cdk1 that synchronize the

cell cycle over different cells in the Xenopus embryo [159, 164].

It is therefore important to include the spatial dimension into the modeling. The simplest way to achieve this is by diffusive coupling. In the FHN model this amounts to adding diffusive flux for both species,

$$\begin{aligned} \dot{u} &= D_u \frac{\partial^2 u}{\partial^2 x} + c\,(v + u - u^3/3) \\ \dot{v} &= D_v \frac{\partial^2 v}{\partial^2 x} - (u - a + bv)/c\ . \end{aligned} \tag{6.2}$$

We now explain how pulses can form and travel in space in the excitable case. The description is also valid for the propagation of oscillations (leading to pulse trains) and a change of the stable state in the bistable case (leading to a traveling wave front). In the ODE system 6.1, a certain threshold needs to be crossed for the system to follow a large loop in phase space before returning to the resting state. The initial crossing can be introduced by increasing the concentration of u, for example. During the course of the trajectory, u is actively produced. By the diffusive coupling, the high local u concentration generates a large diffusive flux towards neighboring points in space. If this flux is high enough such that u crosses the threshold, the same excited trajectory will be induced there, leading to a spread of the initial signal. It is important to note that though neighboring points in space are coupled by diffusion, the propagation speed of a signal does not follow the classical one-dimensional diffusion law $\langle s^2 \rangle = 2Dt$. Instead, it leads to waves with constant speed that can be approximated by $v = 2\sqrt{D/\tau}$, where D is the diffusion constant and τ the supra-threshold doubling time for the propagating species [163, 165].

6.2.1 A Model for an Excitable Actomyosin Network

Recently, Bement and coworkers discovered a feedback mechanism between actin and the small GTPase RhoA that leads to spiral waves on the surface of Xenopus eggs and embryos [166]. They occur during cell division and originate from an activator-inhibitor process. We investigate a similar system given by starfish oocytes, that undergo cortical contraction waves during maturation. The experiments and image acquisition was performed by Johanna Bischof from the Lénárt lab at the European Molecular Biology Laboratory, Heidelberg. Our approach is complementary to that presented in [166], as we focus on the forces that are induced by myosin in the actin cortex. Fig. 6.2 shows the experimental setting. Starfish oocytes are very large cells with a diameter of $180\mu m$ (Fig. 6.2 A). During contraction, the local radius of curvature changes as the cell flattens from its initially spherical shape (Fig. 6.2 B). Fig. 6.2 C shows images of the different stages of a contraction wave that indicate the

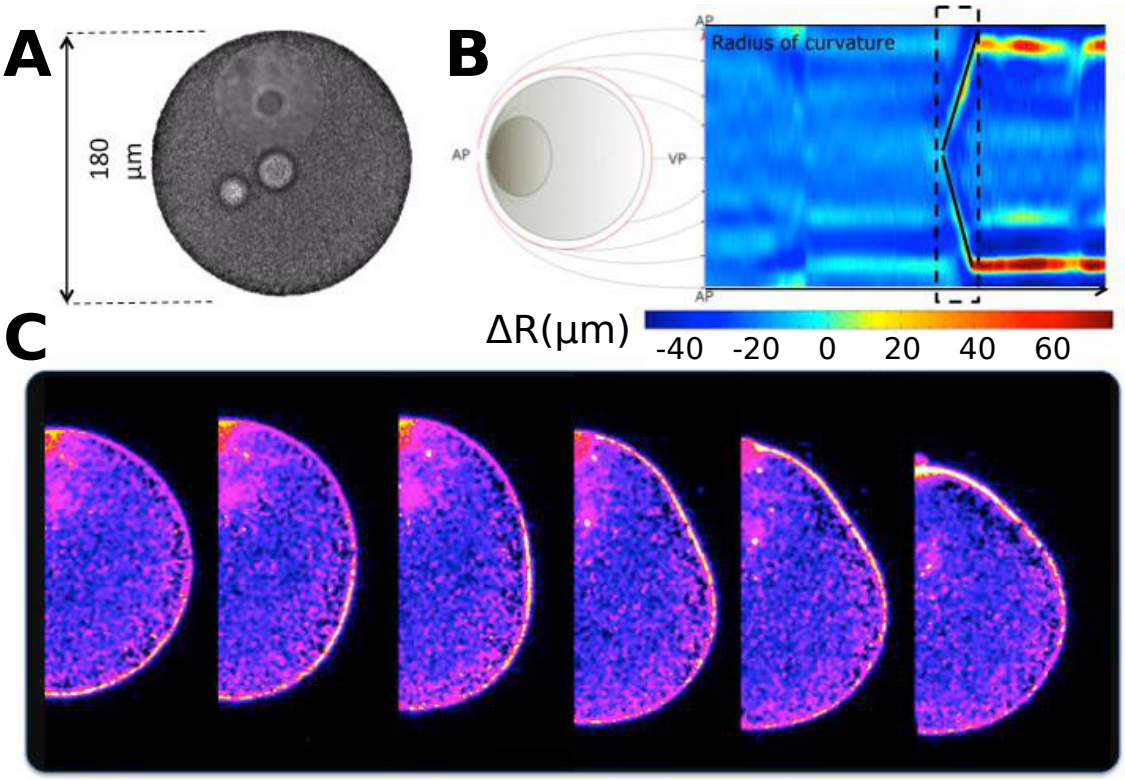

Figure 6.2: Cortical contraction wave in starfish oocytes. (A) Oocyte before contraction. The nucleus is still visible. (B) Kymograph of the change of the radius of curvature along a line from the vegetal pole (VP), where the contraction wave starts, to the animal pole (AP). The box marks the region of the contraction wave. (C) Fluorescence images of myosin motor proteins at different stages of wave progression. Non-muscle myosin II accumulates to the flattened regions of the cortex. Courtesy of Johanna Bischof, Lénárt group, EMBL Heidelberg.

importance of the motor protein myosin for this flattening as high concentrations of myosin colocalize with the flattened region. Note that the myosin signal decreases again behind the wave front. However, the molecular details of the process are largely unknown to this point, such that we consider a general possible feedback mechanism encouraged by experimental findings in the literature.

Interaction of actin and myosin has been a major research interest over the past 20 years [CIT]. Here we are mostly interested in the dynamics of myosin recruitment to the actin cortex. In a recent study, Luo and coworkers specifically investigated this topic by micropipette aspiration experiments and revealed that myosin II accumulates where the cortex is stressed [157]. More specifically only stress that affects the compression and dilation modulus of the cortex leads to myosin recruitment, whereas shear was associated with accumulation of the cross-linking protein filamin. Interestingly, myosin accumulation follows a sigmoidal curve, indicating that it is both self-enhancing and limited. An upper bound for the cortical myosin concen-

tration needs to exist because of e. g. limited binding sites and a limited number of myosin proteins in the cell. The self-enhancing effect has been termed myosin cooperativity (cf. [157, 167, 168], for example). Here we propose that myosin cooperativity and the compression / dilation dependent accumulation of myosin are linked, and can be described as

$$\begin{aligned} \partial_t M &\propto \sigma^2 \left(1 - \frac{M}{M_{\max}}\right) \\ \sigma &\propto M \ . \end{aligned} \tag{6.3}$$

Here, M denotes the concentration of myosin bound to the cortex, $M_{\max}$ its upper limit given by the biochemistry of the system, and σ the contractile force exerted by myosin. We assumed that the force dependent myosin cooperativity induces second order kinetics. Note that the relations 6.3 are enough to reproduce the sigmoidal accumulation. Further, we assume that myosin can detach from the cortex at a constant rate and that it can diffuse to neighboring sites.

The substrate to which myosin is recruited is provided by cortical actin filaments. The actin network itself is not mechanosensitive [157]. However, myosin generated contractility compacts the network [169], which leads to depolymerization and impedes further contraction [155, 156, 170]. The exact mechanisms of the formation of the cortex remain to be elucidated, however it assumes a steady state by protein turnover [155]. We combine these findings to propose the following simple dynamics for contractible actin A in the cortex,

$$\begin{aligned} \partial_t A &= \alpha \left(1 - \frac{A}{A_{\max}}\right) - \beta\sigma \\ \sigma &\propto A \ . \end{aligned} \tag{6.4}$$

The first term of the first equation describes the relaxation to the steady state of the actin network by turnover, while the second phenomenologically covers the compactification and depolymerization related to contractile force. The rates α and β are constant. With the second relation of 6.3 and 6.4 we also propose that force generation is proportional to both the concentration of myosin in the cortex M as well as the concentration of contractible actin A. It follows that $\sigma = \sigma_0 \cdot AM$ to first order. Substituting this relation into the first parts of 6.3 and 6.4 and accounting for myosin detachment and diffusion, we can now summarize our model equations to be

$$\begin{aligned} \partial_t M &= D_M \nabla^2 M + \delta\sigma_0^2 A^2 M^2 \left(1 - \frac{M}{M_{\max}}\right) - \zeta M \\ \partial_t A &= \alpha \left(1 - \frac{A}{A_{\max}}\right) - \beta\sigma_0 AM \ . \end{aligned} \tag{6.5}$$

Here, ∇^2 denotes the Laplace operator, D_M is the diffusion constant for myosin along the cortex, and δ, ζ control the effects of myosin aggregation and detachment.

We will now investigate whether this system can actually give rise to traveling contraction waves such as those occurring in starfish oocytes.

Before we analyze the phase plane, we first non-dimensionalize the system in one spatial dimension in order to concentrate on its qualitative behavior rather than units. For this purpose, we set $M = M_{\max} m$, $A = A_{\max} a$, $t = t_0 \tau$, and $x = l_0 \chi$. The last two relations define a characteristic time and length scale t_0 and l_0, and imply $\partial_t = (\partial\tau/\partial t)\partial_\tau = t_0^{-1}\partial_\tau$ and $\partial_x = (\partial\chi/\partial x)\partial_\chi = l_0^{-1}\partial_\chi$. Substituting these equations into Eq. 6.5 we arive at

$$\begin{aligned} \frac{l_0^2}{D_M t_0}\ \partial_\tau m &= \partial_{\chi\chi} m + \frac{\delta\sigma_0^2 A_{\max}^2 M_{\max} l_0^2}{D_M}\ (a\cdot m)^2\ (1-m) - \frac{\zeta l_0^2}{D_M} m \\ \partial_\tau a &= \frac{\alpha t_0}{A_{\max}}(1-a) - \beta\sigma_0 M_{\max} t_0\ a\cdot m\ . \end{aligned} \tag{6.6}$$

We still have the freedom to choose the length and time scale, which we exploit by setting $t_0 = A_{\max}/\alpha$ and $l_0^2 = D_M A_{\max}/\alpha$. In this way, we identify three dimensionless positive parameters of the system 6.6, namely $\lambda_1 = \delta\sigma_0^2 A_{\max}^3 M_{\max}$, $\lambda_2 = \zeta A_{\max}/\alpha$, and $\lambda_3 = \beta\sigma_0 M_{\max} A_{\max}/\alpha$. With these definitions, we rewrite Eqs. 6.6 in their dimensionless form

$$\begin{aligned} \partial_\tau m &= \partial_{\chi\chi} m + \lambda_1 (a\cdot m)^2 (1-m) - \lambda_2\ m \\ \partial_\tau a &= 1 - a - \lambda_3\ a\cdot m\ . \end{aligned} \tag{6.7}$$

The equations 6.7 constitute an activator inhibitor (AI) model. Actin is needed for myosin recruitment and thus represents the activator. On the other hand, myosin provides negative feedback to the actin concentration and is consequently the inhibitor. Many other AI models have been discussed in the literature. The most prominent example is probably Turing systems, where the homogeneous steady state can become unstable and evolve towards a stable stationary pattern. This instability is driven by diffusion. However, here we are more interested in dynamic systems. The aforementioned work of Bement and coworkers also describes an AI approach [166]. They consider a system of three species, namely filamentous actin (A), inactive RhoA (RD), active RhoA (RT), where RD mainly provides a pool for RT. RT activates actin polymerization and therefore A. In turn, A drives the equilibrium between RD and RT towards RD, and thus acts as an inhibitor for RT. Further, the activator RT exhibits a positive feedback on its production from RD. The model shows spiral wave patterns in two-dimensional space which are driven from noise fluctuations in A. The system can therefore regarded to be excitable.

Another interesting approach was taken by Kumar et al. who investigate an advection diffusion system of two fluid species A and I. The two are considered as activator (A) and inhibitor (I) for a stress field in the fluid that drives convection of both of them. If the concentration of I is low in a region R, then A induces a high

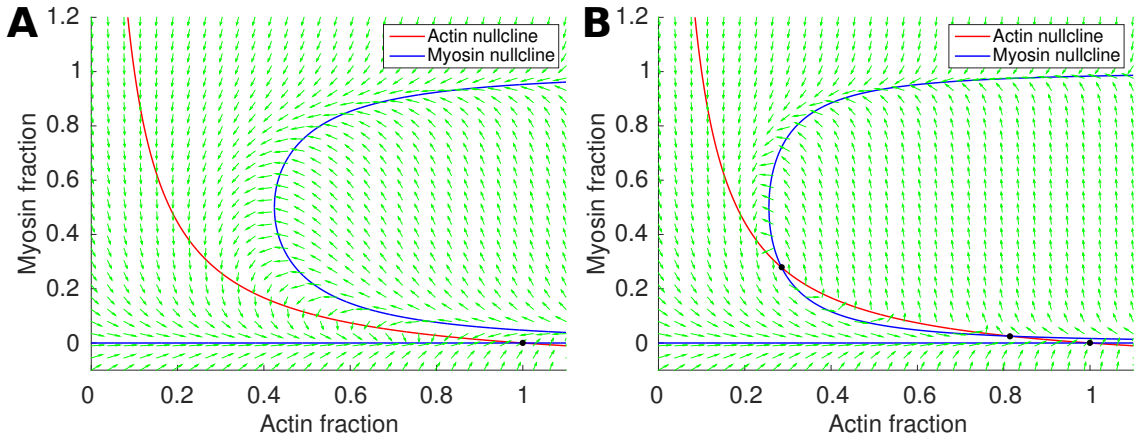

Figure 6.3: Exemplary phase planes for the system 6.7 without diffusive terms. Myosin nullclines are shown as blue lines, actin nullclines are colored in red. The system can exhibit from one (A) up to three FPs (B).

local stress that pulls both A and I into this region. However, A diffuses much faster than I and leaves the region R faster as the stress level decreases. Thus neighboring regions experience an excess of A and follow the same dynamics, pulling A and I out of R. In this way pulsatory patterns arise without reactions between A and I or even intra-species feedback, which means that the total amount of both A and I is conserved individually [171]. However, the AI model pattern is still present. Species A locally leads to higher concentrations of both A and I, which means that A activates both itself and I. At the same time, I predominantly leads to lower A concentration due to the fast diffusion of the latter, thus acting as an inhibitor for A. In this way the system is very similar to the work of Bement and coworkers [166], where the activator also activates the inhibitor and itself, while the inhibitor negatively feeds back on the activator.

The system we propose in Eqs. 6.7 is similar to those systems as actin can be identified as the activator for myosin which in turn inhibits actin. Different from refs. [166, 171], however, not the activator but the inhibitor feeds back positively on itself. We will now evaluate if this system can also give rise to excitability and traveling waves as the one presented by Bement and coworkers [166].

6.2.2 Phase Plane Analysis

In order to develop a deeper understanding of the system 6.7, we investigate the spatially uncoupled system, where we disregard the diffusive term. For this reduced system, we can derive two-dimensional phase plane diagrams. Two examples are shown in Fig. 6.3. For all numerical phase plane calculations we use a custom software implemented in MATLAB. We first determine the nullclines where either

m or a are stationary. In the case of m this amounts to solving the cubic equation $a^2m^2(1-m) - \lambda_2/\lambda_1 m = 0$, where the trivial solution $m = 0$ can be read off immediately. The remaining quadratic equation yields the solutions

$$m_{1,2} = \frac{1}{2}\left(1 \pm \sqrt{1 - \frac{4\lambda_2}{\lambda_1 a^2}}\right) , \tag{6.8}$$

which exist in $\mathbb{R}$ if $a^2 \geq 4\lambda_2/\lambda_1$. As by their definition $a, m \in [0,1]$, these nullclines are only relevant when they cross the square $[0,1] \times [0,1] \in \mathbb{R}^2$. This condition is always fulfilled for the m-coordinate, $m_{1,2} < 1$, but requires $\lambda_1 \geq 4\lambda_2$ for the a coordinate. The actin nullcline is calculated from $1 - a - \lambda_3\ a \cdot m$ and is a shifted hyperbola,

$$m = \lambda_3^{-1}\left(a^{-1} - 1\right) . \tag{6.9}$$

The FPs are defined as the points where the time derivative of both species vanishes, $\partial_\tau m = \partial_\tau a = 0$, which holds true at the intersection points of the nullclines. In this system, either one, two, or three FP exist. The one which is always present is defined by the intersection of the hyperbola with the $m = 0$ line and is located at $P_1 = (a_1, m_1) = (1, 0)$. Additional FPs are defined by the intersections of Eqs. 6.8 and 6.9, which leads to

$$\begin{aligned} \frac{1}{\lambda_3}\left(\frac{1}{a} - 1\right) &= \frac{1}{2}\left(1 \pm \sqrt{1 - \frac{4\lambda_2}{\lambda_1 a^2}}\right) \\ a_{2,3} &= \frac{1}{2}\frac{\lambda_3 + 2}{\lambda_3 + 1} \pm \sqrt{\frac{1}{4}\left(\frac{\lambda_3 + 2}{\lambda_3 + 1}\right)^2 - \frac{\lambda_3^2 \lambda_2/\lambda_1 + 1}{\lambda_3 + 1}} . \end{aligned} \tag{6.10}$$

Eq. 6.10 also provides the criterion to decide how many FPs exists by setting the discriminant equal to zero. This condition simplifies to

$$\bar{\lambda}_1 = 4\lambda_2(1 + \lambda_3) , \tag{6.11}$$

where $\bar{\lambda}_1$ denotes the value for λ_1 where exactly two FPs exist in total. It follows that three FPs are present for the case $\lambda_1 > \bar{\lambda}_1$, and P_1 is the only FP for $\lambda_1 < \bar{\lambda}_1$. We now investigate the location of the FPs and their stability for each of the three cases.

One FP: $\lambda_1 < 4\lambda_2(1 + \lambda_3)$

The location of the the first FP P_1 has already been determined to be $(a_1, m_1) = (1, 0)$. We now investigate its stability using the fact that the full non-linear system

$$\begin{aligned} \dot{m} &= p(m, a) \\ \dot{a} &= q(m, a) \end{aligned} \tag{6.12}$$

has apart from some special cases the same stability properties as its linearized form around the FP $P = (m_P, a_P)$ of interest [172, 173],

$$\begin{aligned} \partial_\tau(m - m_P) &= \left.\frac{\partial p(m,a)}{\partial m}\right|_P (m - m_P) + \left.\frac{\partial p(m,a)}{\partial a}\right|_P (a - a_P) \\ \partial_\tau(a - a_P) &= \left.\frac{\partial q(m,a)}{\partial m}\right|_P (m - m_P) + \left.\frac{\partial q(m,a)}{\partial a}\right|_P (a - a_P) \ . \end{aligned} \tag{6.13}$$

In matrix notation we can rewrite the system 6.13 as $\partial_\tau(m - m_P, a - a_P)^T = J|_P \ (m - m_P, a - a_P)^T$, where J is called the *Jacobian matrix*. We now search for two independent solutions by determining the eigensystem of J. These solutions have the form $\vec{s}_i = \vec{v}_i \ e^{\mu_i t}$, where $\vec{v}_i$ is the eigenvector of J for eigenvalue μ_i.

The Jacobian for the system 6.7 reads

$$J = \begin{pmatrix} \partial_m p & \partial_a p \\ \partial_m q & \partial_a q \end{pmatrix} = \begin{pmatrix} \lambda_1 a^2 m(2 - 3m) - \lambda_2 & 2\lambda_1 a m^2(1 - m) \\ -\lambda_3 a & -1 - \lambda_3 m \end{pmatrix} \ , \tag{6.14}$$

which we can evaluate at P_1 to yield

$$J|_{P_1} = -\begin{pmatrix} \lambda_2 & 0 \\ \lambda_3 & 1 \end{pmatrix} \ . \tag{6.15}$$

The eigenvalues are given by $\mu_1 = -1$ and $\mu_2 = -\lambda_2$, which are both negative since $\lambda_2 > 0$. It follows that all trajectories in the proximity of P_1 approach it, which means P_1 is a stable node for all parameter choices.

Two FPs: $\lambda_1 = 4\lambda_2(1 + \lambda_3)$

Two FPs occur if the hyperbolic a-nullcline touches but not intersects the non-trivial m-nullcline 6.8. This happens if the discriminant in the second part of Eq. 6.10 vanishes, which is equivalent to $\lambda_1 = 4\lambda_2(1 + \lambda_3)$. The a coordinate of the second fixed point, which we will refer to as $P_2 = (m_2, a_2)$, can be read off to be $a_2 = (\lambda_3 + 2)/(2(\lambda_3 + 1))$, and $m_2 = \lambda_3^{-1}(a_2^{-1} - 1) = (\lambda_3 + 2)^{-1}$ follows. Note that the coordinates of P_2 depend only on λ_3, however λ_1, λ_2 have to obey the existence relation for P_2.

In order to assess its stability properties we evaluate the Jacobian 6.14 at P_2,

$$J|_{P_2} = \begin{pmatrix} \frac{\lambda_2\lambda_3}{\lambda_3+1} & 4\lambda_2\frac{\lambda_3+1}{(\lambda_3+2)^2} \\ -\frac{\lambda_3}{2}\frac{\lambda_3+2}{\lambda_3+1} & -2\frac{\lambda_3+1}{\lambda_3+2} \end{pmatrix} \ . \tag{6.16}$$

However, this time the determinant of the Jacobian vanishes, and it therefore exhibits only one non-zero eigenvalue $\mu = \frac{\lambda_2\lambda_3}{\lambda_3+1} - 2\frac{\lambda_3+1}{\lambda_3+2}$. Trajectories in the direction of the corresponding eigenvector approach the FP if $\mu < 0$, i. e. $\lambda_2 < \tilde{\lambda}_2 = \frac{2(\lambda_3+1)^2}{\lambda_3(\lambda_3+2)}$.

This is surely the case if $\lambda_2 \leq 2$, since $\tilde{\lambda}_2 = 2\frac{\lambda_3^2+2\lambda_3+1}{\lambda_3^2+2\lambda_3} > 2$. The eigenvector corresponding to the zero eigenvalue points along the tangent where the two nullclines touch. Stability cannot be inferred from the linear system in this case [173]. Numerical evaluation shows though that it can be both stable (e. g. for $\lambda_1 = 8$, $\lambda_2 = 1$, $\lambda_3 = 1$) or unstable (e. g. for $\lambda_1 = 360$, $\lambda_2 = 9$, $\lambda_3 = 9$).

Three FPs: $\lambda_1 > 4\lambda_2(1+\lambda_3)$

In this case two more FPs $P_3 = (m_3, a_3)$ and $P_4 = (m_4, a_4)$ occur in addition to the first stable fixed point, while P_2 does not exist. Since the a-nullcline is a monotonously decreasing function and the non-trivial m-nullclines are symmetric to the $m = 1/2$ axis, we can always order P_3 and P_4 such that $a_3 > a_4$ and $m_3 < m_4$. In this convention, P_3 is the FP closer to P_1. The coordinates of the FPs evaluate to

$$\begin{aligned} a_{3,4} &= \frac{\lambda_3}{2(\lambda_3+1)}\left(1+\frac{2}{\lambda_3} \pm \sqrt{1-4\frac{\lambda_2}{\lambda_1}(\lambda_3+1)}\right) \\ m_{3,4} &= \frac{1}{\lambda_3}\left(\frac{1}{a_{3,4}}-1\right) \ . \end{aligned} \tag{6.17}$$

Note that both FPs converge towards P_2 for $\lambda_1 \to 4\lambda_2(1+\lambda_3)$.

We first turn towards P_3, whose stability properties will prove to be independent of the parameters. To see this, we calculate the corresponding Jacobian,

$$J|_{P_3} = \begin{pmatrix} \lambda_2\left(1+\frac{1}{\lambda_3+1}\right)+\frac{\lambda_1(q-1)}{2(\lambda_3+1)^2} & -\frac{4\lambda_2(1+\lambda_3)(q-1)}{(2+\lambda_3(q+1))^2} \\ -\frac{\lambda_3(2+\lambda_3(q+1))}{2(\lambda_3+1)} & -\frac{2(\lambda_3+1)}{2+\lambda_3(q+1)} \end{pmatrix} \ . \tag{6.18}$$

Here, $q = \sqrt{1-4\lambda_2/\lambda_1(\lambda_3+1)}$ was used. The exact eigenvalues are rather complex and little insightful, as we are only interested in stability. For this purpose we only need to know whether the eigenvalues are real or complex and whether the sign of its real part is positive or negative. For brevity, we recall that the eigenvalues μ_i of a 2×2 matrix A can be determined by

$$\mu_{1,2} = \frac{1}{2}\left(\mathrm{Tr}A \pm \sqrt{(\mathrm{Tr}A)^2 - 4|A|}\right) \ , \tag{6.19}$$

where $\mathrm{Tr}A$ denotes the trace of A and $|A|$ its determinant. For the Jacobian of interest, the latter evaluates to

$$\left|J|_{P_3}\right| = -\frac{\lambda_1}{2(\lambda_3+1)}\left(1-q^2+\lambda_1(1-q)\right) < 0 \ . \tag{6.20}$$

The inequality holds since $0 < q < 1$ by the condition for the occurrence of three FPs, and $\lambda_i > 0$. As $(\mathrm{Tr}A)^2 \geq 0$, the eigenvalues of the Jacobian at P_3 are always

real numbers. Further, they are of different sign, as the radicand is greater than $(\mathrm{Tr}A)^2$. It follows that P_3 is always a saddle node.

The properties of P_4 are not quite as simple, but give rise to a variety of different behaviors. The corresponding Jacobian is

$$J|_{P_4} = \begin{pmatrix} \frac{\lambda_1(1+q)}{4(1+\lambda_3)^2}\left(\lambda_3(1-q)-2q\right) & \frac{\lambda_1(1-q)(1+q)^2}{(2+\lambda_3(1-q))^2} \\ -\frac{\lambda_3(2+\lambda_3(1-q))}{2(1+\lambda_3)} & -\frac{2(\lambda_3+1)}{2+\lambda_3(1-q)} \end{pmatrix} , \tag{6.21}$$

and its determinant calculates to

$$\left| J|_{P_4} \right| = \frac{\lambda_1 q(q+1)}{2(1+\lambda_3} > 0 \ . \tag{6.22}$$

Thus the real parts of the eigenvalues have the same sign, such that P_4 cannot be a saddle. However, all remaining possibilities are assumed for suitable parameters:

1. $\mathrm{Tr}\ J|_{P_4} > 0$. In this case, the eigenvalues have a positive real part, and P_4 is therefore unstable. More precisely, P_4 is an unstable node if $\left(\mathrm{Tr}\ J|_{P_4}\right)^2 > \left| J|_{P_4} \right|$ and an unstable spiral point if the inequality is inverted.

2. $\mathrm{Tr}\ J|_{P_4} < 0$. As the real part of the eigenvalues is negative, P_4 is either a stable node or stable spiral under the same conditions as above.

3. $\mathrm{Tr}\ J|_{P_4} = 0$. Here, P_4 is a center, since its eigenvalues are purely imaginary.

Fig. 6.4 A shows the different regimes of P_4 stability for $\lambda_2 = \lambda_3$. The red line marks where exactly two FPs occur, $\lambda_1 = 4\lambda_2(1+\lambda_3)$. P_4 only exists above this line. The blue curve marks where $\left(\mathrm{Tr}\ J|_{P_4}\right)^2 = 4\ \left| J|_{P_4} \right|$ is fulfilled and therefore separates real from complex eigenvalues. It segregates unstable nodes (red shaded region) from spirals (blue shaded region). The purple line is found for the same condition as the blue one, but in the regime where P_4 is stable. Thus it separates stable nodes from stable spirals as shown in Fig. 6.4 A (purple and green shaded regions, respectively). The green line is finally obtained by the condition $\mathrm{Tr}A = 0$. It thus separates the phase space in the regions where P_4 is stable (above the green lline) and unstable or non-existent (below). The system is bistable if P_4 is stable, and excitable otherwise. However, excitability measured by the length of trajectory in phase space compared to the initial displacement from the stable FP P_1 may vary for different parameter choices (not shown).

6.2.3 Traveling Pulses

We now reintroduce the diffusive term in the system 6.7 and investigate numerically whether the excitability gives rise to traveling waves. For this purpose we again use the software MATLAB. We prescribe the initial conditions to be ($m(\chi, \tau =$

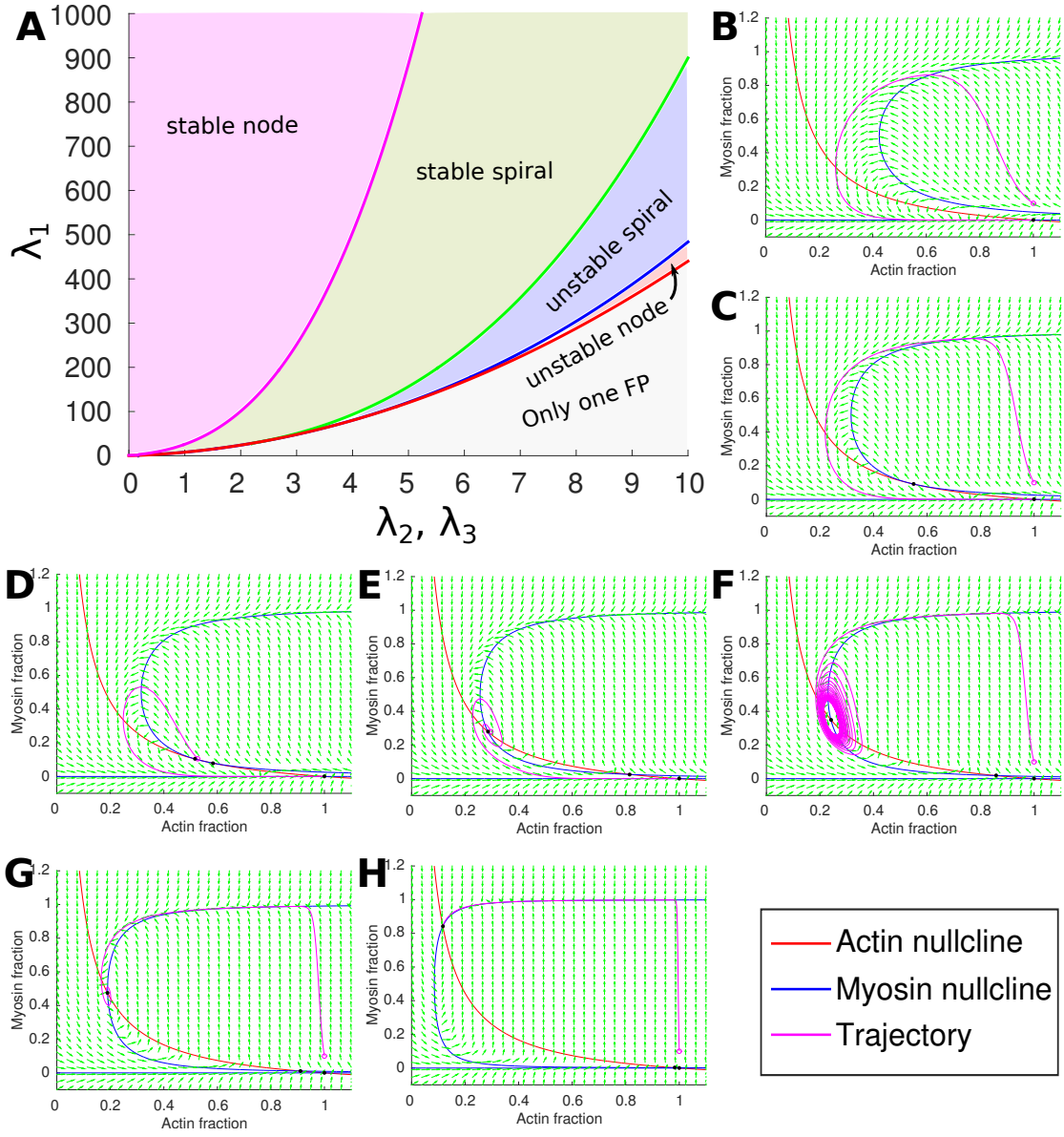

Figure 6.4: Phase space for the stability of P_4 and example trajectories for $\lambda_2 = \lambda_3$. The example phase planes and trajectories are all plotted for $\lambda_2 = \lambda_3 = 9$. (A) Conditions and meaning of the colored lines are explained in the main text. (B, C) The system is excitable if only one ($\lambda_1 = 200$) or two ($\lambda_3 = 360$) FPs exist. The third FP can either be an unstable node (D, $\lambda_1 = 362$), an unstable spiral (E, $\lambda_1 = 550$), a center (F, $\lambda_1 = 682$), a stable spiral (G, $\lambda_1 = 1000$), or a stable node (H, $\lambda_1 = 5000$). The system is bistable if P_4 exists and is stable (F-H), and excitable otherwise (B-E). The starting point of the exemplary trajectory is marked with a purple circle in all phase plane plots. Arrows indicate the direction of the derivative field $(\dot{m}, \dot{a})$.

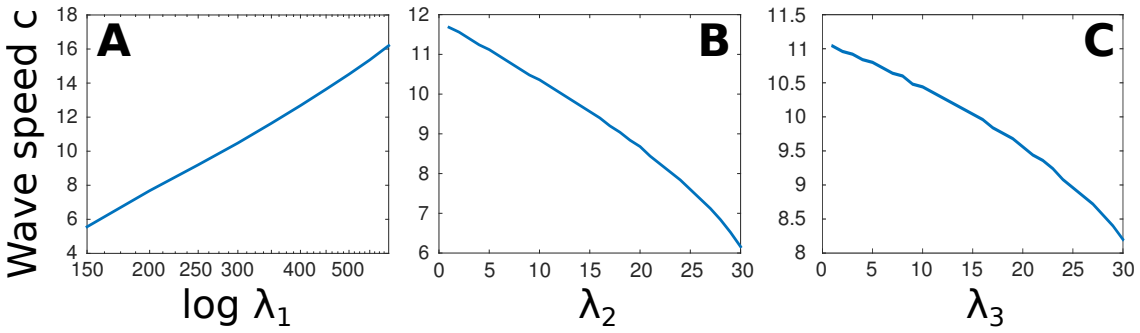

Figure 6.5: Dependence of wave speed c on the parameters λ_i. (A) $\lambda_2 = \lambda_3 = 9$ (B) $\lambda_1 = 300$, $\lambda_3 = 9$ (C) $\lambda_1 = 300$, $\lambda_2 = 9$

$0), a(\chi, \tau = 0)) = ((1-\chi)\Theta(\delta - \chi - 1), 1)$ and numerically observe the development in time and space.

In this way we indeed observe traveling pulses. Fig. 6.6 A shows a representative example. The spatially uncoupled system is excitable, and its phase plane is depicted in Fig. 6.4 B. Once the myosin threshold for following an excited trajectory is passed locally, more myosin is produced before the actin level decreases. The myosin produced in this time span diffuses to neighboring sites, leading to an increase in myosin concentration that excites the system at this site as well. In this way the wave can spread in space and even reoccur periodically when the uncoupled system oscillates (Fig. 6.6 B). However, Fig. 6.6 C, D show that excitability of the local system is not sufficient for pulse propagation. This can be understood in terms of the diffusion constant D_M, which is controlled by the choice of the typical time scale $t_0 = A_{\max}/\alpha$ and length scale $l_0 = \sqrt{D_M t_0}$. If D_M is too low, to few myosin per time arrives from neighboring locations, thus myosin degradation keeps the system below the threshold.

An interesting property of traveling wave fronts and pulses is their speed. While we do not understand the dependence on the parameters λ_i analytically to this point, we can analyze their qualitative influence numerically. As expected, the wave speed increases for higher λ_1, as this parameter is associated with the cooperative myosin accumulation (Fig. 6.5 A). The dependence seems to be logarithmic, which is illustrated by the choice of the logarithmic axis scale. As the two other parameters are linked to either myosin (λ_2) or actin (λ_3) degradation, they both negatively affect wave speed.

6.3 Cell Shape under the Influence of Contractile Rings

We now turn towards the question which shape the starfish oocyte assumes when under a ring-shaped contractile tension. We follow three assumptions in order to model the shape problem:

1. The volume of the oocyte is conserved during the contraction wave.
2. The myosin motor activation leads to an increased tension within the cortex.
3. The cortex acts as an elastic sheet on the time scale of the contraction wave.

While the first two assumptions are valid for many cell types (cf. e. g. [167, 174]), the last one is more difficult. The elasticity of the cortex should depend on the ratio of time scale of typical turn-over (which releases strain) and the time scale of the contraction wave. The latter is on the order of 7 minutes, but experimental observations are still elusive for the former part. We will show that an elastic response reliably reproduces the shapes of the contraction wave sequence. Following the assumptions stated above, the Hamiltonian of the complete system reads $H_{\mathrm{tot}} = H_{\mathrm{elastic}} + H_{\mathrm{active}} + H_{\mathrm{volume}}$, where the first part includes contributions from bending and in-plane deformations, $H_{\mathrm{elastic}} = H_{\mathrm{bending}} + H_{\mathrm{stretch}} + H_{\mathrm{shear}}$. Thus the Hamiltonian is very similar to the one we used to simulate the shapes of RBCs in chapter 2, apart from that we dropped the constraint of constant surface area and added a spatially inhomogeneous active surface tension. Another difference to the RBC Hamiltonian is that we only consider linear elasticity here. Further, we neglect bending effects originating from the difference in area between the two membrane layers and spontaneous curvature. The complete Hamiltonian therefore reads

$$H_{\mathrm{shape}} = 2\kappa_b \int \left(H^2 + \sigma(\vec{x})\right)\ dA + \int \left(\frac{K_\alpha}{2}\alpha^2 + \mu\beta\right)\ dA_0 + \frac{k_V}{2}(V - V_0)^2\ , \quad (6.23)$$

where H denotes the mean curvature, $\sigma(\vec{x})$ the spatially varying surface tension, K_α and μ the stretch and shear modulus, α and β the two strain invariants associated with stretch and strain, k_V the prefactor of the constant volume constraint, and V, V_0 the current and initial volume. Note that the integration for the in-plane elasticity is performed over a reference shape A_0, which in our case is the spherical resting shape of the oocyte. The numerical evaluation is performed with the software SurfaceMaster, which is discussed in chapter 2.

Regarding the parameter choice, the surface tension was found experimentally to be around $\sigma = 1nN/\mu m$ in the presence of the contraction wave, and otherwise well below (Johanna Bischof, personal communication). We therefore assume that the peak active tension generated by myosin motors is also on the order of $1nN/\mu m$ at

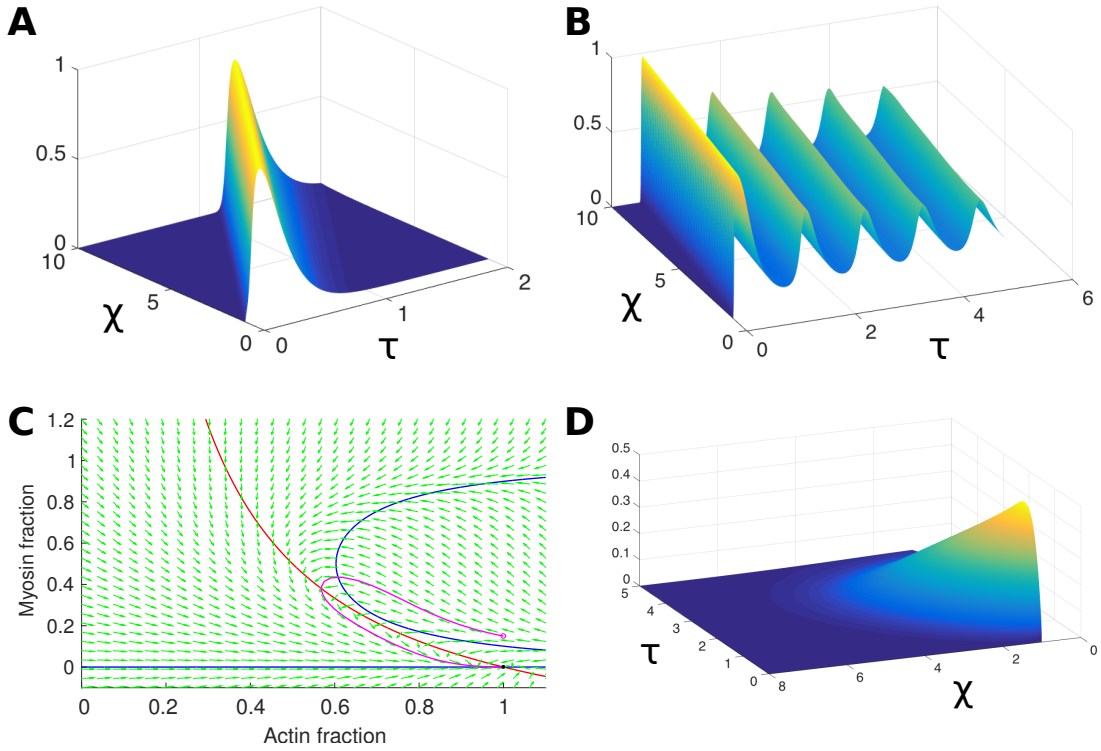

Figure 6.6: Traveling pulses in the excitable media. Single pulses can travel persistently in the system 6.7 (A). If P_3 is a center, we also observe trains of traveling pulses (B). (C), (D) Excitablity is a necessary but not sufficient condition for traveling pulses. The trajectory depicted in (C) can be regarded as excitable, however, an initial pulse decays and does not travel for this parameter setting (D). Parameters choices were $\lambda_2 = \lambda_3 = 9$, $\lambda_1 = 200$ for (A), $\lambda_2 = \lambda_3 = 9$, $\lambda_1 = 682$ for (B), and $\lambda_2 = \lambda_3 = 2$, $\lambda_1 = 22$ for (C), (D).

the peak region and negligible far from the peak. We interpolate between these two levels with a squared cosine function with a period of $w = 100\mu m$, which is a typical lateral extension of the wave in experiments (cf. Fig. 6.2 C). The resting shape and volume are assumed to stem from the spherical shape the oocyte assumes before the contraction wave starts, and k_V is chosen such that $|(V - V_0)/V_0| < 10^{-4}$. The elastic constants can now be fitted by comparing the calculated shapes to the ones measured in experiments. While we assumed $\mu = K_\alpha/2$ like in the case of RBCs, we find that the elastic moduli need to be on the order of $K_\alpha \approx 5 \cdot 10^{-3} J/m^2$, which is 1000-fold higher than for RBCs. Note, however, that starfish oocytes possess a surface area that is about 20.000-fold the one of a RBC. Thus it is a necessity to build a more rigid layer underneath to prevent large deformations on the larger length scales, especially as the oocytes are released to the sea after fertilization and have to resist environmental influences. The resulting shape sequence is shown in Fig. 6.7 and compares well to the experimental observations in Fig. 6.2 C.

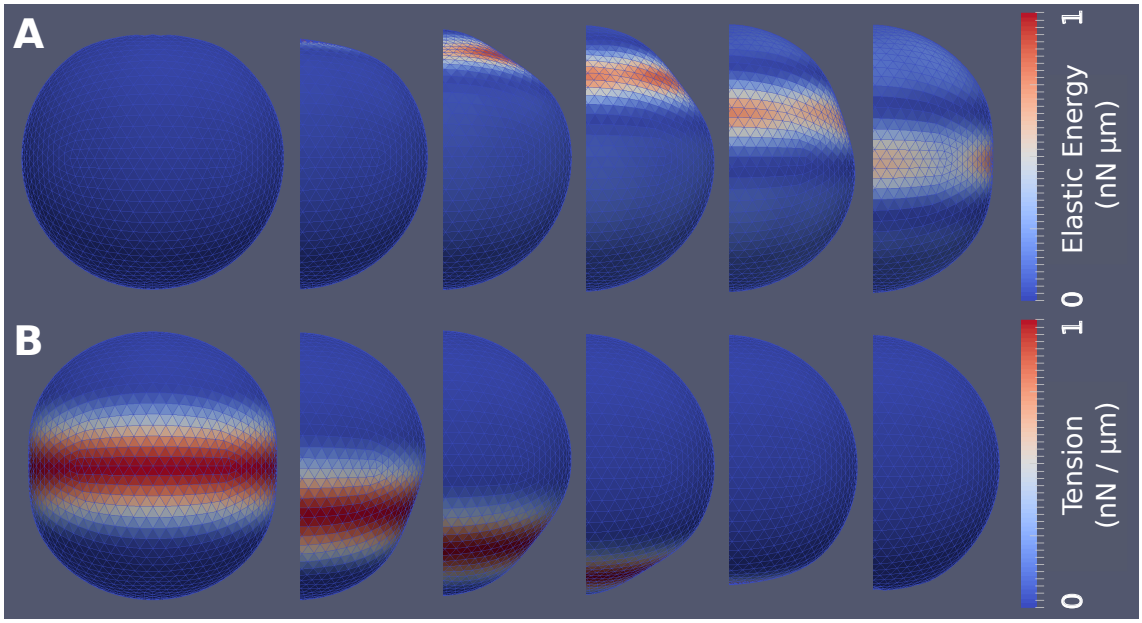

Figure 6.7: Contraction wave in the mechanical model. The active tension follows one period of the function $\sigma(s) = \cos^2(\pi(s - s0)/w)$ symmetric to s_0, where s is the coordinate along the contour measured from the north pole of the sphere, s_0 the mid position of the wave, and $w = 100\mu$ the width of the wave. The color coding shows the in-plane elastic energy stored in the triangle (A) and the surface tension (B).

6.4 Discussion & Outlook

In this chapter we have investigated the cell's cortex as an excitable medium. We first introduced a simple model where we postulated simple interaction kinetics for a filamentous actin network with myosin motor proteins. This model belongs to the class of activator inhibitor models. In contrast to existing models where usually the activator also features auto-activation, in our model this property is set on the inhibitor.

After non-dimensionalization, we thoroughly investigated the phase plane of our model and found that it exhibits either one, two, or three FPs. The first FP P_1 arises from the intersection of the actin nullcline with the trivial myosin solution $m = 0$ and is always stable. In the case of $\lambda_1 = 4\lambda_2 \cdot (\lambda_3 + 1)$, where two FPs exist, we could not determine the stability of the second FP P_2 analytically. Numerically we found both stable and unstable behavior for different parameters. We conjecture that P_2 is stable if the third FP P_4 in the three FP case, which arises for a slight increase of λ_1, is also stable, and that P_2 is unstable otherwise. If all three FPs exist, the one closer to P_1 we called P_3 is always a saddle node. However, the remaining FP P_4 can be everything but a saddle, leading to a rich behavior of the system, including excitability, oscillations, and bistability. We have shown that all

of these behaviors actually occur even if we restrict the model to $\lambda_2 = \lambda_3$ and have investigated the phase space for the two remaining free parameters.

Next we showed that pulses can travel through the system at constant speed if the system is in an excitable state, i. e. P_4 does not exist or is unstable. If conversely P_4 is stable, the system is bistable and only one wave front travels through the system that connects the two stable FPs for $\tau \to \pm\infty$. The experimental situation is clearly that of a pulse though, as we observe that the myosin concentration decreases again behind the propagating wave (cf. Fig. 6.2 C). We also showed that excitability is only a necessary but not sufficient condition for the occurrence of traveling pulses. If the production of myosin is not high enough to lead to sufficient diffusion to neighboring sites, the signal decays over time. Numerical investigation of wave speed has shown the expected results. As λ_1 controls myosin accumulation, it enhances wave speeds. Conversely, λ_2 and λ_3 control myosin and actin degradation, respectively. The wave therefore becomes slower when either of the two is increased.

Recent experimental observations by Johanna Bischof and Peter Lénárt indicate that in the system of starfish oocyte, myosin is more likely to build a feedback loop with the protein RhoA that also controls actin rather than with actin directly. RhoA activity was found to propagate as a single wave front when myosin was suppressed, or as a traveling pulse in the undisturbed oocyte (unpublished data). RhoA further activates myosin through the ROCK pathway (cf. e. g. [80]), thus the role of actin could be reconsidered to be occupied by RhoA. Moreover, the wave speed has been observed to be negatively correlated with the amount of myosin that accumulates at the surface. To include this effect into the model, one could consider contraction-driven convection as in the work of Kumar we discussed in the introduction [171]. The mechanism would be that high myosin concentrations lead to high contraction. Thus convection arises in the direction of highest myosin activity, which works against diffusion that propagates the wave. We leave it to future work to address this problem in detail.

In the last part of this chapter we have shown that surface tension increased in a ring-shaped structure explains the flattening of an elastic cortex. We constrained the volume to be constant at the value of the spherical resting shape of the oocyte. Thus the deviation in shape must result from an increase in surface area, which is driven by the tension gradients and balanced by in-plane elasticity. As the driving tensions are known from experiments to be in the range of $1nN/\mu m$, we could determine the elastic moduli to be on the order of $5 \cdot 10^{-3} N/m^2$, which is three orders of magnitude higher than for RBCs. In the future, it would be interesting to directly couple the reaction diffusion system for the dynamics with the shape equations, as this allowed to investigate the feedback of mechanical distorted space to the chemical system.

7 Summary & Outlook

In this thesis we presented a general framework to model forces and flow in two-dimensional contractile networks. We modeled the networks as two-dimensional surfaces described by triangles and edges embedded in either two- or three-dimensional space. The main results were already discussed at the end of each chapter. Here we summarize our findings and give a short outlook.

In the chapters 3, 4, and 5, we especially considered the heterogeneity introduced to actomyosin networks by thick actin bundles called stress fibers (SFs). In chapter 3, we found that elastic forces are essential for the force balance of peripheral SFs in agreement with the tension elasticity model (TEM) [4]. Refining the TEM, we considered inner SFs that grow from the interior of the cell towards the boundary and connect to inwards curved spanning arcs at the periphery. We compared the model to experiments, where the peripheral SF is severed with a laser. We found that elastic forces in the peripheral SF can be of the same magnitude and higher than active forces generated by myosin motors in individual SFs. Further, the elastic force magnitude not only depends on the active forces and the number of inner SFs connecting to the arc, but also on the locations of the connection points and of the connection angles. Interestingly, we also found that SF elasticity is important in the presence of flow in the interior of the cell as described in chapter 5. There, SFs first contract until elastic forces balance the active tension gradient. However, we found that SFs are viscoelastic, such that the elastic force leads to a persistent flow.

In the absence of tension gradients, the elastic properties of SFs in the interior of the cell are only of minor importance. If an inner SF features a constant active tension along its entire length, it acts as a single active force along each of its straight parts. Thus there is also no flow induced in this situation, because active forces are balanced at each point. We exploited this property in chapter 4, where we used a tension-dominated active cable model to regularize the reconstruction of cellular traction forces in traction force microscopy (TFM) in a novel approach we call model-based TFM (MBTFM). In TFM cells adhere to and deform soft elastic substrates. Solving the inverse problem of elasticity theory, one can infer traction forces from the displacement field of the substrate. However, as this inverse problem is ill-posed, it requires regularization that is usually based on Tikhonov theory. We

briefly discussed how this approach stabilizes reconstruction by altering the operator describing the corresponding forward problem such that the inverse problem becomes well-posed. However, in this framework one has to specify a regularization parameter, whose choice biases the reconstruction result. In MBTFM we take a different approach and combine image processing and biophysical modeling to constrain the solution space for the reconstruction by the construction of the model. Image data is often difficult to analyze, especially in three dimensions. Here new and refined techniques are needed for fast, automatable, and reliable image segmentation. This could facilitate assessing important parameters of cellular mechanics. In MBTFM, we showed that the inverse problem is well-posed on the solution space reduced through image processing and modeling and found that heterogeneous forces along SFs contribute over 80% of total cellular traction force, whereas homogeneous tension in the background adds less than 20% of total traction. We also find that the distribution of tension within single SFs depends on the SF type. Ventral SFs that span between focal adhesions at each end are the strongest, dorsal SFs the weakest, and transverse arcs are on an intermediate level. This is in agreement with recent experimental findings that dorsal SFs do not contain myosin motors and are therefore passive [22]. Transverse arcs do contain myosin II, however they are not directly attached to focal adhesions and therefore cannot transmit tension directly to the extracellular environment.

The finding that SFs are the main active components in the cell is also confirmed by our simulations of flow in the cell in response to a non-homogeneous active tension in chapter 5. Here, striking evidence is given by straight fibers that run outside of the high tension region. If the background network actively contracted due to enhanced myosin activity, the SFs from outside the activation region would get pulled towards the high tension zone. As this is not observed in experiments, we concluded, in agreement with the MBTFM study, that SFs are the main source of contractility in adherent cells. In this way our findings in chapter 5 emphasize the validity of the model assumptions we made for MBTFM. Note that these observations have been made with two different cell types, namely bone cancer cells in MBTFM and connected tissue cells in the flow simulations. The situation needs to be different for cell types that do not develop SFs. It would be interesting to compare force scales of such cells as well as flow directions to the situation we found in cells with many SFs. For cells without SFs it would be appropriate and convenient to apply continuum mechanics and use the finite element method with viscoelastic-plastic bodies. However, new concepts are required for including discrete elements like SFs also in this framework.

Moreover it would be interesting to compare laser ablation experiments, as investigated in chapter 3, and local myosin activation, as described in chapter 5, to more

detail. A marked difference of the two setups is the different time scale of movement. While SF ends retract at the speed of up to $1\mu m/s$ after ablation, the flow speed measured after local myosin activation is typically below $10nm/s$. This indicates that either the difference in active tension in the activated and non-activated regions is small compared to the overall active tension, or that SF extension experiences a much higher viscosity than SF compression. The most likely explanation is that both effects contribute to the difference in the velocities. It would be a substantial advance to combine both experimental techniques in the same setup.

In chapter 3, we also extended the tension elasticity model to three dimensions and found two interesting results. First, in a quasi two-dimensional setup, we found that the enclosed volume condition leads to shapes of peripheral arcs that are not circular but flattened. Interestingly though, we found that the mean curvature along the arc is only slightly affected, and thus the established technique of fitting circles to estimate the ratio of line tension and surface tension is still valid in such assays. In fully three-dimensional scaffolds we find that a model of the whole cell surface as a network of active cables describes cell shape surprisingly well. Moreover, this congruence between model and experiment was achieved for elastic parameters and active tensions that were also estimated for the two-dimensional case in the tension-elasticity model. This indicates that heterogeneities in actomyosin networks become less important in three dimensions. Cells hardly develop SFs in three-dimensional environments, though invaginated arcs are still reinforced in the three-dimensional scaffold experiments. One possible explanation is that cells do not develop a lamellopodium in three-dimensional environments, which seems to be essential for SF formation. However, SF formation is still not completely understood and requires more attention. One step further, the cortex of the initially spherical oocyte we investigated in chapter 6 does not exhibit any structural heterogeneities. We therefore chose an energy description based on triangles rather than edges for the flattened shapes we observed during the contraction wave. We found that a localized contractile ring working against an elastic hull explains the global shape changes at the different stages of the contraction wave. To account for the wave dynamics, we proposed an activator inhibitor model for the excitable nature of the cortex. Different to other models, in our model the inhibitor instead of the activator is self-enhancing, which still yields an excitable system for a wide range of parameters. In future work we will address the counterintuitive observation that the contraction wave slows down when it becomes stronger. As discussed in chapter 6, a possible ansatz would be to account for convection due to stress gradients that counteract diffusion.

Bibliography

[1] Adam J. Engler, Shamik Sen, H. Lee Sweeney, and Dennis E. Discher. "Matrix Elasticity Directs Stem Cell Lineage Specification". In: *Cell* 126.4 (2006), pp. 677–689. ISSN: 00928674. DOI: 10.1016/j.cell.2006.06.044.

[2] C S Chen, M Mrksich, S Huang, G M Whitesides, and D E Ingber. "Geometric control of cell life and death." In: *Science (New York, N.Y.)* 276.5317 (1997), pp. 1425–1428. ISSN: 00368075. DOI: 10.1126/science.276.5317.1425.

[3] *Wikipedia*. URL: en.wikipedia.org.

[4] Ilka B Bischofs, Franziska Klein, Dirk Lehnert, Martin Bastmeyer, and Ulrich S Schwarz. "Filamentous network mechanics and active contractility determine cell and tissue shape." In: *Biophysical journal* 95.7 (2008), pp. 3488–96. ISSN: 1542-0086. DOI: 10.1529/biophysj.108.134296. URL: http://www.pubmedcentral.nih.gov/articlerender.fcgi?artid=2547424&tool=pmcentrez&rendertype=abstract.

[5] Brendon M. Baker, Britta Trappmann, William Y. Wang, Mahmut S. Sakar, Iris L. Kim, Vivek B. Shenoy, Jason A. Burdick, and Christopher S. Chen. "Cell-mediated fibre recruitment drives extracellular matrix mechanosensing in engineered fibrillar microenvironments". In: *Nature Materials* 14.12 (2015), pp. 1262–1268. ISSN: 1476-1122. DOI: 10.1038/nmat4444. URL: http://www.nature.com/doifinder/10.1038/nmat4444.

[6] Narla Mohandas and Patrick G Gallagher. "Red cell membrane: past, present, and future". In: *Blood* 112.10 (2008), pp. 3939–3948. ISSN: 0006-4971. DOI: 10.1182/blood-2008-07-161166. URL: http://www.bloodjournal.org/cgi/doi/10.1182/blood-2008-07-161166.

[7] Alexandra M. Greiner, Benjamin Richter, and Martin Bastmeyer. "Micro-Engineered 3D Scaffolds for Cell Culture Studies". In: *Macromolecular Bioscience* 12.10 (2012), pp. 1301–1314. ISSN: 16165187. DOI: 10.1002/mabi.201200132. URL: http://doi.wiley.com/10.1002/mabi.201200132.

[8] A. Saha, M. Nishikawa, M. Behrndt, C. P. Heisenberg, F. Jülicher, and S. W. Grill. "Determining physical properties of the cell cortex". In: *arXiv preprint* (2015), pp. 1–17. arXiv: 1507.00511. URL: http://arxiv.org/abs/1507.00511.

[9] Narla Mohandas and Xiuli An. "Malaria and Human Red Blood Cells". In: *Med Microbiol Immunol.* 201.4 (2013), pp. 593–598. DOI: 10.1007/s00430-012-0272-z.Malaria.

[10] Ilka Bischofs, Sebastian Schmidt, and Ulrich Schwarz. "Effect of Adhesion Geometry and Rigidity on Cellular Force Distributions". In: *Physical Review Letters* 103.4 (2009), p. 048101. ISSN: 0031-9007. DOI: 10.1103/PhysRevLett.103.048101. URL: http://link.aps.org/doi/10.1103/PhysRevLett.103.048101.

[11] Ekta Seth Chhabra and Henry N Higgs. "The many faces of actin: matching assembly factors with cellular structures." In: *Nature cell biology* 9.10 (2007), pp. 1110–1121. ISSN: 1465-7392. DOI: 10.1038/ncb1007-1110.

[12] Bruce Alberts, Alexander Johnson, Julian Lewis, David Morgan, Martin Raff, Keith Roberts, and Peter Walter. *Molecular Biology of the Cell.* Sixth edit. New York: Garland Science, Taylor & Francis Group, LLC, 2015. ISBN: 978-0-8153-4432-2.

[13] F. Gittes. "Flexural rigidity of microtubules and actin filaments measured from thermal fluctuations in shape". In: *The Journal of Cell Biology* 120.4 (1993), pp. 923–934. ISSN: 0021-9525. DOI: 10.1083/jcb.120.4.923. URL: http://www.jcb.org/cgi/doi/10.1083/jcb.120.4.923.

[14] Michael A Welte. "Bidirectional Transport along Microtubules". In: *Current Biology* 14.13 (2004), R525–R537. ISSN: 09609822. DOI: 10.1016/j.cub.2004.06.045. URL: http://linkinghub.elsevier.com/retrieve/pii/S0960982204004506.

[15] Johanna Block, Viktor Schroeder, Paul Pawelzyk, Norbert Willenbacher, and Sarah Köster. "Physical properties of cytoplasmic intermediate filaments". In: *Biochimica et Biophysica Acta (BBA) - Molecular Cell Research* 1853.11 (2015), pp. 3053–3064. ISSN: 01674889. DOI: 10.1016/j.bbamcr.2015.05.009. URL: http://linkinghub.elsevier.com/retrieve/pii/S016748891500155X.

[16] M Bishr Omary, Pierre a Coulombe, and W H Irwin McLean. "Intermediate filament proteins and their associated diseases." In: *The New England journal of medicine* 351.20 (2004), pp. 2087–2100. ISSN: 1533-4406. DOI: 10.1056/NEJMra040319.

[17] Rob Phillips. *Physical biology of the cell.* 2. ed. London [u.a.]: Garland Science, 2013, XXX, 1057 S. ISBN: 978-0-8153-4450-6.

[18] Beáta Bugyi and Marie-France Carlier. "Control of Actin Filament Treadmilling in Cell Motility". In: *Annual Review of Biophysics* 39.1 (2010), pp. 449–470. ISSN: 1936-122X. DOI: 10.1146/annurev-biophys-051309-103849.

URL: http://www.annualreviews.org/doi/abs/10.1146/annurev-biophys-051309-103849.

[19] Pirta Hotulainen and Pekka Lappalainen. "Stress fibers are generated by two distinct actin assembly mechanisms in motile cells." In: *The Journal of cell biology* 173.3 (2006), pp. 383–94. ISSN: 0021-9525. DOI: 10.1083/jcb.200511093. URL: http://www.pubmedcentral.nih.gov/articlerender.fcgi?artid=2063839&tool=pmcentrez&rendertype=abstract.

[20] Benjamin Geiger, Joachim P Spatz, and Alexander D Bershadsky. "Environmental sensing through focal adhesions." In: *Nature Reviews. Molecular Cell Biology* 10.1 (2009), pp. 21–33. ISSN: 1471-0080. DOI: 10.1038/nrm2593.

[21] Elena Kassianidou and Sanjay Kumar. "A biomechanical perspective on stress fiber structure and function". In: *Biochimica et Biophysica Acta (BBA) - Molecular Cell Research* (2015). ISSN: 01674889. DOI: 10.1016/j.bbamcr.2015.04.006. URL: http://linkinghub.elsevier.com/retrieve/pii/S0167488915001251.

[22] Bianca Kovac, Jessica L Teo, Tomi P Mäkelä, and Tea Vallenius. "Assembly of non-contractile dorsal stress fibers requires α-actinin-1 and Rac1 in migrating and spreading cells." In: *Journal of Cell Science* 126.Pt 1 (2013), pp. 263–273. ISSN: 1477-9137. DOI: 10.1242/jcs.115063.

[23] Sanjay Kumar, Iva Z Maxwell, Alexander Heisterkamp, Thomas R Polte, Tanmay P Lele, Matthew Salanga, Eric Mazur, and Donald E Ingber. "Viscoelastic retraction of single living stress fibers and its impact on cell shape, cytoskeletal organization, and extracellular matrix mechanics." In: *Biophysical Journal* 90.10 (2006), pp. 3762–3773. ISSN: 0006-3495. DOI: 10.1529/biophysj.105.071506.

[24] Achim Besser, Julien Colombelli, Ernst H K Stelzer, and Ulrich S. Schwarz. "Viscoelastic response of contractile filament bundles". In: *Physical Review E* 83.5 (2011), p. 051902. ISSN: 1539-3755. DOI: 10.1103/PhysRevE.83.051902. arXiv: 1102.5295. URL: http://link.aps.org/doi/10.1103/PhysRevE.83.051902.

[25] Philipp J Albert, Thorsten Erdmann, and Ulrich S Schwarz. "Poster: Stochastic dynamics and mechanosensitivity of myosin II minifilaments". In: *CellMech 2015*. Barcelona, 2015.

[26] Ulrich S. Schwarz and Samuel A. Safran. "Physics of adherent cells". In: *Rev. Mod. Phys.* 85 (3 2013), pp. 1327–1381. DOI: 10.1103/RevModPhys.85.1327. URL: http://link.aps.org/doi/10.1103/RevModPhys.85.1327.

[27] F Graner and J a Glazier. “Simulation of Biological Cell Sorting Using Two-Dimensiona Extended Potts Model”. In: *Physical Review Letters* 69.13 (1992), pp. 2013–2016. ISSN: 0031-9007. DOI: 10.1103/PhysRevLett.70.694. arXiv: 0000135489. URL: http://link.aps.org/doi/10.1103/PhysRevLett.69.2013.

[28] Benoit Vianay, Jos Käfer, Emmanuelle Planus, Marc Block, François Graner, and Hervé Guillou. “Single cells spreading on a protein lattice adopt an energy minimizing shape”. In: *Physical Review Letters* 105.SEPTEMBER (2010), pp. 3–6. ISSN: 00319007. DOI: 10.1103/PhysRevLett.105.128101.

[29] Philipp J Albert and Ulrich S Schwarz. “Dynamics of cell shape and forces on micropatterned substrates predicted by a cellular Potts model.” In: *Biophysical journal* 106.11 (2014), pp. 2340–52. ISSN: 1542-0086. DOI: 10.1016/j.bpj.2014.04.036.

[30] Philipp J Albert. “Modeling Cell Dynamics on Micropatterned Substrates with a Cellular Potts Model”. PhD thesis. 2014. ISBN: 9788578110796. DOI: 10.1017/CBO9781107415324.004. arXiv: arXiv:1011.1669v3.

[31] Patrick W. Oakes, Shiladitya Banerjee, M. Cristina Marchetti, and Margaret L. Gardel. “Geometry Regulates Traction Stresses in Adherent Cells”. In: *Biophysical Journal* 107.4 (2014), pp. 825–833. ISSN: 00063495. DOI: 10.1016/j.bpj.2014.06.045. URL: http://www.sciencedirect.com/science/article/pii/S0006349514007176http://linkinghub.elsevier.com/retrieve/pii/S0006349514007176.

[32] Vikram S Deshpande, Robert M McMeeking, and Anthony G Evans. “A bio-chemo-mechanical model for cell contractility.” In: *Proceedings of the National Academy of Sciences of the United States of America* 103.38 (2006), pp. 14015–20. ISSN: 0027-8424. DOI: 10.1073/pnas.0605837103. URL: http://www.pubmedcentral.nih.gov/articlerender.fcgi?artid=1560932&tool=pmcentrez&rendertype=abstract.

[33] Wolfgang Helfrich. “Elastic Properties of Lipid Bilayers - Theory and Possible Experiments”. In: *Z. Naturfosch. C* 28 (1973), pp. 693–703.

[34] Udo Seifert. *Configurations of fluid membranes and vesicles*. Vol. 46. 1. 1997, pp. 13–137. ISBN: 0001873970. DOI: 10.1080/00018739700101488. arXiv: 9809043v1 [arXiv:cond-mat].

[35] W J Lewis. *Tension structures : form and behaviour*. London: Thomas Telford, 2003. ISBN: 978-0727732361.

[36] Binbing Wang. *Free-standing tension structures*. London ; New York: Spon Press, 2004, p. 1 v. ISBN: 0-203-42049-7. URL: http://www.netlibrary.com/urlapi.asp?action=summary&v=1&bookid=115690.

[37] Jost-Hinrich Eschenburg and Jürgen Jost. *Differentialgeometrie und Minimalflächen*. 2., vollst. Berlin ; Heidelberg [u.a.]: Springer, 2007, XV, 256 S. ISBN: 978-3-540-22227-9.

[38] L. Giomi and L. Mahadevan. "Minimal surfaces bounded by elastic lines". In: *Proceedings of the Royal Society A: Mathematical, Physical and Engineering Sciences* 468.2143 (2012), pp. 1851–1864. ISSN: 1364-5021. DOI: 10.1098/rspa.2011.0627. URL: http://rspa.royalsocietypublishing.org/cgi/doi/10.1098/rspa.2011.0627.

[39] Gerhard Dziuk and Charles M. Elliott. "Finite element methods for surface PDEs". In: *Acta Numerica* 22.April 2013 (2013), pp. 289–396. ISSN: 0962-4929. DOI: 10.1017/S0962492913000056. URL: http://www.journals.cambridge.org/abstract_S0962492913000056.

[40] D Weaire and R Phelan. "The physics of foam". In: *Journal of Physics: Condensed Matter* 8.47 (1999), pp. 9519–9524. ISSN: 0953-8984. DOI: 10.1088/0953-8984/8/47/055.

[41] P G de Gennes. "Wetting: statics and dynamics". In: *Reviews of Modern Physics* 57.3 (1985).

[42] P Lenz and R Lipowsky. "Stability of droplets and channels on homogeneous and structured surfaces". In: *The European Physical Journal E* 262 (2000), pp. 249–262.

[43] Udo Seifert, Karin Berndl, and Reinhard Lipowsky. "Shape transformations of vesicles: Phase diagram for spontaneous- curvature and bilayer-coupling models". In: 44.2 (1991), pp. 1182–1202.

[44] P B Canham. "The minimum energy of bending as a possible explanation of the biconcave shape of the human red blood cell." In: *Journal of theoretical biology* 26.1 (1970), pp. 61–81. ISSN: 0022-5193. URL: http://www.ncbi.nlm.nih.gov/pubmed/5411112.

[45] Gerald Lim H W, Michael Wortis, and Ranjan Mukhopadhyay. "Stomatocyte-discocyte-echinocyte sequence of the human red blood cell: evidence for the bilayer- couple hypothesis from membrane mechanics." In: *Proceedings of the National Academy of Sciences of the United States of America* 99.26 (2002), pp. 16766–9. ISSN: 0027-8424. DOI: 10.1073/pnas.202617299. URL: http://www.pubmedcentral.nih.gov/articlerender.fcgi?artid=139218&tool=pmcentrez&rendertype=abstract.

[46] Gerhard Gompper and Michael Schick, eds. *Lipid bilayers and red blood cells*. Weinheim: Wiley-VCH, 2008, XI, 254 S. ISBN: 978-3-527-31502-4.

[47] Ling Miao, Udo Seifert, Michael Wortis, and Hans Günther Döbereiner. "Budding transitions of fluid-bilayer vesicles: The effect of area-difference elasticity". In: *Physical Review E* 49.6 (1994), pp. 5389–5407. ISSN: 1063651X. DOI: 10.1103/PhysRevE.49.5389.

[48] K Berndl, J Käs, R Lipowsky, E Sackmann, and U Seifert. "Shape Transformations of Giant Vesicles: Extreme Sensitivity to Bilayer Asymmetry". In: *Europhysics Letters (EPL)* 13.December (2007), pp. 659–664. ISSN: 0295-5075. DOI: 10.1209/0295-5075/13/7/015.

[49] Serge Dmitrieff and François Nédélec. "Membrane Mechanics of Endocytosis in Cells with Turgor". In: *PLOS Computational Biology* 11.10 (2015). Ed. by Helge Ewers, e1004538. ISSN: 1553-7358. DOI: 10.1371/journal.pcbi.1004538. arXiv: arXiv:1509.00698v1. URL: http://dx.plos.org/10.1371/journal.pcbi.1004538.

[50] Sebastian Knoche and Jan Kierfeld. "Buckling of spherical capsules". In: *Physical Review E* 84.4 (2011), pp. 1–13. ISSN: 1539-3755. DOI: 10.1103/PhysRevE.84.046608. URL: http://link.aps.org/doi/10.1103/PhysRevE.84.046608.

[51] Pierre a Haas and Raymond E Goldstein. "Elasticity and Glocality: Initiation of Embryonic Inversion in Volvox". In: *arXiv preprint* d (2015). arXiv: 1507.01439. URL: http://arxiv.org/abs/1507.01439.

[52] Khaled Khairy, JiJinn Foo, and Jonathon Howard. "Shapes of Red Blood Cells: Comparison of 3D Confocal Images with the Bilayer-Couple Model". In: *Cellular and Molecular Bioengineering* 1.2-3 (2008), pp. 173–181. ISSN: 1865-5025. DOI: 10.1007/s12195-008-0019-5.

[53] Stanley Osher and Ronald Fedkiw. *Level set methods and dynamic implicit surfaces*. Applied mathematical sciences ; 153 ; Applied mathematical sciences 153. New York ; Berlin ; Heidelberg: Springer, 2003, XIII, 273 S., [8] Bl. ISBN: 0-387-95482-1 ; 978-0-387-95482-0.

[54] Milan Sonka, Václav Hlaváč, and Roger Boyle. *Image processing, analysis, and machine vision*. 3. ed., [N. International student edition. Stamford, Conn.: Cengage Learning, 2008, XXV, 829 S. ISBN: 978-0-495-24438-7 ; 0-495-24438-4.

[55] Jc Cuillière. "An adaptive method for the automatic triangulation of 3D parametric surfaces". In: *Computer-Aided Design* 30.2 (1998), pp. 139–149. ISSN: 00104485. DOI: 10.1016/S0010-4485(97)00085-7. URL: http://linkinghub.elsevier.com/retrieve/pii/S0010448597000857.

[56] Kenneth A Brakke. "The Surface Evolver". In: *Experimental Mathematics* 1.2 (1992), pp. 141–165.

[57] *VTK File Formats*. URL: http://www.vtk.org/VTK/img/file-formats.pdf.

[58] Wolfgang Wintz. "Starke Formänderung von Membranen". PhD thesis. University of Potsdam, 1997.

[59] Eric Freeman and Elisabeth Freeman. *Head first design patterns*. 1. ed. Beijing ; Köln [u.a.]: O'Reilly, 2004, XXXVI, 638 S. ISBN: 0-596-00712-4 ; 978-0-596-00712-6.

[60] Charles D Hansen and Chris R Johnson. *The visualization handbook*. Burlington, MA: Elsevier-Butterworth Heinemann, Online–Ressource (xvii, 962, [80] p.) ISBN: 0-12-387582-X ; 978-0-12-387582-2. URL: http://proquest.tech.safaribooksonline.de/9780123875822;.

[61] Frank Jülicher. "The Morphology of Vesicles of Higher Topological Genus: Conformal Degeneracy and Conformal Modes". In: *Journal de Physique II* 6.1797 (1996).

[62] William H Press, Saul A Teukolsky, William T Vetterling, and Brian P Flannery. *Numerical recipes*. Ed. by William H [Hrsg.] Press, Saul A [Hrsg.] Teukolsky, William T [Hrsg.] Vetterling, and Brian P [Hrsg.] Flannery. 3rd ed. Cambridge [u.a.]: Cambridge Univ. Press, 2007, XXI, 1235 S. ISBN: 978-0-521-88407-5 ; 978-0-521-70685-8.

[63] Mark E J Newman and Gerard T Barkema. *Monte Carlo methods in statistical physics*. Oxford [u.a.]: Clarendon Press, 1999, XIV, 475 S. ISBN: 0-19-851797-1 ; 0-19-851796-3 ; 978-0-19-851797-9 ; 978-0-19-851796-2.

[64] Reinhard Lipowsky and Erich Sackmann, eds. *Structure and dynamics of membranes*. Handbook of biological physics ; 1. Amsterdam: North-Holland, 1995, p. 1052. ISBN: 0-444-81975-4 ; 978-0-444-81975-8.

[65] H J Deuling and W Helfrich. "Red blood cell shapes as explained on the basis of curvature elasticity." In: *Biophysical journal* 16.8 (1976), pp. 861–868. ISSN: 00063495. DOI: 10.1016/S0006-3495(76)85736-0.

[66] L D Landau and E M Lifschitz. *Lehrbuch der Theoretischen Physik, Elasticitätstheorie*. Vol. 7. Akademie-Verlag, 1983.

[67] J L Van Hemmen. "Theoretische Membranphysik : vom Formenreichtum der Vesikel". In: *Lecture Notes* (2001).

[68] Ranjan Mukhopadhyay, H.W. Gerald Lim, and Michael Wortis. "Echinocyte Shapes: Bending, Stretching, and Shear Determine Spicule Shape and Spacing". In: *Biophysical Journal* 82.4 (2002), pp. 1756–1772. ISSN: 00063495. DOI: 10.1016/S0006-3495(02)75527-6. URL: http://linkinghub.elsevier.com/retrieve/pii/S0006349502755276.

[69] Aleš Iglič. "A possible mechanism determining the stability of spiculated red blood cells". In: *Journal of Biomechanics* 30.1 (1997), pp. 35–40. ISSN: 00219290. DOI: 10.1016/S0021-9290(96)00100-5. URL: http://www.sciencedirect.com/science/article/pii/S0021929096001005\nhttp://www.ncbi.nlm.nih.gov/pubmed/8970922http://linkinghub.elsevier.com/retrieve/pii/S0021929096001005.

[70] Christophe Geuzaine and Jean-François Remacle. "Gmsh: A 3-D finite element mesh generator with built-in pre- and post-processing facilities". In: *International Journal for Numerical Methods in Engineering* 79.11 (2009), pp. 1309–1331. ISSN: 00295981. DOI: 10.1002/nme.2579. URL: http://doi.wiley.com/10.1002/nme.2579.

[71] Caroline a Schneider, Wayne S Rasband, and Kevin W Eliceiri. "NIH Image to ImageJ: 25 years of image analysis". In: *Nature Methods* 9.7 (2012), pp. 671–675. ISSN: 1548-7091. DOI: 10.1038/nmeth.2089. URL: http://www.nature.com/doifinder/10.1038/nmeth.2089.

[72] Manuel Théry, Victor Racine, Anne Pépin, Matthieu Piel, Yong Chen, Jean-Baptiste Sibarita, and Michel Bornens. "The extracellular matrix guides the orientation of the cell division axis". In: *Nature Cell Biology* 7.10 (2005), pp. 947–953. ISSN: 1465-7392. DOI: 10.1038/ncb1307. URL: http://www.nature.com/doifinder/10.1038/ncb1307.

[73] Manuel Théry, Andrea Jiménez-Dalmaroni, Victor Racine, Michel Bornens, and Frank Jülicher. "Experimental and theoretical study of mitotic spindle orientation". In: *Nature* 447.7143 (2007), pp. 493–496. ISSN: 0028-0836. DOI: 10.1038/nature05786. URL: http://www.nature.com/doifinder/10.1038/nature05786.

[74] Andrea Jime, Victor Racine, Michel Bornens, Frank Ju, Manuel Théry, Andrea Jiménez-Dalmaroni, Frank Jülicher, and Manuel Thery. "Experimental and theoretical study of mitotic spindle orientation". In: *Nature* 447.7143 (2007), pp. 493–496. ISSN: 1476-4687. DOI: 10.1038/nature05786. URL: http://www.nature.com/doifinder/10.1038/nature05786\npapers2://publication/doi/10.1038/nature05786\nhttp://www.ncbi.nlm.nih.gov/pubmed/17495931\nhttp://www.nature.com/nature/journal/v447/n7143/full/nature05786.html.

[75] Timothée Vignaud, Laurent Blanchoin, and Manuel Théry. "Directed cytoskeleton self-organization." In: *Trends in cell biology* 22.12 (2012), pp. 671–82. ISSN: 1879-3088. DOI: 10.1016/j.tcb.2012.08.012. URL: http://www.ncbi.nlm.nih.gov/pubmed/23026031.

[76] Manuel Théry, Anne Pépin, Emilie Dressaire, Yong Chen, and Michel Bornens. "Cell distribution of stress fibres in response to the geometry of the adhesive environment". In: *Cell Motility and the Cytoskeleton* 63.6 (2006), pp. 341–355. ISSN: 08861544. DOI: 10.1002/cm.20126. URL: http://doi.wiley.com/10.1002/cm.20126.

[77] Sari Tojkander, Gergana Gateva, and Pekka Lappalainen. "Actin stress fibers–assembly, dynamics and biological roles." In: *Journal of cell science* 125.Pt 8 (2012), pp. 1855–64. ISSN: 1477-9137. DOI: 10.1242/jcs.098087. URL: http://www.ncbi.nlm.nih.gov/pubmed/22544950.

[78] P. Guthardt Torres, I. B. Bischofs, and U. S. Schwarz. "Contractile network models for adherent cells". In: *Physical Review E* 85.1 (2012), p. 011913. ISSN: 1539-3755. DOI: 10.1103/PhysRevE.85.011913. URL: http://link.aps.org/doi/10.1103/PhysRevE.85.011913.

[79] Philip Guthardt Torres. "Modeling Shape and Rupture of Filament Networks". PhD thesis. Facultiy for Physics and Astronomy, Heidelberg University, 2012.

[80] Stéphanie Pellegrin and Harry Mellor. "Actin stress fibres." In: *Journal of cell science* 120.Pt 20 (2007), pp. 3491–9. ISSN: 0021-9533. DOI: 10.1242/jcs.018473. URL: http://www.ncbi.nlm.nih.gov/pubmed/17928305.

[81] M S Zand and G Albrecht-Buehler. "What structures, besides adhesions, prevent spread cells from rounding up?" In: *Cell motility and the cytoskeleton* 13.3 (1989), pp. 195–211. ISSN: 0886-1544. DOI: 10.1002/cm.970130307. URL: http://www.ncbi.nlm.nih.gov/pubmed/2505936.

[82] Ching-Wei Chang and Sanjay Kumar. "Vinculin tension distributions of individual stress fibers within cell-matrix adhesions." In: *Journal of cell science* 126.Pt 14 (2013), pp. 3021–30. ISSN: 1477-9137. DOI: 10.1242/jcs.119032. URL: http://www.pubmedcentral.nih.gov/articlerender.fcgi?artid=3711198&tool=pmcentrez&rendertype=abstract.

[83] Julien Colombelli, Achim Besser, Holger Kress, Emmanuel G Reynaud, Philippe Girard, Emmanuel Caussinus, Uta Haselmann, John V Small, Ulrich S Schwarz, and Ernst H K Stelzer. "Mechanosensing in actin stress fibers revealed by a close correlation between force and protein localization." In: *Journal of Cell Science* 122 (2009), pp. 1665–1679. ISSN: 0021-9533. DOI: 10.1242/jcs.042986.

[84] Keith Burridge and Erika S Wittchen. "The tension mounts: stress fibers as force-generating mechanotransducers." In: *The Journal of cell biology* 200.1 (2013), pp. 9–19. ISSN: 1540-8140. DOI: 10.1083/jcb.201210090. URL: http:

//www.pubmedcentral.nih.gov/articlerender.fcgi?artid=3542796&tool=pmcentrez&rendertype=abstract.

[85] Sam Walcott and Sean X Sun. "A mechanical model of actin stress fiber formation and substrate elasticity sensing in adherent cells." In: *Proceedings of the National Academy of Sciences of the United States of America* 107.17 (2010), pp. 7757–7762. ISSN: 0027-8424. DOI: 10.1073/pnas.0912739107.

[86] Roland Kaunas, Phu Nguyen, Shunichi Usami, and Shu Chien. "From The Cover: Cooperative effects of Rho and mechanical stretch on stress fiber organization". In: *Proceedings of the National Academy of Sciences* 102.44 (2005), pp. 15895–15900. ISSN: 0027-8424. DOI: 10.1073/pnas.0506041102. URL: http://www.pnas.org/content/102/44/15895.longhttp://www.pnas.org/cgi/doi/10.1073/pnas.0506041102.

[87] Achim Besser. "Modeling the Coupling of Mechanics and Biochemistry in Cell Adhesion". PhD thesis. 2009.

[88] Kandice Tanner, Aaron Boudreau, Mina J Bissell, and Sanjay Kumar. "Dissecting regional variations in stress fiber mechanics in living cells with laser nanosurgery." In: *Biophysical journal* 99.9 (2010), pp. 2775–83. ISSN: 1542-0086. DOI: 10.1016/j.bpj.2010.08.071. URL: http://www.pubmedcentral.nih.gov/articlerender.fcgi?artid=2965957&tool=pmcentrez&rendertype=abstract.

[89] Mirjam Mayer, Martin Depken, Justin S Bois, Frank Jülicher, Stephan W Grill, Mirjam Mayer, Martin Depken, Justin S Bois, Frank Ju, Frank Jülicher, and Stephan W Grill. "Anisotropies in cortical tension reveal the physical basis of polarizing cortical flows." In: *Nature* 467.7315 (2010), pp. 617–21. ISSN: 1476-4687. DOI: 10.1038/nature09376. arXiv: 77957364208. URL: http://www.ncbi.nlm.nih.gov/pubmed/20852613.

[90] Lan Lu, Sara J Oswald, Hai Ngu, and Frank C-P Yin. "Mechanical properties of actin stress fibers in living cells." In: *Biophysical journal* 95.12 (2008), pp. 6060–6071. ISSN: 00063495. DOI: 10.1529/biophysj.108.133462. URL: http://dx.doi.org/10.1529/biophysj.108.133462.

[91] Jérôme R. D. Soiné, Christoph a. Brand, Jonathan Stricker, Patrick W. Oakes, Margaret L. Gardel, and Ulrich S. Schwarz. "Model-based Traction Force Microscopy Reveals Differential Tension in Cellular Actin Bundles". In: *PLOS Computational Biology* 11.3 (2015), e1004076. ISSN: 1553-7358. DOI: 10.1371/journal.pcbi.1004076. URL: http://dx.plos.org/10.1371/journal.pcbi.1004076.

[92] Mona Jaggy. "Einfluss der 3D-Substratgeometrie auf das Zellverhalten". PhD thesis. 2013, p. 66.

[93] Feng Feng and William S. Klug. "Finite element modeling of lipid bilayer membranes". In: *Journal of Computational Physics* 220.1 (2006), pp. 394–408. ISSN: 00219991. DOI: 10.1016/j.jcp.2006.05.023.

[94] Lin Ma and William S. Klug. "Viscous regularization and r-adaptive remeshing for finite element analysis of lipid membrane mechanics". In: *Journal of Computational Physics* 227.11 (2008), pp. 5816–5835. ISSN: 00219991. DOI: 10.1016/j.jcp.2008.02.019. arXiv: 0709.0723.

[95] Wendy F Liu, Celeste M Nelson, Dana M Pirone, and Christopher S Chen. "E-cadherin engagement stimulates proliferation via Rac1". In: *Journal of Cell Biology* 173.3 (2006), pp. 431–441. ISSN: 00219525. DOI: 10.1083/jcb.200510087. URL: http://jcb.rupress.org/cgi/content/abstract/173/3/431.

[96] K. A. Kilian, B. Bugarija, B. T. Lahn, and M. Mrksich. "Geometric cues for directing the differentiation of mesenchymal stem cells". In: *Proceedings of the National Academy of Sciences* 107.11 (2010), pp. 4872–4877. ISSN: 0027-8424. DOI: 10.1073/pnas.0903269107. URL: http://www.pnas.org/cgi/doi/10.1073/pnas.0903269107.

[97] Ben Harland, Sam Walcott, and Sean X Sun. "Adhesion dynamics and durotaxis in migrating cells." In: *Physical biology* 8.1 (2011), p. 015011. ISSN: 00063495. DOI: 10.1088/1478-3975/8/1/015011.

[98] Brenton D Hoffman, Carsten Grashoff, and Martin a Schwartz. "Dynamic molecular processes mediate cellular mechanotransduction." In: *Nature* 475.7356 (2011), pp. 316–23. ISSN: 1476-4687. DOI: 10.1038/nature10316. URL: http://www.ncbi.nlm.nih.gov/pubmed/21776077.

[99] Alex Mogilner and Kinneret Keren. "The shape of motile cells." In: *Current biology : CB* 19.17 (2009), R762–71. ISSN: 1879-0445. DOI: 10.1016/j.cub.2009.06.053. URL: http://www.pubmedcentral.nih.gov/articlerender.fcgi?artid=2864320&tool=pmcentrez&rendertype=abstract.

[100] Ulrich S. Schwarz and Jérôme R.D. Soiné. "Traction force microscopy on soft elastic substrates: A guide to recent computational advances". In: *Biochimica et Biophysica Acta (BBA) - Molecular Cell Research* (2015). ISSN: 01674889. DOI: 10.1016/j.bbamcr.2015.05.028. URL: http://linkinghub.elsevier.com/retrieve/pii/S0167488915001822.

[101] Carsten Grashoff, Brenton D Hoffman, Michael D Brenner, Ruobo Zhou, Maddy Parsons, Michael T Yang, Mark A McLean, Stephen G Sligar, Christopher S Chen, Taekjip Ha, and Martin A Schwartz. "Measuring mechanical tension across vinculin reveals regulation of focal adhesion dynamics".

In: *Nature* 466.7303 (2010), pp. 263–266. ISSN: 0028-0836. DOI: 10.1038/nature09198.

[102] D R Stabley, Carol Jurchenko, S S Marshall, and K S Salaita. "Visualizing mechanical tension across membrane receptors with a fluorescent sensor". In: *Nature methods* 9.1 (2012). DOI: 10.1038/NMETH.1747.

[103] Masatoshi Morimatsu, Armen H Mekhdjian, Arjun S Adhikari, and Alexander R Dunn. "Molecular tension sensors report forces generated by single integrin molecules in living cells." In: *Nano letters* 13.9 (2013), pp. 3985–9. ISSN: 1530-6992. DOI: 10.1021/nl4005145.

[104] Brandon L Blakely, Christoph E Dumelin, Britta Trappmann, Lynn M Mcgregor, K Choi, Peter C Anthony, Van K Duesterberg, Brendon M Baker, Steven M Block, David R Liu, and Christopher S Chen. "A DNA-based molecular probe for optically reporting cellular traction forces". In: October (2014). DOI: 10.1038/nmeth.3145.

[105] John L Tan, Joe Tien, Dana M Pirone, Darren S Gray, Kiran Bhadriraju, and Christopher S Chen. "Cells lying on a bed of microneedles: an approach to isolate mechanical force." In: *Proceedings of the National Academy of Sciences of the United States of America* 100.4 (2003), pp. 1484–1489. ISSN: 0027-8424. DOI: 10.1073/pnas.0235407100.

[106] Olivia du Roure, Alexandre Saez, Axel Buguin, Robert H Austin, Philippe Chavrier, Pascal Silberzan, Pascal Siberzan, and Benoit Ladoux. "Force mapping in epithelial cell migration." In: *Proceedings of the National Academy of Sciences of the United States of America* 102.7 (2005), pp. 2390–2395. ISSN: 0027-8424. DOI: 10.1073/pnas.0408482102.

[107] L. Trichet, J. Le Digabel, R. J. Hawkins, S. R. K. Vedula, M. Gupta, C. Ribrault, P. Hersen, R. Voituriez, and B. Ladoux. "Evidence of a large-scale mechanosensing mechanism for cellular adaptation to substrate stiffness". In: *Proceedings of the National Academy of Sciences* 109.18 (2012), pp. 6933–6938. ISSN: 0027-8424. DOI: 10.1073/pnas.1117810109. URL: http://www.pnas.org/cgi/doi/10.1073/pnas.1117810109.

[108] S. Ghassemi, G. Meacci, S. Liu, a. a. Gondarenko, a. Mathur, P. Roca-Cusachs, M. P. Sheetz, and J. Hone. "Cells test substrate rigidity by local contractions on submicrometer pillars". In: *Proceedings of the National Academy of Sciences* 109.14 (2012), pp. 5328–5333. ISSN: 0027-8424. DOI: 10.1073/pnas.1119886109.

[109] C. Franck, S. Hong, S. a. Maskarinec, D. a. Tirrell, and G. Ravichandran. "Three-dimensional full-field measurements of large deformations in soft materials using confocal microscopy and digital volume correlation". In: *Experimental Mechanics* 47.3 (2007), pp. 427–438. ISSN: 00144851. DOI: 10.1007/s11340-007-9037-9.

[110] James P Butler, Iva Marija Tolić-Nørrelykke, Ben Fabry, and Jeffrey J Fredberg. "Traction fields, moments, and strain energy that cells exert on their surroundings." In: *American journal of physiology. Cell physiology* 282.3 (2002), pp. C595–605. ISSN: 0363-6143. DOI: 10.1152/ajpcell.00270.2001. URL: http://www.ncbi.nlm.nih.gov/pubmed/11832345.

[111] Benedikt Sabass, Margaret L Gardel, Clare M Waterman, and Ulrich S Schwarz. "High resolution traction force microscopy based on experimental and computational advances." In: *Biophysical journal* 94.1 (2008), pp. 207–220. ISSN: 00063495. DOI: 10.1529/biophysj.107.113670.

[112] Sergey V Plotnikov, Benedikt Sabass, Ulrich S Schwarz, and Clare M Waterman. *High-resolution traction force microscopy*. 1st ed. Vol. 123. Elsevier Inc., 2014, pp. 367–94. ISBN: 9780124201385. DOI: 10.1016/B978-0-12-420138-5.00020-3.

[113] Rudolf Merkel, Norbert Kirchgeßner, Claudia M. Cesa, and Bernd Hoffmann. "Cell Force Microscopy on Elastic Layers of Finite Thickness". In: *Biophysical Journal* 93.9 (2007), pp. 3314–3323. ISSN: 00063495. DOI: 10.1529/biophysj.107.111328. URL: http://linkinghub.elsevier.com/retrieve/pii/S0006349507715850.

[114] Jerome Soine. "Reconstruction and Simulation of Cellular Traction Forces". PhD thesis. 2014.

[115] Sergej I Kabanikhin. *Inverse and ill-posed problems*. Inverse and Ill-Posed Problems Series ; 55 ; Inverse and ill-posed problems series 55. Berlin [u.a.]: De Gruyter, 2012, XV, 459 S. ISBN: 978-3-11-022400-9 ; 3-11-022400-3 ; 978-3-11-022401-6.

[116] Heinz W Engl, Martin Hanke-Bourgeois, and Andreas Neubauer. *Regularization of inverse problems*. Mathematics and its applications ¡Dordrecht¿ ; 375 ; Mathematics and its applications ¡Dordrecht¿ 375. Dordrecht [u.a.]: Kluwer Acad. Publ., 2000, VIII, 321 S. ISBN: 0-7923-4157-0 ; 0-7923-6140-7 ; 978-0-7923-6140-4 ; 978-0-7923-4157-4.

[117] "Numerical treatment of inverse problems in differential and integral equations". In: ed. by Peter [Hrsg.] Deuflhard and Ernst [Hrsg.] Hairer. Progress in scientific computing ; 2 ; Progress in scientific computing 2. Boston ; Basel

; Stuttgart: Birkhäuser, 1983, XIII, 357 S. ISBN: 3-7643-3125-9 ; 978-3-7643-3125-2.

[118] Per Christian Hansen. "Analysis of Discrete Ill-Posed Problems by Means of the L-Curve". In: *SIAM Review* 34.4 (1992), pp. 561–580. ISSN: 0036-1445. DOI: 10.1137/1034115. URL: http://epubs.siam.org/doi/abs/10.1137/1034115.

[119] Per Christian Hansen and Dianne Prost O'Leary. "The Use of the L-Curve in the Regularization of Discrete Ill-Posed Problems". In: *SIAM Journal on Scientific Computing* 14.6 (1993), pp. 1487–1503. ISSN: 1064-8275. DOI: 10.1137/0914086. URL: http://epubs.siam.org/doi/abs/10.1137/0914086.

[120] Vikram S. Deshpande, Robert M. McMeeking, and Anthony G. Evans. "A model for the contractility of the cytoskeleton including the effects of stress-fibre formation and dissociation". In: *Proceedings of the Royal Society A: Mathematical, Physical and Engineering Sciences* 463.2079 (2007), pp. 787–815. ISSN: 1364-5021. DOI: 10.1098/rspa.2006.1793. URL: http://rspa.royalsocietypublishing.org/cgi/doi/10.1098/rspa.2006.1793.

[121] Amit Pathak, Vikram S Deshpande, Robert M McMeeking, and Anthony G Evans. "The simulation of stress fibre and focal adhesion development in cells on patterned substrates." In: *Journal of the Royal Society, Interface / the Royal Society* 5.22 (2008), pp. 507–524. ISSN: 1742-5689. DOI: 10.1098/rsif.2007.1182.

[122] Camilla Mohrdieck, Alexander Wanner, Wouter Roos, Alexander Roth, Erich Sackmann, Joachim P Spatz, and Eduard Arzt. "A theoretical description of elastic pillar substrates in biophysical experiments." In: *Chemphyschem : a European journal of chemical physics and physical chemistry* 6.8 (2005), pp. 1492–8. ISSN: 1439-4235. DOI: 10.1002/cphc.200500109. URL: http://www.ncbi.nlm.nih.gov/pubmed/16082672.

[123] Amit Pathak, Christopher S. Chen, Anthony G. Evans, and Robert M. McMeeking. "Structural Mechanics Based Model for the Force-Bearing Elements Within the Cytoskeleton of a Cell Adhered on a Bed of Posts". In: *Journal of Applied Mechanics* 79.6 (2012), p. 061020. ISSN: 00218936. DOI: 10.1115/1.4006452. URL: http://appliedmechanics.asmedigitalcollection.asme.org/article.aspx?articleid=1476695.

[124] Todd Thoresen, Martin Lenz, and Margaret L Gardel. "Reconstitution of contractile actomyosin bundles." In: *Biophysical journal* 100.11 (2011), pp. 2698–705. ISSN: 1542-0086. DOI: 10.1016/j.bpj.2011.04.031. URL: http://www.pubmedcentral.nih.gov/articlerender.fcgi?artid=3117186&tool=pmcentrez&rendertype=abstract.

[125] *Java Delauney Triangulation*. URL: https://code.google.com/p/jdt/wiki/jdtUsage.

[126] Per-olof Persson and Gilbert Strang. "A Simple Mesh Generator in MATLAB". In: 46.2 (2004), pp. 329–345.

[127] W. Bangerth, R. Hartmann, and G. Kanschat. "deal.II—A general-purpose object-oriented finite element library". In: *ACM Transactions on Mathematical Software* 33.4 (2007), 24–es. ISSN: 00983500. DOI: 10.1145/1268776.1268779. URL: http://portal.acm.org/citation.cfm?doid=1268776.1268779.

[128] P. W. Oakes, Y. Beckham, J. Stricker, and M. L. Gardel. "Tension is required but not sufficient for focal adhesion maturation without a stress fiber template". In: *The Journal of Cell Biology* 196.3 (2012), pp. 363–374. ISSN: 0021-9525. DOI: 10.1083/jcb.201107042. URL: http://www.jcb.org/cgi/doi/10.1083/jcb.201107042.

[129] N Q Balaban, U S Schwarz, D Riveline, P Goichberg, G Tzur, I Sabanay, D Mahalu, S Safran, a Bershadsky, L Addadi, and B Geiger. "Force and focal adhesion assembly: a close relationship studied using elastic micropatterned substrates." In: *Nature cell biology* 3.5 (2001), pp. 466–72. ISSN: 1465-7392. DOI: 10.1038/35074532. URL: http://www.ncbi.nlm.nih.gov/pubmed/11331874.

[130] Jonathan Stricker, Benedikt Sabass, Ulrich S Schwarz, and Margaret L Gardel. "Optimization of traction force microscopy for micron-sized focal adhesions." In: *Journal of physics. Condensed matter : an Institute of Physics journal* 22.19 (2010), p. 194104. ISSN: 1361-648X. DOI: 10.1088/0953-8984/22/19/194104. URL: http://www.pubmedcentral.nih.gov/articlerender.fcgi?artid=2879600&tool=pmcentrez&rendertype=abstract.

[131] Patrick W Oakes and Margaret L Gardel. "Stressing the limits of focal adhesion mechanosensitivity." In: *Current opinion in cell biology* 30C (2014), pp. 68–73. ISSN: 1879-0410. DOI: 10.1016/j.ceb.2014.06.003. URL: http://www.ncbi.nlm.nih.gov/pubmed/24998185.

[132] Jonathan Stricker, Yvonne Aratyn-Schaus, Patrick W Oakes, and Margaret L Gardel. "Spatiotemporal constraints on the force-dependent growth of focal adhesions." In: *Biophysical journal* 100.12 (2011), pp. 2883–93. ISSN: 1542-0086. DOI: 10.1016/j.bpj.2011.05.023. URL: http://www.pubmedcentral.nih.gov/articlerender.fcgi?artid=3123981&tool=pmcentrez&rendertype=abstract.

[133] Jianping Fu, Yang-Kao Wang, Michael T Yang, Ravi a Desai, Xiang Yu, Zhijun Liu, and Christopher S Chen. "Mechanical regulation of cell function with geometrically modulated elastomeric substrates". In: *Nature Methods* 7.9 (2010), pp. 733–736. ISSN: 1548-7091. DOI: 10.1038/nmeth.1487. URL: http://www.nature.com/doifinder/10.1038/nmeth.1487.

[134] Cynthia A Reinhart-King, Micah Dembo, and Daniel A Hammer. "The Dynamics and Mechanics of Endothelial Cell Spreading". In: *Biophysical Journal* 89.1 (2005), pp. 676–689. ISSN: 00063495. DOI: 10.1529/biophysj.104.054320. URL: http://linkinghub.elsevier.com/retrieve/pii/S0006349505727132.

[135] Joseph P. Califano and Cynthia A. Reinhart-King. "Substrate Stiffness and Cell Area Predict Cellular Traction Stresses in Single Cells and Cells in Contact". In: *Cellular and Molecular Bioengineering* 3.1 (2010), pp. 68–75. ISSN: 1865-5025. DOI: 10.1007/s12195-010-0102-6. URL: http://link.springer.com/10.1007/s12195-010-0102-6.

[136] Shang-You Tee, Jianping Fu, Christopher S Chen, and Paul A Janmey. "Cell Shape and Substrate Rigidity Both Regulate Cell Stiffness". In: *Biophysical Journal* 100.5 (2011), pp. L25–L27. ISSN: 00063495. DOI: 10.1016/j.bpj.2010.12.3744. URL: http://linkinghub.elsevier.com/retrieve/pii/S0006349511001275.

[137] Fang Li, Bin Li, Qing-Ming Wang, and James H-C. Wang. "Cell shape regulates collagen type I expression in human tendon fibroblasts". In: *Cell Motility and the Cytoskeleton* 65.4 (2008), pp. 332–341. ISSN: 08861544. DOI: 10.1002/cm.20263. URL: http://doi.wiley.com/10.1002/cm.20263.

[138] Ning Wang, Emanuele Ostuni, George M. Whitesides, and Donald E. Ingber. "Micropatterning tractional forces in living cells". In: *Cell Motility and the Cytoskeleton* 52.2 (2002), pp. 97–106. ISSN: 0886-1544. DOI: 10.1002/cm.10037. URL: http://doi.wiley.com/10.1002/cm.10037.

[139] Andrew D. Rape, Wei-hui Guo, and Yu-li Wang. "The regulation of traction force in relation to cell shape and focal adhesions". In: *Biomaterials* 32.8 (2011), pp. 2043–2051. ISSN: 01429612. DOI: 10.1016/j.biomaterials.2010.11.044. URL: http://linkinghub.elsevier.com/retrieve/pii/S0142961210014833.

[140] Katherine Luby-Phelps. "Cytoarchitecture and Physical Properties of Cytoplasm: Volume, Viscosity, Diffusion, Intracellular Surface Area". In: 1999, pp. 189–221. DOI: 10.1016/S0074-7696(08)60527-6. URL: http://linkinghub.elsevier.com/retrieve/pii/S0074769608605276.

[141] M S Hamaguchi and Y Hiramoto. "Protoplasmic movement during polar-body formation in starfish oocytes." In: *Experimental cell research* 112.1 (1978), pp. 55–62. ISSN: 00144827. DOI: 10.1016/0014-4827(78)90524-4.

[142] A. Esseling-Ozdoba, D. Houtman, A. A M Van Lammeren, E. Eiser, and A. M C Emons. "Hydrodynamic flow in the cytoplasm of plant cells". In: *Journal of Microscopy* 231.2 (2008), pp. 274–283. ISSN: 00222720. DOI: 10.1111/j.1365-2818.2008.02033.x.

[143] Tom Shemesh, Alexander B Verkhovsky, Tatyana M Svitkina, Alexander D Bershadsky, and Michael M Kozlov. "Role of Focal Adhesions and Mechanical Stresses in the Formation and Progression of the Lamellum Interface". In: *Biophysj* 97.5 (2009), pp. 1254–1264. ISSN: 0006-3495. DOI: 10.1016/j.bpj.2009.05.065. URL: http://dx.doi.org/10.1016/j.bpj.2009.05.065.

[144] Tom Shemesh, Alexander D Bershadsky, and Michael M Kozlov. "Physical Model for Self-Organization of Actin Cytoskeleton and Adhesion Complexes at the Cell Front". In: *Biophysj* 102.8 (2012), pp. 1746–1756. ISSN: 0006-3495. DOI: 10.1016/j.bpj.2012.03.006. URL: http://dx.doi.org/10.1016/j.bpj.2012.03.006.

[145] Hal F. Brinson and L. Catherine Brinson. *Polymer Engineering Science and Viscoelasticity*. Boston, MA: Springer US, 2008, pp. 1–14. ISBN: 978-0-387-73860-4. DOI: 10.1007/978-0-387-73861-1. URL: http://link.springer.com/10.1007/978-0-387-73861-1_1http://link.springer.com/10.1007/978-0-387-73861-1.

[146] Alain Goriely, Mark Robertson-Tessi, Michael Tabor, and Rebecca Vandiver. "Elastic growth models". In: *Mathematical Modelling of Biosystems*. Applied Optimization 102 (2008). Ed. by Rubem P. Mondaini and Panos M. Pardalos, pp. 1–44. DOI: 10.1007/978-3-540-76784-8. URL: http://www.springerlink.com/content/x8u4244722023711/http://link.springer.com/10.1007/978-3-540-76784-8.

[147] Sham Tlili, Cyprien Gay, François Graner, Philippe Marcq, François Molino, and Pierre Saramito. "Colloquium: Mechanical formalisms for tissue dynamics". In: *The European Physical Journal E* 38.5 (2015), p. 33. ISSN: 1292-8941. DOI: 10.1140/epje/i2015-15033-4. URL: http://link.springer.com/10.1140/epje/i2015-15033-4.

[148] J Prost, F Jülicher, and J-f Joanny. "Active gel physics". In: *Nature physics* 11.February (2015). DOI: 10.1038/NPHYS3224.

[149] S. Hyder Ali Muttaqi Shah and Haitao Qi. "Starting solutions for a viscoelastic fluid with fractional Burgers' model in an annular pipe". In: *Nonlinear Analysis: Real World Applications* 11.1 (2010), pp. 547–554. ISSN: 14681218. DOI: 10.1016/j.nonrwa.2009.01.012. URL: http://dx.doi.org/10.1016/j.nonrwa.2009.01.012.

[150] B Launay. "A Simplified Nonlinear Model for Describing the Viscoelastic Properties of Wheat Flour Doughs at High Shear Strain". In: *Cereal Chemistry* 67.1 (1990), pp. 25–31.

[151] H Schiessel, R Metzler, a Blumen, and T F Nonnenmacher. "Generalized viscoelastic models: their fractional equations with solutions". In: *Journal of Physics A: Mathematical and General* 28.23 (1999), pp. 6567–6584. ISSN: 0305-4470. DOI: 10.1088/0305-4470/28/23/012.

[152] P. Lindstrom and G. Turk. "Fast and memory efficient polygonal simplification". In: *Proceedings Visualization '98 (Cat. No.98CB36276)* (1998). ISSN: 1. DOI: 10.1109/VISUAL.1998.745314.

[153] Devin Strickland, Yuan Lin, Elizabeth Wagner, C Matthew Hope, Josiah Zayner, Chloe Antoniou, Tobin R Sosnick, Eric L Weiss, and Michael Glotzer. "TULIPs: tunable, light-controlled interacting protein tags for cell biology". In: *Nature Methods* 9.4 (2012), pp. 379–384. ISSN: 1548-7091. DOI: 10.1038/nmeth.1904. URL: http://www.nature.com/doifinder/10.1038/nmeth.1904.

[154] G. T. Charras, C.-K. Hu, M. Coughlin, and T. J. Mitchison. "Reassembly of contractile actin cortex in cell blebs". In: *The Journal of Cell Biology* 175.3 (2006), pp. 477–490. ISSN: 0021-9525. DOI: 10.1083/jcb.200602085. URL: http://www.jcb.org/cgi/doi/10.1083/jcb.200602085.

[155] Guillaume Salbreux, Guillaume Charras, and Ewa Paluch. "Actin cortex mechanics and cellular morphogenesis". In: *Trends in Cell Biology* 22.10 (2012), pp. 536–545. ISSN: 09628924. DOI: 10.1016/j.tcb.2012.07.001. arXiv: 84866882608. URL: http://www.ncbi.nlm.nih.gov/pubmed/22871642http://linkinghub.elsevier.com/retrieve/pii/S0962892412001110.

[156] Kausalya Murthy and Patricia Wadsworth. "Myosin-II-Dependent Localization and Dynamics of F-Actin during Cytokinesis". In: *Current Biology* 15.8 (2005), pp. 724–731. ISSN: 09609822. DOI: 10.1016/j.cub.2005.02.055. URL: http://linkinghub.elsevier.com/retrieve/pii/S0960982205002289.

[157] Tianzhi Luo, Krithika Mohan, Pablo a Iglesias, and Douglas N Robinson. "Molecular mechanisms of cellular mechanosensing". In: *Nature Materials* 12.11 (2013), pp. 1064–1071. ISSN: 1476-1122. DOI: 10.1038/nmat3772. URL:

http://www.ncbi.nlm.nih.gov/pubmed/24141449http://www.nature.com/doifinder/10.1038/nmat3772.

[158] Péter Lénárt, Christian P Bacher, Nathalie Daigle, Arthur R Hand, Roland Eils, Mark Terasaki, and Jan Ellenberg. "A contractile nuclear actin network drives chromosome congression in oocytes". In: *Nature* 436.7052 (2005), pp. 812–818. ISSN: 0028-0836. DOI: 10.1038/nature03810. URL: http://www.nature.com/doifinder/10.1038/nature03810.

[159] Stuart a. Newman. "E.E. Just's "independent irritability" revisited: The activated egg as excitable soft matter". In: *Molecular Reproduction and Development* 76.10 (2009), pp. 966–974. ISSN: 1040452X. DOI: 10.1002/mrd.21094. URL: http://doi.wiley.com/10.1002/mrd.21094.

[160] A. L. Hodgkin, A. F. Huxley, and B Katz. "Measurement of current-voltage relations in the membrane of the giant axon of Loligo". In: *The Journal of Physiology* 116.4 (1952), pp. 424–448. ISSN: 00223751. DOI: 10.1113/jphysiol.1952.sp004716. URL: http://www.ncbi.nlm.nih.gov/pmc/articles/PMC1392219/http://doi.wiley.com/10.1113/jphysiol.1952.sp004716.

[161] Richard FitzHugh. "Impulses and Physiological States in Theoretical Models of Nerve Membrane". In: *Biophysical Journal* 1.6 (1961), pp. 445–466.

[162] J. Nagumo, S. Arimoto, and S. Yoshizawa. "An Active Pulse Transmission Line Simulating Nerve Axon". In: *Proceedings of the IRE* 50.10 (1962), pp. 2061–2070. ISSN: 0096-8390. DOI: 10.1109/JRPROC.1962.288235. URL: http://ieeexplore.ieee.org/lpdocs/epic03/wrapper.htm?arnumber=4066548.

[163] Lendert Gelens, Graham A Anderson, and James E Ferrell. "Spatial trigger waves: positive feedback gets you a long way". In: *Molecular Biology of the Cell* 25.22 (2014), pp. 3486–3493. ISSN: 1059-1524. DOI: 10.1091/mbc.E14-08-1306. URL: http://www.molbiolcell.org/cgi/doi/10.1091/mbc.E14-08-1306.

[164] Jeremy B. Chang and James E. Ferrell Jr. "Mitotic trigger waves and the spatial coordination of the Xenopus cell cycle". In: *Nature* 500.7464 (2013), pp. 603–607. ISSN: 0028-0836. DOI: 10.1038/nature12321. URL: http://www.pubmedcentral.nih.gov/articlerender.fcgi?artid=3758429&tool=pmcentrez&rendertype=abstracthttp://www.nature.com/doifinder/10.1038/nature12321.

[165] John J Tyson and P Keener. "SINGULAR PERTURBATION Theory of traveling waves in excitable media (A REVIEW)". In: *Physica D* 32 (1988), pp. 327–361. ISSN: 01672789. DOI: 10.1016/0167-2789(88)90062-0.

[166] William M. Bement, Marcin Leda, Alison M. Moe, Angela M. Kita, Matthew E. Larson, Adriana E. Golding, Courtney Pfeuti, Kuan-Chung Su, Ann L. Miller, Andrew B. Goryachev, and George von Dassow. "Activator–inhibitor coupling between Rho signalling and actin assembly makes the cell cortex an excitable medium". In: *Nature Cell Biology* 17.11 (2015), pp. 1471–1483. ISSN: 1465-7392. DOI: 10.1038/ncb3251. URL: http://dx.doi.org/10.1038/ncb3251http://www.nature.com/doifinder/10.1038/ncb3251.

[167] Tianzhi Luo, Krithika Mohan, Vasudha Srivastava, Yixin Ren, Pablo A. Iglesias, and Douglas N. Robinson. "Understanding the Cooperative Interaction between Myosin II and Actin Cross-Linkers Mediated by Actin Filaments during Mechanosensation". In: *Biophysical Journal* 102.2 (2012), pp. 238–247. ISSN: 00063495. DOI: 10.1016/j.bpj.2011.12.020. URL: http://dx.doi.org/10.1016/j.bpj.2011.12.020http://linkinghub.elsevier.com/retrieve/pii/S0006349511054221.

[168] Albina Orlova and Edward H Egelman. "Cooperative rigor binding of myosin to actin is a function of F-actin structure". In: *Journal of Molecular Biology* 265.5 (1997), pp. 469–474. ISSN: 00222836. DOI: 10.1006/jmbi.1996.0761. URL: http://linkinghub.elsevier.com/retrieve/pii/S0022283696907615.

[169] Marina Soares e Silva, Martin Depken, Björn Stuhrmann, Marijn Korsten, Fred C MacKintosh, and Gijsje H Koenderink. "Active multistage coarsening of actin networks driven by myosin motors". In: *Proceedings of the National Academy of Sciences* 108.23 (2011), pp. 9408–9413. ISSN: 0027-8424. DOI: 10.1073/pnas.1016616108. URL: http://www.pnas.org/cgi/doi/10.1073/pnas.1016616108.

[170] Matthew R Stachowiak, Mark a Smith, Elizabeth Blankman, Laura M Chapin, Hayri E Balcioglu, Shuyuan Wang, Mary C Beckerle, and Ben O'Shaughnessy. "A mechanical-biochemical feedback loop regulates remodeling in the actin cytoskeleton." In: *Proceedings of the National Academy of Sciences of the United States of America* 111.49 (2014). ISSN: 1091-6490. DOI: 10.1073/pnas.1417686111. URL: http://www.ncbi.nlm.nih.gov/pubmed/25422436.

[171] K. Vijay Kumar, Justin S. Bois, Frank Jülicher, and Stephan W. Grill. "Pulsatory patterns in active fluids". In: *Physical Review Letters* 112.20 (2014), pp. 1–5. ISSN: 10797114. DOI: 10.1103/PhysRevLett.112.208101. arXiv: NIHMS150003.

[172] JD Logan. *An introduction to nonlinear partial differential equations*. 2010. ISBN: 9780470225950. URL: http://books.google.com/books?hl=en&lr=&id=Zk4se2vNw2YC&oi=fnd&pg=PT4&dq=An+Introduction+to+

Nonlinear+Partial+Differential+Equations&ots=OOXQ4V-_K_&sig=VOc4kAXygT6yRAWiTppsqJumBh0.

[173] Steven H. Strogatz. *Nonlinear Dynamics and Chaos*.

[174] Hervé Turlier, Basile Audoly, Jacques Prost, and Jean-François Joanny. "Furrow constriction in animal cell cytokinesis." In: *Biophysical journal* 106.1 (2014), pp. 114–23. ISSN: 1542-0086. DOI: 10.1016/j.bpj.2013.11.014. URL: http://www.ncbi.nlm.nih.gov/pubmed/24411243.

Acknowledgment

First and foremost I would like to sincerely thank my supervisor Prof. Dr. Ulrich Schwarz. Without his advice and support this thesis would not have been possible. From him I have learned much about biophysics, physics, and research in general. I am grateful for many interesting discussions and for the opportunity to be a part of his group.

I thank Prof. Dr. Heinz Horner for kindly agreeing to review this thesis.

I warmly thank the current and former members of the Schwarz group for the great and inspiring time we have spent together. I cordially thank Marco Linke and Anna Battista for sharing the office with me and many helpful spontaneous discussions. I further thank Marco Linke for his contributions in image processing to the project on cells in three-dimensional scaffolds. Many thanks go to Jerome Soine for the great time in the Bioquant and elsewhere, and for the inspiring joint work on MBTFM. I thank Dimitri Probst for his simulations of continuum mechanics models that are similar to the discrete model used in chapter 5. I thank Max Hoffmann, Niko Schnellbächer, and Marco Linke for organizing our trips to many conferences.

I gratefully thank my collaboration partners Benjamin Richter, Mona Jaggy, and Martin Bastmeyer from Karlsruhe, Elena Kassianidou and Sanjay Kumar from Berkeley, Jonathan Stricker, Patrick Oakes, Margaret Gardel, and Elizabeth Wagner and Michael Glotzer from Chicago, and Johanna Bischof and Peter Lénárt from EMBL for stimulating discussions and sharing their expertise on the biological systems.

I thank the Konrad Adenauer Foundation for financial support and many interesting seminars.

Cordial thanks also go to my parents and my brothers for their continuous support and believing in me. I warmly and gratefully thank Silke Bergeler for her continuous love, encouragement and support, many interesting discussions, proof-reading this thesis, and for many unforgettable moments.